

Christian Schelte

Dynamics of Optical Localized Structures
in Passively Mode-Locked Lasers

2021

Theoretische Physik

Dynamics of Optical Localized Structures in Passively Mode-Locked Lasers

Inaugural-Dissertation
zur Erlangung des Doktorgrades
der Naturwissenschaften im Fachbereich Physik
der Mathematisch-Naturwissenschaftlichen Fakultät
der Westfälischen Wilhelms-Universität Münster

angefertigt im Rahmen eines Cotutelle-Verfahrens
zwischen der Westfälischen Wilhelms-Universität Münster
und der Universitat de les Illes Balears

vorgelegt von
Christian Schelte
aus Iserlohn

2021

Dekan: Prof. Dr. Michael Rohlfing
Erste Gutachterin: PD Dr. Svetlana V. Gurevich
Zweite Gutachterin: Prof. Dr. Kathy Lüdge
Tag der mündlichen Prüfung:
Tag der Promotion:



Universitat
de les Illes Balears

**DOCTORAL THESIS
2021**

Doctoral Programme of Physics

**DYNAMICS OF OPTICAL LOCALIZED STRUCTURES
IN PASSIVELY MODE-LOCKED LASERS**

Christian Schelte

**Thesis Supervisor: Julien J. P. Javaloyes
Thesis Supervisor: Svetlana V. Gurevich
Thesis tutor: Damià Gomis Bosch**

Doctor by the Universitat de les Illes Balears

Abstract

This thesis focuses on the theoretical analysis of passively mode-locked (PML) lasers and in particular on the dynamics of mutually independent pulses called temporal localized structures (TLSs). These can exist below the lasing threshold in the presence of a saturable absorber with low saturation intensity and sufficiently large modulation of the nonlinear absorption in relation to the amount of linear cavity losses. Pulses above a critical energy may persist by first spending part of their energy to saturate the absorber in order to achieve net gain and replenish the lost photons. In a long cavity regime, the gain medium has enough time to fully rebuild the population inversion before the pulse returns. However, when operating below threshold, the off solution remains stable and small perturbations die out. This way, TLSs can be separated arbitrarily far apart without additional pulses growing in between as they would, e.g., in the harmonic mode-locking regime above threshold. Indeed, well separated pulses do not interact at all since the gain is fully recovered and thus these optical pulses become independent, individually addressable localized structures. They may be placed in arbitrary arrangements and naturally remain at their relative positions if not moved by an additional perturbation such as a modulation of the gain. This renders them of great interest for applications like telecommunications because they could lead, for instance, to reconfigurable bit arrays.

In this thesis, models for four different setups are derived and analyzed both via direct numerical simulations and numerical path continuation using the Matlab package DDE-BIFTOOL. All of the models contain time-delay and the specific details of their numerical treatment are discussed. In particular, a novel functional mapping approach is introduced which significantly reduces the computational effort of simulating TLSs.

First, an already well established unidirectional ring laser delay differential equation (DDE) model is used to build a baseline of TLS behavior with a focus on studying the influence of the gain bias and linewidth enhancement factor (Henry factor), as well as their interplay. The saddle-node bifurcations that give rise to the TLSs are found for a stable single peak solution and several unstable profiles which exhibit additional ringing peaks. Pairs of these solutions intersect at specific points in the parameter space thus forming an intricate single manifold. In addition, an oscillatory regime is analyzed where the trailing edge of the pulse oscillates due to amplitude-phase coupling mediated by the linewidth enhancement factor.

Next, specific models for practically relevant vertical external-cavity surface-emitting lasers (VECSELs) are investigated. Here, the modeling of strong feedback and multiple reflections requires the use of delay algebraic equations (DAEs) that pose an additional theoretical challenge as compared to standard DDEs. Specifically, models are considered for a vertical-cavity surface-emitting laser coupled to a resonant saturable absorber mirror and a mode-locked integrated external-cavity surface-emitting laser (MIXSEL). The cavity geometry of coupled nonlinear mirrors incurs strong third order dispersion (TOD) that

Abstract

can induce a series of low intensity satellites on the leading edge of a pulse. In this regime, a new kind of instability involving a global bifurcation with features of excitability is found where a satellite replaces its parent pulse.

From the comparison of the results obtained in the different models it can be concluded that the unidirectional ring laser DDE model in its standard form is not sufficient to accurately describe all aspects of the dynamics in VECSEL setups. It neglects the dispersive nature of microcavities that is conserved in the DAE approach. In particular, we identify TOD to be a dominant effect in pulse destabilization. It affects short pulses more strongly, thus rendering the optimization of the pulse duration a trade-off inherent to such systems.

Finally, a Gires-Tournois interferometer containing a Kerr nonlinear medium is considered. This passive microcavity is arranged with an external cavity geometry where energy is supplied via optical injection by a continuous wave (CW) laser. While this system is qualitatively different from the VECSELs it can be modeled using the same DAE approach and exhibits strong influence of TOD. The coherent CW pump is converted into phase-locked pulses thus forming a Kerr frequency comb. They are made up of interlocking fronts that connect two bistable CW background states and can form complex patterns of TLSs.

Kurzzusammenfassung

Diese Doktorarbeit befasst sich mit der theoretischen Analyse von passiv modengekoppelten (PML, engl. *passive mode-locking*) Lasern, insbesondere mit der Dynamik von von-einander unabhängigen Pulsen, die als zeitlich lokalisierte Strukturen (TLS, engl. *temporal localized structure*) bezeichnet werden. In Gegenwart eines sättigbaren Absorbers mit geringer Sättigungsintensität und ausreichend großer Modulation der nichtlinearen Absorption im Verhältnis zu den linearen Resonatorverlusten können solche Pulse unterhalb der Laserschwelle existieren. Über einem kritischen Energiewert können Pulse dauerhaft bestehen, indem sie zunächst einen Teil ihrer Energie für die Sättigung des Absorbers aufwenden, sodass eine Nettoverstärkung erzielt wird und die verlorenen Photonen zurück gewonnen werden können. Unter Verwendung eines ausreichend langen Resonators hat das Verstärkungsmedium genug Zeit, um die Populationsinversion vollständig wiederherzustellen, bevor der Puls im nächsten Resonatorumlauf zurückkehrt. Da man jedoch unterhalb der Laserschwelle arbeitet, bleibt der homogene, ausgeschaltete Zustand stabil und kleine Störungen sind gedämpft. Auf diese Weise können TLS beliebig weit voneinander getrennt werden, ohne dass zwischen ihnen zusätzliche Pulse entstehen, wie es z.B. im harmonischen Modenkopplungsbereich oberhalb des Schwellenwertes der Fall wäre. In der Tat interagieren weit getrennte Pulse überhaupt nicht miteinander, da sich das Verstärkungsmedium dazwischen vollständig wieder aufbaut und die optischen Pulse somit zu unabhängigen, individuell adressierbaren lokalisierten Strukturen werden. Sie können willkürlich angeordnet werden und bleiben von allein an ihren relativen Positionen, wenn sie nicht durch eine zusätzliche Störung wie eine Modulation der Pumprate beeinflusst werden. Dies macht sie sehr interessant für Anwendungen wie Telekommunikation, wo sie beispielsweise als rekonfigurierbare Bit-Arrays eingesetzt werden könnten.

In dieser Doktorarbeit werden Modelle für vier verschiedene PML-Laser Aufbauten hergeleitet und analysiert, sowohl mithilfe von direkten numerischen Simulationen als auch durch numerische Pfad-Kontinuierung von Lösungssäten mithilfe des Matlab-Pakets DDE-BIFTOOL. Alle Modelle enthalten zeitverzögerte Terme, deren numerische Behandlung im Detail diskutiert wird. Insbesondere wird ein neuartiger Behandlungsansatz solcher Gleichungen als funktionale Abbildung eingeführt, der den Rechenaufwand für die Simulation von TLS erheblich reduziert.

Zunächst wird ein bereits gut etabliertes zeitverzögertes Differentialgleichungsmodell (DDE, engl. *delay differential equation*) für einen unidirektionalen Ringlaser verwendet, um eine Vergleichsgrundlage für das Verhalten von TLS zu erhalten, wobei der Schwerpunkt auf der Untersuchung des Einflusses der Pumprate, des Steigerungsfaktors der Linienbreite (Henry Faktor) und deren beider Zusammenspiel liegt. Die Sattel-Knoten-Bifurkationen, die den TLS unterliegen, werden sowohl für eine stabile Lösung mit einem einzelnen Intensitätsmaximum, als auch für mehrere instabile Profile gefunden, welche zusätzliche lokale Maxima aufweisen. Diese Lösungen schneiden sich paarweise an bestimmten Punkten

im Parameterraum und bilden so eine komplizierte zusammenhängende Gesamtstruktur. Zusätzlich wird ein Instabilitätsregime analysiert, bei dem die hintere Flanke eines Pulses oszilliert. Dies geschieht aufgrund von Amplituden-Phasen-Kopplung, die durch den Steigerungsfaktor der Linienbreiten vermittelt wird.

Als nächstes werden spezifische Modelle für anwendungsrelevante vertikale oberflächenemittierende Laser mit externem Resonator (VECSEL, engl. *vertical external-cavity surface-emitting laser*) untersucht. Zur Modellierung starker Rückkopplungen mit Mehrfachreflexionen sind zeitverzögerte algebraische Gleichungen (DAEs, engl. *delay algebraic equation*) notwendig, deren theoretische Behandlung im Vergleich zu gewöhnlichen DDEs eine zusätzliche Herausforderung darstellt. Konkret werden in diesem Zusammenhang zwei Modelle betrachtet, erstens für einen oberflächenemittierenden Laser mit vertikalem Resonator, der an einen resonanten sättigbaren Absorberspiegel gekoppelt ist, und zweitens für einen modengekoppelten integrierten oberflächenemittierenden Laser mit externem Resonator. Die Resonatorgeometrie von gekoppelten nichtlinearen Spiegeln weist starke Dispersion dritter Ordnung (TOD, engl. *third order dispersion*) auf, welche eine Reihe von Satelliten mit geringer Intensität an der Vorderflanke eines Pulses induzieren kann. In diesem Regime tritt eine neue Art von Instabilität auf, bei der ein Puls von einem seiner Satelliten ersetzt wird. Diesem Verhalten liegt eine globale Bifurkation mit Merkmalen von Erregbarkeit zugrunde.

Aus dem Vergleich der in den verschiedenen Modellen erzielten Ergebnisse kann geschlossen werden, dass das unidirektionale Ringlaser DDE Modell in seiner klassischen Form nicht ausreicht, um alle Aspekte der Dynamik in VECSEL-Aufbauten genau zu beschreiben. Es vernachlässigt die dispersiven Effekte von Mikroresonatoren, die im DAE-Ansatz erhalten bleiben, wo Dispersion dritter Ordnung als dominanter Effekt bei der Pulsdestabilisierung identifiziert werden kann. Diese wirkt sich insbesondere auf kurze Pulse aus, weshalb zur Optimierung der Pulsdauer in VECSEL Systemen Kompromisse eingegangen werden müssen, da ihnen TOD inhärent ist.

Schließlich wird ein Gires-Tournois-Interferometer betrachtet, welches ein nichtlineares Kerr-Medium enthält. Ein solcher passiver Mikroresonator kann mit einem äußeren Resonator gekoppelt werden, dem Energie durch optische Injektion mittels eines Dauerstrichlasers (CW, engl. *continuous wave*) zugeführt wird. Obwohl sich dieses System qualitativ von den vorher behandelten VECSELS unterscheidet, kann es mit demselben DAE-Ansatz beschrieben werden und weist einen starken Einfluss von TOD auf. Die kohärente CW-Strahlung wird in phasengekoppelte Pulse umgewandelt, wodurch ein Kerr-Frequenzkamm gebildet wird. Diese bestehen aus ineinandergrifffenden Fronten, die zwei bistabile CW-Hintergrundzustände verbinden und komplexe TLS-Muster bilden können.

Resumen

Esta tesis se centra en el análisis teórico de láseres con bloqueo de modo pasivo (PML, por el acrónimo inglés de *passive mode-locking*) y, en particular, en la dinámica de pulsos mutuamente independientes denominados estructuras localizadas temporales (TLS, por el acrónimo inglés de *temporal localized structure*). Estos pueden existir por debajo del umbral de emisión láser en presencia de un absorbente saturable con baja intensidad de saturación y modulación de la absorción no lineal suficientemente grande en relación con la cantidad de pérdidas lineales de cavidad. Los pulsos por encima de una energía crítica pueden persistir gastando un parte de su energía para saturar el absorbente con el fin de experimentar una ganancia neta y reponer los fotones perdidos. En un régimen de cavidad larga, el medio de ganancia tiene suficiente tiempo para recuperarse hasta que el pulso regresa para recuperar completamente la inversión de la población. Sin embargo, dado que operamos por debajo del umbral, la solución para el láser apagado permanece estable y las pequeñas perturbaciones desaparecen. De esta manera, los TLS se pueden separar arbitrariamente lejos sin que crezcan pulsos adicionales en medio, como lo harían, por ejemplo, en el régimen de bloqueo de modo armónico por encima del umbral. De hecho, los pulsos bien separados no interactúan en absoluto, ya que la ganancia se recupera completamente y, por lo tanto, estos pulsos ópticos se convierten en estructuras localizadas independientes y direccionables individualmente. Pueden disponerse de forma arbitraria y, naturalmente, permanecer en sus posiciones relativas si no son movidas por una perturbación adicional como la modulación de la ganancia. Por eso, se vuelven de gran interés para aplicaciones en campos como el de las telecomunicaciones, pues permitirían crear matrices de bits reconfigurables.

En esta tesis, se derivan y analizan modelos para cuatro configuraciones diferentes mediante simulaciones numéricas directas y continuación numérica de ramas de soluciones utilizando el paquete Matlab DDE-BIFTOOL. Todos los modelos contienen retardo de tiempo y se discuten los detalles específicos de su tratamiento numérico. En particular, se introduce un enfoque nuevo llamado el mapeo funcional que reduce significativamente el esfuerzo computacional de simular los TLS.

Primero, se utiliza un modelo de ecuación diferencial de retardo (DDE, por el acrónimo inglés de *delay differential equation*) ya bien establecido para un láser de anillo unidireccional. Así se produce una línea de base del comportamiento de los TLS con un enfoque en estudiar la influencia de la fuerza de la ganancia y el factor de aumento del ancho de línea (factor de Henry) y su interacción. Las bifurcaciones silla-nodo de ciclos límites que dan lugar a los TLS, se encuentran para una solución estable con un pico único y también para varios perfiles inestables que exhiben picos adicionales. Estas soluciones se cruzan en pares en puntos específicos del espacio de parámetros, formando así una única variedad intrincada. Además, se analiza un régimen oscilatorio en el que el flanco de bajada del pulso oscila debido al acoplamiento de amplitud-fase mediado por el factor de aumento

del ancho de línea.

A continuación, se investigan modelos específicos para láseres emisores de superficie con cavidad vertical externa (VECSEL, por el acrónimo inglés de *vertical external-cavity surface-emitting laser*) que son relevantes en varias aplicaciones. Aquí, la descripción de la fuerte retroalimentación y de las reflexiones múltiples requiere utilizar ecuaciones algebraicas con retardo (DAE, por el acrónimo inglés de *delay algebraic equation*) que plantean un desafío teórico adicional en comparación con las DDE estándar. Específicamente, los modelos se consideran para un láser emisor de superficie de cavidad vertical acoplado a un espejo resonante absorbente saturable y también un láser integrado de bloqueado de modo emisor de superficie con cavidad externa (MIXSEL, por el acrónimo inglés de *mode-locked integrated external-cavity surface-emitting laser*). La geometría de estas cavidades con espejos no lineales acoplados incurre en una fuerte dispersión de tercer orden (TOD, por el acrónimo inglés de *third order dispersion*) que puede inducir una serie de satélites de baja intensidad en el flanco de subida de los pulsos. En este régimen, se encuentra un nuevo tipo de inestabilidad que involucra una bifurcación global con características del fenómeno de excitabilidad donde un satélite reemplaza al pulso principal.

De la comparación de los resultados obtenidos en los diferentes modelos se puede concluir que el modelo DDE de láser de anillo unidireccional en su forma estándar no es suficiente para describir con exactitud todos los aspectos de la dinámica en las configuraciones VECSEL. El modelo DDE no contempla la naturaleza dispersiva de las microcavidades que sí se tiene en cuenta en el enfoque DAE. En particular, identificamos la TOD como un efecto dominante en la desestabilización de los pulsos. Afecta a los pulsos cortos con más fuerza, por lo que la optimización de la duración del pulso se torna en una compensación inherente a dichos sistemas.

Finalmente, se considera un interferómetro de Gires-Tournois que contiene un medio no lineal de tipo Kerr. Esta microcavidad pasiva se dispone con una geometría de cavidad externa donde la energía se suministra por inyección óptica mediante un láser de onda continua (CW, por el acrónimo inglés de *continuous wave*). Si bien este sistema es cuantitativamente diferente de los VECSEL, se puede modelizar utilizando el mismo enfoque DAE y exhibe una fuerte influencia de la TOD. La bomba CW coherente se convierte en pulsos bloqueados en fase, formando así un peine de frecuencia Kerr. Están formados por frentes entrelazados que conectan dos estados de fondos CW biestables y que pueden formar patrones complejos de TLS.

Resum

Aquesta tesi se centra en l'anàlisi teòrica de lòsers amb bloqueig de mode passiu (PML, per l'acrònim anglès de *passive mode-locking*) i, en particular, en la dinàmica de polsos mítuament independents anomenats estructures localitzades temporals (TLS, per l'acrònim anglès de *temporal localized structure*). Aquests poden existir per sota del llindar d'emissió lòser en presència d'un absorbent saturable amb baixa intensitat de saturació i modulació de l'absorció no lineal prou gran en relació amb la quantitat de pèrdues lineals de cavitat. Els polsos per sobre d'una energia crítica poden persistir gastant un part de la seva energia per saturar l'absorbent per tal d'experimentar un guany net i reposar els fotons perduts. En un règim de cavitat llarga, el mitjà de guany té prou temps per recuperar-se fins que el pols torna per recuperar completament la inversió de la població. No obstant això, atès que operem per sota del llindar, la solució per el lòser apagat roman estable i les petites pertorbacions desapareixen. D'aquesta manera, els TLS es poden separar arbitràriament lluny sense que creixin polsos addicionals entremig, com ho farien, per exemple, en el règim de bloqueig de manera harmònica per sobre del llindar. De fet, els polsos ben separats no interactuen en absolut, ja que el guany es recupera completament i, per tant, aquests polsos òptics es converteixen en estructures localitzades independents i direccionalment. Poden disposar-se de forma arbitrària i, naturalment, romando en les seves posicions relatives si no són mogudes per una pertorbació addicional com la modulació del guany. Per això, es tornen de gran interès per a aplicacions en camps com el de les telecomunicacions, ja que permetrien crear matrius de bits reconfigurables.

En aquesta tesi, es deriven i analitzen models per a quatre configuracions diferents mitjançant simulacions numèriques directes i continuació numèrica de branques de solucions utilitzant el paquet Matlab DDE-BIFTOOL. Tots els models contenen retard de temps i es discuteixen els detalls específics del seu tractament numèric. En particular, s'introduceix un enfocament nou anomenat el mapeig funcional que redueix significativament l'esforç computacional de simular els TLS.

Primer, s'utilitza un model d'equació diferencial de retard (DDE, per l'acrònim anglès de *delay differential equation*) ja ben establert per a un lòser d'anell unidireccional. Així es produeix una línia de base del comportament dels TLS amb un enfocament en estudiar la influència de la força del guany i el factor d'augment de l'ample de línia (factor d'Henry) i la seva interacció. Les bifurcacions cadira-node de cicles límits que donen lloc als TLS, es troben per a una solució estable amb un pic únic i també per a diversos perfils inestables que exhibeixen pics addicionals. Aquestes solucions es creuen en parells en punts específics de l'espai de paràmetres, formant així una única varietat intricada. A més, s'analitza un règim oscillatori en el qual el flanc de baixada del pols oscilla causa de l'acoblament d'amplitud-fase intervingut pel factor d'augment de l'ample de línia.

A continuació, s'investiguen models específics per a lòsers emissors de superfície amb cavitat vertical externa (VECSEL, per l'acrònim anglès de *vertical external-cavity surface-*

emitting laser) que són rellevants en diverses aplicacions. Aquí, la descripció de la forta retroalimentació i de les reflexions múltiples requereix utilitzar equacions algebraiques amb retard (DAE, per l'acrònim anglès de *delay algebraic equation*) que plantegen un desafiament teòric addicional en comparació amb les DDE estàndard. Específicament, els models es consideren per a un làser emissor de superfície de cavitat vertical acoblat a un mirall ressonant absorbent saturable i també un làser integrat de bloquejat de mode emissor de superfície amb cavitat externa (MIXSEL, per l'acrònim anglès de *mode-locked integrated external-cavity surface-emitting laser*). La geometria d'aquestes cavitats amb miralls no lineals acoblats incorre en una forta dispersió de tercer ordre (TOD, per l'acrònim anglès de *third order dispersion*) que pot induir una sèrie de satèl·lits de baixa intensitat en el flanc de pujada dels polsos. En aquest règim, es troba un nou tipus d'inestabilitat que involucra una bifurcació global amb característiques del fenomen de excitabilitat on un satèl·lit reemplaça al pols principal.

De la comparació dels resultats obtinguts en els diferents models es pot concloure que el model DDE de làser d'anell unidireccional en la seva forma estàndard no és suficient per descriure amb exactitud tots els aspectes de la dinàmica en les configuracions VECSEL. El model DDE no contempla la naturalesa dispersiva de les microcavitats que sí es té en compte en l'enfocament DAE. En particular, identifiquem la TOD com un efecte dominant en la desestabilització dels polsos. Afecta els polsos curts amb més força, de manera que l'optimització de la durada del pols es torna en una compensació inherent a aquests sistemes.

Finalment, es considera un interferòmetre de Gires-Tournois que conté un mitjà no lineal de tipus Kerr. Aquesta microcavidad passiva es disposa amb una geometria de cavitat externa on l'energia es subministra per injecció òptica mitjançant un làser d'ona contínua (CW, per l'acrònim anglès de *continuous wave*). Si bé aquest sistema és qualitativament diferent dels VECSEL, es pot modelitzar utilitzant el mateix enfocament DAE i exhibeix una forta influència de la TOD. La bomba CW coherent es converteix en polsos bloquejats en fase, formant així una pinta de freqüència Kerr. Estan formats per fronts entrellaçats que connecten dos estats de fons CW biestables i que poden formar patrons complexos de TLS.

Contents

Abstract	i
Kurzzusammenfassung	iii
Resumen	v
Resum	vii
Contents	ix
1 Introduction	1
1.1 Passive mode-locking	3
1.2 Localized structures	7
1.3 Outline of this thesis	10
2 Theoretical Modeling	13
2.1 Transverse electromagnetic wave equation	13
2.1.1 Maxwell's equations in materials	13
2.1.2 Wave equation with electric polarization	14
2.1.3 Transverse mode	15
2.2 Electric susceptibility model	16
2.3 Unidirectional traveling wave model	18
2.4 Unidirectional ring laser model	20
2.4.1 Introducing a co-moving coordinate	20
2.4.2 Dimensionless scaling	21
2.4.3 Integrating the co-moving coordinate	22
2.4.4 Introducing a causal filter	23
2.4.5 Case of a Lorentzian filter	23
2.5 Alternative approach	24
2.5.1 Scaled dimensionless model	24
2.5.2 Constructing the general solution	24
2.5.3 Calculating the Green's function	25
2.5.4 Introducing a useful difference expression	26
2.5.5 Active and passive sections	27
2.5.6 Connecting the sections	27
2.5.7 Carrier rate equations	28
2.6 Injected microcavity with thin quantum well region	29
2.6.1 Solving the intracavity field	29

2.6.2	Expansion around a cavity mode	32
2.6.3	Scaling the fields	33
2.7	Delay algebraic differential equation model for VECSELs	34
2.8	VCSEL coupled to resonant saturable absorber mirror	36
2.9	Mode-locked integrated external-cavity surface-emitting-laser	38
2.10	Injected Gires-Tournois interferometer with Kerr nonlinearity	40
3	Methods	41
3.1	Numerical integration of time-delayed equations	41
3.2	4th-Order Runge-Kutta with delay interpolation	42
3.3	Semi-implicit leapfrog integration	43
3.3.1	Concept	44
3.3.2	VCSEL-RSAM update	45
3.3.3	MIXSEL update	45
3.3.4	KGTI update	46
3.4	Functional mapping	46
3.4.1	Concept	47
3.4.2	Drift compensation	48
3.4.3	Carrier reconnection as a boundary condition	48
3.4.4	Ring model implementation	49
3.4.5	VCSEL-RSAM implementation	49
3.4.6	MIXSEL implementation	50
3.5	Continuation in DDE-BIFTOOL	50
3.5.1	Implementing a DAE as a singularly perturbed differential equation	50
3.5.2	Phase invariance	51
3.5.3	Rotational symmetry extension	52
4	Unidirectional Ring Laser	55
4.1	Lasing threshold	55
4.2	Temporal localized structures	57
4.2.1	Obtaining a TLS in DDE-BIFTOOL	57
4.2.2	Parameter set	59
4.2.3	Typical TLS profile and branch structure	59
4.2.4	Bistable region	60
4.2.5	Multi-peak solutions	60
4.3	Amplitude-phase coupling	63
4.3.1	Trailing edge instability	64
4.3.2	Bifurcation diagrams	65
4.3.3	Combined 2-parameter scan in the fully localized regime	67
4.4	Solution manifold	68
4.4.1	Symmetric case without absorber linewidth enhancement	68
4.4.2	Transcritical crossover of multi-peaked solutions	68
4.4.3	Asymmetric case with absorber linewidth enhancement	71
4.5	Bifurcation branches	74
4.5.1	Secondary fold profiles	75

4.5.2	Convergence toward the localized regime	75
4.5.3	Comparision with direct numerical simulations	76
4.5.4	Comparison with an exponential Haus PDE model	78
4.6	Functional mapping performance	79
4.6.1	Timing jitter analysis	79
4.6.2	Q-switched model-locking	81
5	VCSEL with Resonant Saturable Absorber Mirror	83
5.1	Continuous wave analysis	83
5.1.1	Mirror reflectivities	83
5.1.2	Lasing threshold	85
5.2	Temporal localized structures	87
5.2.1	Bistable TLS region and multistability	88
5.2.2	Influence of the linewidth enhancement factors	88
5.3	Satellites on the leading edge	92
5.3.1	The case of the empty cavity	92
5.3.2	Satellites replacing the main pulse	95
5.3.3	Low frequency dynamics	95
5.4	Satellite instability	97
5.4.1	Progression of the dynamics	97
5.4.2	Experimental parameters	103
5.4.3	Comparison with the CCQGLE	105
6	Mode-locked Integrated External-Cavity Surface-Emitting-Laser	109
6.1	Lasing threshold	109
6.2	Satellite instability	110
6.2.1	Bistability	113
6.2.2	Regions of dynamical behaviors	116
6.3	Numerical path continuation	119
6.3.1	Typical pulse profiles	119
6.3.2	Singular perturbation convergence	121
6.3.3	Stability limitations	122
6.3.4	Folding solution branch	122
6.4	Linear stability analysis using the functional mapping	124
6.5	Saddle-node infinite-period to Andronov-Hopf transition	127
6.5.1	Period scaling	127
6.5.2	Andronov-Hopf oscillation	128
6.5.3	Transition dynamics	130
6.6	Excitability	131
6.7	Comparison with a dispersive Haus-PDE model	134
7	Injected Kerr Gires-Tournois Interferometer	139
7.1	Continuous wave solutions	139
7.1.1	Linear stability in the long delay limit	140

7.2	Temporal localized structures	145
7.2.1	Dark and bright solitons	145
7.2.2	Hysteresis	146
7.3	Bifurcation analysis	148
7.3.1	Coinciding drift velocities	150
7.3.2	Regions of localized solutions	152
7.4	Complex patterns	153
7.4.1	Complex molecules	153
7.4.2	Coexistence of TLSs	153
7.5	Time-advanced equation	155
8	Summary and Outlook	159
List of Publications		I
List of Acronyms		III
List of Figures		V
Bibliography		IX

1 Introduction

On the verge of the past century new and, at the time, unexplainable experimental observations led to the paradigm shift of quantum physics. The explanation of the photoelectric effect by A. Einstein [Ein05] made a strong case for the notion of the quantification of light that was previously proposed by M. Planck [Pla01]. Light can neither be described by particles nor waves alone, but as a wave packet that encompasses the properties of both. These quanta of the electromagnetic field are called photons. Science and technology have been striving to exploit the unique opportunities that lie in quantum effects ever since.

The quantum description of light and matter interaction [Ein17] allows for three distinct elementary processes: absorption, spontaneous emission and stimulated emission. Figure 1.1 shows schematics of these. In contrast to the random spontaneous emission of a photon, the stimulated kind produces a true copy of an already present, resonant photon. While both kinds have the same energy, as they are converted from the potential energy of an excited electronic transition, the stimulated photon indeed shares the direction and phase of its parent. When the occupation number of excited electrons in a medium is larger than for the ground state, the stimulated emission can outweigh the resonant absorption, thus creating a coherent amplification of photons that pass through the material. This situation is called population inversion and the amplification process is referred to as gain. It paved the road for the development of the very influential MASER, which is an acronym for Microwave Amplification by Stimulated Emission of Radiation [ST58]. One of the most important and widely applied technologies of the modern age is the laser which is derived from the same concept, but operates at optical frequencies. The term laser simply comes from replacing the word microwave with light. The first realization of such a device was build using a ruby crystal [Mai60].

Using gain, one can not only build lasers but also optical amplifiers that strengthen an arbitrary incoming light signal at the price of the outgoing signal containing additional noise. An important use case exists in long distance optical fiber communications to counteract the attenuation of the signal. Nowadays, the term laser is typically used for

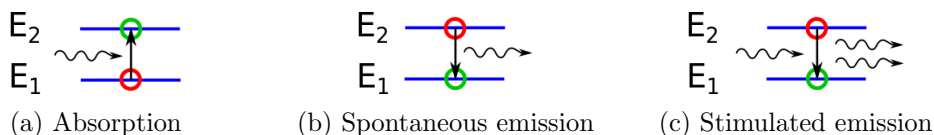


Figure 1.1: Schematics of elementary light and matter interactions. An electron can transition between two distinct energy levels E_1 and E_2 together with the creation or annihilation of photons (wavy arrows) corresponding to the energy difference. Initial and final occupations of electronic states are represented by red and green circles, respectively.

the combination of gain with optical feedback. A gain medium is placed in an optical resonator called the laser cavity, typically formed by a set of mirrors. Depending on the geometry, photons will go back and forth or in circles around the cavity, thus passing the gain medium repeatedly. This way, the intensity of radiation in the cavity is able to grow very large with a portion of it being extracted at each roundtrip. This process only works for photons in a resonant mode of the cavity. If the angle of the propagation direction diverges even slightly from the cavity axis, the photon will exit the cavity prematurely and only experience limited gain. Therefore, the resulting laser signal is a highly directional and monochromatic beam of light. Spontaneous emission into the laser mode creates a superposition between coherent and incoherent emission. The latter is usually considered an undesirable source of noise during laser operation. In addition, it reduces the gain available to the resonant mode. Note, however, that this incoherent fraction is fundamental in seeding the lasing process above threshold.

Lasers can generally be described by three differential equations: one each for the electromagnetic field, the polarization of the gain material and the population inversion of its electronic states. Depending on the photon lifetime in the cavity and the materials used, some of these processes can be very fast relative to the others. Exploiting this time scale separation, one may assume a fast equation to instantaneously follow another which often allows for solving it as a function of the other and then substituting it. This technique is called adiabatic elimination. Effectively, the number of dynamical equations necessary to describe the laser is reduced. Depending on this number, lasers are usually categorized as class A, B and C lasers [AH87]. Here, class C means a full system using all three variables, class B means the polarization is fast and eliminated and, finally, class A means the inversion is also fast so only the differential equation for the field remains. This thesis will concentrate on class B lasers which encompass, e.g., semiconductor and solid state lasers.

Designing lasers encompasses a large variety of elements and their combinations so only an incomplete overview of the most important ones can be given here. Many factors have to be taken into consideration including output power, the noise and transverse polarization of the signal, size and heat dissipation. For commercial use additional requirements come into play, e.g. efficiency, temperature stability and resistance to damage. The choice of resonator designs and gain media further depends on the required type of laser signal such as single frequency continuous wave (CW) emission, tunability or pulse generation. Generally optimization of any characteristic will incur compromises for others.

Typical cavity designs are Fabry-Pérot interferometers, ring topologies build with mirrors, waveguides on a chip, single or multi-mode fibers and monolithic structures where the cavity is closed by reflective coatings or simply total internal reflection on the facets.

Gain media can be created using many materials that differ in a wide range of properties like the bandwidth of the gain, its quantum efficiency, gain per unit length, the upper-state lifetime and the damage threshold, to name but a few important ones. Some of the most common types are discussed in the following: A comparatively simple setup is a confined gas that is ionized by an electrical discharge. Ions offer sharp atomic transitions with long lifetimes of the excited states. However, in a hot gas the movement and collisions of an ion with other particles are detrimental as its velocity shifts the wavelength of the emitted photon and the excited state can be perturbed. This issue does not occur when

an insulator is doped with ions (typically rare earths or transition elements) because their positions will be fixed. The corresponding gain media can be built in bulk using single crystals or glass that usually has less desirable properties due to its amorphous structure but is very cost-efficient. More recently, ceramic compounds have been used as well. In addition, glass (usually in the form of fused silica) can be drawn into optical fibers that act as a waveguide and are bendable. In contrast to gases, these types of gain media have to be pumped optically since the insulating matrix does not conduct electricity. Depending on the specific material, an appropriate laser may be required to pump, but in some cases a simple flash lamp is sufficient. Another kind of optically pumped medium is a dye in liquid solution, typically a complex fluorescent aromatic molecule [SL66, SSV66]. Such compounds offer a very wide bandwidth for both emission and pumping. Finally, an important class is direct band gap semiconductors which provide a very large amount of gain as compared to other materials at the cost of an increased linewidth [Hen82]. Doped semiconductors can be combined to build diodes and heterojunctions that allow for pumping with electric current. They are often used to build optical pumps to drive other lasers. However, some semiconductors can be optically pumped themselves without the need for doping.

Recently, a cavity design called Vertical-Cavity Surface-Emitting-Laser (VCSEL) has been increasingly applied and investigated [JHS⁺91]. It consists of an active layer sandwiched between two distributed Bragg reflectors (DBRs). These are made up of thin layers with alternating refractive indices in a stacked arrangement. They hence feature very high reflectivity around resonant wavelengths. Compared to other lasers, VCSELs can be built very thin and compact while allowing wide lasing apertures such that large intensities can be distributed in the transverse spatial dimension along with very good beam quality. It is possible to build large arrays of VCSELs on a single wafer for cost savings or specific applications. They are either pumped by current injection, typically from a circular electrode around the lasing area, or optically by, e.g., a lower wavelength CW diode laser from the side at the Brewster angle, where no light is reflected, for maximum efficiency.

1.1 Passive mode-locking

Pulsed laser emission is interesting from a technical point of view because of the high peak powers that can be reached, e.g. for industrial cutting and welding, and to produce signals that can be used in optical information transmission and processing.

A technique for high energy pulse generation is Q-switching. It consists in modulating the losses of a laser, i.e. its Q (quality) factor. When the losses are high, no significant resonant buildup of photons in the cavity is possible, hence, the gain can accumulate a large inversion. The losses are then lowered for normal laser operation to occur. A large intensity builds up until the gain is depleted again which results in a large pulse in the output. The required Q-switch can be an active change in the cavity like, e.g., a shutter or realignment of a mirror, but more recently passive Q-switches have been realized using materials whose transmittivities are sensitive to the light intensity [SLLP64, KMM64, BG64]. An important drawback of Q-switching is the relatively long duration of the generated pulses which is incurred by the underlying gain lifetime.

For high peak power and high bandwidth data transmission the focus lies on the pulse

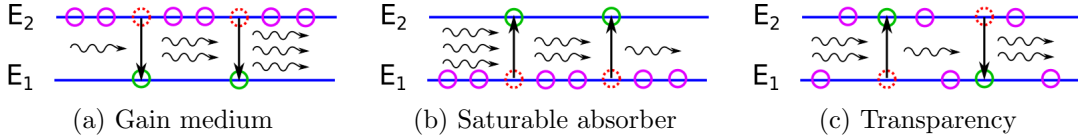


Figure 1.2: Schematics of active materials used in passively mode-locked lasers. Occupied electronic states are shown as purple circles, other representations are the same as in Fig. 1.1. (a) In a gain device the carrier population must be inverted. Photons can be created in a cascade thus realizing amplification of an initial resonant photon. (b) Without carrier inversion, photons are annihilated in exchange for excited states causing absorption. (c) Both processes will saturate for sufficiently large intensities where the carriers approach the threshold of inversion. Here, creation and annihilation of photons becomes equally likely, effectively rendering the material transparent.

duration. To form short pulses a different mechanism must be found. Usually these consists of a superposition of many laser modes. For their coherent sum to result in a pulse, their relative phases must be properly aligned. This phase locking is therefore called mode-locking [HFP64]. It can be achieved by modulating the cavity losses by external means, e.g., by modulating the pump, the phase change per roundtrip or even by blocking the beam. In this regime, the photons experience different amplification or losses as a function of time and thus will concentrate at a favorable position, i.e., the intensity will synchronize with the modulation. Due to the intrusive nature of this technique one speaks of active mode-locking. The repetition rate and pulse length are limited by the speed at which the external modulation can be imposed.

In order to overcome this limit one needs to exploit fast dynamics intrinsic to the used materials. Such a form of pulse generation is consequently termed passive mode-locking (PML). More recently Kerr-lensing was used to produce very short pulses [SSP91]. Here, a high intensity causes a laser beam to self-focus when passing a Kerr nonlinear medium while an iris cuts the outer part of the beam. A more focused beam experiences less absorption and thus lumped intensities are preferred. Note, that to the end of reaching shorter pulses other methods like pulse compression may be applied [Tre69]. These are, however, a completely separate concept from PML and focus on modifying the output signal instead of its generation.

The most common technique to implement PML is introducing a saturable absorber into the cavity. This can simply be an unpumped section of the gain material in a monolithic laser or an additional device like a resonant saturable absorber mirror (RSAM). A large incident intensity will excite electrons in a semiconductor until the occupation of carriers approaches the threshold to inversion, i.e. transparency. In this situation, an equilibrium of absorption and stimulated emission is reached. Creation and annihilation of a photon become equally likely, rendering the device transparent. Ultimately, this results in the relative losses being intensity dependent. Figure 1.2 shows schematics of the processes in gain and absorber materials, as well as their saturation. In a gain medium a photon will pass and interact with many excited electrons such that the amplification will depend not only on the occupation inversion but on the length of the gain section as well. The same

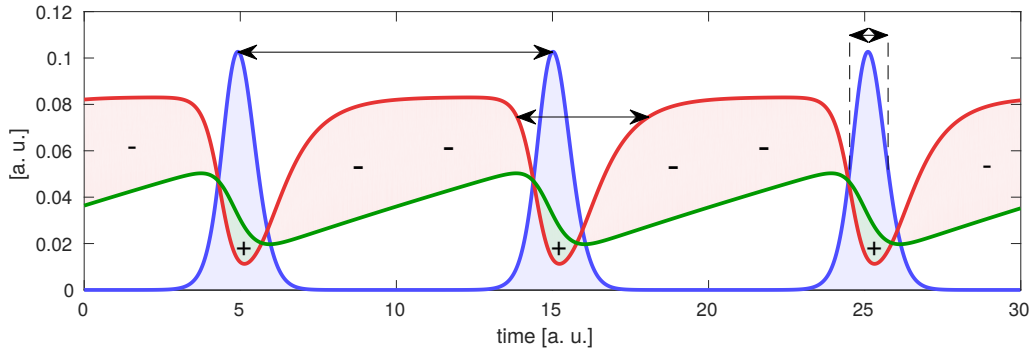


Figure 1.3: Schematic of the principle of passive mode-locking in a laser system with a saturable absorber. The lines show the temporal profiles of the pulse intensity in blue, the gain in green and the absorption in red. The light green (red) area marked with plus (minus) signs represents the interval of net gain (losses). The arrows highlight the different scales of the pulse width, the absorber recovery and the repetition rate.

goes for the attenuation when crossing an absorber medium.

Figure 1.3 shows how the interplay of the gain and absorber carrier densities can lead to the formation of intensity pulses: The pulse spends a part of its photons in order to saturate the absorber and significantly lower the losses. As a consequence, the gain may outweigh the absorption for a time where the intensity can grow. This interval is limited by the gain saturating in turn until absorption wins out again. The window where gain is larger than absorption is called the net-gain window. Here, the pulse can replenish the photons lost in the absorber, by attenuation and from signal extraction. Both gain and absorber carriers recover after the pulse has passed and the cycle repeats at the next roundtrip.

The time scales of the field evolution and the carrier relaxation are typically very different. This incurs a strong stiffness in the mathematical modeling of the phenomenon. Several strategies have been used to model such systems. Pulse iterative models that restrict the analysis to an area around the pulse can lead to a qualitative partial differential equation (PDE) model called the Haus master equations [Hau00]. One may further assume a certain analytical pulse shape to obtain rate equations describing only the pulse parameters [UA05b, UA05a]. Further, delay differential equation (DDE) models, such as [VT05], have been able to successfully describe many aspects of PML. At any fixed point in the cavity, the field returns after one roundtrip. This happens after a roundtrip time that corresponds to the cavity length divided by the propagation velocity. In other words, the field depends both on the current state of the laser and itself in the past. Therefore, lasers can naturally be described using time-delay.

Generally, delays are found where some process requires a certain amount of time to complete before its result affects the system again. This can be as simple as the transport to a destination and is thus a typical property of networks. Time-delays are encountered in many scientific fields. Some examples in biology are neural networks, like the brain and nervous system, hormone regulation and population dynamics where pregnancy and

nursing periods are important factors. Similar effects are found throughout modern life in logistics, traffic jams (caused by the finite reaction times of drivers) and the distribution of information. Technological application of delays is prevalent in the form of control loops used in manufacturing, process engineering and electronics; see [YG17] for a review. Of particular interest to this thesis is the natural appearance of time-delays in the propagation of electromagnetic waves and thus laser signals.

Among the most promising current subjects of investigation in the area of PML are Vertical-External-Cavity Surface-Emitting-Lasers (VECSELs) that consist of a VCSEL gain mirror coupled with an external cavity to promote PML [HDT⁺00, HPG⁺01, HPA⁺02, TFG⁺04]. One way to both introduce saturable absorption and to close the external cavity at the same time is to couple the VCSEL to an RSAM face to face. An alternative lies in placing a saturable absorber layer directly into the VCSEL, i.e., next to the gain. The external cavity can then be closed by a simple feedback mirror. Such a setup is called a Mode-locked Integrated External-Cavity Surface-Emitting-Laser or in short MIXSEL [MBR⁺07, RWM⁺10]. The active mirrors are microcavities and are spaced far apart, i.e., they are very small ($\sim 1 \mu\text{m}$) as compared to the length of the external cavity where the field propagates unperturbed ($\sim 10 \text{ cm}$). Thus, the signal returns after one roundtrip to become an injection to the microcavity which can be described using time-delay. The roundtrip time of the internal microcavity field is very short in comparison to the external cavity and can be modeled with ordinary differential equations (monomode microcavity).

Trains of consecutive pulses are periodic signals with their spectra being composed of equally spaced modes. Because of its particular shape, such a spectrum is called a frequency comb. The distance between modes is called the free spectral range and relates to the repetition rate of the pulses. Frequency combs can be used as a set of well known reference frequencies for spectroscopy and metrology by using beatings of a signal of interest with the comb.

Another type of frequency comb generation is injected Kerr fiber loops that have a set of cavity resonances. Since the group velocity in the fiber depends on the intensity of the radiation, these resonances shift as a function of the intensity which causes second order dispersion. In these systems, localized states can appear on the injected CW background. This constitutes a distinct mechanism to achieve passive mode-locking which, due to the injection, does not have phase invariance.

Typically, bright solitons, i.e. peaks on a low intensity background, appear under anomalous dispersion [DSA⁺07] and dark solitons, i.e. dips on a high intensity background, for normal dispersion [PRGK⁺16, GWM⁺17]. Both types can have variable widths. However, under the influence of third order dispersion both types can be found to coexist [TG10]. Due to the distributed nature of the nonlinearity over the whole fiber cavity, these systems are described very successfully by another PDE, namely the one-dimensional version of the so-called Lugiato-Lefever equation [GBCC14].

A pulse can be viewed as a lump of photons that moves in the cavity periodically. If one imagines to take a snapshot of the cavity at every roundtrip, i.e. at multiples of the delay time, the pulse would appear to have an almost constant position. When cutting the time trace into pieces with the length of the delay time and then stacking these pieces, we can observe the pulse as it slowly evolves from roundtrip to roundtrip. This is called a pseudo-space-time representation. Here, the pseudo-time corresponds to the

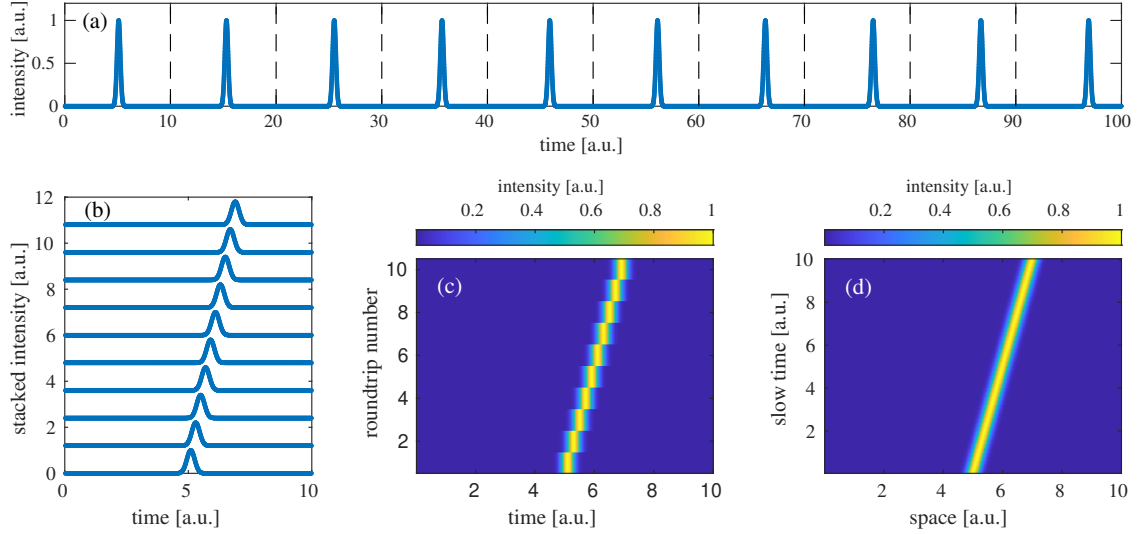


Figure 1.4: Schematic of the pseudo-space-time representation of a simple pulse. (a) A regular pulse train obtained in a DDE model. Due to causality, the repetition period is longer than the delay time. The dashed vertical lines mark multiples of the delay time where the time trace is cut. (b) The resulting roundtrips are shown in a stacked manner. (c) The respective pseudo-space-time representation which always contains a residual staggered motion. (d) A corresponding PDE representation for comparison. Here, the pulse drifts along the continuous slow time variable. Such a drift can be canceled by introducing an advection term.

roundtrip number and real time in the delay interval has become a space-like coordinate. Note, that the slow roundtrip time is actually not a continuous dimension. A schematic of these concepts and their relation is presented in Figure 1.4. In this framework, the idea to develop PDE models indeed appears intuitive [AGLM92, GP96, EJWY17]. The evolution of the pulse profile in the pseudo-space representation is then described with the help of partial differential operators. Here, an advection term (the first derivative of the profile) can be artificially added to the model with a prefactor that, when chosen appropriately, compensates for the residual drift of the pulse thus rendering it stationary, i.e., in a pseudo-space-time plot the pulse appears vertical. This would correspond to taking snapshots at multiples of the actual period of the pulse rather than the cold cavity roundtrip time.

1.2 Localized structures

Nature is full of examples for the spontaneous formation of self-organized patterns. They can be the energetically favored in systems like the Swift-Hohenberg model for thermal fluctuations on a convective instability [SH77] where a patterned state has the least free energy. In open complex systems the collective behavior of many degrees of freedom

can form so-called dissipative structures. They typically appear in out of equilibrium situations where a system is energetically driven and, at the same time, subjected to losses [AA08]. This can be as simple as heating and cooling a substance, but may involve a plethora of complex processes, e.g. in biological organisms. Usually such systems can be described by PDEs containing spatial operators. Their homogeneous solutions can undergo a Turing bifurcation which means that periodic perturbations around a dominant finite wavelength become unstable and grow in amplitude, thus giving rise to periodic or more complicated patterns. Prominent examples are convective flows in hydrodynamics like Rayleigh-Bénard cells [Bén01], colloids in a dewetting suspension [MBPV⁺07], color patterns on the skin of animals [Kon02] and naturally occurring vegetation patterns in low precipitation regions [vHMSZ01]. Different types of patterns appear in, e.g., oscillatory reaction-diffusion systems in chemistry like the famous Belousov-Zhabotinsky reaction [SE03], the accumulation of granular media like dunes and sand ripples in the desert caused by wind or underwater by currents [NO93], filamentation of electric discharges in gases [AP01], magnetization domains in ferromagnetism [LN79] and ice crystals in snow [ML66].

One of the most prevalent equations in pattern formation is the cubic Ginzburg-Landau equation (GLE) which is an amplitude equation, e.g. for an order parameter in systems with phase transitions. Its real-valued form can model many macroscopic systems like Rayleigh-Bénard convection. From a mathematical standpoint, it can be considered to be the normal form of a finite wavelength instability [AK02]. In optics however, the nature of the electromagnetic field requires a complex-valued version of the GLE. The cubic terms of the standard equation suffice only to describe gain saturation. With additional quintic terms a saturable absorber can be modelled in passive mode-locking, thus allowing for the pattern state to become subcritical [vH92].

Another important model is the nonlinear Schrödinger equation which can be obtained from the complex GLE by keeping only the imaginary parts of the complex parameters or, vice versa, the GLE can be considered as a dissipative version of the nonlinear Schrödinger equation. It describes passive waveguides and fibers with a Kerr nonlinearity [CGT64] that can exhibit solitons [HT73, MSG80], as well as many other phenomena in nature such as gravity waves in deep water [Zak68] and plasma oscillations [Zak72].

The GLE and the nonlinear Schrödinger equation both have a phase invariance as the equations only contain terms that are at least first order in the field. In contrast, the Lugiato-Lefever equation [LL87] has a constant forcing term which describes a CW pumping beam in an otherwise passive cavity. This breaks the phase symmetry, but otherwise resembles a dissipative version of the nonlinear Schrödinger equation. Among many things, it successfully describes Kerr frequency combs obtained in such systems. The modes that constitute such combs can, in addition, be phase-locked to give pulses which are called dissipative cavity solitons. In a sufficiently long fiber cavity these pulses can become localized as their mutual interactions vanish with increasing distance.

Localized structures can appear in several ways. One possible scenario is the interlocking of fronts that connect different domains of a system, e.g. liquid and solid phases. Another example is bistability of a homogeneous background state and a periodic state where a localized structure can be considered as a finite number of periods living on the stable background state. Given a large aspect ratio between the domain and the correlation width

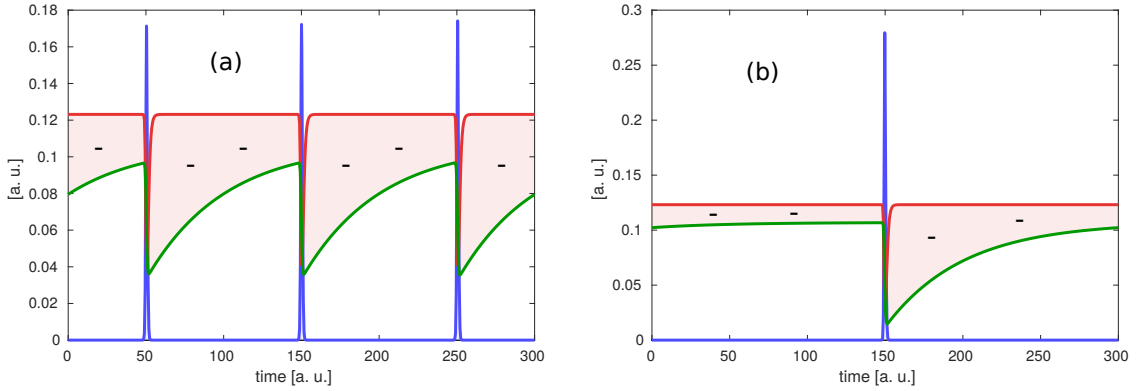


Figure 1.5: Schematic of the transition of PML pulses to the localized regime. The pulse intensity is drawn in blue while gain and absorption are drawn in green and red, respectively. (a) Three identical and equally spaced pulses in the subcritical harmonic mode-locking regime below threshold. (b) The same system but with a single pulse. The carriers have time to relax virtually to the equilibrium state before the pulse returns, making it a temporal localized structure. Because of the background being stable, the two regimes are bistable.

of such a structure, the interactions between neighbors can become negligible if they are sufficiently far apart. In laser optics, an example is lasing spots in the transverse section of wide area VCSEL called cavity solitons [BPT⁺05, GBGT08]. These can individually be arranged and moved around arbitrarily, provided they will not come too close to each other.

Under certain conditions, PML pulses can become temporal localized structures (TLSs). In standard PML the system is operated above threshold and the pulsation regime appears in a supercritical Andronov-Hopf bifurcation [VRW11]. The off-state is unstable meaning small perturbations will grow, causing the whole cavity to eventually become filled with pulses. They are not independent but rather feel each other via the temporal trails they leave in the form of gain depletion. In a stable pulsation regime, an equilibrium distance is formed between all the pulses and the resulting situation is called harmonic mode locking. Such a pulse train can be considered a periodic pattern state. If the dissipation of an unsaturated absorber is stronger than the maximum gain the zero background remains stable. Small perturbations decay as the corresponding photons are absorbed. However, with a strong modulation of the absorption, combined with a low saturation energy of the absorber as compared to that of the gain, a large enough pulse can cut a temporal hole in the absorption. Similar to standard PML, this still opens a net-gain window for the pulse to sustain itself. Thus, a stable pulsation pattern state can exist below threshold which corresponds to a subcritical form of PML [MJBG14]. Unlike the supercritical PML regime, a single pulse can exist alone in a long cavity as nothing else may grow from the stable off-solution that occupies the rest of the cavity. Figure 1.5 illustrates the transition to this regime. Such pulses are TLSs and several of them can coexist in a large enough cavity without significant interactions among them. They can be individually addressed [JCMG16, CJMG16], i.e., they are writable, erasable and movable independently from each

other. In VECSELs, such TLSs could potentially be combined with spatial localization in the transverse section of the laser to confine light in all three dimensions of space, thus forming so-called light bullets [WT02, Jav16, GJ17, PJGV18].

Note, that a pulse can only be considered a TLS when in the long cavity limit or when the gain relaxation is virtually complete, i.e., the product of the gain relaxation rate γ and the roundtrip time τ must be large $\gamma\tau \gg 1$. In this case the word pulse will often be used synonymously with TLS throughout this thesis.

1.3 Outline of this thesis

This thesis is organized as follows:

- In Chapter 2 the different time-delay models for PML which are analyzed in this thesis are derived from first principles. These include a well-established delay differential equation model for a unidirectional ring laser [VT05] and differential equation models for the internal fields of microcavities which are coupled to each other by delay algebraic equations that are specifically tailored to the VECSEL setups of interest [MB05].
- In Chapter 3 the methods used for the numerical treatment of the models are explained. These include the algorithms for direct numerical simulations, the implementations of the models in DDE-BIFTOOL [ELR02] for numerical path continuation and finally a functional mapping approach that offers an efficient yet accurate way to deal with the stiffness inherent to the localized regime [2].
- Chapter 4 presents the results obtained for the unidirectional ring laser DDE model. The existence of temporal localized structures in the model has already been presented in [MJBG14]. Here, we concentrate on the influence of the linewidth enhancement factors of the gain and absorber sections to set a baseline of TLS dynamics. Both direct numerical simulations and numerical path continuation are applied for extensive parameter scans and to compare with a corresponding Haus master PDE model [1]. Finally this model is used to test and showcase the performance of the functional mapping approach.
- Chapter 5 presents the results obtained for a VCSEL coupled with an RSAM. TLSs have previously been realized in a corresponding experimental setup by focusing the beam on the RSAM [MJBG15]. First we discuss how the experimental properties are transferred to the model parameters. Using these, TLS pulse trains are simulated using the full system to showcase the very good agreement with the experiment in self-imaging conditions [3]. In addition, a new satellite instability is presented which arises due to third order dispersion incurred by the particular cavity geometry [5].
- Chapter 6 presents the results obtained for a MIXSEL system. It can be seen as a simplified version of the VCSEL-RSAM system from the previous chapter but with the same classes of behavior. An instructive parameter set is chosen to analyze the origin of the satellite instability including limited numerical path continuation. The

properties of the instability and how it relates to, and interferes with, other types of TLS behavior is analyzed extensively and compared to both a corresponding Haus master PDE model and the unidirectional ring laser [7].

- Chapter 7 deals with a different kind of setup roughly related to Kerr fiber loops. A microcavity with a layer of Kerr nonlinear material instead of the normally used active material. As with the VECSELs, an external cavity is closed by a mirror and the same kind of DAE modeling can be applied here. The system as such is passive and is driven by a CW injection beam. One finds bistability of CW solutions together with dark and bright TLSs on respective high and low intensity backgrounds. A rich set of solutions forms a transition between the two types of TLSs and is fully analyzed using path continuation [6].

2 Theoretical Modeling

To begin, we will set some conventions that will be used throughout this thesis. We use a complex description for the electric field in order to benefit from complex exponential functions that can greatly simplify analytical calculations. Physically, the electric field is real \mathbf{E}_r and several conventions exist how to convert between it and a complex description. We will use the form $\mathbf{E}_r = \text{Re}[\mathbf{E}]$.

It is always possible to exchange the field, together with any equations containing it, by their respective complex conjugates without changing the overall structure. For real functions the Fourier transform will generally be symmetric and either half of the frequency space is sufficient for a complete description. Physically, positive and negative frequencies contain the same information if one considers the spectrum of a real variable.

We use the ansatz for rotating plane waves

$$\mathbf{E}(z, t) = \mathbf{E}_0 e^{iq_0 z - i\omega_0 t} \quad (2.1)$$

propagating along the z -axis with a wave vector q_0 and a frequency ω_0 as time t increases. With these sign conventions the wave moves toward positive z for positive q_0 and toward negative z for negative q_0 , respectively. Along with this we use the following definition of the Fourier transform

$$\mathcal{F}[f(t)] = \int_{-\infty}^{\infty} f(t) e^{i\omega t} dt = \hat{f}(\omega), \quad (2.2)$$

$$\mathcal{F}^{-1}[\hat{f}(\omega)] = \frac{1}{2\pi} \int_{-\infty}^{\infty} f(\omega) e^{-i\omega t} d\omega = f(t), \quad (2.3)$$

and thus

$$\mathcal{F}^{-1}[-i\omega \hat{f}(\omega)] = \frac{\partial}{\partial t} f(t). \quad (2.4)$$

2.1 Transverse electromagnetic wave equation

To analyze the properties of temporal localized structures we are interested in systems that can be described by their temporal evolution alone. Therefore, we will reduce the influences of transverse spatial dimensions down to a single guided transverse mode and focus on the propagation direction that can be related to the time coordinate.

2.1.1 Maxwell's equations in materials

We assume that the used materials in our system are non-magnetizable and that there are no free charges or currents. In this situation Maxwell's equations for the dynamics of the

electric field \mathbf{E} and the magnetic flux density \mathbf{B} are

$$\nabla \cdot \mathbf{D} = 0, \quad (2.5)$$

$$\nabla \cdot \mathbf{B} = 0, \quad (2.6)$$

$$\nabla \times \mathbf{E} = -\dot{\mathbf{B}}, \quad (2.7)$$

$$\nabla \times \mathbf{H} = \dot{\mathbf{D}}, \quad (2.8)$$

with the electric displacement and magnetic fields

$$\mathbf{D} = \epsilon_0(1 + \chi)\mathbf{E} = \epsilon_0\mathbf{E} + \mathbf{P}, \quad (2.9)$$

$$\mathbf{H} = \frac{\mathbf{B}}{\mu_0}, \quad (2.10)$$

where χ and \mathbf{P} are the electric susceptibility and polarization of the material, respectively, while ϵ_0 and μ_0 are the respective permittivity and permeability of the vacuum [FLS11].

We will assume the electric susceptibility to separate into a background χ_b and a nonlinear medium χ_{nl} in the active region

$$\mathbf{D} = \epsilon_0(1 + \chi_b)\mathbf{E} + \epsilon_0\chi_{nl}\mathbf{E} = \epsilon_0\epsilon_r\mathbf{E} + \mathbf{P}_{nl}, \quad (2.11)$$

where \mathbf{P}_{nl} is the nonlinear electric polarization and the relative electric susceptibility ϵ_r is responsible for the background refractive index n_b .

2.1.2 Wave equation with electric polarization

We write the curl of the third Maxwell equation (2.7) and use Eq. (2.10) and the linearity of the curl

$$\nabla \times (\nabla \times \mathbf{E}) = \nabla \times (-\dot{\mathbf{B}}) = -\mu_0 \nabla \times \dot{\mathbf{H}}. \quad (2.12)$$

Using the vector calculus identity for a vector \mathbf{A}

$$\nabla \times (\nabla \times \mathbf{A}) = \nabla (\nabla \cdot \mathbf{A}) - \nabla^2 \mathbf{A}, \quad (2.13)$$

on the left hand side and substitute the fourth Maxwell equation (2.8) on the right, where we can pull the time derivative out the curl, we get

$$\nabla (\nabla \cdot \mathbf{E}) - \nabla^2 \mathbf{E} = -\mu_0 \ddot{\mathbf{D}}. \quad (2.14)$$

Here, for $\nabla \cdot \mathbf{P}_{nl} \ll 1$ we may assume $\nabla \cdot \mathbf{E} = 0$ and use Eq. (2.9) to reach the wave equation with nonlinear polarization

$$\nabla^2 \mathbf{E} - \frac{n_b^2}{c^2} \ddot{\mathbf{E}} = \mu_0 \ddot{\mathbf{P}}_{nl}. \quad (2.15)$$

By applying the Fourier transform we can write the wave equation in the frequency domain

$$\left(\nabla^2 + \omega^2 \frac{n_b^2}{c^2} \right) \hat{\mathbf{E}} = -\omega^2 \mu_0 \hat{\mathbf{P}}_{nl}. \quad (2.16)$$

Here, the hats mark the Fourier amplitudes.

2.1.3 Transverse mode

Appropriate cavity design entails some kind of focusing, typically a waveguide, lenses or curved mirrors, that can be modeled by a transverse profile of the background refractive index $n_{\perp}(\mathbf{r}_{\perp})$, where \mathbf{r} denotes the position vector. We will assume a constant transverse mode $\Phi(\mathbf{r}_{\perp})$ [Sie86] that solves

$$\left(\nabla_{\perp}^2 + \frac{\omega^2}{c^2} n_{\perp}^2(\mathbf{r}_{\perp}, \omega) \right) \Phi(\mathbf{r}_{\perp}, \omega) = \frac{\omega^2}{c^2} n_e^2 \Phi(\mathbf{r}_{\perp}, \omega), \quad (2.17)$$

with the effective refractive index n_e . It factorizes with the field

$$\hat{\mathbf{E}}(\mathbf{r}, \omega) = \Phi(\mathbf{r}_{\perp}, \omega) \hat{E}_{\perp}(z, \omega) \mathbf{e}_{\perp}, \quad (2.18)$$

where \mathbf{e}_{\perp} is a unit vector in the transverse plane and we insert this in the wave equation

$$\left(\frac{\partial^2}{\partial z^2} + \nabla_{\perp}^2 + \frac{\omega^2}{c^2} n_{\perp}^2(\mathbf{r}_{\perp}, \omega) \right) \Phi(\mathbf{r}_{\perp}, \omega) \hat{E}_{\perp}(z, \omega) \mathbf{e}_{\perp} = -\omega^2 \mu_0 \hat{\mathbf{P}}_{\text{nl}}, \quad (2.19)$$

$$\Phi(\mathbf{r}_{\perp}, \omega) \left(\frac{\partial^2}{\partial z^2} + \omega^2 \frac{n_e^2}{c^2} \right) \hat{E}_{\perp}(z, \omega) \mathbf{e}_{\perp} = -\omega^2 \mu_0 \hat{\mathbf{P}}_{\text{nl}}. \quad (2.20)$$

Next, we multiply with the conjugate of the mode Φ^* and integrate over the transverse dimensions

$$\int_{-\infty}^{\infty} \int_{-\infty}^{\infty} |\Phi(\mathbf{r}_{\perp})|^2 d^2 \mathbf{r}_{\perp} \left(\frac{\partial^2}{\partial z^2} + \omega^2 \frac{n_e^2}{c^2} \right) \hat{E}_{\perp}(z) \mathbf{e}_{\perp} = -\omega^2 \mu_0 \int_{-\infty}^{\infty} \int_{-\infty}^{\infty} \Phi^*(\mathbf{r}_{\perp}) \hat{\mathbf{P}}_{\text{nl}}(\mathbf{r}) d^2 \mathbf{r}_{\perp}. \quad (2.21)$$

For the transverse field the polarization reads

$$\hat{\mathbf{P}}_{\text{nl}}(\mathbf{r}) = \varepsilon_0 \chi_{\text{nl}}(\mathbf{r}) \Phi(\mathbf{r}_{\perp}) \hat{E}_{\perp}(z) \mathbf{e}_{\perp}, \quad (2.22)$$

so we can write the right hand side of (2.21) as the projection of the susceptibility on the transverse mode

$$\text{R.H.S.} = -\frac{\omega^2}{c^2} \int_{-\infty}^{\infty} \int_{-\infty}^{\infty} \Phi^*(\mathbf{r}_{\perp}) \chi_{\text{nl}}(\mathbf{r}_{\perp}, z) \Phi(\mathbf{r}_{\perp}) d^2 \mathbf{r}_{\perp} \hat{E}_{\perp}(z) \mathbf{e}_{\perp}. \quad (2.23)$$

We assume the active region to be centered around $\mathbf{r}_{\perp} = 0$ and the transverse profile of the susceptibility $\chi_{\text{nl}}(\mathbf{r}_{\perp}, z)$ to be constant inside the active region (AR) and zero otherwise. The projection then simplifies

$$\text{R.H.S.} = -\frac{\omega^2}{c^2} \int \int_{\text{AR}} |\Phi(\mathbf{r}_{\perp})|^2 d^2 \mathbf{r}_{\perp} \chi_{\text{nl}}(0, z) \hat{E}_{\perp}(z) \mathbf{e}_{\perp}. \quad (2.24)$$

We define the transverse confinement factor as

$$\Gamma_{\perp} = \frac{\int \int_{\text{AR}} |\Phi(\mathbf{r}_{\perp})|^2 d^2 \mathbf{r}_{\perp}}{\int_{-\infty}^{\infty} \int_{-\infty}^{\infty} |\Phi(\mathbf{r}_{\perp})|^2 d^2 \mathbf{r}_{\perp}}, \quad (2.25)$$

which we substitute to get

$$\left(\frac{\partial^2}{\partial z^2} + \omega^2 \frac{n_e^2}{c^2} \right) \hat{E}_\perp(z) \mathbf{e}_\perp = -\frac{\omega^2}{c^2} \Gamma_\perp \chi_{\text{nl}}(0, z) \hat{E}_\perp(z) \mathbf{e}_\perp, \quad (2.26)$$

where we can now drop the unit vector \mathbf{e}_\perp . Finally we define the transverse polarization

$$\hat{P}_\perp(z) = \varepsilon_0 \chi_{\text{nl}}(0, z) \hat{E}_\perp(z), \quad (2.27)$$

so we can write the wave equation for the transverse field

$$\frac{\partial^2}{\partial z^2} \hat{E}_\perp + \omega^2 \frac{n_e^2}{c^2} \hat{E}_\perp = -\omega^2 \mu_0 \Gamma_\perp \hat{P}_\perp. \quad (2.28)$$

2.2 Electric susceptibility model

To describe the interplay of the laser light with the nonlinear medium we choose a semi-classical approach. A polarization model containing the most important quantum effects of a semiconductor medium is solved for the electric field. In Maxwell's equations this polarization is then used to calculate the field evolution, thus forming a self-consistent theory. Following [CKSI94], we assume a nonlinear region made of quantum wells that have a simple parabolic band structure, see Figure 2.1 for a schematic. This corresponds to a free electron gas for the conduction electrons and analogously for the valence band holes. For fast intraband relaxations, as compared to the rate of optical transitions, one may further assume that the conduction band electrons and valence band holes will each have a Fermi distribution. This approximation limits the validity of our model to dynamics on a picosecond time scale. The population inversion can then be described by the total carrier density \mathcal{N} . Note, that this free carrier model only constitutes a valid approximation for low carrier densities where many body coulomb effects are negligible. Details like the explicit dependence of the Fermi distributions on temperature are hidden by the following linearization. The numeric parameters that appear in the final model will generally depend on the exact structure and composition of the material, the carrier density and temperature. Precise quantitative prediction of these coefficients is an active field of research in its own right and beyond the scope of this thesis, see [CKSI94] for an entry point to the vast literature on this topic.

We will assume the gain spectrum to be broad as compared to the microcavity modes such that the susceptibility does not depend on the frequency $\chi(\omega) \approx \chi(\omega_0)$ and linearize it for a small change of the carrier density around the transparency level $\mathcal{N}^{(\text{tr})}$

$$\chi_{\text{nl}} \approx \frac{\partial \chi_{\text{nl}}}{\partial N} \left(\mathcal{N} - \mathcal{N}^{(\text{tr})} \right). \quad (2.29)$$

Here, we split the real and imaginary parts

$$\chi_{\text{nl}} = \left(\frac{\partial \text{Re}[\chi_{\text{nl}}]}{\partial N} + i \frac{\partial \text{Im}[\chi_{\text{nl}}]}{\partial N} \right) \left(\mathcal{N} - \mathcal{N}^{(\text{tr})} \right), \quad (2.30)$$

and by defining the differential gain coefficient

$$g_0 = -\frac{\partial \text{Im}[\chi_{\text{nl}}]}{\partial N}, \quad (2.31)$$

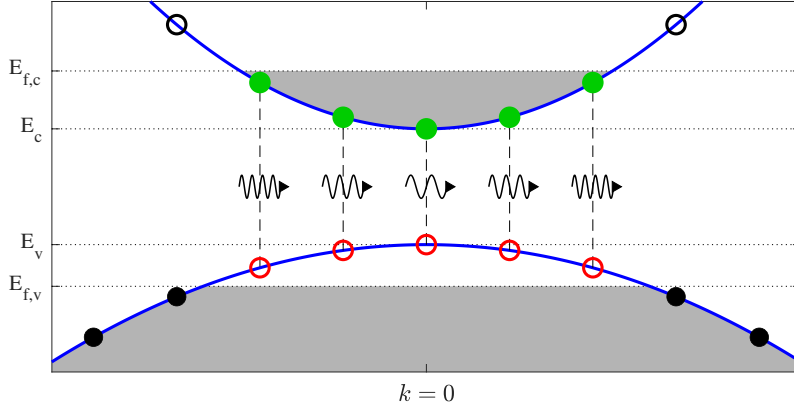


Figure 2.1: Schematic band structure of a direct band gap semiconductor. The band gap between the extrema E_c and E_v of the parabolic conduction and valence bands determines the resonance energy of amplified photons. The bands are filled up to the respective Fermi levels $E_{f,c}$ and $E_{f,v}$ as indicated by the shaded areas. Additional excited electrons have higher wavevectors k and the transition energy increases. Thus, resonant photons become bluer which is illustrated exaggeratedly.

and the linewidth enhancement factor

$$\alpha = \frac{\frac{\partial \text{Re}[\chi_{\text{nl}}]}{\partial N}}{\frac{\partial \text{Im}[\chi_{\text{nl}}]}{\partial N}}, \quad (2.32)$$

we can shorten the expression to reach the susceptibility model

$$\chi_{\text{nl}} = -g_0 (\alpha + i) (\mathcal{N} - \mathcal{N}^{(\text{tr})}). \quad (2.33)$$

This equation thus describes the gain (absorption) and the relative refractive index change of the nonlinear medium.

The carrier evolution is modeled by a differential equation to capture the dynamic saturation of the nonlinear material that is essential to passive model-locking. We only consider radiative and nonradiative recombinations of carriers that are linear in \mathcal{N} since we limited ourselves to a free carrier model. Accordingly, the carrier density can be assumed small enough to neglect nonlinear terms, e.g. bimolecular and Auger recombinations. The model then reads

$$\frac{\partial \mathcal{N}}{\partial t} = \mathcal{J} - \gamma \mathcal{N} + \frac{\varepsilon_b}{2\hbar} \text{Im}[\chi_{\text{nl}}] |E|^2, \quad (2.34)$$

with the carrier relaxation rate γ and the scaled bias current $\mathcal{J} = \frac{\eta J}{ed}$, where η is the quantum efficiency of the current injection, J is the current density, e is the elementary charge and d is the thickness of the active region. Stimulated emission enters the equation as a term proportional to the intensity of the field $|E|^2$. With the approximative susceptibility (2.33) we get the carrier model

$$\frac{\partial \mathcal{N}}{\partial t} = \mathcal{J} - \gamma \mathcal{N} - \frac{\varepsilon_b}{2\hbar} g_0 (\mathcal{N} - \mathcal{N}^{(\text{tr})}) |E|^2. \quad (2.35)$$

2.3 Unidirectional traveling wave model

We assume a unidirectional monochromatic traveling plane wave with a carrier wave frequency ω_0 and the corresponding wave vector $q_0 = \frac{n_e}{c}\omega_0$

$$E_{\perp}(z, t) = E(z, t)e^{i(q_0 z - \omega_0 t)}, \quad (2.36)$$

where $E(z, t)$ is the slowly varying envelope of the electric field. It causes a polarization of the form

$$P_{\perp}(z, t) = P(z, t)e^{i(q_0 z - \omega_0 t)}, \quad (2.37)$$

with $P(z, t)$ being the slowly varying envelope of the polarization. The temporal Fourier transform of this ansatz simply results in a shift of the frequency

$$\hat{E}_{\perp} = \mathcal{F}[E_{\perp}(z, t)] = \int_{-\infty}^{\infty} E(z, t)e^{i(q_0 z - \omega_0 t)}e^{i\omega t} dt =, \quad (2.38)$$

$$\hat{E}_{\perp} = \int_{-\infty}^{\infty} E(z, t)e^{iq_0 z}e^{i\Delta\omega t} dt = \hat{E}(z, \Delta\omega)e^{iq_0 z}, \quad (2.39)$$

where we defined the frequency shift $\Delta\omega = \omega - \omega_0$ that describes the sidebands around the carrier wave frequency. The same goes for the polarization

$$\hat{P}_{\perp} = \mathcal{F}[P_{\perp}(z, t)] = \hat{P}(z, \Delta\omega)e^{iq_0 z}. \quad (2.40)$$

Using this ansatz in the wave equation (2.28) we expand the spatial derivative term to get

$$\left[\frac{\partial^2}{\partial z^2} + 2iq_0 \frac{\partial}{\partial z} - q_0^2 \right] \hat{E} e^{iq_0 z} + \omega^2 \frac{n_e^2}{c^2} \hat{E} e^{iq_0 z} = -\omega^2 \mu_0 \Gamma_{\perp} \hat{P} e^{iq_0 z}, \quad (2.41)$$

where we can use $q = \frac{n}{c}\omega$ and drop the exponential functions

$$\left[\frac{\partial^2}{\partial z^2} + 2iq_0 \frac{\partial}{\partial z} + q^2 - q_0^2 \right] \hat{E} = -\omega^2 \mu_0 \Gamma_{\perp} \hat{P}. \quad (2.42)$$

Now we perform the slowly varying approximation which consists in assuming the spatial derivative of the field to be small $\frac{\partial}{\partial z} \hat{E} \ll 1$ such that the second order derivative can be neglected $\frac{\partial^2}{\partial z^2} \hat{E} \approx 0$. After dividing by the prefactor of the first derivative we have

$$\left[\frac{\partial}{\partial z} + \frac{q^2 - q_0^2}{2iq_0} \right] \hat{E} = -\frac{\omega^2}{2iq_0} \mu_0 \Gamma_{\perp} \hat{P}. \quad (2.43)$$

We expand the wave vector around the carrier wave frequency

$$q(\omega) = \frac{n}{c}\omega_0 + \left. \frac{\partial q}{\partial \omega} \right|_{\omega=\omega_0} \Delta\omega + \mathcal{O}(\Delta\omega^2). \quad (2.44)$$

With the group velocity v_g as defined by

$$\frac{1}{v_g} = \left. \frac{\partial q}{\partial \omega} \right|_{\omega=\omega_0}, \quad (2.45)$$

the wave vector can be approximated as

$$q \approx q_0 + \frac{\Delta\omega}{v_g}. \quad (2.46)$$

After plugging this in we have

$$\left[\frac{\partial}{\partial z} + \frac{q_0^2 + 2q_0 \frac{\Delta\omega}{v_g} + \mathcal{O}(\Delta\omega^2) - q_0^2}{2iq_0} \right] \hat{E} = -\frac{\omega^2}{2iq_0} \mu_0 \Gamma_{\perp} \hat{P}, \quad (2.47)$$

where we can neglect higher order terms in $\Delta\omega$ and simplify

$$\left[\frac{\partial}{\partial z} - i \frac{\Delta\omega}{v_g} \right] \hat{E} = -\frac{\omega^2}{2iq_0} \mu_0 \Gamma_{\perp} \hat{P}. \quad (2.48)$$

On the polarization side, we then expand ω and neglect higher terms again

$$\left[\frac{\partial}{\partial z} - i \frac{\Delta\omega}{v_g} \right] \hat{E} = -\frac{\omega_0^2 + 2\omega_0 \Delta\omega}{2iq_0} \mu_0 \Gamma_{\perp} \hat{P}, \quad (2.49)$$

and by substituting $q_0 = \frac{n_e}{c} \omega_0$ we can simplify further

$$\left[\frac{\partial}{\partial z} - i \frac{\Delta\omega}{v_g} \right] \hat{E} = -\frac{\omega_0^2 + 2\omega_0 \Delta\omega}{2i \frac{n_e}{c} \omega_0} \mu_0 \Gamma_{\perp} \hat{P}, \quad (2.50)$$

$$\left[\frac{\partial}{\partial z} - i \frac{\Delta\omega}{v_g} \right] \hat{E} = i \frac{c}{n_e} \left[\frac{\omega_0}{2} + \Delta\omega \right] \mu_0 \Gamma_{\perp} \hat{P}. \quad (2.51)$$

At this point we transform back to time using that $-i\Delta\omega \rightarrow \frac{\partial}{\partial t}$

$$\left[\frac{\partial}{\partial z} + \frac{1}{v_g} \frac{\partial}{\partial t} \right] E = \frac{c}{n_e} \left[i \frac{\omega_0}{2} - \frac{\partial}{\partial t} \right] \mu_0 \Gamma_{\perp} P. \quad (2.52)$$

The rate of change of the polarization is proportional to the relaxation rate $\gamma \ll \omega_0$ and can be neglected as compared to optical frequencies

$$\left[\frac{\partial}{\partial z} + \frac{1}{v_g} \frac{\partial}{\partial t} \right] E = i \Gamma_{\perp} \frac{c}{n_e} \frac{\omega_0}{2} \mu_0 P. \quad (2.53)$$

We write this with the nonlinear susceptibility instead of the polarization

$$\left[\frac{\partial}{\partial z} + \frac{1}{v_g} \frac{\partial}{\partial t} \right] E = i \Gamma_{\perp} \frac{c}{n_e} \frac{\omega_0}{2} \mu_0 \varepsilon_0 \chi_{\text{nl}} E, \quad (2.54)$$

$$\left[\frac{\partial}{\partial z} + \frac{1}{v_g} \frac{\partial}{\partial t} \right] E = i \Gamma_{\perp} \frac{\omega_0}{2n_e c} \chi_{\text{nl}} E, \quad (2.55)$$

and use the susceptibility approximation from previous section to reach a simple traveling wave model [JB10a]

$$\left[\frac{\partial}{\partial z} + \frac{1}{v_g} \frac{\partial}{\partial t} \right] E = -i \Gamma_{\perp} \frac{\omega_0}{2n_e c} g_0 (\alpha + i) (\mathcal{N} - \mathcal{N}^{(\text{tr})}) E, \quad (2.56)$$

$$\left[\frac{\partial}{\partial z} + \frac{1}{v_g} \frac{\partial}{\partial t} \right] E = g_0 \Gamma_{\perp} \frac{\omega_0}{n_e c} \frac{1 - i\alpha}{2} (\mathcal{N} - \mathcal{N}^{(\text{tr})}) E. \quad (2.57)$$

If we assume that the change of reflective index with the frequency is negligible $\frac{\partial n}{\partial \omega} \ll 1$ the group velocity will be

$$v_g = \frac{c}{n_e}. \quad (2.58)$$

With this we can write the traveling wave model in the alternative form

$$\frac{\partial}{\partial z} E + \frac{1}{v_g} \frac{\partial}{\partial t} E = \frac{\omega_0 v_g}{c^2} g_0 \Gamma_\perp \frac{1 - i\alpha}{2} \left(\mathcal{N} - \mathcal{N}^{(tr)} \right) E. \quad (2.59)$$

2.4 Unidirectional ring laser model

This section mostly follows the approach of [VT05]. We consider a ring shaped laser cavity of length L in which light propagation is assumed to be unidirectional. It shall contain an absorber section between $z_2 < z < z_3$, a gain section between $z_3 < z < z_4$ and a filtering element between $z_5 < z < z_1 + L$, with z_j in ascending order along the propagation direction. A schematic of the setup is shown in Figure 2.2.

We write a simple traveling wave model as discussed in the previous section for the slowly varying electromagnetic field envelope $E(t, z)$ and the excited carrier densities in the active regions $\mathcal{N}_r(t, z)$. The subscript r distinguishes the different section ($r = g$ gain, $r = q$ absorber, $r = p$ passive, $r = f$ filter)

$$\frac{\partial E}{\partial z} + \frac{1}{v} \frac{\partial E}{\partial t} = \frac{\omega_0 v}{c^2} g_r \Gamma_r \frac{1 - i\alpha_r}{2} \left(\mathcal{N}_r - \mathcal{N}_r^{(tr)} \right) E, \quad (2.60)$$

$$\frac{\partial \mathcal{N}_r}{\partial t} = \mathcal{J}_r - \gamma_r \mathcal{N}_r - \frac{\varepsilon_b}{2\hbar} g_r \left(\mathcal{N}_r - \mathcal{N}_r^{(tr)} \right) |E|^2, \quad (2.61)$$

with the propagation velocity v , differential gains g_r , transverse confinement factors Γ_r , line-width enhancement factors α_r , transparency carrier densities $\mathcal{N}_r^{(tr)}$, injection currents \mathcal{J}_r ($\mathcal{J}_q = 0$) and carrier relaxation rates γ_r .

The field after the filter $\hat{f}'(\omega')$ in the angular frequency domain reads

$$\hat{E}(\omega', z_1 + L) = \hat{f}'(\omega') \hat{E}(\omega', z_5), \quad (2.62)$$

with ω' being the conjugate variable of t . Elsewhere free propagation is assumed

$$\frac{\partial E}{\partial z} + \frac{1}{v} \frac{\partial E}{\partial t} = 0. \quad (2.63)$$

2.4.1 Introducing a co-moving coordinate

In the traveling wave model (2.60) the slowly varying electromagnetic field envelope is described as a PDE similar to an advection equation. It can be transformed into an ordinary differential equation (ODE) along a characteristic curve, i.e., in the co-moving frame of a photon. We introduce a co-moving coordinate $\sigma = \frac{z}{v} + t$ [YG17] giving the total derivative

$$\frac{d}{d\sigma} = \frac{\partial}{\partial z} \frac{dz}{d\sigma} + \frac{\partial}{\partial t} \frac{dt}{d\sigma} = v \frac{\partial}{\partial z} + \frac{\partial}{\partial t}, \quad (2.64)$$

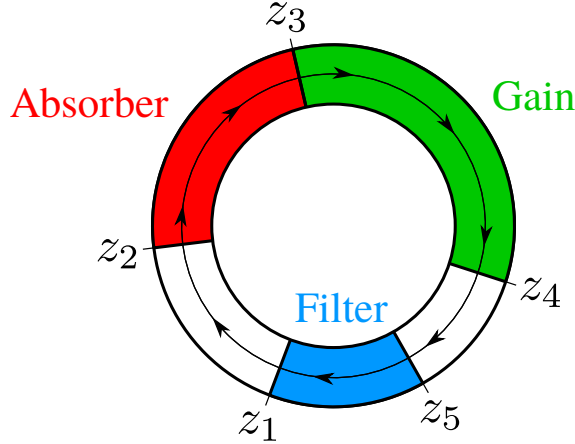


Figure 2.2: Schematic setup of a ring cavity with absorber (red) and gain (green) sections and a filtering element (blue) that describes the bandwidth of the nonlinear material. The coordinates z_i describe the interfaces between the sections and free space along the propagation length of the cavity.

that we can use in Eq. (2.60). After multiplying Eq. (2.60) with v and dividing both Eqs. (2.60) and (2.61) by γ_q we can write

$$\frac{1}{\gamma_q} \frac{\partial E}{\partial \sigma} = \frac{1 - i\alpha_r}{2} g'_r N_r E, \quad (2.65)$$

$$\frac{1}{\gamma_q} \frac{\partial N_r}{\partial t} = J_r - \frac{\gamma_r}{\gamma_q} N_r - s_r N_r |E|^2, \quad (2.66)$$

with the carrier inversion $N_r = \mathcal{N}_r - \mathcal{N}_r^{(tr)}$ and the rescaled gain parameters $g'_r = \frac{\omega_0}{n_e^2} \frac{g_r \Gamma_r}{\gamma_q}$, injection currents $J_r = \left(\mathcal{J}_r - \gamma_r \mathcal{N}_r^{(tr)} \right) \gamma_q^{-1}$ and saturation factors $s_r = \frac{\varepsilon_b}{2\hbar} \frac{g_r}{\gamma_q}$.

2.4.2 Dimensionless scaling

We can now normalize time to the absorber relaxation rate to get a system with the dimensionless coordinates $\zeta = \gamma_q \sigma$, $\tau = \gamma_q t$ and variables $A(\tau, \zeta) = \sqrt{s_g} E$, $n_r(\tau, \zeta) = g'_r N_r$

$$\frac{\partial A}{\partial \zeta} = \frac{1 - i\alpha_r}{2} n_r A, \quad (2.67)$$

$$\frac{\partial n_r}{\partial \tau} = j_r - \frac{\gamma_r}{\gamma_q} n_r - \frac{s_r}{s_g} n_r |A|^2, \quad (2.68)$$

where $j_r = g'_r J_r$. Substituting the ratios of the carrier relaxations $\Gamma = \frac{\gamma_q}{\gamma_q}$ and the saturation parameters $s = \frac{s_q}{s_g} = \frac{g_q}{g_g}$, we expand the carrier rate equations for both active sections

$$\frac{\partial n_g}{\partial \tau} = j_g - \Gamma n_g - n_g |A|^2, \quad (2.69)$$

$$\frac{\partial n_q}{\partial \tau} = j_q - n_q - n_q s |A|^2. \quad (2.70)$$

2.4.3 Integrating the co-moving coordinate

In the passive sections (2.63) transforms to

$$\frac{\partial A(\tau, \zeta)}{\partial \zeta} = 0, \quad (2.71)$$

i.e., the field just propagates freely and therefore

$$A(\tau, \zeta_1) = A(\tau, \zeta_2), \quad A(\tau, \zeta_4) = A(\tau, \zeta_5), \quad (2.72)$$

with $\zeta_k = z_k \frac{\gamma_q}{v}$. We can divide Eq. (2.67) by A to separate the variables and integrate

$$\int_{\zeta_k}^{\zeta_l} \frac{1}{A} \frac{\partial A}{\partial \zeta} d\zeta = [\ln(A)]_{\zeta_k}^{\zeta_l} = \frac{1 - i\alpha_r}{2} \int_{\zeta_k}^{\zeta_l} n_r d\zeta. \quad (2.73)$$

After exponentiation we have relations of the field at the interfaces of the different sections

$$\frac{A(\tau, \zeta_4)}{A(\tau, \zeta_3)} = e^{\frac{1-i\alpha_g}{2} G(\tau)}, \quad (2.74)$$

$$\frac{A(\tau, \zeta_3)}{A(\tau, \zeta_2)} = e^{-\frac{1-i\alpha_q}{2} Q(\tau)}, \quad (2.75)$$

where $G(\tau) = \int_{\zeta_3}^{\zeta_4} n_g d\zeta$ and $Q(\tau) = - \int_{\zeta_2}^{\zeta_3} n_q d\zeta$ describe the cumulative gain and loss in the respective sections after the field has passed through. To treat the intensity terms $|A^2|$ in Eqs. (2.69), (2.70) we write an ODE for the intensity using (2.67) and integrate

$$\frac{\partial}{\partial \zeta} (A^* A) = A^* \frac{\partial A}{\partial \zeta} + A \frac{\partial A^*}{\partial \zeta} = n_r A^* A, \quad (2.76)$$

$$|A(\tau, \zeta_l)|^2 - |A(\tau, \zeta_k)|^2 = \int_{\zeta_k}^{\zeta_l} n_r |A(\tau, \zeta)|^2 d\zeta. \quad (2.77)$$

With this, Eqs. (2.69), (2.70) yield

$$\frac{\partial G(\tau)}{\partial \tau} = g_0 - \Gamma G(\tau) - |A(\tau, \zeta_4)|^2 + |A(\tau, \zeta_3)|^2, \quad (2.78)$$

$$\frac{\partial Q(\tau)}{\partial \tau} = q_0 - Q(\tau) + s|A(\tau, \zeta_3)|^2 - s|A(\tau, \zeta_2)|^2, \quad (2.79)$$

where $g_0 = \int_{\zeta_3}^{\zeta_4} j_g d\zeta$ and $q_0 = - \int_{\zeta_2}^{\zeta_3} j_q d\zeta$ are the integrated current injections. Finally, using the relations (2.74), (2.75) and (2.72) we obtain

$$A(\tau, \zeta_5) = e^{\frac{1-i\alpha_g}{2} G(\tau) - \frac{1-i\alpha_q}{2} Q(\tau)} A(\tau, \zeta_1), \quad (2.80)$$

$$\frac{\partial G(\tau)}{\partial \tau} = g_0 - \Gamma G(\tau) - e^{-Q(\tau)} \left(e^{G(\tau)} - 1 \right) |A(\tau, \zeta_1)|^2, \quad (2.81)$$

$$\frac{\partial Q(\tau)}{\partial \tau} = q_0 - Q(\tau) - s \left(1 - e^{-Q(\tau)} \right) |A(\tau, \zeta_1)|^2, \quad (2.82)$$

where on the right hand side the field is only evaluated at ζ_1 .

2.4.4 Introducing a causal filter

With ω being the conjugate variable of τ , (2.62) reads

$$\hat{A}(\omega, \zeta_1 + T) = \hat{F}(\omega) \hat{A}(\omega, \zeta_5), \quad (2.83)$$

where $T = \frac{\gamma_q}{v} L$. The inverse Fourier Transform is a convolution

$$A(\tau, \zeta_1 + T) = F(\tau) * A(\tau, \zeta_5) = \int_{-\infty}^{\infty} F(\tau - \theta) A(\theta, \zeta_5) d\theta. \quad (2.84)$$

The filter must be causal, i.e., its response function is not defined in the past. Therefore it has to be of the form

$$F(t) = \Theta(t) f(t), \quad (2.85)$$

with the Heaviside step-function $\Theta(t)$ making it vanish for negative time in the convolution. This is equivalent to limiting the integral's upper bound to τ

$$A(\tau, \zeta_1 + T) = \int_{-\infty}^{\tau} f(\tau - \theta) A(\theta, \zeta_5) d\theta. \quad (2.86)$$

The ring shaped cavity implies the periodic boundary condition $A(\tau, \zeta + T) = A(\tau + T, \zeta)$ giving

$$A(\tau + T, \zeta_1) = \int_{-\infty}^{\tau} f(\tau - \theta) R(\theta) A(\theta, \zeta_1) d\theta, \quad (2.87)$$

where $R(\tau) = e^{\frac{1-i\alpha_g}{2}G - \frac{1-i\alpha_q}{2}Q}$. All expressions now contain only ζ_1 , which can be discarded $A(\tau, \zeta_1) \equiv A(\tau)$. After taking the derivative with respect to τ the system reads

$$\frac{\partial A(\tau + T)}{\partial \tau} = \frac{\partial}{\partial \tau} \int_{-\infty}^{\tau} f(\tau - \theta) R(\theta) A(\theta) d\theta, \quad (2.88)$$

$$\frac{\partial G(\tau)}{\partial \tau} = g_0 - \Gamma G(\tau) - e^{-Q(\tau)} \left(e^{G(\tau)} - 1 \right) |A(\tau)|^2, \quad (2.89)$$

$$\frac{\partial Q(\tau)}{\partial \tau} = q_0 - Q(\tau) - s \left(1 - e^{-Q(\tau)} \right) |A(\tau)|^2. \quad (2.90)$$

2.4.5 Case of a Lorentzian filter

The response function $\Theta(t) \gamma e^{(-\gamma + i\omega_0)t}$ corresponds to a Lorentzian line shape in Fourier space $\frac{\gamma}{\gamma - i(\omega + \omega_0)}$. Let

$$f(t) = \sqrt{\kappa} \gamma e^{(-\gamma + i\omega_0)t}, \quad (2.91)$$

represent both a bandwidth-limiting element and a beam-splitter with a power transmission ratio of κ . Using Leibnitz' Integral Rule on (2.88) we get

$$\frac{\partial A(\tau + T)}{\partial \tau} = f(0) R(\tau) A(\tau) + \int_{-\infty}^{\tau} \frac{\partial}{\partial \tau} f(\tau - \theta) R(\theta) A(\theta) d\theta. \quad (2.92)$$

For the filter function (2.91) it takes the form

$$\frac{\partial A(\tau + T)}{\partial \tau} = \sqrt{\kappa} \gamma R(\tau) A(\tau) + (-\gamma + i\omega_0) \int_{-\infty}^{\tau} f(\tau - \theta) R(\theta) A(\theta) d\theta, \quad (2.93)$$

where the integral is just $A(\tau + T)$. After shifting τ by T

$$\frac{\partial A(\tau)}{\partial \tau} = \sqrt{\kappa} \gamma R(\tau - T) A(\tau - T) + (-\gamma + i\omega_0) A(\tau), \quad (2.94)$$

we assume $A e^{i\omega_0 \tau}$ to rotate its phase at the central frequency of the filter and divide by γ to arrive at

$$\frac{1}{\gamma} \frac{\partial A(\tau)}{\partial \tau} = \sqrt{\kappa} R(\tau - T) e^{-i\phi} A(\tau - T) - A(\tau), \quad (2.95)$$

where $\phi = \omega_0 T$. Finally we expand R and shift τ by T for the carrier terms to obtain a system of ordinary delay differential equations [VT05]

$$\frac{1}{\gamma} \frac{\partial A(\tau)}{\partial \tau} = \sqrt{\kappa} e^{\frac{1-i\alpha_g}{2} G(\tau) - \frac{1-i\alpha_q}{2} Q(\tau) - i\phi} A(\tau - T) - A(\tau), \quad (2.96)$$

$$\frac{\partial G(\tau)}{\partial \tau} = g_0 - \Gamma G(\tau) - e^{-Q(\tau)} (e^{G(\tau)} - 1) |A(\tau - T)|^2, \quad (2.97)$$

$$\frac{\partial Q(\tau)}{\partial \tau} = q_0 - Q(\tau) - s (1 - e^{-Q(\tau)}) |A(\tau - T)|^2. \quad (2.98)$$

2.5 Alternative approach

An alternative approach to obtain Eqs. (2.80)–(2.82) using Green's function [BMSM05] allowing for more intuitive coordinates at the cost of a longer calculation.

2.5.1 Scaled dimensionless model

We define $\zeta = \frac{\gamma_g}{v} z$ and use the other scalings from the previous section to get

$$\frac{\partial A}{\partial \zeta} + \frac{\partial A}{\partial \tau} = \frac{1 - i\alpha_r}{2} n_r A, \quad (2.99)$$

$$\frac{\partial n_g}{\partial \tau} = j_g - \Gamma n_g - n_g |A|^2, \quad (2.100)$$

$$\frac{\partial n_q}{\partial \tau} = j_q - n_q - n_q s |A|^2. \quad (2.101)$$

Note, that in this approach ζ and τ have purely spatial and temporal character, respectively.

2.5.2 Constructing the general solution

We look at the operator

$$\mathcal{L}(\zeta, \tau) = \epsilon + \frac{\partial}{\partial \zeta} + \frac{\partial}{\partial \tau}, \quad (2.102)$$

with a small linear loss term ϵ . For a given source \mathcal{S} we shall call the corresponding solution u

$$\mathcal{L}[u(\zeta, \tau)] = S(\zeta, \tau). \quad (2.103)$$

For a Dirac δ source the solution is called Green's function \mathcal{G}

$$\mathcal{L}[\mathcal{G}(\zeta, \tau)] = \delta(\zeta, \tau). \quad (2.104)$$

In general, \mathcal{S} can then be written as the convolution with δ

$$\mathcal{S}(\zeta, \tau) = \int_{-\infty}^{\infty} \int_{-\infty}^{\infty} \delta(\zeta - \zeta', \tau - \tau') \mathcal{S}(\zeta', \tau') d\zeta' d\tau', \quad (2.105)$$

where \mathcal{S} and δ can be substituted by $\mathcal{L}[u]$ and $\mathcal{L}[\mathcal{G}]$, respectively

$$\mathcal{S}(\zeta, \tau) = \int_{-\infty}^{\infty} \int_{-\infty}^{\infty} \mathcal{L}[\mathcal{G}(\zeta - \zeta', \tau - \tau')] \mathcal{S}(\zeta', \tau') d\zeta' d\tau'. \quad (2.106)$$

$\mathcal{L}(\zeta, \tau)$ can then be pulled out as rest of integral depends only on $\zeta' \tau'$

$$\mathcal{L}[u(\zeta, \tau)] = \mathcal{L} \left[\int_{-\infty}^{\infty} \int_{-\infty}^{\infty} \mathcal{G}(\zeta - \zeta', \tau - \tau') \mathcal{S}(\zeta', \tau') d\zeta' d\tau' \right]. \quad (2.107)$$

The operands must now be equal, thus we obtain the general solution

$$u(\zeta, \tau) = \int_{-\infty}^{\infty} \int_{-\infty}^{\infty} \mathcal{G}(\zeta', \tau') \mathcal{S}(\zeta - \zeta', \tau - \tau') d\zeta' d\tau', \quad (2.108)$$

where we used the commutativity of the convolution for the sake of notation.

2.5.3 Calculating the Green's function

To make use of the general solution we first have to solve the Green's function which becomes a trivial division in Fourier space

$$\left(\epsilon + \frac{\partial}{\partial \zeta} + \frac{\partial}{\partial \tau} \right) [\mathcal{G}(\zeta, \tau)] = \delta(\zeta, \tau), \quad (2.109)$$

$$(\epsilon + i\omega + iq) \tilde{\mathcal{G}}(q, \omega) = 1. \quad (2.110)$$

Now, we first transform the following expression back to the time domain

$$\hat{\mathcal{G}}(q, \tau) = \int_{-\infty}^{\infty} \frac{e^{i\omega\tau}}{\epsilon + i\omega + iq} \frac{d\omega}{2\pi} = \frac{1}{2i\pi} \int_{-\infty}^{\infty} \frac{e^{i\omega\tau}}{\omega - \omega_p} d\omega, \quad (2.111)$$

where $\omega_p = i\epsilon - q$ is a pole. After introducing separate real and imaginary parts $\omega = \omega_r + i\omega_i$, we look at the different limit cases. For $\omega_r \rightarrow \pm\infty$ and $\omega_i\tau \rightarrow \infty$

$$\lim_{\omega_r + i\omega_i - \omega_p \rightarrow 0} \frac{e^{i\omega_r\tau} e^{-\omega_i\tau}}{\omega_r + i\omega_i - \omega_p} = 0, \quad (2.112)$$

i.e., $\omega_i \rightarrow \infty$ for positive τ and $\omega_i \rightarrow -\infty$ for negative τ , respectively. Therefore a line integration of a closed loop around the upper complex half-space for $\tau > 0$ and around

the lower half-space for $\tau < 0$, respectively, coincides with our integral. With the single pole ω_p in the upper half-space, applying the residue theorem yields

$$\frac{1}{2i\pi} \int_{-\infty}^{\infty} \frac{e^{i\omega\tau}}{\omega - \omega_p} d\omega = \sum \text{Res} \frac{e^{i\omega\tau}}{\omega - \omega_p} = \lim_{\omega \rightarrow \omega_p} (\omega - \omega_p) \frac{e^{i\omega\tau}}{\omega - \omega_p} = e^{-(\epsilon+iq)\tau}, \quad (2.113)$$

for $\tau > 0$ and

$$\frac{1}{2i\pi} \int_{-\infty}^{\infty} \frac{e^{i\omega\tau}}{\omega - \omega_p} d\omega = \sum \text{Res} \frac{e^{i\omega\tau}}{\omega - \omega_p} = 0, \quad (2.114)$$

for $\tau < 0$, and thus

$$\hat{\mathcal{G}}(q, \tau) = \Theta(\tau) e^{-(\epsilon+iq)\tau}. \quad (2.115)$$

Finally, we can transform back to space

$$\mathcal{G}(\zeta, \tau) = \int_{-\infty}^{\infty} \Theta(\tau) e^{-(\epsilon+iq)\tau} e^{iq\zeta} \frac{dq}{2\pi} = \Theta(\tau) e^{-\epsilon\tau} \int_{-\infty}^{\infty} e^{i(\zeta-\tau)q} \frac{dq}{2\pi}, \quad (2.116)$$

$$\mathcal{G}(\zeta, \tau) = \Theta(\tau) e^{-\epsilon\tau} \delta(\zeta - \tau). \quad (2.117)$$

2.5.4 Introducing a useful difference expression

We now use the found \mathcal{G} in Eq. (2.108)

$$u(\zeta, \tau) = \int_{-\infty}^{\infty} \int_{-\infty}^{\infty} \Theta(\tau') e^{-\epsilon\tau'} \delta(\zeta' - \tau') \mathcal{S}(\zeta - \zeta', \tau - \tau') d\zeta' d\tau', \quad (2.118)$$

$$u(\zeta, \tau) = \int_0^{\infty} d\tau' e^{-\epsilon\tau'} \int_{-\infty}^{\infty} \delta(\zeta' - \tau') \mathcal{S}(\zeta - \zeta', \tau - \tau') d\zeta', \quad (2.119)$$

$$u(\zeta, \tau) = \int_0^{\infty} d\tau' e^{-\epsilon\tau'} \mathcal{S}(\zeta - \tau', \tau - \tau'). \quad (2.120)$$

To continue after some coordinate transformations

$$u(\zeta, \tau) = \int_{-\infty}^0 e^{\epsilon\sigma} \mathcal{S}(\zeta + \sigma, \tau + \sigma) d\sigma, \quad (2.121)$$

$$u(\zeta + a, \tau + a) = \int_{-\infty}^0 e^{\epsilon\sigma} \mathcal{S}(\zeta + a + \sigma, \tau + a + \sigma) d\sigma, \quad (2.122)$$

$$u(\zeta + a, \tau + a) = \int_{-\infty}^a e^{\epsilon(\sigma-a)} \mathcal{S}(\zeta + \sigma, \tau + \sigma) d\sigma, \quad (2.123)$$

we have to neglect the passive losses $\epsilon \rightarrow 0$ so we can build a useful difference expression from the previous equations

$$\lim_{\epsilon \rightarrow 0} \mathcal{L} = \mathcal{L}' = \frac{\partial}{\partial \zeta} + \frac{\partial}{\partial \tau}, \quad (2.124)$$

$$u(\zeta + a, \tau + a) - u(\zeta, \tau) = \int_0^a \mathcal{S}(\zeta + \sigma, \tau + \sigma) d\sigma. \quad (2.125)$$

Note, that in order for the previous approach to work, the absence of linear losses along the propagation is necessary as well.

2.5.5 Active and passive sections

For the active sections we bring the equations into the form of Eq. (2.103)

$$\frac{1}{A} \left[\frac{\partial A}{\partial \zeta} + \frac{\partial A}{\partial \tau} \right] = \frac{1 - i\alpha_r}{2} n_r, \quad (2.126)$$

$$\left(\frac{\partial}{\partial \zeta} + \frac{\partial}{\partial \tau} \right) [\ln A] = \frac{1 - i\alpha_r}{2} n_r. \quad (2.127)$$

We identify the terms

$$u(\zeta, \tau) = \ln A, \quad (2.128)$$

$$S(\zeta, \tau) = \frac{1 - i\alpha_r}{2} n_r, \quad (2.129)$$

to plug into the difference expression (2.125). After exponentiation we get the relation of the field after propagation

$$\ln A(\zeta + a, \tau + a) - \ln A(\zeta, \tau) = \frac{1 - i\alpha_r}{2} \int_0^a n_r(\zeta + \sigma, \tau + \sigma) d\sigma, \quad (2.130)$$

$$A(\zeta + a, \tau + a) = e^{\frac{1-i\alpha_r}{2} \int_0^a n_r(\zeta + \sigma, \tau + \sigma) d\sigma} A(\zeta, \tau). \quad (2.131)$$

In the passive sections the corresponding propagation is trivial

$$u(\zeta, \tau) = A, \quad S(\zeta, \tau) = 0, \quad (2.132)$$

$$A(\zeta + a, \tau + a) = A(\zeta, \tau). \quad (2.133)$$

2.5.6 Connecting the sections

We can now connect the different sections and define the lengths of the sections $a_{lk} = \zeta_l - \zeta_k$. The first section is passive and only corresponds to a shift in time

$$A(\zeta_2, \tau + a_{21}) = A(\zeta_1, \tau). \quad (2.134)$$

In the following absorber section we need to evaluate an integral over the carrier density

$$A(\zeta_3, \tau + a_{31}) = e^{-\frac{1-i\alpha_q}{2} Q'(\tau + a_{21})} A(\zeta_2, \tau + a_{21}), \quad (2.135)$$

$$Q'(\tau + a_{21}) = - \int_0^{a_{32}} n_q(\zeta_2 + \sigma, \tau + a_{21} + \sigma) d\sigma, \quad (2.136)$$

as well as for the gain section

$$A(\zeta_4, \tau + a_{41}) = e^{\frac{1-i\alpha_g}{2} G'(\tau + a_{31})} A(\zeta_3, \tau + a_{31}), \quad (2.137)$$

$$G'(\tau + a_{31}) = \int_0^{a_{43}} n_g(\zeta_3 + \sigma, \tau + a_{31} + \sigma) d\sigma. \quad (2.138)$$

After the second passive section

$$A(\zeta_5, \tau + a_{51}) = A(\zeta_4, \tau + a_{41}), \quad (2.139)$$

we can sum up the effects of the sections so far

$$A(\zeta_5, \tau + a_{51}) = R(\tau)A(\zeta_1, \tau), \quad (2.140)$$

$$R(\tau) = e^{\frac{1-i\alpha_g}{2}G'(\tau+a_{31}) - \frac{1-i\alpha_q}{2}Q'(\tau+a_{21})}. \quad (2.141)$$

This expression corresponds to Eq. (2.80) and the rest of the way to Eq. (2.96) is the same as before. The time offset a_{51} plus the time spend in the filter τ_f directly add up to the delay time $T = a_{51} + \tau_f$.

2.5.7 Carrier rate equations

We differentiate Eqs. (2.138) and (2.136) to obtain the ordinary differential equations

$$\begin{aligned} \frac{\partial G'(\tau + a_{31})}{\partial \tau} &= g_0 - \Gamma G'(\tau + a_{31}) - \\ &- \int_0^{a_{43}} n_g(\zeta_3 + \sigma, \tau + a_{31} + \sigma) |A(\zeta_3 + \sigma, \tau + a_{31} + \sigma)|^2 d\sigma, \end{aligned} \quad (2.142)$$

$$\begin{aligned} \frac{\partial Q'(\tau + a_{21})}{\partial \tau} &= q_0 - Q'(\tau + a_{21}) + \\ &+ s \int_0^{a_{32}} n_q(\zeta_2 + \sigma, \tau + a_{21} + \sigma) |A(\zeta_2 + \sigma, \tau + a_{21} + \sigma)|^2 d\sigma, \end{aligned} \quad (2.143)$$

where $g_0 = a_{43}j_g$ and $q_0 = -a_{32}j_q$. Using the difference expression (2.125) again, we obtain an expression to replace remaining integrals

$$\left(\frac{\partial}{\partial \zeta} + \frac{\partial}{\partial \tau} \right) [A^* A] = n_r A^* A, \quad (2.144)$$

$$u(\zeta, \tau) = |A|^2, \quad S(\zeta, \tau) = n_r |A|^2, \quad (2.145)$$

$$\int_0^a n_r(\zeta + \sigma, \tau + \sigma) |A(\zeta + \sigma, \tau + \sigma)|^2 d\sigma = |A(\zeta + a, \tau + a)|^2 - |A(\zeta, \tau)|^2, \quad (2.146)$$

After applying it we have

$$\frac{\partial G'(\tau + a_{31})}{\partial \tau} = g_0 - \Gamma G'(\tau + a_{31}) - |A(\zeta_4, \tau + a_{41})|^2 + |A(\zeta_3, \tau + a_{31})|^2, \quad (2.147)$$

$$\frac{\partial Q'(\tau + a_{21})}{\partial \tau} = q_0 - Q'(\tau + a_{21}) + s |A(\zeta_3, \tau + a_{31})|^2 - s |A(\zeta_2, \tau + a_{21})|^2. \quad (2.148)$$

With the propagation relations (2.134), (2.137) and (2.135) we find

$$\frac{\partial G'(\tau + a_{31})}{\partial \tau} = g_0 - \Gamma G'(\tau + a_{31}) - \left(e^{G'(\tau+a_{31})} - 1 \right) e^{-Q'(\tau+a_{21})} |A(\zeta_1, \tau)|^2 \quad (2.149)$$

$$\frac{\partial Q'(\tau + a_{21})}{\partial \tau} = q_0 - Q'(\tau + a_{21}) - s \left(1 - e^{-Q'(\tau+a_{21})} \right) |A(\zeta_1, \tau)|^2 \quad (2.150)$$

Finally we shift the time at which the carriers are evaluated to align the ODEs and get Eqs. (2.81) and (2.82)

$$\frac{\partial G(\tau)}{\partial \tau} = g_0 - \Gamma G(\tau) - e^{-Q(\tau)} \left(e^{G(\tau)} - 1 \right) |A(\zeta_1, \tau)|^2, \quad (2.151)$$

$$\frac{\partial Q(\tau)}{\partial \tau} = q_0 - Q(\tau) - s \left(1 - e^{-Q(\tau)} \right) |A(\zeta_1, \tau)|^2, \quad (2.152)$$

$$G(\tau) = G'(\tau + a_{31}), \quad Q(\tau) = Q'(\tau + a_{21}). \quad (2.153)$$

Note, that these different points in time were hidden in the coordinates of the previous approach.

2.6 Injected microcavity with thin quantum well region

In the following sections use the approach to model passive mode-locking introduced in [MB05] for. A schematic of the principal injected microcavity setup is shown in Figure 2.3.

2.6.1 Solving the intracavity field

We write the wave equation (2.28)

$$\frac{\partial^2 \mathcal{E}(\omega, z)}{\partial z^2} + \omega^2 \frac{n^2}{c^2} \mathcal{E}(\omega, z) = -\omega^2 \mu_0 \Gamma_{\perp} \mathcal{P}(\omega, z), \quad (2.154)$$

where, \mathcal{P} is the polarization of the quantum well (QW) region, Γ_{\perp} is the confinement factor of the transverse mode and n the effective index of refraction of the transverse

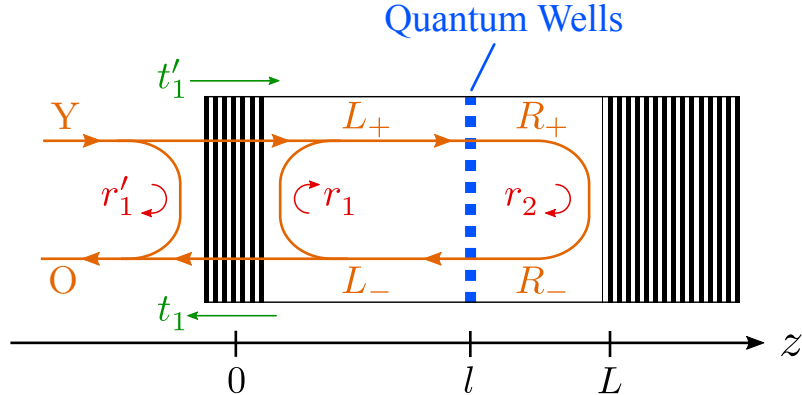


Figure 2.3: Micro-cavity with a quantum well layer at l between two Bragg mirrors at $z = 0$ and $z = L$. The intra-cavity field is split into left ($-$) and right ($+$) moving waves to the left L_- and right R_+ of the quantum wells. The output and injected fields are denoted O and Y , respectively. The transmission and reflection coefficients are indicated by t_j and r_j , respectively, where the index $j = 1$ stands for the top and $j = 2$ for the bottom mirror. Primes mark the case on the outside of the microcavity.

mode. The transverse electromagnetic field in Fourier space \hat{E}_\perp has been replaced by \mathcal{E} for brevity. We assume the QW region to be very thin as compared to the wavelength $W \ll \lambda$ and located at $z = l$.

$$\left(\frac{\partial^2}{\partial z^2} + \omega^2 \frac{n^2}{c^2} \right) \mathcal{E}(\omega, z) = -\omega^2 \mu_0 W \Gamma_\perp P'(\omega) \delta(z - l). \quad (2.155)$$

To simplify notation we define $P = W \Gamma_\perp P'$ and integrate over z in a small interval around the QW region

$$\int_{l-\epsilon}^{l+\epsilon} \frac{\partial^2 \mathcal{E}(z)}{\partial z^2} + \omega^2 \frac{n^2}{c^2} \mathcal{E}(z) dz = - \int_{l-\epsilon}^{l+\epsilon} \omega^2 \mu_0 P \delta(z - l) dz, \quad (2.156)$$

$$\left[\frac{\partial \mathcal{E}(z)}{\partial z} \right]_{l-\epsilon}^{l+\epsilon} + \omega^2 \frac{n^2}{c^2} \int_{l-\epsilon}^{l+\epsilon} \mathcal{E}(z) dz = -\omega^2 \mu_0 P, \quad (2.157)$$

$$\frac{\partial}{\partial z} \mathcal{E}(l + \epsilon) - \frac{\partial}{\partial z} \mathcal{E}(l - \epsilon) + \omega^2 \frac{n^2}{c^2} \int_{l-\epsilon}^{l+\epsilon} \mathcal{E}(z) dz = -\omega^2 \mu_0 P. \quad (2.158)$$

We define the field amplitudes to the left and right of the QW as L and R , respectively, while subset $+$ and $-$ symbols mark right and left propagating waves, respectively. The electric field can then be defined as

$$\mathcal{E}(\omega, z) = \begin{cases} L(\omega, z) = L_+ e^{iqz} + L_- e^{-iqz} & \text{for } 0 < z < l \\ R(\omega, z) = R_+ e^{iqz} + R_- e^{-iqz} & \text{for } l < z < L \end{cases}, \quad (2.159)$$

with the wave vector $q = \omega \frac{n}{c}$. With this Eq. (2.158) reads

$$\frac{\partial}{\partial z} R(l + \epsilon) - \frac{\partial}{\partial z} L(l - \epsilon) + \omega^2 \frac{n^2}{c^2} \int_{l-\epsilon}^{l+\epsilon} \mathcal{E}(z) dz = -\omega^2 \mu_0 P, \quad (2.160)$$

where we take the limit $\epsilon \rightarrow 0$ to get the boundary conditions at the QWs

$$L(\omega, l) = R(\omega, l) = \mathcal{E}(\omega, l), \quad (2.161)$$

$$\frac{\partial}{\partial z} R(\omega, l) - \frac{\partial}{\partial z} L(\omega, l) = -\omega^2 \mu_0 P(\omega). \quad (2.162)$$

The boundary conditions at the mirrors are

$$r_1 L_- + t'_1 Y = L_+, \quad (2.163)$$

$$r_2 R_+ e^{iqL} = R_- e^{-iqL}, \quad (2.164)$$

and the output of the cavity is the superposition of the emission from the microcavity and the reflection of the injected field Y

$$O = t_1 L_- + r'_1 Y, \quad (2.165)$$

where $r_j(\omega)$ and $t_j(\omega)$ are the frequency-dependent reflection and transmission coefficients of the Bragg mirrors inside the cavity. The indices 1 and 2 stand for the top and bottom mirror, respectively. Primes indicate the reverse case on the outside of the cavity.

From the boundary conditions we know that

$$L_+ = r_1 L_- + t'_1 Y, \quad L_- = \frac{L_+ - t'_1 Y}{r_1}, \quad (2.166)$$

$$R_+ = \frac{R_- e^{-2iqL}}{r_2}, \quad R_- = r_2 R_+ e^{2iqL}, \quad (2.167)$$

and using Eq. (2.161) yields

$$R_+ = \frac{e^{-iql} \mathcal{E}}{1 + r_2 e^{2iq(L-l)}}, \quad R_- = \frac{r_2 e^{iql} \mathcal{E}}{r_2 + e^{2iq(l-L)}}, \quad (2.168)$$

$$L_+ = \frac{r_1 e^{iql} \mathcal{E} + t'_1 Y}{1 + r_1 e^{2iql}}, \quad L_- = \frac{e^{-iql} \mathcal{E} - t'_1 Y}{r_1 + e^{-2iql}}. \quad (2.169)$$

These we can use in Eq. (2.162) when expanded as

$$iq \left(R_+ e^{iql} - R_- e^{-iql} - L_+ e^{iql} + L_- e^{-iql} \right) = -\omega^2 \mu_0 P. \quad (2.170)$$

The term in parentheses then reads

$$\frac{\mathcal{E}}{1 + r_2 e^{2iq(L-l)}} - \frac{r_2 \mathcal{E}}{r_2 + e^{2iq(l-L)}} - \frac{r_1 e^{2iql} \mathcal{E} + t'_1 Y e^{iql}}{1 + r_1 e^{2iql}} + \frac{e^{-2iql} \mathcal{E} - t'_1 Y e^{-iql}}{r_1 + e^{-2iql}}, \quad (2.171)$$

and can be reduced to only two different denominators

$$\frac{1 - r_2 e^{2iq(L-l)}}{1 + r_2 e^{2iq(L-l)}} \mathcal{E} + \frac{1 - r_1 e^{2iql}}{1 + r_1 e^{2iql}} \mathcal{E} - \frac{2t'_1 e^{iql}}{1 + r_1 e^{2iql}} Y. \quad (2.172)$$

After multiplication with both denominators Eq. (2.170) can then be written as

$$F_1(q) \mathcal{E} = -\omega^2 \frac{\mu_0}{2i} \Gamma(q) P + F_2(q) Y, \quad (2.173)$$

or equally

$$F_1(q) \mathcal{E} = i\omega \frac{\mu_0 c}{2n} \Gamma(q) P + F_2(q) Y, \quad (2.174)$$

with

$$F_1(q) = 1 - r_1 r_2 e^{2iqL}, \quad (2.175)$$

$$F_2(q) = t'_1 e^{iql} \left(1 + r_2 e^{2iq(L-l)} \right), \quad (2.176)$$

and the confinement factor

$$\Gamma(q) = \left(1 + r_1 e^{2iql} \right) \left(1 + r_2 e^{2iq(L-l)} \right). \quad (2.177)$$

In general the reflection coefficients are complex. We assume that the modulus does not depend on the frequency and as such $r_j(\omega) = \rho_j \exp[i\phi_j(\omega)]$

$$F_1(q) = 1 - \rho_1 \rho_2 e^{2iqL + i\phi_1 + i\phi_2}, \quad (2.178)$$

$$F_2(q) = t'_1 e^{iql} \left(1 + \rho_2 e^{2iq(L-l) + i\phi_2} \right), \quad (2.179)$$

$$\Gamma(q) = \left(1 + \rho_1 e^{2iql + i\phi_1} \right) \left(1 + \rho_2 e^{2iq(L-l) + i\phi_2} \right). \quad (2.180)$$

2.6.2 Expansion around a cavity mode

Injection and emission will take place around a carrier wave frequency ω_0 , i.e. $q_0 = \omega_0 \frac{n}{c}$, at a minimum of F_1 leading to the condition

$$2q_0L + \phi_1(\omega_0) + \phi_2(\omega_0) = 2\pi m, m \in \mathbb{Z}, \quad (2.181)$$

that describes the modes of the cavity. The position l of the QW is chosen in order to maximize the confinement factor yielding two more conditions

$$2q_0l + \phi_1(\omega_0) = 2\pi n_1, \quad (2.182)$$

$$2q_0(L - l) + \phi_2(\omega_0) = 2\pi n_2, \quad (2.183)$$

where n_1 and n_2 are integers. This guarantees the strongest possible coupling of the intra-cavity field with the polarization as well as the injection, that shares one of the factors. When adding these two equations together, we see that this condition will always coincide with a cavity mode.

To get a temporal description of the dynamics of the field, we assume small frequency variations around the carrier wave frequency, i.e., $\omega = \omega_0 + \delta\omega$ with $\delta\omega \ll 1$. We assume the refractive index to be constant around the carrier wave frequency and expand F_1 up to first order around ω_0

$$F_1(\omega_0 + \delta\omega) \approx F_1(\omega_0) + \left. \frac{\partial F_1}{\partial \omega} \right|_{\omega=\omega_0} \delta\omega = 1 - \rho_1 \rho_2 - 2i\rho_1 \rho_2 L_e \frac{n}{c} \delta\omega, \quad (2.184)$$

with the effective length

$$L_e = L + \frac{c}{2n} \frac{\partial}{\partial \omega} [\phi_1(\omega_0) + \phi_2(\omega_0)], \quad (2.185)$$

that contains the linearized change of the group delays of the DBRs. After inserting (2.184) in Eq. (2.174) we have

$$\left[F_1(\omega_0) + \left. \frac{\partial F_1}{\partial \omega} \right|_{\omega=\omega_0} \delta\omega \right] \mathcal{E} = i\omega_0 \frac{\mu_0 c}{2n} \Gamma(\omega_0) P + F_2(\omega_0) Y. \quad (2.186)$$

As the frequency of the injection ω_Y was assumed to be close to the mode ω_0 , we define the small detuning $\Delta = \omega_Y - \omega_0$. We can then shift the small frequency variation by the detuning $\delta\omega = \Delta + \Delta\omega$ and transform back to time using that $-i\Delta\omega \rightarrow \frac{\partial}{\partial t}$

$$\tau_c \rho_1 \rho_2 \left(\frac{\partial \mathcal{E}}{\partial t} - i\Delta \right) = i\omega_0 \frac{\mu_0 c}{2n} (1 + \rho_1) (1 + \rho_2) P - (1 - \rho_1 \rho_2) \mathcal{E} + t'_1 e^{iq_0 l} (1 + \rho_2) Y, \quad (2.187)$$

with the cavity roundtrip time $\tau_c = 2L_e \frac{n}{c}$.

2.6.3 Scaling the fields

We define the photon lifetime κ , the scaled detuning δ , the polarization prefactor b and the injection coupling factor \tilde{h}

$$\kappa = \frac{1 - \rho_1 \rho_2}{\rho_1 \rho_2} \tau_c^{-1}, \quad (2.188)$$

$$\delta = \frac{\Delta}{\kappa}, \quad (2.189)$$

$$b = \frac{\omega_0}{2nc} \frac{(1 + \rho_1)(1 + \rho_2)}{1 - \rho_1 \rho_2}, \quad (2.190)$$

$$\tilde{h} = t'_1 e^{i(\pi n_1 - \frac{\phi_1(\omega_0)}{2})} \frac{1 + \rho_2}{1 - \rho_1 \rho_2}, \quad (2.191)$$

where we used $c^{-2} = \varepsilon_0 \mu_0$ and the condition (2.182) for positioning the QW in the microcavity. Note, that the factor $\exp[i\pi n_1] = (-1)^{n_1}$ can alternatively be absorbed into the definition of the injection field Y . Thus, we obtain a compact equation for the field evolution

$$\kappa^{-1} \frac{\partial \mathcal{E}}{\partial t} = i \frac{b}{\varepsilon_0} P - \mathcal{E} + i\delta\mathcal{E} + \tilde{h}Y. \quad (2.192)$$

Next, we will rescale the field \mathcal{E} in such a way that it has the same order of magnitude as the injection Y . The second amplitude in (2.169) can be written as

$$L_- = \frac{e^{-iql} \mathcal{E} - t'_1 Y}{1 + r_1 e^{i2ql}} e^{i2ql}, \quad (2.193)$$

and at resonance where r is quasi-constant

$$L_- = \frac{(-1)^{n_1} e^{-i\frac{\phi_1}{2}}}{1 + \rho_1} \mathcal{E} - \frac{t'_1 e^{-i\phi_1}}{1 + \rho_1} Y, \quad (2.194)$$

which we substitute in the output relation (2.165)

$$O = \frac{(-1)^{n_1} t_1 e^{-i\frac{\phi_1}{2}}}{1 + \rho_1} \mathcal{E} + \left(r'_1 - \frac{t_1 t'_1 e^{-i\phi_1}}{1 + \rho_1} \right) Y. \quad (2.195)$$

We define the prefactors

$$\xi = \frac{(-1)^{n_1} t_1 e^{-i\frac{\phi_1}{2}}}{1 + \rho_1}, \beta = r'_1 - \frac{t_1 t'_1 e^{-i\phi_1}}{1 + \rho_1}, \quad (2.196)$$

to write the output as

$$O = \xi \mathcal{E} + \beta Y. \quad (2.197)$$

We assume the DBRs to be loss-less so that the Stokes relations $t't = 1 + r'r$ and $r = -r'$ hold

$$\beta = -r_1 - \frac{1 - r_1 r_1}{1 + \rho_1} e^{-i\phi_1} = \frac{(r_1^2 - 1) e^{-i\phi_1} - r_1 (1 + \rho_1)}{1 + \rho_1}. \quad (2.198)$$

Indeed, at resonance the DBR reflectivities become real numbers in this situation, i.e. $r_1 = \pm \rho_1$. Assuming the reflective index outside the cavity is lower than the other materials (typically air and semiconductors), r_1 will be positive (i.e. $\phi_1 = 0$) and r'_1 negative, causing a π phase-shift upon reflection on the outer face of the microcavity. The prefactors then simplify

$$\xi = \frac{(-1)^{n_1} t_1}{1 + \rho_1}, \quad (2.199)$$

$$\beta = \frac{\rho_1^2 - 1 - \rho_1 - \rho_1^2}{1 + \rho_1} = -1. \quad (2.200)$$

Finally, we rescale Eq. (2.192) by defining the field $E(t) = \xi \mathcal{E}(t, l)$ and the injection coupling factor $h = \xi \tilde{h}$ where the powers of -1 cancel

$$h = \frac{t_1 t'_1}{1 + \rho_1} \frac{1 + \rho_2}{1 - \rho_1 \rho_2} = \frac{(1 - \rho_1)(1 + \rho_2)}{1 - \rho_1 \rho_2}. \quad (2.201)$$

The final scaled model of the response of a microcavity with a thin quantum well region to an injected field is

$$\kappa^{-1} \frac{\partial E}{\partial t} = i \frac{b}{\varepsilon_0} P - E + i \delta E + h Y, \quad (2.202)$$

or equivalently with the scaled electric susceptibility $\chi = b \chi_{\text{nl}}$

$$\kappa^{-1} \frac{\partial E}{\partial t} = [i\chi - 1 + i\delta] E + h Y, \quad (2.203)$$

and we can write the output relation simply as

$$O = E - Y. \quad (2.204)$$

2.7 Delay algebraic differential equation model for VECSELs

We now consider using the microcavity in an external cavity design. Either a microcavity may be coupled to itself using a feedback mirror or several microcavities can be coupled head to head or in a V-shape. Such arrangements typically appear in the designs of vertical-external-cavity surface-emitting lasers.

In the simplest case the output O will be re-injected into the microcavity, i.e., it will become the new Y after a certain time of flight τ that appears as a time-delay in

$$Y(t) = \eta O(t - \tau) = \eta [E(t - \tau) - Y(t - \tau)], \quad (2.205)$$

where the attenuation factor per roundtrip η can be, e.g., the reflection coefficient from a partly transmitting feedback mirror like in the schematic shown in Figure 2.4, the transmission of a beam-splitter or a fiber optic coupler. The resulting condition is a delay algebraic equation (DAE).

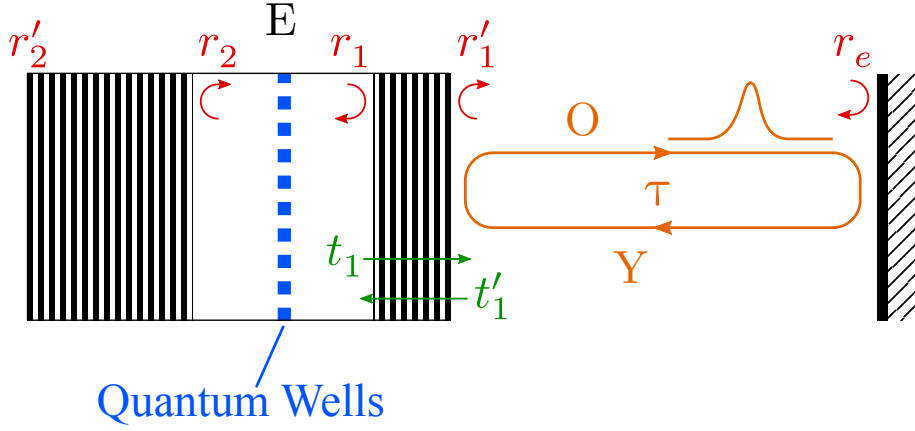


Figure 2.4: Schematic of an external cavity setup consisting of a microcavity and a feedback mirror. The intra-cavity field E is shown along with the output of the microcavity O which returns as the injection field Y after the external cavity roundtrip time τ . It is attenuated by the external mirrors reflection coefficient r_e . The coefficients of the Bragg mirrors are defined as in Fig. 2.3.

We will use the slightly shorter notation $A_\tau = A(t - \tau)$ in the following. Together with the microcavity response (2.203) we can now write a generic delay algebraic differential equation model for our microcavity subjected to strong time-delayed feedback

$$\kappa^{-1} \frac{\partial E}{\partial t} = [i\chi - 1 + i\delta] E + hY, \quad (2.206)$$

$$Y = \eta [E_\tau - Y_\tau]. \quad (2.207)$$

Notice how the DAE contains itself at an earlier time. This describes a recursive structure; it can be expanded by inserting the right hand side of the equation into itself with increasing multiples of the delay time

$$Y = \eta(E_\tau - Y_\tau), \quad (2.208)$$

$$Y = \eta \left[E_\tau - \eta(E_{2\tau} - Y_{2\tau}) \right], \quad (2.209)$$

$$Y = \eta \left\{ E_\tau - \eta \left[E_{2\tau} - \eta(E_{3\tau} - Y_{3\tau}) \right] \right\}, \quad (2.210)$$

$$Y = \eta \left\langle E_\tau - \eta \left\{ E_{2\tau} - \eta \left[E_{3\tau} - \eta(E_{4\tau} - Y_{4\tau}) \right] \right\} \right\rangle, \quad (2.211)$$

⋮

that we can rewrite as

$$Y = \eta E_\tau - \eta^2 E_{2\tau} + \eta^3 E_{3\tau} - \eta^4 E_{4\tau} + \dots, \quad (2.212)$$

$$Y = \sum_{j=1}^{\infty} (-1)^{(j-1)} \eta^j E(t - j\tau). \quad (2.213)$$

For $\eta \ll 1$ one can truncate this series, i.e. neglect multiple reflections, and obtain weak single roundtrip feedback similar to the Lang-Kobayashi model [LK80]. For $\eta \rightarrow 1$, however, one cannot easily argue at which j to truncate because none of the multiple reflections will have a significantly lower influence than the previous one. This leaves the DAE to be the appropriate description for systems subjected to strong time-delayed feedback as it correctly describes all the multiple reflections that play an essential role in the evolution of these systems.

2.8 VCSEL coupled to resonant saturable absorber mirror

One possible VECSEL setup consists of separate microcavities for the gain and saturable absorbers, respectively. Figure 2.5 shows a schematic of the simplest implementation with the nonlinear mirrors head to head and a beam splitter in the middle for signal extraction.

Using Eqs. (2.206),(2.207) and (2.33),(2.35) we write two sets of equations for the gain mirror

$$\kappa_1^{-1} \frac{\partial E'_1}{\partial t} = [i\chi_1 - 1] E'_1 + hY'_1, \quad (2.214)$$

$$\chi_1 = -b_1 g_1 (\alpha_1 + i) (\mathcal{N}_1 - \mathcal{N}_1^{(\text{tr})}), \quad (2.215)$$

$$\frac{\partial \mathcal{N}_1}{\partial t} = \mathcal{J}_1 - \gamma_1 \mathcal{N}_1 - \frac{\varepsilon_b}{2\hbar} g_1 (\mathcal{N}_1 - \mathcal{N}_1^{(\text{tr})}) \left| \frac{E'_1}{\xi_1} \right|^2, \quad (2.216)$$

and the absorber mirror

$$\kappa_2^{-1} \frac{\partial E'_2}{\partial t} = [i\chi_2 - 1 + i\delta] E'_2 + hY'_2, \quad (2.217)$$

$$\chi_2 = -b_2 g_2 (\alpha_2 + i) (\mathcal{N}_2 - \mathcal{N}_2^{(\text{tr})}), \quad (2.218)$$

$$\frac{\partial \mathcal{N}_2}{\partial t} = \mathcal{J}_2 - \gamma_2 \mathcal{N}_2 - \frac{\varepsilon_b}{2\hbar} g_2 (\mathcal{N}_2 - \mathcal{N}_2^{(\text{tr})}) \left| \frac{E'_2}{\xi_2} \right|^2. \quad (2.219)$$

A mode of the gain mirror is chosen as the carrier wave frequency, i.e., the detuning term only appears in the evolution of the absorber mirror. The injection fields are the delayed outputs of the respective opposite mirror

$$Y'_1 = O_2(t - \tau) = \eta [E'_{2,\tau} - Y'_{2,\tau}], \quad (2.220)$$

$$Y'_2 = O_1(t - \tau) = \eta [E'_{1,\tau} - Y'_{1,\tau}], \quad (2.221)$$

with the transmission of the beam-splitter $\eta = t_{\text{bs}}$.

To simplify, we first put the susceptibilities into the field evolutions

$$\kappa_1^{-1} \frac{\partial E'_1}{\partial t} = \left[(1 - i\alpha_1) b_1 g_1 (\mathcal{N}_1 - \mathcal{N}_1^{(\text{tr})}) - 1 \right] E'_1 + hY'_1, \quad (2.222)$$

$$\kappa_2^{-1} \frac{\partial E'_2}{\partial t} = \left[(1 - i\alpha_2) b_2 g_2 (\mathcal{N}_2 - \mathcal{N}_2^{(\text{tr})}) - 1 + i\delta \right] E'_2 + hY'_2, \quad (2.223)$$

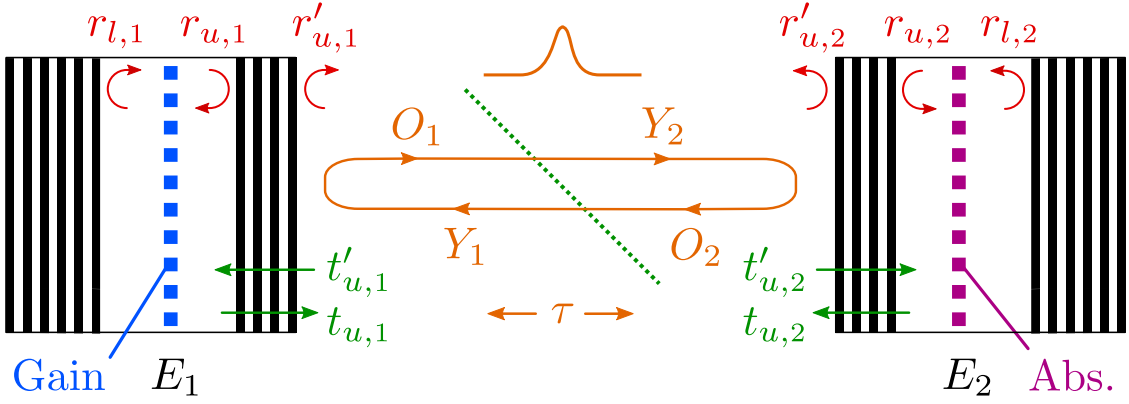


Figure 2.5: Schematic of a VECSEL consisting of a 1/2-VCSEL gain mirror and a resonant saturable absorber mirror at a distance corresponding to the time of flight τ . The fields in the microcavities are denoted E_j for the gain mirror $j = 1$ and the absorber mirror $j = 2$, respectively. The output field O_j of each mirror turns into the injection field Y_j of the other mirror after passing a beam splitter that is used to extract a signal. The transmission and reflection coefficients of the Bragg mirrors are denoted $t_{m,j}$ and $r_{m,j}$, respectively. Here, $m = u$ and $m = l$ stand for the each of the top and bottom mirrors. Further, on the external cavity side the coefficients are marked with primes. A similar version of this figure was used in [5].

and shift the rescaled carrier densities by their transparency levels $N_j = b_j g_j (\mathcal{N}_j - \mathcal{N}_j^{(\text{tr})})$ to obtain concise equations for the field evolutions

$$\kappa_1^{-1} \frac{\partial E'_1}{\partial t} = [(1 - i\alpha_1)N_1 - 1] E'_1 + h Y'_1, \quad (2.224)$$

$$\kappa_2^{-1} \frac{\partial E'_2}{\partial t} = [(1 - i\alpha_2)N_2 - 1 + i\delta] E'_2 + h Y'_2. \quad (2.225)$$

The carrier equations multiplied by $b_j g_j$ read

$$b_j g_j \frac{\partial \mathcal{N}_j}{\partial t} = b_j g_j \mathcal{J}_j - \gamma_j b_j g_j \mathcal{N}_j - b_j \frac{\varepsilon_b}{2\hbar} g_j^2 (\mathcal{N}_j - \mathcal{N}_j^{(\text{tr})}) \left| \frac{E'_j}{\xi_j} \right|^2, \quad (2.226)$$

where we substitute the redefinition of the carriers from above

$$\frac{\partial N_j}{\partial t} = b_j g_j \mathcal{J}_j - \gamma_j (N_j + b_j g_0 \mathcal{N}_j^{(\text{tr})}) - \frac{\varepsilon_b}{2\hbar} g_j N_j \left| \frac{E'_j}{\xi_j} \right|^2, \quad (2.227)$$

$$\frac{\partial N_j}{\partial t} = \gamma_j b_j g_j \left(\frac{\mathcal{J}_j}{\gamma_j} - \mathcal{N}_j^{(\text{tr})} \right) - \gamma_j N_j - \frac{\varepsilon_b}{2\hbar} \frac{g_j}{|\xi_j|^2} N_j |E'_j|^2. \quad (2.228)$$

Be defining the scaled current $J_j = b_j g_j \left(\frac{\mathcal{J}_j}{\gamma_j} - \mathcal{N}_j^{(\text{tr})} \right)$ and the saturation factors $s_j = \frac{\varepsilon_b}{2\hbar} \frac{g_j}{|\xi_j|^2}$ we can write the carriers evolution as

$$\frac{\partial N_j}{\partial t} = \gamma_j J_j - \gamma_j N_j - N_j s_j |E'_j|^2 \quad (2.229)$$

As a last step we rescale the fields $E_j = \sqrt{s_1}E'_j$ and $Y_j = \sqrt{s_1}Y'_j$ and define the ratio of the saturation energies $s = \frac{s_2}{s_1} = \frac{g_2}{g_1} \frac{|\xi_1|^2}{|\xi_2|^2}$. The final scaled equations then read for the gain mirror

$$\kappa_1^{-1} \frac{\partial E_1}{\partial t} = [(1 - i\alpha_1)N_1 - 1] E_1 + h_1 Y_1, \quad (2.230)$$

$$\frac{\partial N_1}{\partial t} = \gamma_1(J_1 - N_1) - |E_1|^2 N_1, \quad (2.231)$$

the absorber mirror

$$\kappa_2^{-1} \frac{\partial E_2}{\partial t} = [(1 - i\alpha_2)N_2 - 1 + i\delta] E_2 + h_2 Y_2, \quad (2.232)$$

$$\frac{\partial N_2}{\partial t} = \gamma_2(J_2 - N_2) - s|E_2|^2 N_2, \quad (2.233)$$

and the injection fields

$$Y_1 = \eta [E_{2,\tau} - Y_{2,\tau}], \quad (2.234)$$

$$Y_2 = \eta [E_{1,\tau} - Y_{1,\tau}]. \quad (2.235)$$

It can be convenient to rescale time with the photon lifetime of the gain mirror, i.e. $\kappa_1 = 1$. This leads to all numbers being closer to one.

2.9 Mode-locked integrated external-cavity surface-emitting-laser

The second case of possible VECSEL setups considered in this thesis uses a single microcavity containing both a gain and saturable absorber medium. Figure 2.6 shows a schematic of an implementation where the external cavity is simply closed by a highly reflective feedback mirror.

Using Eqs. (2.206),(2.207) and (2.33),(2.35) we write

$$\kappa^{-1} \frac{\partial E'}{\partial t'} = [i\chi - 1] E' + h Y', \quad (2.236)$$

$$\chi = -bg_1(\alpha_1 + i) \left(\mathcal{N}_1 - \mathcal{N}_1^{(\text{tr})} \right) - bg_2(\alpha_2 + i) \left(\mathcal{N}_2 - \mathcal{N}_2^{(\text{tr})} \right), \quad (2.237)$$

$$\frac{\partial \mathcal{N}_1}{\partial t'} = \mathcal{J}_1 - \gamma'_1 \mathcal{N}_1 - \frac{\varepsilon_b}{2\hbar} g_1 (\mathcal{N}_1 - \mathcal{N}_1^{(\text{tr})}) \left| \frac{E'}{\xi} \right|^2, \quad (2.238)$$

$$\frac{\partial \mathcal{N}_2}{\partial t'} = \mathcal{J}_2 - \gamma'_2 \mathcal{N}_2 - \frac{\varepsilon_b}{2\hbar} g_2 (\mathcal{N}_2 - \mathcal{N}_2^{(\text{tr})}) \left| \frac{E'}{\xi} \right|^2, \quad (2.239)$$

$$Y' = O(t' - \tau') = \eta [E'_{\tau'} - Y'_{\tau'}], \quad (2.240)$$

with the reflectivity of the feedback mirror $\eta = r_e$.

To simplify, we first shift the rescaled carrier densities by their transparency levels $N'_j = bg_j \left(\mathcal{N}_j - \mathcal{N}_j^{(\text{tr})} \right)$. We get

$$\chi = -(\alpha_1 + i)N'_1 - (\alpha_2 + i)N'_2, \quad (2.241)$$

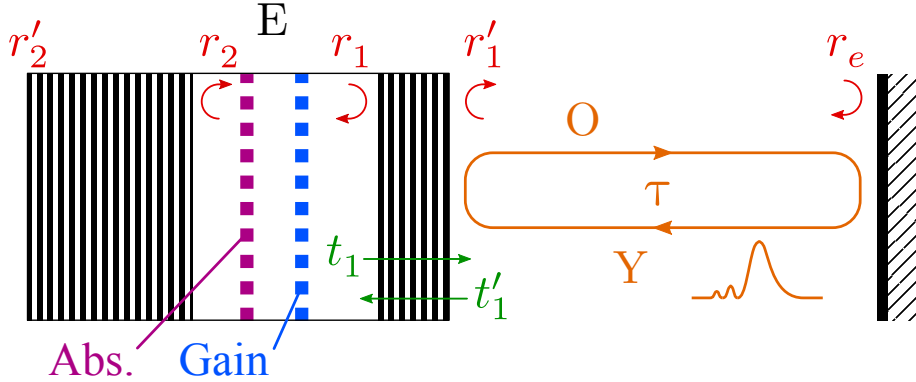


Figure 2.6: Schematic of a VECSEL where the microcavity contains both a gain medium and a saturable absorber medium. The field in the microcavity is E , its output O is re-injected, after one roundtrip of time τ , as Y after being reflected from a feedback mirror that closes the external cavity. The coefficients of the Bragg mirrors are defined as in Fig. 2.3. A similar version of this figure was used in [7].

and

$$\frac{\partial N'_j}{\partial t'} = \gamma'_j b g_j \left(\frac{\mathcal{J}_j}{\gamma'_j} - \mathcal{N}_j^{(\text{tr})} \right) - \gamma'_j N'_j - \frac{\varepsilon_b}{2\hbar} g_j N'_j \left| \frac{E'}{\xi} \right|^2. \quad (2.242)$$

After defining the scaled current $J_j = b g_{0,j} \left(\frac{\mathcal{J}_j}{\gamma'_j} - \mathcal{N}_j^{(\text{tr})} \right)$ and the saturation factors $s'_j = \frac{\varepsilon_b}{2\hbar} \frac{g_j}{|\xi|^2}$ we can write the carrier evolutions as

$$\frac{\partial N'_j}{\partial t'} = \gamma'_j (J_j - N'_j) - N'_j s'_j |E'|^2. \quad (2.243)$$

Also, we now substitute the susceptibility (2.241) into the field evolution (2.236) to get

$$\kappa^{-1} \frac{\partial E'}{\partial t'} = [(1 - i\alpha_1) N'_1 - (1 - i\alpha_2) N'_2 - 1] E' + h Y'. \quad (2.244)$$

Next, we will rescale the time variable $t = \kappa t'$, $\tau = \kappa \tau'$

$$\frac{\partial E'}{\partial t} = [(1 - i\alpha_1) N'_1 - (1 - i\alpha_2) N'_2 - 1] E' + h Y', \quad (2.245)$$

$$\kappa \frac{\partial N'_j}{\partial t} = \gamma'_j (J_j - N'_j) - N'_j s'_j |E'|^2, \quad (2.246)$$

$$Y' = O(\kappa^{-1}[t - \tau]), \quad (2.247)$$

and lastly we rescale $E(t) = \sqrt{s'_1} E'(\kappa t')$ and $Y(t) = \sqrt{s'_1} Y'(\kappa t')$ and define $N(t) = N'(\kappa t')$, $\gamma_j = \kappa^{-1} \gamma'_j$ and $s = \frac{s'_2}{s'_1} = \frac{g_2}{g_1}$ to reach the final dimensionless scaled form of the MIXSEL model

$$\frac{\partial E}{\partial t} = [(1 - i\alpha_1)N_1 + (1 - i\alpha_2)N_2 - 1] E + hY, \quad (2.248)$$

$$\frac{\partial N_1}{\partial t} = \gamma_1(J_1 - N_1) - |E|^2 N_1, \quad (2.249)$$

$$\frac{\partial N_2}{\partial t} = \gamma_2(J_2 - N_2) - s|E|^2 N_2, \quad (2.250)$$

$$Y = \eta [E_\tau - Y_\tau]. \quad (2.251)$$

2.10 Injected Gires-Tournois interferometer with Kerr nonlinearity

If we insert a simple third order nonlinearity $\chi = i|E|^2$ for the susceptibility in equation (2.206) we get an equation that describes a VCSEL like microcavity with a Kerr nonlinear medium instead of the quantum wells. Such a passive cavity can then be driven with a CW injection beam with amplitude Y_0 through an external feedback mirror. A schematic of such a setup is shown in Figure 2.7. With appropriate scaling we get a DAE model for this system

$$\frac{\partial E}{\partial t} = [i(\delta - |E|^2) - 1] E + hY, \quad (2.252)$$

$$Y = \eta [E_\tau - Y_\tau] + \sqrt{1 - |\eta|^2} Y_0, \quad (2.253)$$

where in (2.253) we added the injection with the attenuation factor of the feedback mirror in transmission to (2.207).

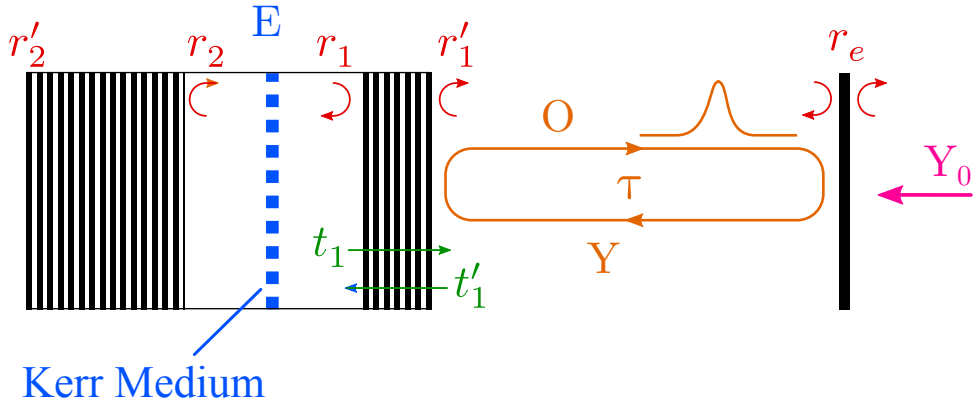


Figure 2.7: Schematic of a setup that is geometrically similar to the MIXSEL but where the microcavity contains a Kerr nonlinear medium. The system is driven by a CW injection field Y_0 through the outside mirror. The fields and coefficients are defined analogous to Fig. 2.4. A similar version of this figure was used in [6].

3 Methods

3.1 Numerical integration of time-delayed equations

To integrate delay differential equation models one needs to remember the time trace of the delayed variables for at least the delay time. Generally, one will only have access to those points that have actually been calculated in the past. Any other point in time will have to be interpolated using the closest points available. Models corresponding to temporal localized structures inherently contain a large stiffness and one would be inclined to use an adaptive mesh. However, the distance to the closest known points can vary strongly, undermining the accuracy of the interpolated delay terms where the resolution is low. We therefore choose an equidistant discretization. Thus, all needed points will either have been calculated or can be interpolated consistently. Moreover, this allows for the consistent introduction of noise. Figure 3.1 shows a schematic of the memory arrangement.

In addition to the current state of the system one needs $M = \frac{\tau}{\Delta t}$ additional points, where τ is the delay time and Δt the time step. One can put the delay memory and current state together as a single structure with $M + 1$ elements. After calculating the next time step with last known point, this last point is no longer needed and can be overwritten by the newly calculated one. This is achieved by wrapping the index corresponding to the current time into the interval, i.e., using the modulo operation with $M + 1$.

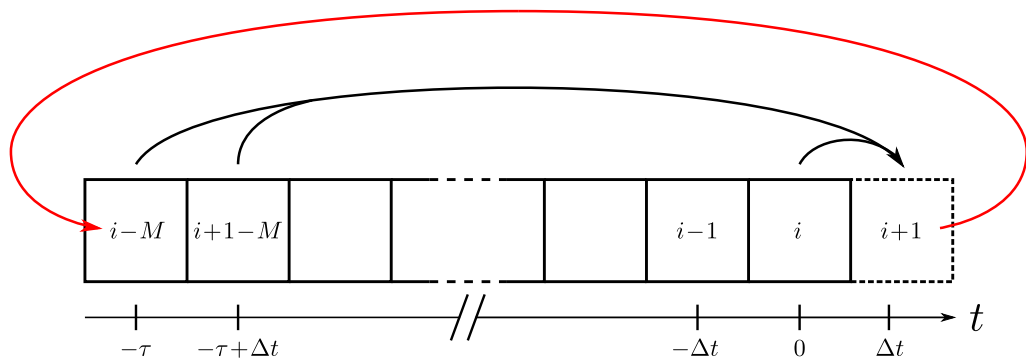


Figure 3.1: Representation of the array data structure containing the memory for the delayed variable and the current state of the system. The last points can be used to interpolate delayed terms. The black arrows indicate all points used in the calculation for the next. After a new step, the oldest point is no longer needed and is overwritten. Thus, the index i that represents the current time loops through the array of size $M + 1$ as indicated by the red arrow.

3.2 4th-Order Runge-Kutta with delay interpolation

Because of the exponential terms in the unidirectional ring model (2.96)–(2.98) we are limited to explicit methods. For a feasible compromise between accuracy and step size we use the classical fourth-order Runge-Kutta (RK) method [PTVF07]

$$k_1 = \Delta t f(t^{(n)}, y^{(n)}), \quad (3.1)$$

$$k_2 = \Delta t f\left(t^{(n)} + \frac{\Delta t}{2}, y^{(n)} + \frac{k_1}{2}\right), \quad (3.2)$$

$$k_3 = \Delta t f\left(t^{(n)} + \frac{\Delta t}{2}, y^{(n)} + \frac{k_2}{2}\right), \quad (3.3)$$

$$k_4 = \Delta t f\left(t^{(n)} + \Delta t, y^{(n)} + k_3\right), \quad (3.4)$$

$$y^{(n+1)} = y^{(n)} + \frac{k_1}{6} + \frac{k_2}{3} + \frac{k_3}{3} + \frac{k_4}{6} + \mathcal{O}(\Delta t^5), \quad (3.5)$$

where $y^{(n)} = (A^{(n)}, G^{(n)}, Q^{(n)})$ is the state vector at the step n , f is the right hand side of the model and Δt is the time step.

To retain fourth-order accuracy we need an appropriate interpolation scheme for the delay term at the half steps $y^{(n-M+\frac{1}{2})}$. We use fourth-order Hermite interpolation, i.e., we need to find a third order polynomial

$$y = a_0 + a_1 t + a_2 t^2 + a_3 t^3, \quad (3.6)$$

$$y' = a_1 + 2a_2 t + 3a_3 t^2. \quad (3.7)$$

that crosses the known points with coinciding first derivatives. Figure 3.2 shows a schematic demonstrating the method.

We choose the origin in the middle of the interval such that $y^{(n-M+\frac{1}{2})}$ is at $t = 0$. This way we only need to find the constant coefficient of the polynomial

$$y^{(n-M+\frac{1}{2})} = a_0 + a_1 0 + a_2 0 + a_3 0 = a_0. \quad (3.8)$$

The known points are then situated at $t = \pm \frac{\Delta t}{2}$ and yield four conditions

$$y^{(n-M)} = a_0 - a_1 \frac{\Delta t}{2} + a_2 \frac{\Delta t^2}{4} - a_3 \frac{\Delta t^3}{8}, \quad (3.9)$$

$$y^{(n-M+1)} = a_0 + a_1 \frac{\Delta t}{2} + a_2 \frac{\Delta t^2}{4} + a_3 \frac{\Delta t^3}{8}, \quad (3.10)$$

$$y'^{(n-M)} = a_1 - 2a_2 \frac{\Delta t}{2} + 3a_3 \frac{\Delta t^2}{4}, \quad (3.11)$$

$$y'^{(n-M+1)} = a_1 + 2a_2 \frac{\Delta t}{2} + 3a_3 \frac{\Delta t^2}{4}. \quad (3.12)$$

We add the first two together and subtract the third from the fourth to get

$$2a_0 + 2a_2 \frac{\Delta t^2}{4} = y^{(n-M+1)} + y^{(n-M)}, \quad (3.13)$$

$$4a_2 \frac{\Delta t}{2} = y'^{(n-M+1)} - y'^{(n-M)}. \quad (3.14)$$

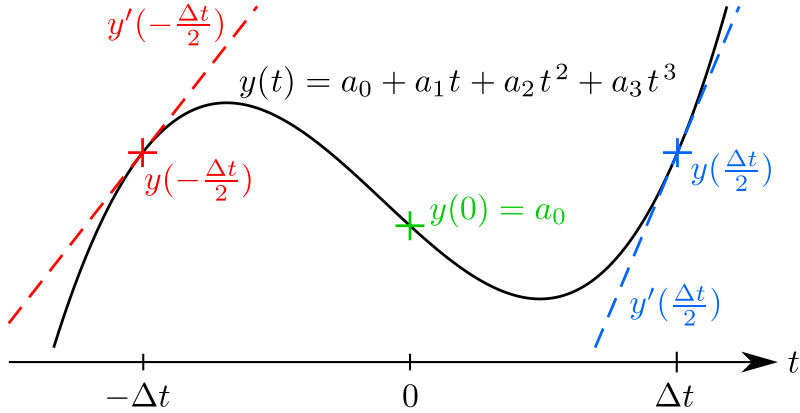


Figure 3.2: Schematic for Hermite interpolation of the central point $y(0)$ in green. A third order polynomial is determined from two known points and their first derivatives in red and green.

Here, the second equation defines the quadratic prefactor

$$a_2 = \frac{y'^{(n-M+1)} - y'^{(n-M)}}{2\Delta t}, \quad (3.15)$$

and that is all we need to solve the remaining equation

$$a_0 + \frac{y'^{(n-M+1)} - y'^{(n-M)}}{8} \Delta t = \frac{y^{(n-M+1)} + y^{(n-M)}}{2}. \quad (3.16)$$

The needed delay term is therefore

$$y^{(n-M+\frac{1}{2})} = \frac{y^{(n-M)} + y^{(n-M+1)}}{2} + \frac{\Delta t}{8} \frac{\partial}{\partial t} [y^{(n-M)} - y^{(n-M+1)}]. \quad (3.17)$$

The required first derivative must be remembered for the whole delay time. Conveniently, it is immediately available from the RK integration.

Note, that noise can only be included to second order, limiting the asymptotic order of this integration scheme. In practice however, for low noise levels this does not pose an issue.

3.3 Semi-implicit leapfrog integration

The differential equation models used to represent the dynamics of the electric field in microcavities allow for a semi-implicit integration algorithm that is computationally very efficient and allows for consistent introduction of noise in the simulation. The delay algebraic equations that appear in the models to describe the external cavities are compatible with this scheme as well.

3.3.1 Concept

The models for the VECSELs have a common structure of three recurring equations (cf. sections 2.8, 2.9)

$$\dot{E} = U(N)E + hY, \quad (3.18)$$

$$\dot{N} = \gamma J - V(|E|^2)N, \quad (3.19)$$

$$Y = \eta[E_\tau + Y_\tau]. \quad (3.20)$$

Notice that each of the differential equations is actually linear with a prefactor that depends only on the respective other variable. As a result, we can trivially solve for implicit terms. The fields and carriers may be approximated by applying the trapezoidal integration rule to combine the explicit and the implicit time-step. In addition we shift the mesh-points of the carrier evolution (3.19) by half a time step with respect to the fields (3.18) and (3.20). That way we can write

$$\frac{E^{(n+1)} - E^{(n)}}{\Delta t} = U^{(n+\frac{1}{2})} \frac{E^{(n)} + E^{(n+1)}}{2} + h \frac{Y^{(n)} + Y^{(n+1)}}{2} + \sigma \xi(t), \quad (3.21)$$

$$\frac{N^{(n+\frac{3}{2})} - N^{(n+\frac{1}{2})}}{\Delta t} = \gamma J + V^{(n+1)} \frac{N^{(n+\frac{1}{2})} + N^{(n+\frac{3}{2})}}{2}, \quad (3.22)$$

where the trapezoidal approximation of the delay term can readily be computed from already known points as it depends only on the past

$$\frac{Y^{(n)} + Y^{(n+1)}}{2} = \eta \frac{E^{(n-M)} - Y^{(n-M)} + E^{(n-M+1)} - Y^{(n-M+1)}}{2}, \quad (3.23)$$

and must be saved to be used in the next delay interval.

The interspersed stepping—called leapfrog integration [PTVF07]—makes it so, that the whole right hand side is effectively evaluated in the center of the integration interval. Together with the trapezoid terms the resulting semi-implicit method is therefore accurate to second order and is highly suitable for dealing the stiffness inherent to temporal localized structures efficiently. Solving these equations then yields the final update rule for the system variables

$$E^{(n+1)} = \frac{\left(1 + \frac{\Delta t}{2} U^{(n+\frac{1}{2})}\right) E^{(n)} + \Delta t h \bar{Y} + \sqrt{\Delta t} \sigma \xi}{1 - \frac{\Delta t}{2} U^{(n+\frac{1}{2})}}, \quad (3.24)$$

$$N^{(n+\frac{3}{2})} = \Delta t \gamma J + \frac{\left(1 + \frac{\Delta t}{2} V^{(n+1)}\right) N^{(n+\frac{1}{2})}}{1 - \frac{\Delta t}{2} V^{(n+1)}}, \quad (3.25)$$

where ξ is a complex normally distributed random number with a standard deviation of σ that approximates a random walk to second order.

3.3.2 VCSEL-RSAM update

Applying the semi-implicit leapfrog method to the VCSEL-RSAM system (2.230)–(2.235) yields the following updating rule

$$E_1^{(n+1)} = \frac{\left(1 + \frac{\Delta t}{2} U_1^{(n+\frac{1}{2})}\right) E_1^{(n)} + \Delta t h \bar{Y}_1 + \sqrt{\Delta t} \sigma \xi_1}{1 - \frac{\Delta t}{2} U_1^{(n+\frac{1}{2})}}, \quad (3.26)$$

$$E_2^{(n+1)} = \frac{\left(1 + \frac{\Delta t}{2} U_2^{(n+\frac{1}{2})}\right) E_2^{(n)} + \Delta t h \bar{Y}_2 + \sqrt{\Delta t} \sigma \xi_2}{1 - \frac{\Delta t}{2} U_2^{(n+\frac{1}{2})}}, \quad (3.27)$$

$$N_1^{(n+\frac{3}{2})} = \Delta t \gamma_1 J_1 + \frac{\left(1 + \frac{\Delta t}{2} V_1^{(n+1)}\right) N_1^{(n+\frac{1}{2})}}{1 - \frac{\Delta t}{2} V_1^{(n+1)}}, \quad (3.28)$$

$$N_2^{(n+\frac{3}{2})} = \Delta t \gamma_2 J_2 + \frac{\left(1 + \frac{\Delta t}{2} V_2^{(n+1)}\right) N_2^{(n+\frac{1}{2})}}{1 - \frac{\Delta t}{2} V_2^{(n+1)}}, \quad (3.29)$$

with

$$U_1 = [(1 - i\alpha_1) N_1 - 1], \quad U_2 = [(1 - i\alpha_2) N_2 - 1 + i\delta], \quad (3.30)$$

$$V_1 = -(\gamma_1 + |E|^2), \quad V_2 = -(\gamma_2 + s |E|^2), \quad (3.31)$$

and

$$\bar{Y}_1 = \eta \frac{E_1^{(n-M)} - Y_1^{(n-M)} + E_1^{(n-M+1)} - Y_1^{(n-M+1)}}{2}, \quad (3.32)$$

$$\bar{Y}_2 = \eta \frac{E_2^{(n-M)} - Y_2^{(n-M)} + E_2^{(n-M+1)} - Y_2^{(n-M+1)}}{2}. \quad (3.33)$$

3.3.3 MIXSEL update

Applying the semi-implicit leapfrog method to the MIXSEL system (2.248)–(2.251) yields the following updating rule

$$E^{(n+1)} = \frac{\left(1 + \frac{\Delta t}{2} U^{(n+\frac{1}{2})}\right) E^{(n)} + \Delta t h \bar{Y} + \sqrt{\Delta t} \sigma \xi}{1 - \frac{\Delta t}{2} U^{(n+\frac{1}{2})}}, \quad (3.34)$$

$$N_1^{(n+\frac{3}{2})} = \Delta t \gamma_1 J_1 + \frac{\left(1 + \frac{\Delta t}{2} V^{(n+1)}\right) N_1^{(n+\frac{1}{2})}}{1 - \frac{\Delta t}{2} V^{(n+1)}}, \quad (3.35)$$

$$N_2^{(n+\frac{3}{2})} = \Delta t \gamma_2 J_2 + \frac{\left(1 + \frac{\Delta t}{2} W^{(n+1)}\right) N_2^{(n+\frac{1}{2})}}{1 - \frac{\Delta t}{2} W^{(n+1)}}, \quad (3.36)$$

with

$$U = [(1 - i\alpha_1) N_1 + (1 - i\alpha_2) N_2 - 1] , \quad (3.37)$$

$$V = - \left(\gamma_1 + |E|^2 \right) , \quad (3.38)$$

$$W = - \left(\gamma_2 + s |E|^2 \right) , \quad (3.39)$$

and

$$\bar{Y} = \eta \frac{E^{(n-M)} - Y^{(n-M)} + E^{(n-M+1)} - Y^{(n-M+1)}}{2} . \quad (3.40)$$

3.3.4 KGTI update

In the case of the Kerr GTI the presence of the $|E|^2 E$ nonlinearity in the evolution of the E field itself prevents one from directly solving for the implicit step. An easy way to circumvent the problem lies in using only the explicit value of $E^{(n)}$ in the nonlinearity. That leads to a mixed form

$$E^{(n+1)} = \frac{(1 + \frac{\Delta t}{2} U) E^{(n)} + \Delta t h \bar{Y} + \sqrt{\Delta t} \sigma \xi}{1 - \frac{\Delta t}{2} U} , \quad (3.41)$$

with

$$U = i \left(\delta - |E^{(n)}|^2 \right) - 1 , \quad (3.42)$$

and

$$\bar{Y} = \eta \frac{E^{(n-M)} - Y^{(n-M)} + E^{(n-M+1)} - Y^{(n-M+1)}}{2} + \sqrt{1 - |\eta|^2} Y_0 . \quad (3.43)$$

Note, that asymptotically this algorithm is only strictly accurate to first order. One may use the result as a predictor step to then recalculate $E^{(n+1)}$ up to second order

$$E^{(n+1)} = \frac{(1 + \frac{\Delta t}{2} V) E^{(n)} + \Delta t h \bar{Y} + \sqrt{\Delta t} \sigma \xi}{1 - \frac{\Delta t}{2} V} , \quad (3.44)$$

with

$$V = i \left(\delta - \left| \frac{E^{(n)} + \tilde{E}^{(n+1)}}{2} \right|^2 \right) - 1 , \quad (3.45)$$

where E is approximated by a linear interpolation of $E^{(n)}$ and a predicted $\tilde{E}^{(n+1)}$. In practice, however, the additional error of using the mixed order single step integration alone turns out to be very small.

3.4 Functional mapping

The concept of the functional mapping approach has been published in [2]. Figure 3.3 shows a schematic of this concept with the various details that are discussed in the following sections.

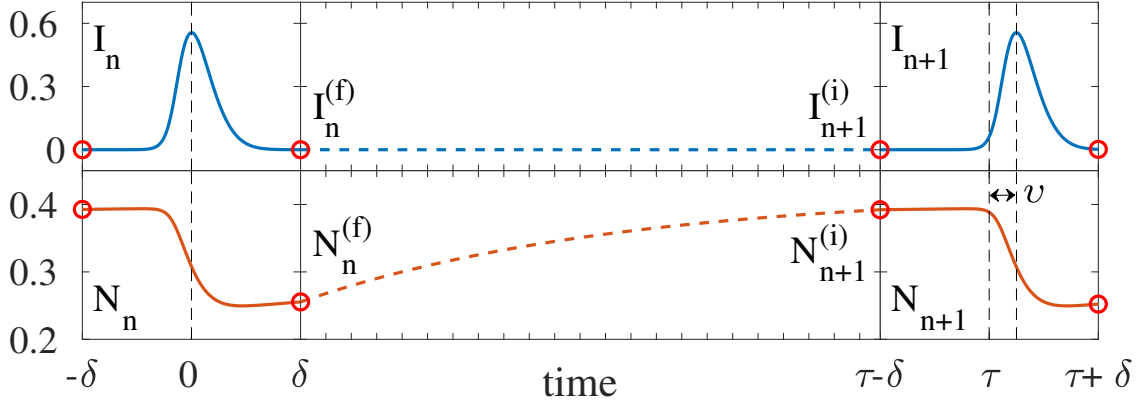


Figure 3.3: Schematic illustrating the functional mapping concept (3.48). The intensity $I = |E|^2$ and gain carrier density N are shown for an exemplary PML regime obtained in the unidirectional ring laser with. Integration of the system is limited to a small box of size $\tau_{\text{box}} = 2\delta$ around pulse (fast stage). The time in between the boxes is not drawn up to scale and can be very large (slow stage). The boxes are numbered n and the next state $n+1$ is obtained from previous. One needs the initial conditions at the beginning of the next box. For TLS the intensity virtually vanishes in the slow stage. Thus $I_{n+1}^{(i)} = 0$ and $N_{n+1}^{(i)}$ can be calculated analytically from last known value $N_n^{(f)}$. In addition, the pulse drift v must be negated. A similar version of this figure was used in [2].

3.4.1 Concept

When looking at a pulse train of temporal localized structures one notices that only the pulses themselves make the problem stiff. The system variables change quickly around the pulse, also called the fast stage. The rest of the temporal profile of the electric field is virtually constant, and in the case of passive mode-locking with a saturable absorber it is generally zero. This causes the carrier inversions to recover exponentially during most of the roundtrip, also called the slow stage. Thus, calculating the whole roundtrip with a small time step appears very inefficient. In this section we will develop a method that combines the efficiency of pulse iterative models while preserving the physical phenomena predicted by time-delay models.

In the respective PML models discussed in this thesis, time-delayed terms only appear for the electric fields. This means that only the field must be stored to define the state of the system. For carrier inversions the last values are sufficient. One may choose to integrate the equations in chunks of τ . The state of the system can then be numbered

$$E_n = E(t), \quad t \in [-\tau, 0], \quad (3.46)$$

plus the final carrier values

$$N_n^{(f)} = N(0). \quad (3.47)$$

In this picture the next state is function of old state

$$E_{n+1} = f(E_n, N_n^{(f)}), \quad (3.48)$$

i.e., the system has the structure of a functional mapping (FM).

When assuming the field to be zero outside of a small box around a pulse one can actually constrict the integration to this box to save a lot of time. The speed-up factor is on the order of the ratio τ/τ_{box} . We position the box of size 2δ around a pulse at $t = 0$ such that the field profile of the state n is defined as

$$E_n = E(t), \quad t \in [-\tau - \delta, -\tau + \delta]. \quad (3.49)$$

To calculate the next state $n + 1$

$$E_{n+1} = E(t), \quad t \in [-\delta, \delta], \quad (3.50)$$

one needs the initial values for the carriers at the start of the next box

$$N_{n+1}^{(i)} = N(-\delta). \quad (3.51)$$

They can typically be calculated analytically or at least with much larger time step from last known carriers

$$N_n^{(f)} = N(-\tau + \delta). \quad (3.52)$$

Note, that this method is not strictly limited to the zero background case, but can work for any constant CW background.

3.4.2 Drift compensation

For causality reasons the period T of TLS is larger than the delay time τ . Pulses would drift with respect to the FM integration box by an amount $v = T - \tau$ and thus slowly out of it. Therefore, before each iteration the pulse needs to be shifted back to a fixed point in the box, e.g. by fixing peak intensity in the center. One may simply shift by a number of mesh points or use some continuous method via Fourier Transform or interpolation. For the non-Fourier cases one has to choose whether to shift circularly or to discard points on one side while padding on the other with the constant field value. With a sufficiently large box this makes little difference in practice, however. An alternative view is that the box is shifted forward in time by v . The old state is then

$$E_n = E(t), \quad t \in [-\tau - \delta + v, -\tau + \delta + v]. \quad (3.53)$$

The exact speed-up factor is then T/τ_{box} .

3.4.3 Carrier reconnection as a boundary condition

After the shift adjustment of E_n in the old box n by v the last known carrier values N_n are still at $t_n^{(f)} = -\tau - \delta$. However, we need them at $t_{n+1}^{(i)} = -\delta + v$ for next step. The time difference between them is therefore the delay time minus the box size and, importantly, plus the shift

$$\Delta\tau = \tau - 2\delta + v. \quad (3.54)$$

Since we assume constant intensity the stimulated emission term in the carrier evolution is a constant, specifically zero for TLS. The carrier model is then linear and just yields

an exponential decay toward the equilibrium value N_0 . Generally, the decay rate would still depend on the stimulated emission while for TLS only the carrier relaxation rate γ_N remains, i.e.,

$$N_{n+1}^{(i)} = N_0 - \left(N_0 - N_n^{(f)} \right) e^{-\gamma_N \Delta\tau}. \quad (3.55)$$

3.4.4 Ring model implementation

For the unidirectional ring model (2.96)–(2.98) the implementation of the FM is straight forward. One simply has to integrate the box using the known field envelope profile A_n and the initial conditions build from the integrated gain G_n and absorption Q_n values of the previous step

$$A_{n+1}^{(i)} = 0, \quad (3.56)$$

$$G_{n+1}^{(i)} = \Gamma^{-1} g_0 - \left(\Gamma^{-1} g_0 - G_n^{(f)} \right) e^{-\Gamma \Delta\tau}, \quad (3.57)$$

$$Q_{n+1}^{(i)} = q_0 - \left(q_0 - Q_n^{(f)} \right) e^{-\Delta\tau}. \quad (3.58)$$

3.4.5 VCSEL-RSAM implementation

For the implementation of the VCSEL-RSAM model (2.230)–(2.235) one has to deal with the fact that the temporal localized structures are alternating between two different cavities. When choosing to start with the gain mirror, the state of the system is defined by the absorber output $O_{2,n}$ and the final values of the carrier inversions $N_{1,n}^{(f)}, N_{2,n}^{(f)}$.

The value $Y_{1,n+1}$ can already be calculated from the last step

$$Y_{1,n+1} = \eta O_{2,n}. \quad (3.59)$$

With this and the and initial conditions

$$E_{1,n+1}^{(i)} = 0, \quad (3.60)$$

$$N_{1,n+1}^{(i)} = J_1 - \left(J_1 - N_{1,n}^{(f)} \right) e^{-\gamma_1 \Delta\tau}, \quad (3.61)$$

the temporal profile of the gain intra-cavity field $E_{1,n+1}$ can be integrated. For absorber mirror both previous fields then combine to form the injection field

$$Y_{2,n+1} = \eta [E_{1,n+1} - Y_{1,n+1}]. \quad (3.62)$$

Analogously as for the gain mirror, this is used to integrated the absorber field profile $E_{2,n+1}$ using the initial conditions

$$E_{2,n+1}^{(i)} = 0, \quad (3.63)$$

$$N_{2,n+1}^{(i)} = J_2 - \left(J_2 - N_{2,n}^{(f)} \right) e^{-\gamma_2 \Delta\tau}. \quad (3.64)$$

Finally both of the absorber fields combine to form the state of the next step

$$O_{2,n+1} = E_{2,n+1} - Y_{2,n+1}. \quad (3.65)$$

Integrating one box for each mirror like this constitutes a full step step of the FM. Which mirror goes first is a matter of choice. Note, that for the VCSEL-RSAM setup the roundtrip time is twice the delay time so the time between FM integration boxes is

$$\Delta\tau = 2\tau - 2\delta + v. \quad (3.66)$$

Shifting only one injection field before every full step is sufficient as the pulse is not retarded much in either mirror. When shifting twice, the time difference must be adjusted slightly

$$\Delta\tau = 2\tau - 2\delta + v_1 + v_2. \quad (3.67)$$

3.4.6 MIXSEL implementation

The implementation of the MIXSEL (2.248)–(2.251) is analogous to the VCSEL-RSAM model from the previous section. However, it is simpler in having only one microcavity and thus does not require the interspersed step.

The injection of the new step simply reads

$$Y_{n+1} = \eta O_n. \quad (3.68)$$

Along with the initial conditions

$$E_{n+1}^{(i)} = 0, \quad (3.69)$$

$$N_{1,n+1}^{(i)} = J_1 - \left(J_1 - N_{1,n}^{(f)} \right) e^{-\gamma_1 \Delta\tau}, \quad (3.70)$$

$$N_{2,n+1}^{(i)} = J_2 - \left(J_2 - N_{2,n}^{(f)} \right) e^{-\gamma_2 \Delta\tau}, \quad (3.71)$$

the new temporal field profile E_{n+1} is integrated. The next step can then be started from

$$O_{n+1} = E_{n+1} - Y_{n+1}. \quad (3.72)$$

3.5 Continuation in DDE-BIFTOOL

DDE-BIFTOOL [ELR02] is a framework for bifurcation analysis of delay differential equations, however, it was not designed with delay algebraic equations in mind and cannot handle this specific case directly. We therefore need to approximate DAEs in an appropriate form. Also, the symmetry in the complex phase of the systems has to be dealt with specially for both DDE and DAE problems.

3.5.1 Implementing a DAE as a singularly perturbed differential equation

We can add a singular perturbation to the generic delay algebraic equation (2.207) to obtain a delay differential equation

$$Y = \eta [E_\tau - Y_\tau], \quad (3.73)$$

$$\epsilon \frac{\partial Y}{\partial t} \approx 0 = \eta [E_\tau - Y_\tau] - Y, \quad (3.74)$$

with $\epsilon \ll 1$. In the limit $\epsilon \rightarrow 0$ this DDE becomes equal to the original DAE. In this approximate form we can analyze the DAE models in DDE-BIFTOOL at the cost of introducing additional stiffness to the systems which can lead to numerical difficulties when calculating the linear stability of periodic orbits.

3.5.2 Phase invariance

Due to the complex valued nature of the electric field, both the unidirectional ring and the VECSEL models have an inherent phase symmetry. The fields may be rotated freely since there is no fixed reference point. Thus, if a TLS profile is entirely rotated by some phase the resulting dynamics will be exactly the same up to said phase offset which remains conserved. For the solution structure this means that any steady state is actually an infinite set of steady states. Branches for a given intensity—or temporal profile thereof—are indeed tubes. During continuation in DDE-BIFTOOL, this means that the algorithm would tend to not follow the desired branch but instead loop around the polar coordinate of the tube, i.e., the complex phase of the solution. To counteract this problem one needs to break the phase symmetry.

Let us consider a delay model in a generalized form

$$\frac{\partial E}{\partial t} = f(t)E(t) + g(t - \tau)E(t - \tau). \quad (3.75)$$

We write the ansatz $E(t) = E_0(t) \exp[-i\omega t]$, where ω is the rate at which $E_0(t)$ will rotate in the complex plane while retaining a constant phase profile. Introducing this ansatz in the model we get

$$\frac{\partial E_0(t)}{\partial t} e^{-i\omega t} - i\omega E_0(t) e^{-i\omega t} = f(t)E_0(t) e^{-i\omega t} + g(t - \tau)E_0(t - \tau) e^{-i\omega(t-\tau)}, \quad (3.76)$$

$$\frac{\partial E_0(t)}{\partial t} = [f(t) + i\omega] E_0(t) + e^{i\omega\tau} g(t - \tau) E_0(t - \tau). \quad (3.77)$$

We can implement this form of the model in standard DDE-BIFTOOL and introduce an additional condition C that determines the phase of E_0 . A convenient choice for CW solutions is

$$C = \text{Im}E_0 = 0. \quad (3.78)$$

The same can be defined for a specific mesh point of a periodic orbit. In the case of temporal localized structures most of the field is close to zero and thus its phase is not well defined. Therefore the mesh point containing the maximum field intensity is chosen to lock the complex phase. After associating the new free continuation parameter ω with the extra condition, DDE-BIFTOOL will adjust it to fulfill the condition, thus reducing the solution manifolds to simple branches.

Note that in the KGTI model (2.252),(2.253) the intra-cavity field is phase-locked to the injection, i.e. a driven oscillator. Thus, the problem does not appear here and the standard methods of DDE-BIFTOOL are sufficient.

Ring model implementation

The phase-locked form of the unidirectional ring model as implemented in DDE-BIFTOOL reads

$$\frac{1}{\gamma} \frac{\partial A(\tau)}{\partial \tau} = \sqrt{\kappa} e^{\frac{1-i\alpha_g}{2}G(\tau) - \frac{1-i\alpha_q}{2}Q(\tau) + i(T-\phi)} A(\tau - T) + (i\frac{\omega}{\gamma} - 1)A(\tau), \quad (3.79)$$

$$\frac{\partial G(\tau)}{\partial \tau} = g_0 - \Gamma G(\tau) - e^{-Q(\tau)} (e^{G(\tau)} - 1) |A(\tau - T)|^2, \quad (3.80)$$

$$\frac{\partial Q(\tau)}{\partial \tau} = q_0 - Q(\tau) - s (1 - e^{-Q(\tau)}) |A(\tau - T)|^2. \quad (3.81)$$

MIXSEL implementation

The phase-locked form of the MIXSEL model as implemented in DDE-BIFTOOL reads

$$\frac{\partial E}{\partial t} = [(1 - i\alpha_1)N_1 + (1 - i\alpha_2)N_2 - 1 + i\omega] E + hY, \quad (3.82)$$

$$\frac{\partial N_1}{\partial t} = \gamma_1(J_1 - N_1) - |E|^2 N_1, \quad (3.83)$$

$$\frac{\partial N_2}{\partial t} = \gamma_2(J_2 - N_2) - s|E|^2 N_2, \quad (3.84)$$

$$Y = \eta [E_\tau - Y_\tau] e^{i\omega\tau}. \quad (3.85)$$

3.5.3 Rotational symmetry extension

Alternatively to the extra condition approach (3.78), as of version 3 DDE-Biftool comes with an extension for dealing with rotational symmetries. To make use of it, the complex fields have to be split into their real and imaginary parts and then combined with the real carrier inversions into a real valued vector-function. The state vector will be of the form

$$\rho = \begin{pmatrix} \text{Re}[E] \\ \text{Im}[E] \\ N \end{pmatrix}. \quad (3.86)$$

In addition, one has to provide a rotation matrix of the form

$$\mathbf{R}(\omega t) = \begin{pmatrix} \cos(\omega t) & \sin(\omega t) & 0 \\ -\sin(\omega t) & \cos(\omega t) & 0 \\ 0 & 0 & 1 \end{pmatrix}. \quad (3.87)$$

It must contain rotations for the fields and unity for carriers. Alternatively, the generator of the rotation matrix

$$\mathbf{G} = \begin{pmatrix} 0 & 1 & 0 \\ -1 & 0 & 0 \\ 0 & 0 & 0 \end{pmatrix} \quad (3.88)$$

can be used. Given such a matrix, the extension provides automated routines to set up and use an extended system created from the original one containing the phase symmetry.

The end result is equivalent to the phase invariant form. Note however, that as of now the rotational symmetry extension is not compatible with user provided Jacobian functions and is limited to using the numerical approximation supplied by DDE-BIFTOOL. This can be detrimental to computational accuracy and efficiency in exchange for more convenient usability.

Ring model implementation

For the implementation of the unidirectional ring model (2.96)–(2.98) the state vector is

$$\rho = \begin{pmatrix} \text{Re}[A] \\ \text{Im}[A] \\ G \\ Q \end{pmatrix}, \quad (3.89)$$

the rotation matrix is

$$\mathbf{R}(\omega t) = \begin{pmatrix} \cos(\omega t) & \sin(\omega t) & 0 & 0 \\ -\sin(\omega t) & \cos(\omega t) & 0 & 0 \\ 0 & 0 & 1 & 0 \\ 0 & 0 & 0 & 1 \end{pmatrix}, \quad (3.90)$$

and the generator is

$$\mathbf{G} = \begin{pmatrix} 0 & 1 & 0 & 0 \\ -1 & 0 & 0 & 0 \\ 0 & 0 & 0 & 0 \\ 0 & 0 & 0 & 0 \end{pmatrix}. \quad (3.91)$$

MIXSEL implementation

For the implementation of the MIXSEL model (2.248)–(2.251) the state vector is

$$\rho = \begin{pmatrix} \text{Re}[E] \\ \text{Im}[E] \\ \text{Re}[Y] \\ \text{Im}[Y] \\ N_1 \\ N_2 \end{pmatrix}, \quad (3.92)$$

the rotation matrix is

$$\mathbf{R}(\omega t) = \begin{pmatrix} \cos(\omega t) & \sin(\omega t) & 0 & 0 & 0 & 0 \\ -\sin(\omega t) & \cos(\omega t) & 0 & 0 & 0 & 0 \\ 0 & 0 & \cos(\omega t) & \sin(\omega t) & 0 & 0 \\ 0 & 0 & -\sin(\omega t) & \cos(\omega t) & 0 & 0 \\ 0 & 0 & 0 & 0 & 1 & 0 \\ 0 & 0 & 0 & 0 & 0 & 1 \end{pmatrix}, \quad (3.93)$$

and the generator is

$$\mathbf{G} = \begin{pmatrix} 0 & 1 & 0 & 0 & 0 & 0 \\ -1 & 0 & 0 & 0 & 0 & 0 \\ 0 & 0 & 0 & 1 & 0 & 0 \\ 0 & 0 & -1 & 0 & 0 & 0 \\ 0 & 0 & 0 & 0 & 0 & 0 \\ 0 & 0 & 0 & 0 & 0 & 0 \end{pmatrix}. \quad (3.94)$$

4 Unidirectional Ring Laser

We analyze the dynamics of temporal localized structures that appear in the widely used model for passive mode-locking established in [VT05]. The focus lies on the influences of gain bias and of the linewidth enhancement factors. This sets a baseline for TLS behavior in order to compare with the more specific setups and models discussed in the subsequent chapters. Most of the results presented in this chapter have been published in [1] and [2].

4.1 Lasing threshold

We use the model (2.96)–(2.98) where we refer to time as t and to the delay as τ . Also, we rescale the pump rate $g_0 \rightarrow \Gamma g_0$ so we have

$$\frac{1}{\gamma} \frac{\partial A(t)}{\partial t} = \sqrt{\kappa} e^{\frac{1-i\alpha_g}{2}G(t) - \frac{1-i\alpha_q}{2}Q(t) - i\phi} A(t - \tau) - A(t), \quad (4.1)$$

$$\frac{\partial G(t)}{\partial t} = \Gamma(g_0 - G(t)) - e^{-Q(t)} (e^{G(t)} - 1) |A(t - \tau)|^2, \quad (4.2)$$

$$\frac{\partial Q(t)}{\partial t} = q_0 - Q(t) - s(1 - e^{-Q(t)}) |A(t - \tau)|^2. \quad (4.3)$$

To find the CW solutions we use the ansatz $A = A_0 e^{-i\omega t}$ with a constant amplitude A_0 and get

$$-i\frac{\omega}{\gamma} A_0 e^{-i\omega t} = \sqrt{\kappa} e^{\frac{1-i\alpha_g}{2}G - \frac{1-i\alpha_q}{2}Q - i\phi} A_0 e^{-i\omega(t-\tau)} - A_0 e^{-i\omega t}, \quad (4.4)$$

$$1 - i\frac{\omega}{\gamma} = \sqrt{\kappa} e^{\frac{1-i\alpha_g}{2}G - \frac{1-i\alpha_q}{2}Q + i(\omega\tau - \phi)}, \quad (4.5)$$

with constant carriers G and Q that solve

$$0 = \Gamma(g_0 - G) - e^{-Q} (e^G - 1) |A_0|^2, \quad (4.6)$$

$$0 = q_0 - Q - s(1 - e^{-Q}) |A_0|^2. \quad (4.7)$$

In the limit of $|A_0| \rightarrow 0$ the carriers are simply

$$G = g_0, \quad (4.8)$$

$$Q = q_0, \quad (4.9)$$

so the condition for a CW solution becomes

$$1 - i\frac{\omega}{\gamma} = \sqrt{\kappa} e^{\frac{1-i\alpha_g}{2}g_0 - \frac{1-i\alpha_q}{2}q_0 + i(\omega\tau - \phi)}. \quad (4.10)$$

Because of the exponential on the right hand side, the solutions of this equation are transcendental. We take the modulus squared of this condition and solve for g_0

$$g_0 = q_0 - \ln \kappa + \ln \left(1 + \frac{\omega^2}{\gamma^2} \right). \quad (4.11)$$

From this equation we know what g_0 to put in order to get a CW solution with frequency ω as a function of the other parameters, however, ω may not be chosen freely. As will be shown in the next paragraph, only a countable set of $\omega = \omega^{(k)}$ yield actual solutions. Among the possible $\omega^{(k)}$, the smallest $g_0^{(k)}$ will be the threshold of the laser and we see that, indeed, we need to find the $\omega^{(k)}$ closest to zero.

For a CW solution we must not only match the modulus of (4.10) but also the complex phase. We can write the imaginary part of (4.10) as

$$\frac{\theta}{\gamma\tau} = \sqrt{\kappa} \sin(\Theta - \theta). \quad (4.12)$$

where we defined the delay phase due to the frequency shift $\theta = \omega\tau$ and the overall phase-shift per roundtrip $\Theta = \frac{\alpha_g g_0 - \alpha_q q_0}{2} + \phi$. When considering the long delay limit $\tau \rightarrow \infty$, we simply need to solve $\sin(\Theta - \theta) = 0$ which means $\theta = \Theta + 2\pi z$ for any integer $z \in \mathbb{Z}$. After substituting back the definition of θ we get

$$\omega = \frac{\Theta + 2\pi z}{\tau}, \quad z \in \mathbb{Z} \quad (4.13)$$

where we have to take the limit to infinite τ again. This expression can be interpreted as equally spaced modes $\omega^{(k)} = \frac{2\pi}{\tau}k$, $k \in \mathbb{Z}$ with a residual phase shift $\Theta\tau^{-1}$ that tends to zero for large delay times. See Figure 4.1 for an illustration of the mode behavior. We may therefore safely take the limit $|\omega| \rightarrow 0$ in (4.11) to get the threshold

$$g_0^{(\text{th})} = q_0 - \ln \kappa, \quad (4.14)$$

in the long delay limit $\tau \rightarrow \infty$.

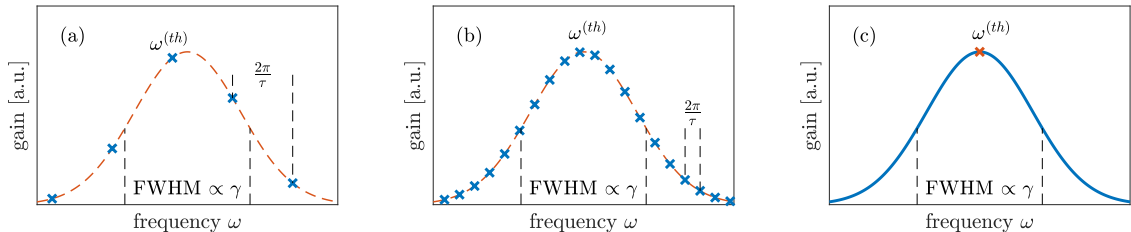


Figure 4.1: External cavity modes (crosses) of a laser with bandwidth γ . (a) The modes spreading is approximately proportional to the inverse roundtrip (delay) time τ^{-1} . (b) For large τ a mode closer to the maximum of the gain curve (dashed line) is available to become the threshold mode $\omega^{(\text{th})}$. (c) The modes become continuous in the long cavity (long delay) limit where the threshold frequency can be chosen freely.

More generally, consider the phase $\exp[i\omega\tau]$ coming from the delay term. For some large delay $\tau \gg 1$ a very small change in the frequency $|\Delta\omega| \ll 1$ is always sufficient to get an arbitrary delay phase, i.e., $\omega\tau \in [-\pi, \pi]$ that cancels any remaining phase contributions. In the long delay limit the required change is infinitesimal such that the laser may operate at the optimal gain frequency (cf. Panel (c) of Fig. 4.1).

4.2 Temporal localized structures

The origin of the localized regime of pulses in the model at interest was explained in [MJBG14] including fundamental results obtained via numerical path continuation and the dynamics of stable temporal localized structures were investigated in [JCMG16, CJMG16]. The following sections focus on the bifurcation analysis of these TLSs including the influence of the linewidth enhancement factors that can lead to oscillating pulse profiles.

4.2.1 Obtaining a TLS in DDE-BIFTOOL

A branch of TLS solutions typically connects to a CW solution in an Andronov-Hopf bifurcation that is directly related to the delay time τ . In order for this bifurcation to occur, the delay time needs to be sufficiently large. It roughly coincides with the period of the periodic orbit born at the bifurcation. Otherwise the oscillation cannot fit into the roundtrip and the CW solution remains stable. This makes τ an important control parameter for bifurcation analysis.

Directly beyond the bifurcation point, the periodic orbit can be easily constructed. A small harmonic perturbation is created around the underlying steady CW solution as an initial guess. After correction, this solution can then be continued up in τ to compute the branch of TLS solutions. It deforms from the initial harmonic perturbation into a nonlinear pulse shape that corresponds to a typical passively mode-locked solution. Such a pulse can already be intense enough to saturate the absorber sufficiently in order to be continued down in the gain bias g_0 below threshold. From there τ can then, in principle, be increased to arbitrary numbers. The field intensity after the pulse will go increasingly close to zero while the gain and absorber carriers will relax increasingly close to the bias values g_0 and q_0 , thus increasing the level of localization. See Figure 4.2 for the development of an exemplary TLS from the corresponding harmonic perturbation.

Note, that qualitatively different Andronov-Hopf instabilities of the CW state can exist, where the period does not follow the delay time. Here, a possible occurrence of commensurate period and delay time would be purely coincidental and hence would not lead to PML. A way to spot the right kind of bifurcation is to see whether additional Andronov-Hopf bifurcations with similar frequency appear at multiples of the delay time for the same CW solution. These give rise to periodic solutions with two or more periods of the same original harmonic perturbation. They belong to the higher harmonics of the PML solution which necessarily exist as well. Physically one can always imagine an external cavity of twice the length with twice as many equal and equally spaced pulses to be an almost equivalent system. The main difference is that higher harmonics offer additional types of instabilities that stem from pulse interactions.

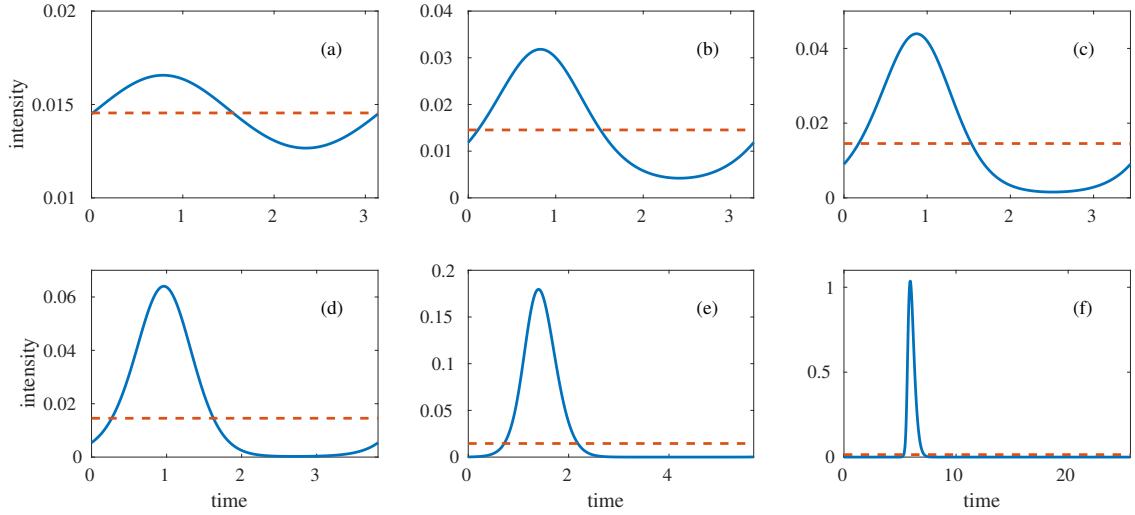


Figure 4.2: Evolution of the solution profiles along a branch of periodic orbits starting from an Andronov-Hopf bifurcation point with the delay time τ increasing from panels (a) to (f). The temporal profiles of the intensity in solid blue originate from a small harmonic perturbation around the underlying unstable CW solution in dashed orange and develop into a TLS with increasing period.

Alternatively one may choose to import a time trace from direct numerical simulations that represents the periodic orbit. Ideally by integrating the equations in the form that is used in DDE-BIFTOOL itself as described in Section 3.5. Usually, this would involve calculating a sufficiently accurate initial guess of the frequency shift associated with the periodic orbit from the standard system. It can then be used to find the equivalent orbit again. One might just try letting DDE-BIFTOOL correct the original trace and maybe even free some of the parameters. However, this may result in an orbit far away from the original one or on a different branch altogether and, of course, this approach is not guaranteed to work at all.

In practice, too large a τ will eventually lead to a situation where the number of mesh-points is insufficient to accurately resolve the profiles. Interestingly, the continuation of TLS solutions breaks only for rather large values of τ . This is due to the fact that, effectively, the profile is only stiff around the pulse. Here, the field intensity is large and the carriers evolve quickly while far from the pulse the carriers only relax slowly. This leads the mesh adaption of DDE-BIFTOOL to cluster the majority of mesh-points at the pulse.

The issue lies in the fact that the field still evolves fast everywhere and thus becomes undersampled for most of the roundtrip. Here, small errors on few meshpoints hardly affect the residual error of the whole profile, however, the intensity is so small that the relative errors are actually very large. This can lead to artifacts building up far from the pulse while continuing a branch since the solutions are accepted anyway, yet eventually the continuation gets stuck. More importantly, the strongly varying resolution makes the Floquet analysis numerically unstable; the exponential tail of the gain carriers is undersampled which results in the Floquet multiplier of high frequency modes being spurious.

They tend to jump erratically, even for minute changes to the profile or mesh. The continuation of bifurcations points of periodic orbits does not work properly in this situation either. This problem might be solved in the future by extending the approach introduced in [YRSW19].

4.2.2 Parameter set

If not stated otherwise, the following set of parameters is used throughout this chapter. The time scale of the model is normalized to the absorber relaxation time τ_q , which for a semiconductor medium it will be around 20 ps. The rate of the filter is set to $\gamma = 10$ that would then correspond to a bandwidth of $\gamma/(\pi\tau_q) \approx 160$ GHz as a Lorentzian spectral line shape was assumed for the model. The gain relaxation rate is set to $\Gamma = 0.04$ and thus corresponds to $\tau_g = 500$ ps. The linear losses are set to $\kappa = 0.8$ and the absorber bias to $q_0 = 0.3$ which corresponds to a modulation of the nonlinear losses of $1 - \exp(-q_0) \approx 26\%$. The ratio of the gain to absorber saturation energies is set to $s = 30$. The delay time is set to $\tau = 100$ which corresponds to 2 ns. The product $\Gamma\tau = 4$ means the gain has time to relax by a factor of approximately e^{-4} per roundtrip and is a good way to measure the level of localization, i.e., the how much a pulse will interact with the next. The delay phase is discarded, i.e. set to $\phi = 0$, since in the long delay limit it can be negated by an infinitesimal change of the frequency shift (cf. previous section).

Temporal localized structures always emerge subcritical, i.e., they exist only below the lasing threshold. Thus, it is more convenient to work with a normalized gain coefficient $g = g_0/g_0^{(\text{th})}$.

4.2.3 Typical TLS profile and branch structure

Figure 4.3 shows results obtained using DDE-BIFTOOL for a typical typical branch of TLSs. In panel (a) the branch is represented by the maximum of the intensity $I = |A|^2$ of the corresponding pulse as a function of the normalized gain g . The curve reaches very small intensities close to the threshold. Towards lower gain, it evolves as an unstable solution on top of the stable off solution, i.e. subcritically. It then folds back toward higher gain forming a typical C shape. The branch then continues on beyond the threshold where secondary Andronov-Hopf (or torus) bifurcations destabilize it.

Panel (b) of Figure 4.3 shows the so-called period deviation. In the long delay limit the period approaches constant offset to the delay time $\delta = T - \tau$. The period is on the order of $T_0 = \tau + 1/\gamma$ where the $1/\gamma$ term comes from the inertia of the filter. The period deviation is then $T - T_0$ which is the residual part of the period that is characteristic of a given pulse profile. It is typically of small magnitude and close to zero, thus yielding a handy measure to plot. For the stable part the period deviation decreases roughly proportional to the peak intensity which hints at its connection with the absorber depletion; a large pulse saturates the absorber faster and is thereby slowed less by passing it.

The panels (c) and (d) of Figure 4.3 show the full temporal profiles of the periodic orbits marked in the previous panels. The stable pulse in (c) is much larger than the unstable one in (d). The absorber returns quickly to its equilibrium value as compared to the gain which needs most of the roundtrip. A residual saturation of the gain always

remains in front of the pulse, mathematically this is unavoidable. However, the difference to the equilibrium value is already relatively small at $T \approx \tau = 100$ - approximately $\exp(-\Gamma T) \approx \exp(-4) \approx 1.8\%$. Thus, one may consider this the beginning of the localized regime.

Finally, panels (e) and (f) of Figure 4.3 show a zoom on the area around pulse of the profiles in (c) and (d), respectively. The pulse length is only on the order of ~ 1 which is very short as compared to the roundtrip. Note however, that the effective length of the localized structure is not defined by the pulse but by the trail it leaves in the carrier inversion, specifically the gain recovery, which is the slowest variable. When imagining a much larger external cavity with several pulses in it, their mutual interactions will be governed by the gain trail of the respective pulse in front of each.

4.2.4 Bistable region

Figure 4.4 shows how the saturation ratio s and the linewidth enhancement factor α affect the fold of the TLS branch. In panel (a) the full branches are illustrated using the peak intensity of the pulse as a function of the normalized gain g for different values of s . With a higher saturation ratio the fold moves further toward lower g , thereby increasing the region where TLS are bistable with the off solution. This is intuitively clear from the fact that less energy is needed to saturate the absorber, hence smaller pulses can do so and less gain is needed to support them. Also for not too large s the peak intensity of the pulses grows at a given g for the same reason. This effect is limited, however, as the gain also saturates and a maximum pulse energy is reached. Further increases in s then only affects the low g part of the branch and generally exhibits diminishing returns.

Panel (b) shows the branch of the fold itself as a function g and s for increasing α . Generally one sees a diagonal trend of the fold curve and more g or s is required to make up for the effect of α . High α typically leads to broader pulses, i.e., the pulse energy is spread out more in time. This affects the evolution of the gain and absorber carriers differently. Since the absorber recovers relatively quickly it becomes harder to saturate for the broader pulse. It needs more time to pass the absorber and thus has to saturate repeatedly the carriers that thermalize. At the same time the saturation happens slower and becomes less effective. Indeed at some point the recovery would completely cancel the saturation caused by the pulse. Overall this means more losses for a broadened pulse and results in a bigger minimal pulse for stable existence. For the much slower gain there is not such a big difference due to pulse broadening.

4.2.5 Multi-peak solutions

The previously introduced single pulses are not the only TLS solutions found in this system. Using numerical continuation techniques one can explore the full solution space, including all the unstable solutions which are inaccessible by direct numerical simulations. There exists a series of mostly unstable TLS solutions with an increasing numbers of maxima in their intensity profiles, not unlike soliton molecules in dissipative systems [GSC08]. In Figure 4.5 the first two of these multi-peak solutions are presented along with the single pulse from before. Panel (a) shows the corresponding branches with the maximum

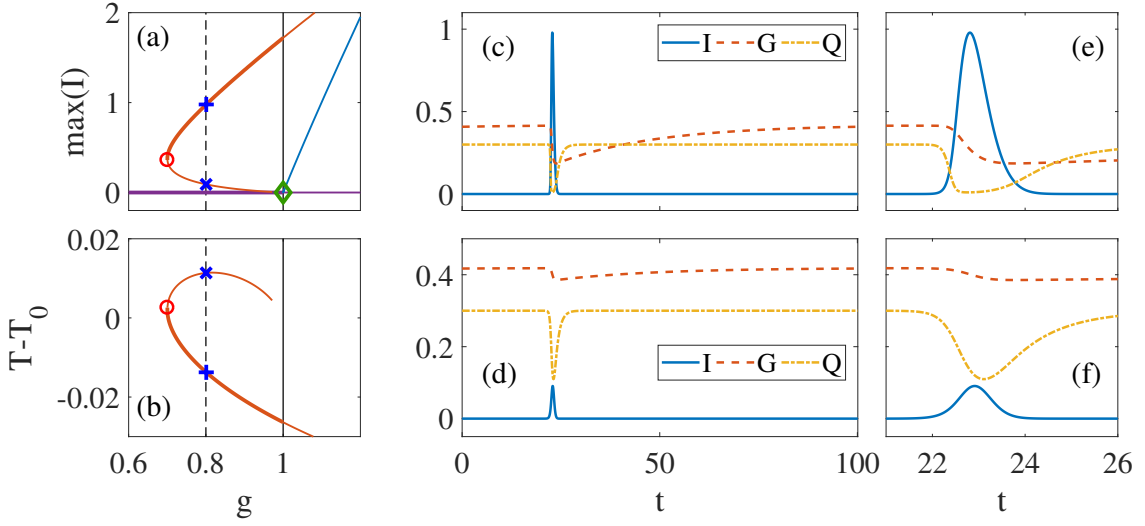


Figure 4.3: Branch of the principal TLS as a function of the normalized gain g . (a) Intensity at the peak of the pulse in solid orange for stable solutions and thin for unstable. The blue line represents the CW solution branch with its intensity multiplied by 10^2 for comparison. (b) Period deviation of the TLS from the nominal period of the laser $T_0 = \tau + \gamma^{-1}$. (c) Temporal profiles for the stable solution marked in (a,b) at $g = 0.8$. (d) The respective unstable solution on the opposite part of the branch. (e,f) Zoomed view of the profiles around the pulses in (c,d). Other parameters are $(\alpha, \beta) = (0, 0)$. A similar version of this figure was used in [1].

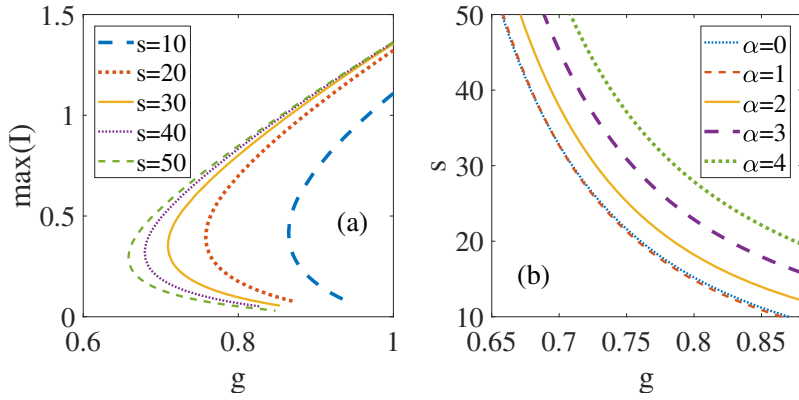


Figure 4.4: (a) C-shaped peak intensity of TLS branches as a function of the gain normalized to threshold g . For an increasing saturation ratio s of the absorber the existence region of the TLS grows, i.e., the fold of the branch moves to lower g . Other parameters are $(\alpha, \beta) = (1, 0.5)$. (b) The fold of the TLS branch as a function of both g and s at different values of the gain linewidth enhancement factor α . More gain or saturation ratio are necessary in order to achieve a similar range of existence when increasing α . A similar version of this figure was used in [1].

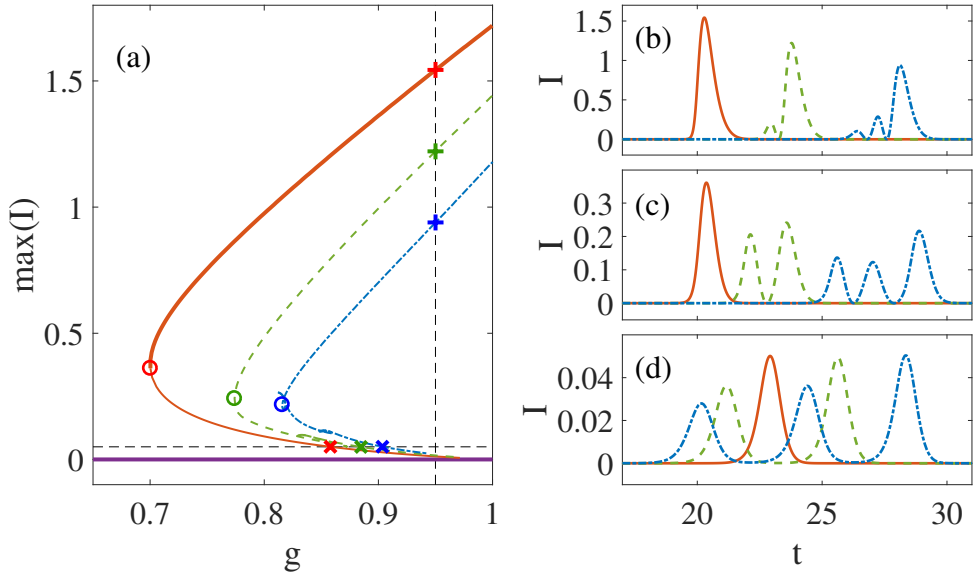


Figure 4.5: (a) Branches of the maximum intensities of TLS with multiple peaks as a function of the normalized gain g . In this case, only the single peak pulse becomes stable (thick orange) after a fold at $g_{SNL}^{(1)} = 0.7$. The double (green) and triple (blue) peak solutions stay unstable after their respective folds at $g_{SNL}^{(2)} = 0.774$ and $g_{SNL}^{(3)} = 0.816$. (b) The profiles of the three TLS solutions at a common high gain level $g = 0.95$, see vertical dashed line in (a). The extra maxima appear as small bumps on the leading edge. (c) The profiles of the three TLS solutions at the respective folds. The various peaks are of comparable size and clustered close together. (c) The profiles of the three TLS solutions on the subcritical parts at a common maximum intensity of $\max(I) = 0.05$, see horizontal line in (a). The various peaks are ordered with ascending intensity and relatively widely spread. Other parameters are $(\alpha, \beta) = (0, 0)$. A similar version of this figure was used in [1].

intensity as a function of the normalized gain g . For zero α and β factors the branches show little qualitative difference, apart from additional pairs of close by folds on the lower part of the branches. Generally, the main folds go closer to the threshold for higher order solutions and all but the single peak TLS remain unstable after their respective folds. This structure appears to keep going to as many peaks as can fit in the cavity, which would be infinitely many in the long delay limit. However, the folds approach the threshold and potentially cross it for large order multi-peak TLS and are very unstable. Therefore, the analysis of them was not continued much beyond the third order and representing them here would not further the understanding of the system.

Panel (b) shows the temporal profiles of the intensity of the first three TLS at a common high gain level $g = 0.95$, panel (c) at their respective folds and panel (d) at a small intensity $\max(I) = 0.05$ on the unstable lower part of the branches. Close to threshold the profiles start as neighbouring separate small pulses of increasing size. Up the subcritical part of

the branches the peaks move closer together and start to touch and merger around the folds. The resulting pulse shapes on the upper part of the branches then appear as a main pulse with a series of leading bumps of intensity.

4.3 Amplitude-phase coupling

Mathematically, temporal localized structures are themselves periodic orbits of the model system. An oscillating TLS is therefore a higher order periodic orbit—in general a quasi-periodic solution, since the periods of the pulse and the slower dynamics of its shape do not have to be commensurate. Such oscillations are therefore not born in a normal Andronov-Hopf bifurcation but a so-called secondary AH bifurcation also called torus bifurcation. Analogous to a pair of complex conjugate eigenvalues that crosses the imaginary axis in the standard AH case, here a pair of complex conjugate Floquet multipliers crosses the unit circle. Such an instability appears for TLS in the unidirectional ring model for high values of the gain linewidth enhancement factor α in combination with a large normalized gain g parameter.

The α factor measures the strength of an indirect coupling of the amplitude and the complex phase of the electromagnetic field in nonlinear semiconductor media. This coupling is mediated via the carrier interactions as the refractive index changes dependent on the carrier density. A pulse with a given intensity profile creates a smooth drop in the carrier density due to stimulated emission when passing the respective sections. The resultant index change leads to the pulse acquiring a non-constant phase profile called chirp which equivalently means that the instantaneous frequency is not constant.

A special case of this is known as the Kerr effect which can be interpreted as instantaneously reacting carriers. In this regime, the carriers can be adiabatically eliminated so they no longer appear in the model and the index change is approximated as the product of a coefficient with the intensity. The resulting effect on the pulse is then called self phase modulation. For an accurate description of picosecond pulses in semiconductors, however, the carrier dynamics need to be taken into account.

Qualitatively, one can envision a mechanism how this coupling leads to oscillations: Larger pulse intensity leads to more acquired chirp from passing through the nonlinear medium and, consequently, the spectrum of the pulse is broadened. However, these new frequencies are less resonant with the cavity and are subject to additional linear losses or damping. In addition, the pulse typically ends up further from the transform limit (where a pulse is shortest for a given spectral bandwidth) and thus gets broader in time and flatter in peak intensity. As discussed in the previous section this leads to a weaker saturation of the absorber and therefore also more nonlinear losses. In this situation the pulse will hence shrink. This in turn reduces the amplitude-phase coupling to inverse effect so the pulse can become narrower and then grow again.

The absorber linewidth enhancement factor causes an opposed effect compared to the gain. Both can compensate for each other when the parameters are appropriately chosen. At realistic values for semiconductor materials, however, this plays a minor role in this system.

4.3.1 Trailing edge instability

Figure 4.6 shows an oscillating TLS at realistic values for the linewidth enhancement factors of semiconductor materials $\alpha = 3.8$ $\beta = 0.5$. The time trace of quasi-periodic orbit at a high normalized gain $g = 0.95$ was obtained through direct numeric simulation. Cutting the time-trace at multiples of the average period of the dynamics and stacking them yields a pseudo-space-time representation of the intensity as a function of the (fast) time variable and the (slow) roundtrip number. Using the average period instead of the delay time has the advantage of adjusting for the drift of the pulse in the cavity that would otherwise appear.

An oscillation of the overall intensity of the pulse is observed. While the leading edge of the pulse is otherwise little affected, the trailing edge appears to move back and forth a lot along with the intensity oscillation. This results in an oscillation of the width and the asymmetry of the shape of the pulse as well. The peak of the pulse stays roughly at the same position in this representation, i.e., the drift is approximately constant. This becomes intuitively clear from the principle of causality. Only the interaction with the nonlinear materials affects the pulse, namely by saturating the carrier inversion toward transparency. For TLS where the pulses always hit quasi equilibrated carriers the back of the pulse profile is affected by what came in front of it but never the other way around. The increasing carrier saturation also means that the interaction with the gain has a higher frequency on the leading edge than the trailing one and vice-versa for the absorber. With

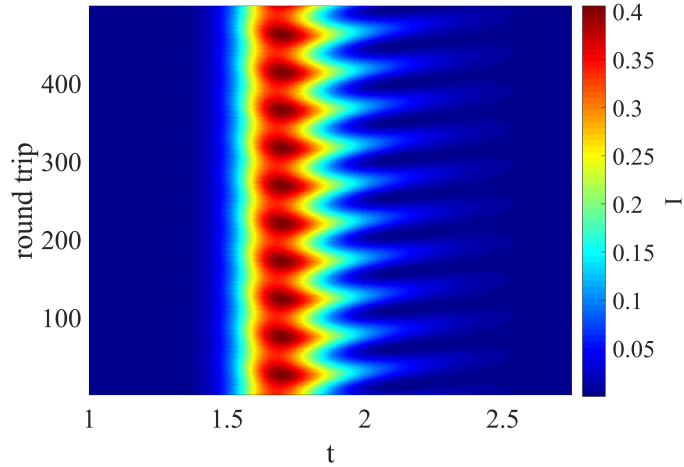


Figure 4.6: Pseudo-space-time representation of an oscillating TLS close to the lasing threshold $g = 0.95$ and realistic linewidth enhancement factors for semiconductor materials $\alpha = 3.8$ and $\beta = 0.5$. The slow evolution from one roundtrip to the next reveals an oscillation of the size of the pulse in both its peak intensity and width of the temporal profile. This deformation is mostly located at the trailing edge of the pulse that moves back and forth with the intensity oscillation while the leading edge is affected little. A similar version of this figure was used in [1].

the different timescales of the nonlinear sections their interplay leads to complicated phase profile of the pulse.

4.3.2 Bifurcation diagrams

Figure 4.7 shows the results from direct numeric simulations for different values of α . The minima and maxima of the peak intensities of the pulses are plotted to characterize the dynamics of a pulse train. By increasing or decreasing the normalized g in a step-wise manner and then giving the dynamics time to converge to pass the resulting transients

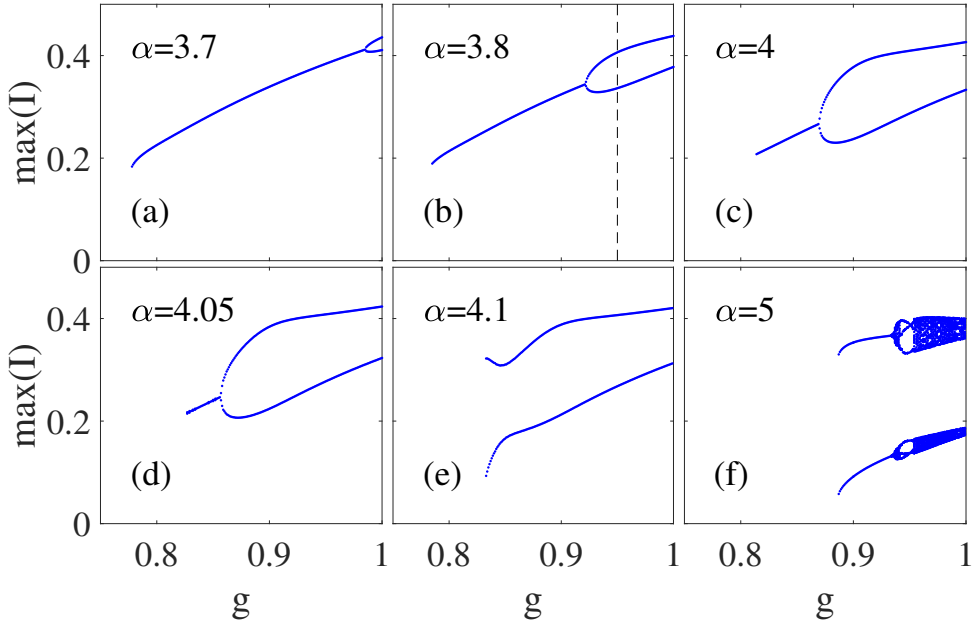


Figure 4.7: Results from direct numerical simulations of TLSs of Eqs. (2.96)–(2.98) as a function of the normalized gain g for different values of the gain linewidth enhancement factor α . The plotted points are the minima and maxima of the peak intensities of the TLSs in a time trace. (a) For $\alpha = 3.7$ most of the branch is stable with a secondary Andronov-Hopf bifurcation close to the threshold. On the other end the branch folds down visibly. (b) For $\alpha = 3.8$ the torus bifurcation has moved to lower g . The dashed line is corresponds to the pseudo-space-time diagram in Fig. 4.6. On the other end the branch ends before completing the fold. (c) For $\alpha = 4$ the torus bifurcation kept moving to lower g and the other end of the branch to higher g . (d) For $\alpha = 4.05$ both limits of the stable part are about to merge. (e) For $\alpha = 4.1$ only oscillating behavior remains after the merger. The corresponding periodic orbit ends abruptly at the low g end. (f) For $\alpha = 5$ a quasi-periodic regime appears on top of the periodic orbit with a period tripling window. The low g end moved to higher g and is clearly fold-shaped. Other parameters: $\beta = 0.5$. A similar version of this figure was used in [1].

one obtains a branch like structure. A single point means the peak intensity is constant, indicating a stable pulse. Two points represent an oscillation between those two points. The same goes for more than 2 points. Finally, an apparent horizontal line means there are extrema of the peak intensity in the whole interval. This situation arises with quasi-periodic oscillations made up of several frequencies. As the periods are not commensurate, extrema appear anywhere between the extrema of the envelope of the slower frequency.

At lower α stable the whole branch remains stable in g and ends in a fold on the low g side. Close below $\alpha = 3.7$ a secondary Andronov-Hopf bifurcation enters the bistable region below the lasing threshold. Panel (a) shows the situation shortly after this point. The bifurcation point moves down in g for increasing α as shown in panel (b) where the oscillation shown in the pseudo-space-time diagram of Figure 4.6 is marked. In addition, on the lower end of the branch a subcritical secondary AH bifurcation appears, i.e., the branch simply stops which can be clearly seen in panel (c). The corresponding periodic orbit is unstable and cannot be found in the simulations. Both bifurcations move toward each other (panel d) and finally merge. Panel (e) shows a point shortly after the merger, where no stable pulses remain. Instead a periodic overlaps the formerly stable part of the branch. This appears to be a connection with the unstable orbit from the subcritical torus bifurcation. Finally a higher order torus develops on top of the already oscillating dynamics. In panel (f) at high g a region of quasi periodic pulsing can be seen. It contains a window with period tripling behavior, making the following quasi-periodic oscillations potentially chaotic. In addition the orbit developed a clearly visible fold on left end.

Figure 4.8 takes a look from the opposite point of view, i.e., the branch is calculated as a function of α for different g . Otherwise the method is the same as before. For lower values of α the peak intensity is larger and the maximum occurs where α is close

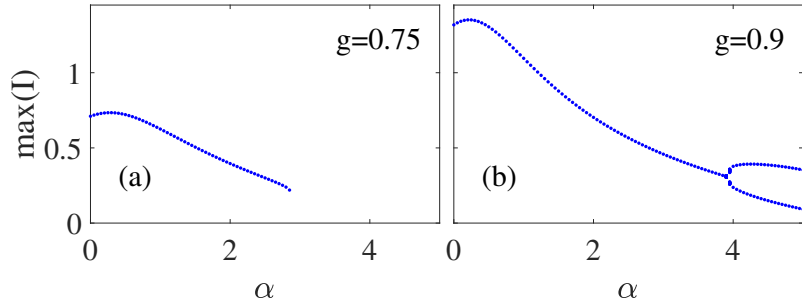


Figure 4.8: Results from direct numerical simulations of TLSs as a function of the gain linewidth enhancement factor α for different values of the normalized gain g . The plotted points are the minima and maxima of the peak intensities of the TLSs in a time trace. (a) A fully stable branch at $g = 0.75$ with large peak intensity at small values α . The maximum peak intensity lies close to $\alpha \approx \beta$. The branch tapers off toward larger α , then folds down and stops. (b) For $g = 0.9$ the peak intensity has roughly doubled and the branch extends much further in α . Close below $\alpha = 4$ a secondary Andronov-Hopf bifurcation destabilizes the branch causing a transition to an oscillatory pulse. Other parameters: $\beta = 0.5$. A similar version of this figure was used in [1].

to $\beta = 0.5$. Here, their mutual compensation is optimal and the pulse is least broadened by the amplitude-phase coupling. Conversely, for larger α the peak intensity shrinks. For a low gain level the whole branch is stable and ends in a fold at $\alpha \approx 3$ as can be seen in panel (a). With more gain the intensity grows along the whole branch which is shown in panel (b). TLS exist for much higher values of α than before and also the stable region is wider. Above $\alpha \approx 4$, however, the periodic regime is entered.

4.3.3 Combined 2-parameter scan in the fully localized regime

Figure 4.9 presents results of a high resolution 2-parameter scan that was conducted using the functional mapping introduced in Sec.3.4. Calculating this diagram when simulating the full roundtrip would take several weeks. The concept used is a similar numerical continuation scheme as used before; the final state of one point is the initial state for a neighbouring point. Like this the whole manifold of solutions can be explored in an automated manner. Per point 3000 roundtrips were calculated, without any prior relaxation in this case. The resolution is 501 points for both parameters.

The left panel shows the average peak intensity of the TLS which is largest for low α and high g . The border of the region of existence bends around $\alpha = 4$ and is jagged for very

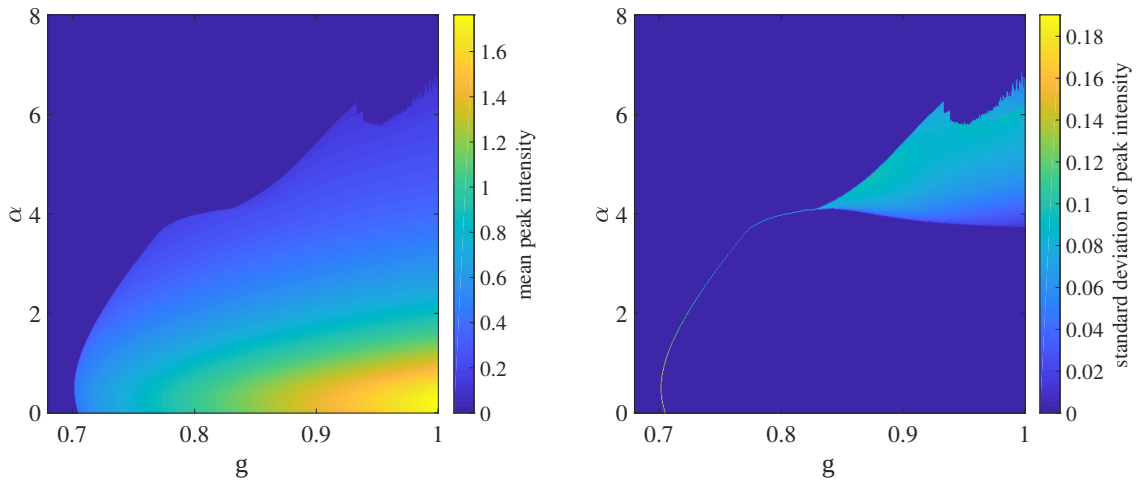


Figure 4.9: Two-dimensional bifurcation diagrams in the normalized gain g and the gain linewidth enhancement factor α obtained from direct numerical simulations using the functional mapping (see Sec. 3.4) with fully equilibrated carriers. This corresponds to the fully localized regime in the long delay limit $\tau = \infty$. (left) Average maximum intensity of 3000 consecutive pulses. (right) Standard deviation of the same data. A large region of stable pulses exists with its widest extent in gain for $\alpha \approx \beta$. Towards the threshold a large peak intensity builds up for low α while above it is not changing much. At high values of both α and g there is a region of oscillating pulses. The onset of the oscillations moves down in g quickly for increasing α . The drop to the off solution is visible as thin line because of slow transients close to the responsible bifurcation. Other parameters: $\beta = 0.5$.

high α where the dynamics was found to be quasi-periodic before.

The right panel shows the standard deviation of the peak intensities. The borders of stability become clearly visible in this representation. For high α we see the oscillatory region that exhibits a pointy, cusp like shape on the low g side. The torus bifurcation goes back down in α for large gain as it could be seen in Figure 4.7. Distinguishing the quasi-periodic region from the simple oscillation is not possible in this representation, the standard deviation appears to transition smoothly.

4.4 Solution manifold

The temporal localized structures form a manifold of solutions. In the direction of the normalized gain g the solution branches are C-shaped. Considering that the bistable region becomes smaller for increasing α this means slices of the manifold in α take the shape of a loop. Overall, we can infer that the manifold has the shape of a cone with a rounded tip.

4.4.1 Symmetric case without absorber linewidth enhancement

By continuing the pulses in α for various g using DDE-BIFTOOL we can obtain the loop shaped branches. One finds that each multi-peaked TLS is born in a saddle-node bifurcation and each then develops its own loop in α when increasing the gain. Each loops forms a cone shaped manifold with a rounded tip as a starting point stemming from the respective saddle-node. Figure 4.10 shows slices through the solution manifold. The loops start out circular, then deform growing more pointed at low α and develop flat toe-like extensions at large α . Along with this, the connecting parts in between become concave. This behavior is roughly similar for the different multi-peaked solutions. The panels (a-c) show the maximum pulse intensities along the branch while panels (d-f) show the period deviation which are roughly proportional to the inverse of each other. However, for large g the period deviation of the unstable part becomes concave in contrast to the peak intensity that remains convex.

4.4.2 Transcritical crossover of multi-peaked solutions

For larger values g a series of crossovers between the various multi-peaked solutions occurs. Figure 4.11 shows the first of the crossovers. It recombines the single peak and the double peak TLS loops. Roughly in the middle of the concave part of the single peak loop, a pair of folds is born in a saddle-node bifurcation. The inner one of the folds then connects to the fold of the double peak loop in a transcritical bifurcation. After this point the branches split again such that the stable single peak TLS at high α now actually stems from the unstable double peak solution and the loop possesses two separate stable sections.

The transcritical can be most readily seen in the zoomed insets. In the absence of absorber linewidth enhancement $\beta = 0$ the process happens symmetrically for both negative and positive α . Indeed, in this case the crossovers happen always in pairs such that the number of loops conserved. For large g increasingly higher order multi-peak solutions are involved in further crossovers. This leads to a very complicated structure close to threshold where it becomes hard to tell the multi-peaked solutions apart. They lie mixed up on

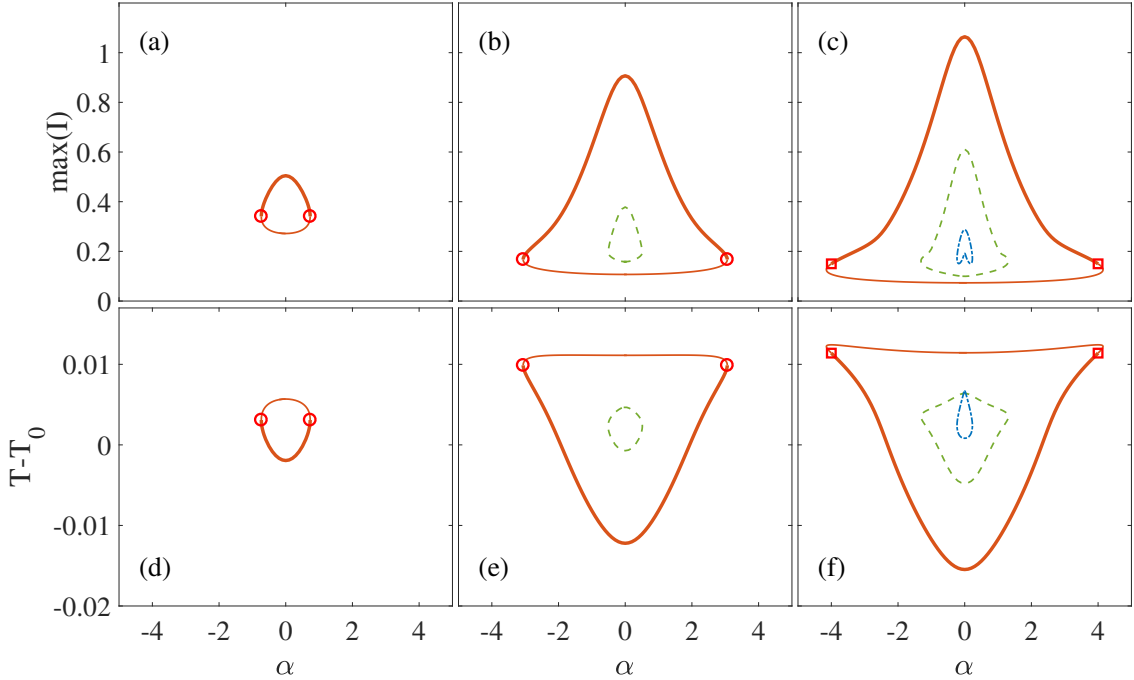


Figure 4.10: Bifurcation diagrams of TLS branches in α for different values of g . The branches are represented by both the peak intensity and the period deviation. Stable solutions are shown with thick lines and unstable solutions with thin lines. Loss of stability is marked with circles for folds and squares for torus bifurcations. (a,d) At $g = 0.707$ the branch of the single peak TLS in solid orange forms a loop in α . (b,e) At $g = 0.784$ a second loop for the double peak solutions in dashed green has appeared. The first loop deforms and develops toe-shaped extensions. (c,f) At $g = 0.822$ a third loop for the triple peak solution in dash-dotted blue has appeared. The toes extend further. The multi-peak solutions loops appear as saddle-node bifurcations when increasing g . The period deviation is roughly proportional to the inverse peak intensity. The loops are slices of a solution manifold and are symmetric in α for $\beta = 0$. A similar version of this figure was used in [1].

the various loops. Because of the crossovers all the multi-peak solutions really form just one interconnected and self crossing manifold of a very intricate, yet symmetrical shape.

Figure 4.12 shows a zoom on the transcritical bifurcation with the period deviation of branches in small interval of g . The curvature of the folds on both branches grow rapidly and diverge to infinity toward the transcritical bifurcation where they finally touch. At this point, the two loops are connected in a degenerate solution, i.e., they truly cross each other. This crossing is therefore visible in any measure one chooses to represent the branches and is not an artifact of the measure itself. Directly before and after the bifurcation point the loops have virtually exactly the same shape, except close for the crossover. However half of either loop has switched over to the respective other.

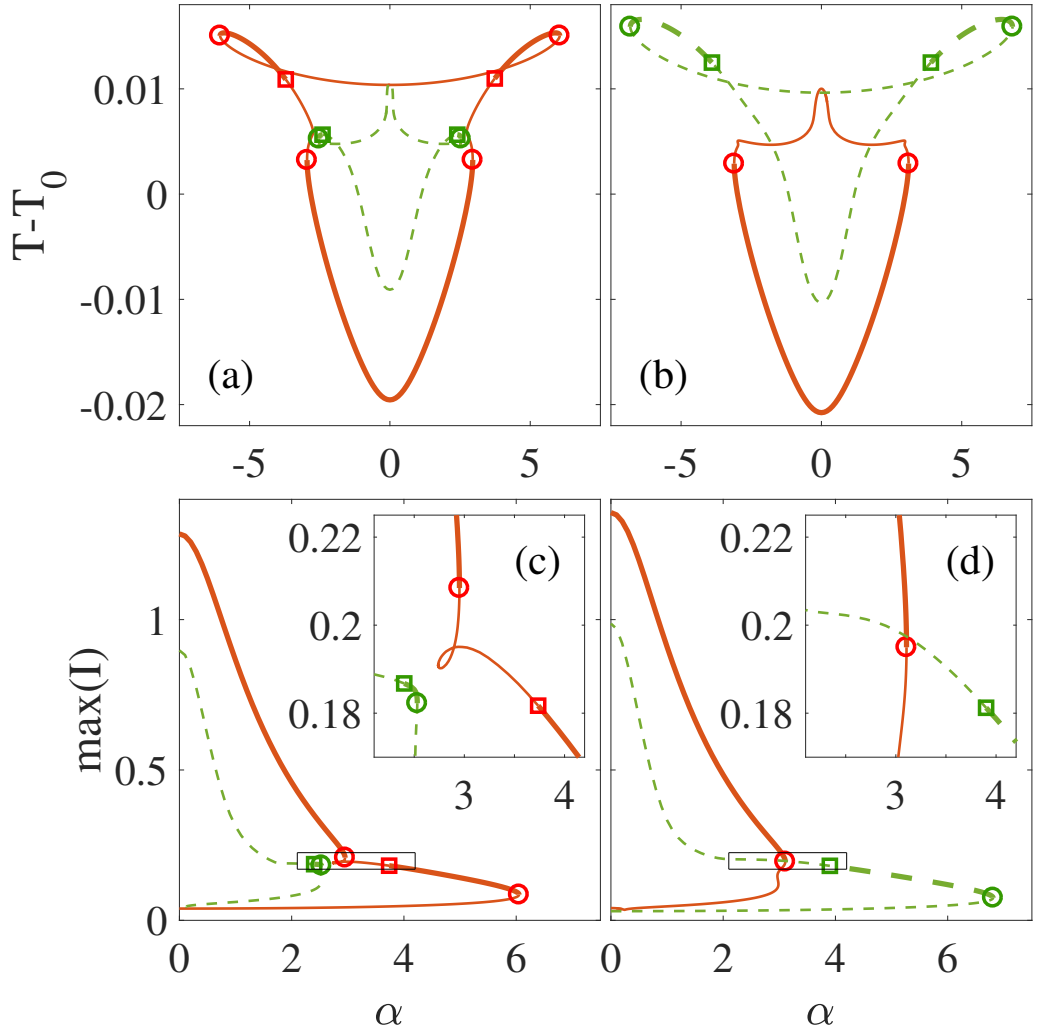


Figure 4.11: Cross-over of the solution loops corresponding to the single and double peaked TLS. Stability is indicated by thick lines and loss thereof is marked with circles for folds and squares for torus bifurcations. (a) Period deviation at $g = 0.879$. The loop of the double peak solutions in dashed green has come close to the respective loop of the single peak TLS in solid orange. (b) At $g = 0.898$ the loops have crossed over. Part of the single TLS loop is now connected to the double peaked one and vice-versa. This happens symmetrically on both sides at the same time. (c,d) The respective peak intensity representations of the loops in (a,b) for the positive α side. A zoom on the crossover is shown in the insets. The single peak TLS loop forms a small extra loop in order to reconnect with the double peak loop. Other parameters: $\beta = 0$. A similar version of this figure was used in [1].

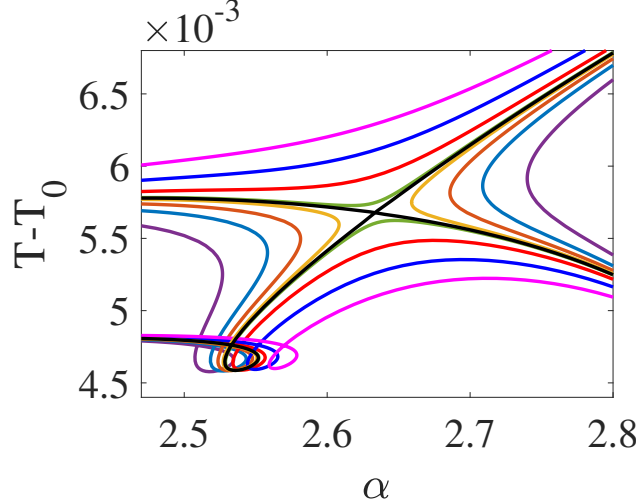


Figure 4.12: High resolution representation of the transcritical bifurcation responsible for the crossover shown in Fig. 4.11. The period deviation is shown for solution loops in an interval of $g \in [0.8793; 0.8812]$. Other parameters: $\beta = 0$. A similar version of this figure was used in [1].

4.4.3 Asymmetric case with absorber linewidth enhancement

With absorber linewidth enhancement $\beta \neq 0$ the loops are no longer symmetric in α . The crossovers no longer happen simultaneously in the negative and positive α half-planes. Instead the pairs from the $\beta = 0$ case now appear at different values of g which leads to the number of loops not being conserved. A single crossover between two loops joins them together to form a double loop that goes around the center twice. In the opposite case such a double loop can split into two single loops via a crossover with itself.

This does not necessarily happen in an interspersed order. A newly formed double loop can connect to a third loop before splitting back up again on the other side. For $\beta = 0.5$ this leads to an even more intricate manifold of solutions than in the earlier symmetric case. The first three crossovers are presented in Figures 4.13 and 4.14 showing the peak intensity and the period deviation of the loops, respectively. The panels (a) and (b) show the situation before and after the first crossover. It joins the single peak and the double peak loops on the negative α side. Both loops now form a single loop going around twice. Between panels (c) and (d) two crossovers occur on the positive α side. The double loop crosses over itself to disjoin at that point while the innermost part joins with the triple peak loop. The upper single peak part ended up being connected to the lower double peak part. The toe shaped extended part at high α is now part of a loop that consists of components stemming from all the multi peak loops up to order three.

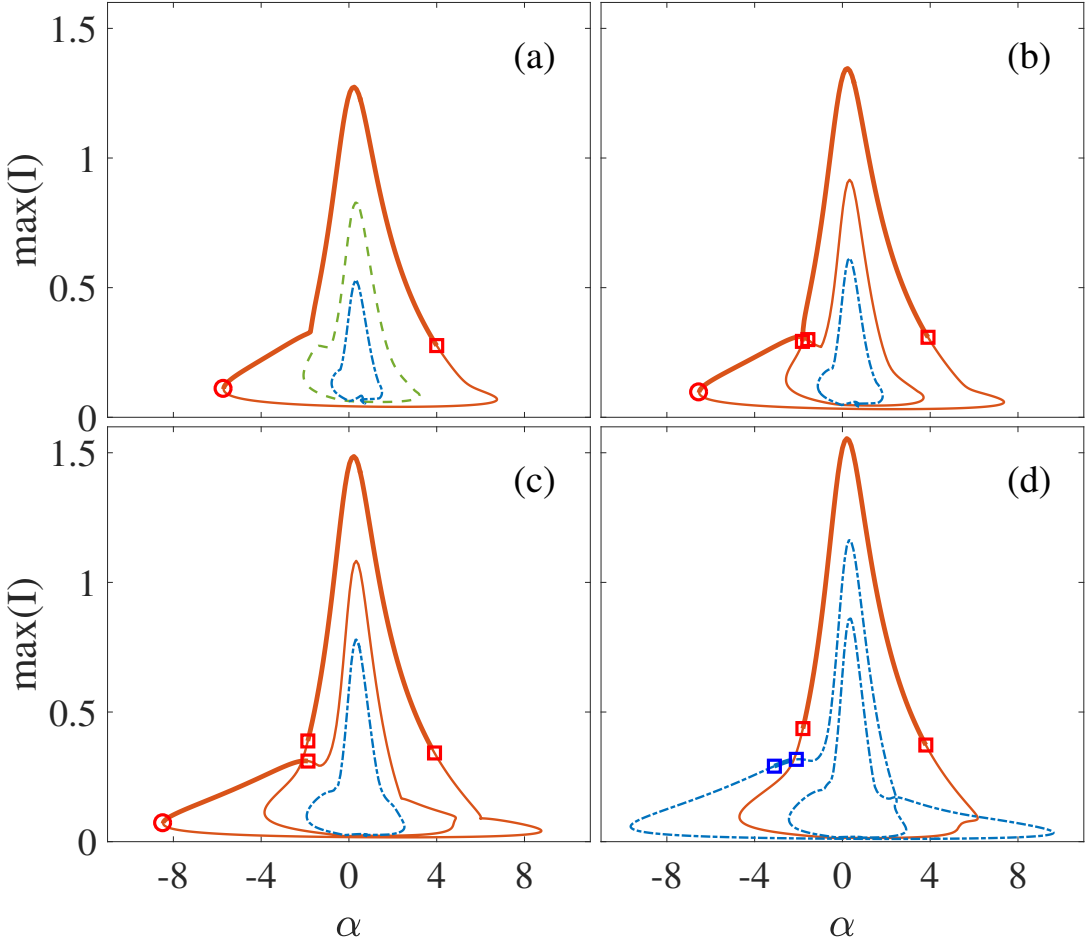


Figure 4.13: Bifurcation diagrams showing the peak intensity of TLS as branches in α for different values of g . Single, double and triple peak pulses are represented with solid orange, dashed green and dash-dotted blue lines, respectively. Stability is indicated by thick lines and loss thereof is marked with circles for folds and squares for torus bifurcations. Several transcritical bifurcation lead to crossovers between the different loops. This happens in an asymmetric fashion for $\beta = 0.5$ such that the number of independent loops not conserved. (a) At $g = 0.879$ the three loops exist independently. (b) At $g = 0.898$ The single peak TLS loop has combined with the double peak loop on the negative α side and form a double loop that goes around the center twice. (c) At $g = 0.937$ the combined loop comes closed to itself around $\alpha \approx 5$ and to the triple peak loop around $\alpha \approx 2$. (d) At $g = 0.956$ two additional crossovers have occurred at positive α in rapid succession. The double loop has split again such that upper single peak half and lower double peak half form a loop. The rest has combined with the triple peak loop. A similar version of this figure was used in [1].

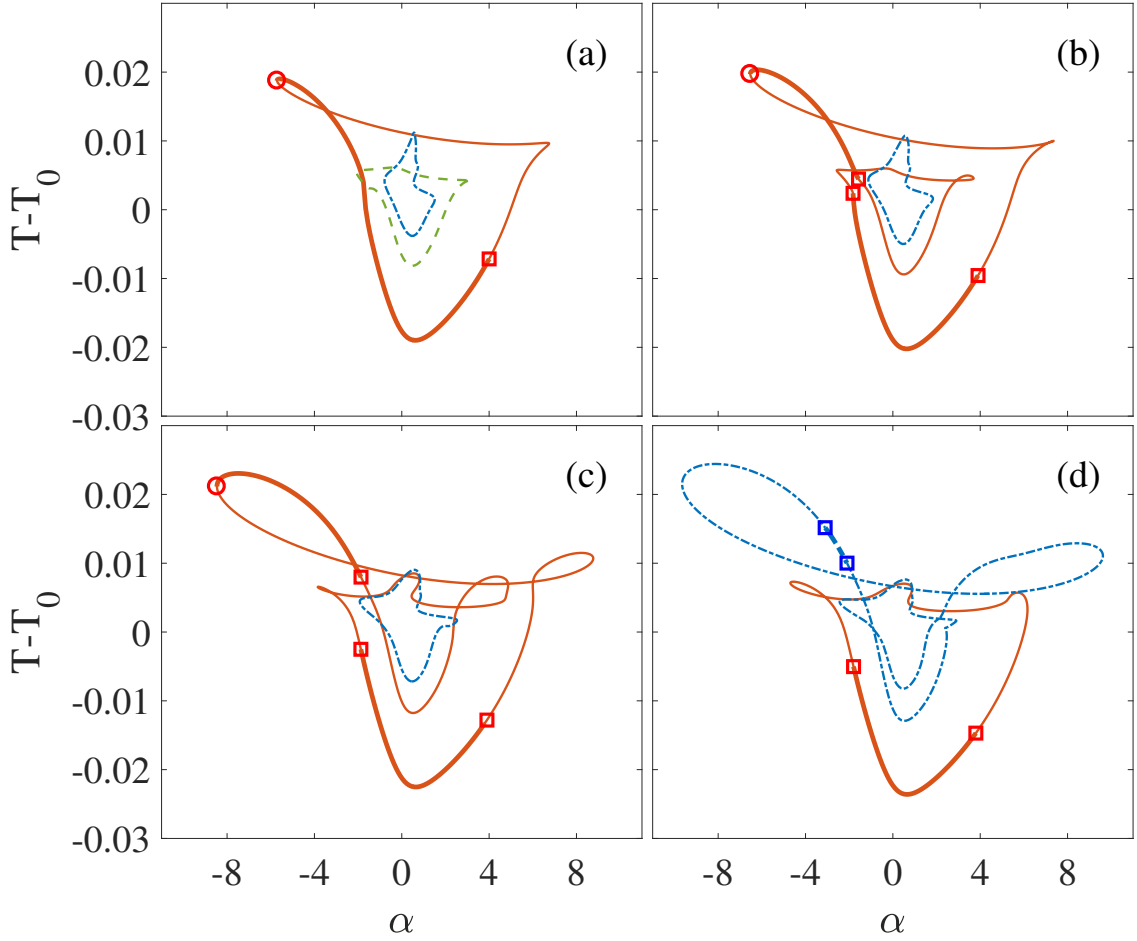


Figure 4.14: Bifurcation diagram showing the period deviation of the TLS loops in Fig. 4.13 with the same color coding. The loops recombine in a complicated pattern when increasing the normalized g toward the lasing threshold to form a single manifold of solutions. For $\beta = 0.5$ this manifold is very complex as the loops cross over asymmetrically in the positive and negative α half-planes and in no particular order. Unlike the symmetric $\beta = 0$ case, the number of independent loops is not constant. A similar version of this figure was used in [1].

4.5 Bifurcation branches

The temporal localized structures found in the ring laser model are themselves periodic orbits in time. Two of their possible bifurcations are the saddle-node on limit cycle bifurcation and the secondary Andronov-Hopf or torus bifurcation. These correspond to a fold of the TLS branch or the onset of an oscillation of the TLS profile. Both can be detected and continued using DDE-BIFTOOL while the oscillations stemming from torus bifurcations form a quasi-periodic orbit that DDE-BIFTOOL cannot currently handle.

Figure 4.15 shows results from the continuation of the folds of both the single and double peaked pulses as well as the torus bifurcation of the single peak solutions. The first fold defines the bistable region where TLS can exist. Its maximal protrusion below threshold is found for $\alpha \approx \beta$ and then it continues to slants up in a roughly straight line. The torus bifurcation starts on the fold, first moves up in α and then back down toward the lasing threshold. The first part is subrcitital and then switches to supercritical when the α direction changes, as can be seen from direct numerical simulatins shown in Figures 4.7 and 4.9. The second fold branch of the double peak TLS has mostly the same shape as the first fold. However, there exists a cusp point where the transcritcial bifurcation from the previous section occurs between the single and double peaked TLS. The point where the torus is born on the fold curve and the cusp of the double peak fold are co-dimension two bifurcation points.

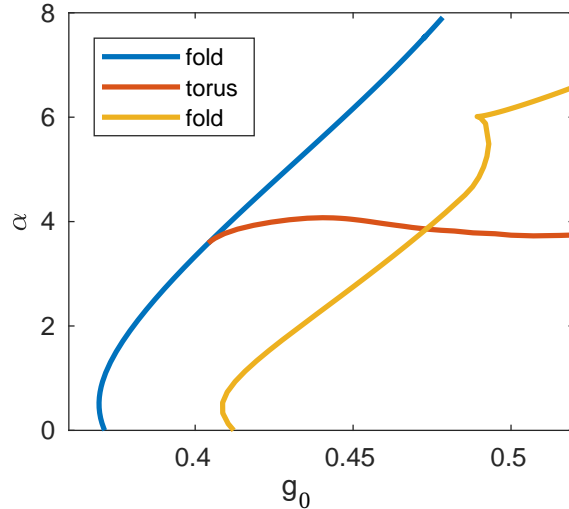


Figure 4.15: Two-dimensional bifurcation diagram of the TLSs in the gain pumping parameter g_0 and the gain linewidth enhancement factor α obtained with DDE-BIFTOOL. The fold curve of the saddle-node bifurcation that gives birth to the bistable TLS region (blue) is shown as well as the torus bifurcation (orange) that destabilizes it. The fold of the double peak TLS (yellow) exhibits a cusp where the transcritcial bifurcation with the single peak solutions occurs. Other parameters: $\beta = 0.5$.

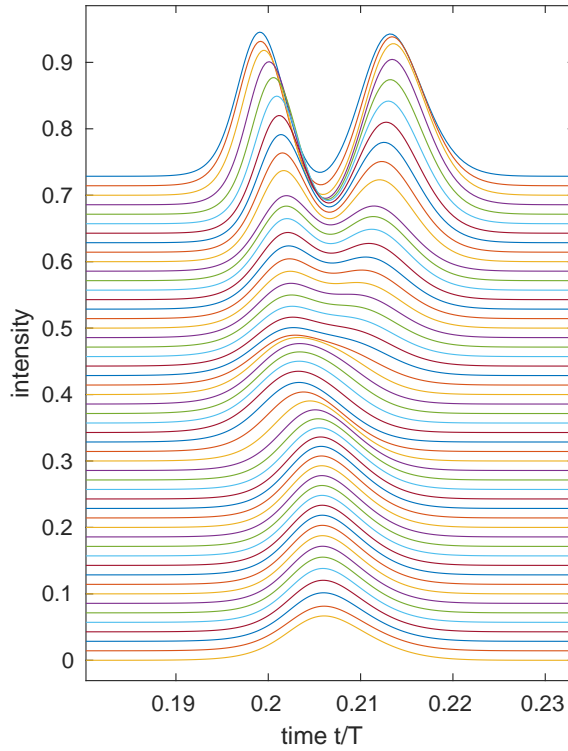


Figure 4.16: Intensity profiles of the pulses along the second fold branch in Fig. 4.15. The profiles are stacked to give an overview, the intensity scale is only for reference. The upper end of the stack shows the profiles for lower α . The double peak profile for α close to zero deforms into a single peak profile at high α .

4.5.1 Secondary fold profiles

Figure 4.16 shows the profiles along the fold branch of the double peaked pulses. They change from double to single bump as the crossover between the single and double peak solutions occurs at the cusp found on the branch. The profiles are presented in a stacked fashion meaning that the peak intensity axis is for reference only. Indeed all of the profiles start and end with virtually zero intensity. The double peaked profiles on top of the stack are for α close to zero. They then transform to single peaked profile on the bottom that correspond to large values of α that have almost the same shape but require a rapidly increasing minimal gain.

4.5.2 Convergence toward the localized regime

In order to test whether the chosen value of the delay time $\tau = 100$ yields pulses in the localized regime the branches of the pulse bifurcations are compared to the case of $\tau = 500$, which is shown in Figure 4.17. No big changes can be observed however they are systematic. The fold moves slightly toward lower gain g_0 which is immediately intuitive

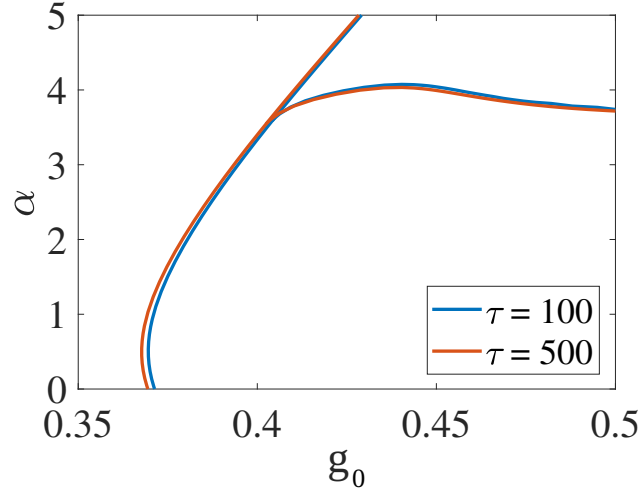


Figure 4.17: Comparison of the principal fold and the torus bifurcation branches for $\tau = 100$ and $\tau = 500$. $\tau = 100$ can already be considered to be part of the localized regime. No significant difference is observed for even larger delay times.

since the gain has more time to relax and therefore reaches a comparable value in front of the pulse. The torus bifurcation moves slightly toward both lower gain and lower linewidth enhancement α which is also intuitive when considering the slightly larger effective gain reached by the longer relaxation. At the same value g_0 the $\tau = 500$ pulse will be larger than the $\tau = 100$ one and therefore undergo stronger amplitude-phase coupling. The critical amount is thus reached earlier. For even larger delay times one runs into difficulties with DDE-BIFTOOL related to the resolution of the orbits, either numerical instabilities due to bad resolution or bad scaling of the computation time for too many mesh points. as the effect diminishes exponentially and would not yield significant differences. Overall one can consider the case of $\tau = 100$ to be well enough converged toward full localization to justify its use in the direct numerical simulations.

4.5.3 Comparison with direct numerical simulations

Figure 4.18 shows results from direct numerical simulations of the full DDE ring model together with the bifurcation branches from DDE-BIFTOOL. Thus the bifurcations limiting the stable region can be identified. The DNS data is represented by different colors that correspond to different types of behavior. The off solution is easily detectable by measuring the energy contained in the roundtrip profile. When it reaches below some sufficiently small value the following dynamics can be assumed to keep falling to the off solution, since the smallest stable pulse has significantly more energy. To analyze the pulse dynamics, first their peak intensities are considered as a time trace. The minima and maxima of that time trace contain all the necessary information. Stable oscillations are characterized by having two points between which the time trace alternates, i.e. two extrema. Period doubling has four such extrema and so on. Thus, one only needs to search for clusters in the extrema of the peak intensities and count them to characterize

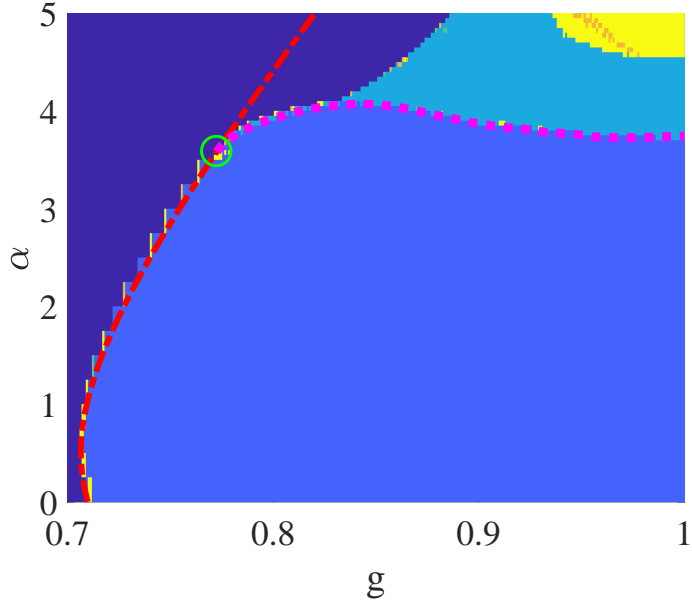


Figure 4.18: Two-dimensional bifurcation diagram in the normalized gain parameter g and the gain linewidth enhancement factor α . The behavior observed in direct numerical simulations is color-coded. Dark blue: off solution, blue: stable TLS, light blue: periodic oscillation, yellow: quasi-periodic, orange: period tripling. The bifurcation branches obtained with DDE-BIFTOOL are superposed as a red dash-dotted line for the principal fold and a pink dashed line for the torus bifurcation with a green circle marking their intersection. Most of the stable pulse region is limited by the fold up to where the torus bifurcation is born on the fold branch which is marked with a green circle. The oscillatory region only starts where the torus bifurcation turns to slope down changing from subcritical to supercritical. A similar version of this figure was used in [1].

these dynamics. Quasi-periodic oscillations are characterized by not having clusters. In practice, after some large amount of round-tips this situation can assumed.

On the low g side the single peak TLS fold is responsible for the destabilization up to the co-dimension two point where the torus bifurcation is born on the fold branch. After that point the stable pulses are already limited by the torus bifurcation for larger g than the fold branch. In both cases the dynamics simply drops to the off solution. This identifies the torus as subcritical in this section, i.e., the newly created orbit is unstable around the bifurcation and cannot appear in the DNS. At $\alpha \approx 4$ the torus bifurcation turns to slope downward. This is another co-dimension two point where a regime of pulse oscillations appears with a cusp shaped tip. The torus bifurcation has therefore become supercritical. The associated dynamics are quasi-periodic orbits—the pulses are already periodic orbits—and as such cannot be handled by DDE-BIFTOOL. However, we can see from DNS (cf. Figure 4.7) that the left border of the quasi-periodic region appears to be a fold.

4.5.4 Comparison with an exponential Haus PDE model

A Haus master partial differential model was derived from the unidirectional ring delay differential equation model [CJMG16]. A rigorous multiple timescale analysis is just possible in the uniform field limit (small changes per roundtrip) and expanding around the empty cavity. This implies small gain and absorption as well as small intensities. The exponential terms found in the DDE model are linearized.

Using a two timescale ansatz it is possible to keep the exponential terms [1]. While the derivation is not strictly rigorous, the obtained equations yield results that agree much better with the original DDE model. This exponential Haus master equation reads

$$\frac{\partial E}{\partial \sigma} = \left(\sqrt{\kappa} e^{\frac{1-i\alpha}{2}G - \frac{1-i\beta}{2}Q + i\Theta} - 1 + \frac{1}{2\gamma^2} \frac{\partial^2}{\partial z^2} \right) E, \quad (4.15)$$

$$\frac{\partial G}{\partial z} = \Gamma(G_0 - G) - e^{-Q} (e^G - 1) |E|^2, \quad (4.16)$$

$$\frac{\partial Q}{\partial z} = Q_0 - Q - s(1 - e^{-Q}) |E|^2. \quad (4.17)$$

As a PDE this equation has some advantages over the DDE model. The physical time t is replaced by a space-like coordinate z and the effect of the delay is modeled by spatial derivatives with respect to z . While the DDE has to be integrated along t the PDE is integrated in the slow time variable σ that has the unit of the roundtrip time, i.e., the period of the TLS solutions. In contrast to t , there is no dependence on previous points in the z domain. Thus, when integrating the PDE one can make use of various parallelization schemes to speed up simulations significantly as compared to the DDE model. In addition, the PDE model enables direct control of group velocity dispersion by introducing an imaginary component to the second order partial derivative term. In the original DDE model, an equivalent task can only be achieved with much greater difficulty [PSHV17].

Pulses are just steady states of the PDE while they are periodic orbits in the DDE. Similarly, oscillations of pulses are periodic orbits and not quasi-periodic orbits and a torus bifurcation in the DDE model reduces to Andronov-Hopf bifurcation in the PDE. Figure 4.19 shows results from bifurcation analysis of the Haus PDE conducted in the path-continuation software pde2path [UWR14]. For comparison with DDE model the results from DDE-BIFTOOL for the DDE model are superposed. The different fold curves are reproduced very well by the PDE approximation as well as the co-dimension two points. The AH curve of the PDE follows the torus curve of the DDE only close to the origin on the fold. For increasing g it does not bend back down which is qualitatively quite different. It means that the prediction for a passively mode-locked laser made by the Haus PDE is that for sufficiently large α one obtains stable pulsation below the lasing threshold that destabilizes when reducing the gain below a certain critical value where it starts to oscillate. This is exactly the opposite as for the DDE model which predicts the onset of oscillations when turning the pump rate up instead.

Some discrepancy is not surprising when considering that the exponential Haus PDE remains only an approximation. The PDE approach assumes continuous evolution of the pulse profile while in the DDE model large changes per roundtrip can be observed in the regime where gain and absorption are strong.

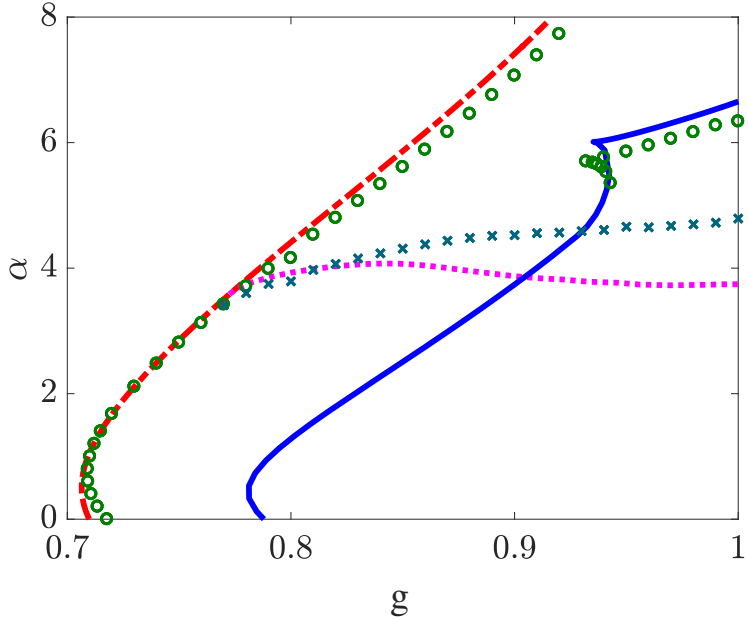


Figure 4.19: Comparison with results from the Haus PDE for the unidirectional ring model obtained with pde2path. For the DDE model the single peak fold is shown in dotted red, the double peak fold in solid blue and the secondary AH bifurcation in dotted pink. For the PDE model the fold points are depicted as green circles and the AH points as cyan crosses. The folds lie in good agreement. So do the co-dimension two points where the fold and AH branches connect, as well as the cusps of the double peak fold branches. The AH branches, however, take significantly diverging paths toward threshold. In the PDE model the branch slopes upward in α which is qualitatively contrary to the DDE model. An oscillatory region is found for low gain, not large. Other parameters are $\beta = 0.5$. A similar version of this figure was used in [1].

4.6 Functional mapping performance

This section presents some sanity checks for the functional mapping method described in Section 3.4 using the example of the unidirectional ring laser model (2.96)–(2.98). It demonstrates how little of an effect the assumptions of the FM have in practice for the TLS regime.

4.6.1 Timing jitter analysis

To compare the statistical properties of the TLS when simulated using the full DDE model and the functional mapping time traces of over ten million roundtrips have been calculated for each. For a delay time of $\tau = 100$ an even longer integration of the full DDE model becomes too time consuming. The size of the integration box for the FM was only $2\delta = 3$. Thus, the integration time is more than 30 times shorter and insignificant in comparison. Under the influence of noise in the field evolution the pulse movement has a stochastic

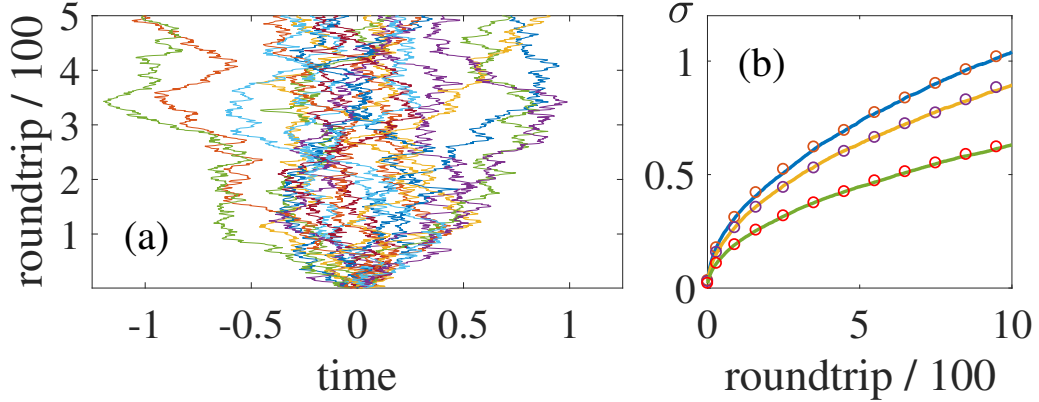


Figure 4.20: Statistical results for the temporal jitter of passively mode-locked pulses under the influence of noise. (a) Relative position of the pulses as compared to the average period of 20 time traces. The motion is a Brownian random walk. (b) The standard deviation of the pulse jitter for $(g_0, \tau) = (0.6, 5)$, $(0.5, 10)$ and $(0.4, 100)$. The lines show the results obtained using the functional mapping while the circles are from integrating the full DDE system. The functional mapping conserves the statistical properties of the original system. Other parameters are $\alpha = 2$ and $\beta = 0.5$. A similar version of this figure was used in [2].

component. This manifests in a small variation of the repetition period that is called timing jitter. When cutting the long pulse train at multiples of the average period one can observe a residual movement of the pulse in the roundtrip that stems from the stochastic component. When using the FM one simply remembers the amounts by which the pulses were shifted back each roundtrip. The variance of the noise was set to $\sigma = 0.01$. Note that, this noise level is very strong when compared to realistic situation and thus creates very strong jitter. Given the limited simulation time that can be achieved in the full DDE integration, however, this is helpful for this analysis.

Figure 4.20 shows results from the analysis of the previously described time traces. The consecutive trace was cut into 10000 pieces of 1000 roundtrips each. Using the position of the first pulse in each piece as the origin one obtains 10000 random walks of length 1000. Panel (a) shows the first 500 roundtrips of the first 20 pieces of the mapping time trace for illustration. For each roundtrip number along the random walks the standard deviation σ of pulse position was calculated. From Brownian motion the standard deviation is known to $\sigma = \sqrt{2Dt}$ with the diffusion coefficient D . A square root function was fitted to the data points to obtain an estimate for D . Panel (b) shows the superposed standard deviations as a function of the roundtrip number for both the full DDE and the FM at different cavity lengths and appropriate pumping parameters. While residual differences between the approaches are to be expected, the statistics still virtually coincide such that it is not clear how much of the difference is systematic or inaccuracy due to the finite sample size. Overall one may assume that the FM conserves the statistical properties of the corresponding full system, even for very large noise amplitudes.

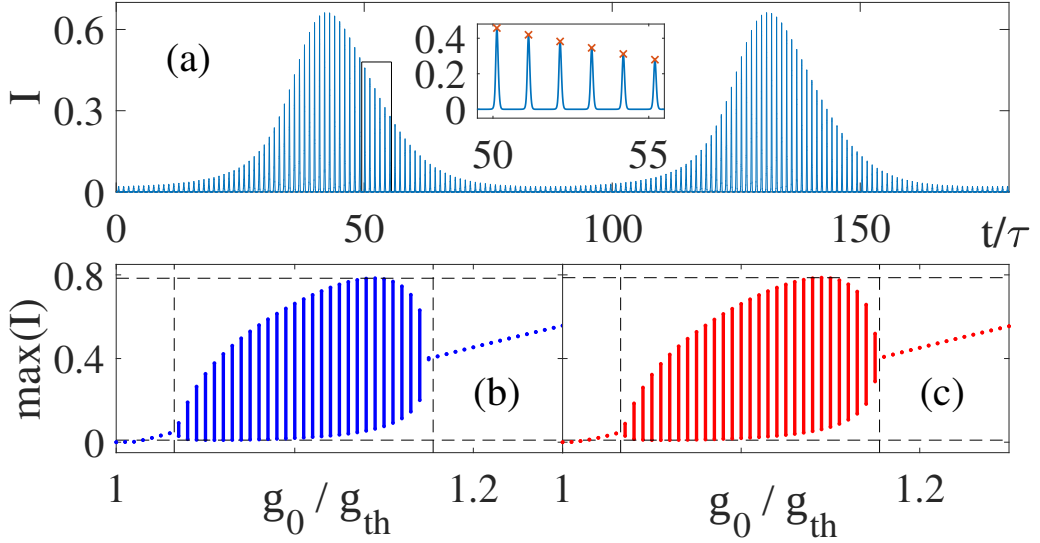


Figure 4.21: Passively mode-locked pulses in the Q-switched regime. At a high repetition rate and slow gain recovery the pulses experience undamped relaxation oscillations. (a) Time trace of the Q-switched regime close above the lasing threshold. (b) Bifurcation diagram obtained by plotting the extrema of the maximum peak intensities of the pulses obtained in the full DDE model. (c) In the functional mapping the diagram is reproduced very accurately. Parameters are $\tau = 2$ and $Q_0 = 0.6$. A similar version of this figure was used in [2].

4.6.2 Q-switched model-locking

Q-switched mode-locking [Hau76, KBK⁺95, HPMG⁺99] is an oscillatory instability that stems from the interplay of pulse intensity with the carrier saturations and relaxations. It typically appears for a repetition rate much higher than the gain recovery rate close above the lasing threshold. The pulses are still short as compared to the roundtrip time and the absorber saturates and relaxes quickly. In this situation low intensity pulses let the lots of carrier inversion of the gain material build up. With the consequently strong gain the pulses grow almost exponentially while the gain saturates over several roundtrips in a step-wise manner. At some point the gain will be sufficiently saturated for the losses to take over and the pulses shrink again. This keeps going until the gain carriers can recover and the process repeats.

This regime is quite different from the temporal localized structures. The residual intensity between pulses is much larger and impedes the carrier relaxation that mediates the instability. For the functional mapping, however, the intensity was assumed to be zero between pulses and the carriers to thus relax exponentially. In the case of Q-switched mode-locking these assumptions are not justified. Deviations from the full DDE system are therefore to be expected. Also, the potential speed-up is small as the pulses occupy much more of the roundtrip. The single purpose of the analysis in this section is to demonstrate how well the FM yet performs in this unfavourable situation. Indeed, for the

very short roundtrip time used in the following example a more detailed traveling wave model [JB10a, JB10b, JB12] would be in order, rather than a DDE model.

Figure 4.21 shows results in the Q-switched regime for both the full DDE model and the respective FM implementation. The parameters are $\gamma = 40$, $\kappa = 0.8$, $\alpha = 2$, $\beta = 0.5$, $\phi = 0$, $\tau = 2$, $Q_0 = 0.6$ and $s = 30$ and the integration box of the mapping is $2\delta = 1$. Panel (a) shows the oscillating pulse train obtained from integrating the full system. A large modulation of the maximum peak intensity is observed. The pulses are short but relatively closely spaced as seen in the zoomed inset. Panels (b) and (c) show bifurcation diagrams of the Q-switching instability for both the full system and the FM, respectively, with the gain bias g_0 as the control parameter. Minor deviations of the bifurcation points are observed but the results are still very well reproduced. Indeed the qualitative behavior remains until the pulse hardly fits into the FM integration box.

Note, that the Q-switched model-locking instability was not found in Haus PDE model (4.15)–(4.17) which was discussed in the previous section. The functional mapping offers comparable computational efficiency to PDEs while conserving all dynamic regimes of the physically more accurate DDE model. Recently, carrier memory was successfully introduced into the Haus PDE model as a boundary condition between consecutive pulses using the same idea underlying the FM [HLGJ20].

5 VCSEL with Resonant Saturable Absorber Mirror

This chapter describes the results obtained for the DAE model of a vertical-cavity surface-emitting-laser coupled to a resonant saturable absorber mirror. Via the analysis of CW solutions the parameters are matched to reproduce the properties of the nonlinear mirrors used in a corresponding experimental setup. With these parameters the temporal localized structures and pulse trains of the experiment are reproduced. In addition, a new type of instability due to strong third order dispersion, which is incurred by the cavity geometry, is discussed. Finally, this effect is compared to the influence of TOD in a different type of mode-locked laser. Some of the results presented in this chapter have been published in [3], [5] and [4].

5.1 Continuous wave analysis

The nonlinear mirrors used in the corresponding experiment have been characterized by measurements of their CW reflectivities. To match the parameters of the model to these mirrors we can analyze the CW solutions in an analogous way.

5.1.1 Mirror reflectivities

Under CW injection the output of the mirrors will also be a CW when the carriers have equilibrated. From the relation of the injection and output fields we can find the reflectivity coefficients of the mirrors. We use the CW ansatz $Y_j(t) = Y_j \exp[-i\omega t]$, $E_j(t) = E_j \exp[-i\omega t]$, $O_j(t) = O_j \exp[-i\omega t]$ and plug it in the model equations (2.230)–(2.233)

$$-i\frac{\omega}{\kappa_1}E_1 = [(1 - i\alpha_1)N_1 - 1]E_1 + h_1Y_1, \quad (5.1)$$

$$-i\frac{\omega}{\kappa_2}E_2 = [(1 - i\alpha_2)N_2 - 1 + i\delta]E_2 + h_2Y_2, \quad (5.2)$$

$$0 = \gamma_1J_1 - \gamma_1N_1 - |E_1|^2N_1, \quad (5.3)$$

$$0 = \gamma_2J_2 - \gamma_2N_2 - s|E_2|^2N_2. \quad (5.4)$$

The reflection coefficient is defined by $O = rY$ so we have to find

$$r_j = \frac{O_j}{Y_j} = \frac{E_j - Y_j}{Y_j} = \frac{E_j}{Y_j} - 1. \quad (5.5)$$

The equations (5.3) and (5.4) can easily be solved for the equilibrium carrier inversions

$$N_1 = \frac{\gamma_1 J_1}{\gamma_1 + |E_1|^2}, \quad N_2 = \frac{\gamma_2 J_2}{\gamma_2 + s|E_2|^2}, \quad (5.6)$$

After using these in the field evolutions (5.1) and (5.2) we separating the E_j and Y_j fields to get

$$-h_1 Y_1 = \left[\frac{(1 - i\alpha_1)\gamma_1 J_1}{\gamma_1 + |E_1|^2} - 1 + i \frac{\omega}{\kappa_1} \right] E_1, \quad (5.7)$$

$$-h_2 Y_2 = \left[\frac{(1 - i\alpha_2)\gamma_2 J_2}{\gamma_2 + s|E_2|^2} - 1 + i \left(\delta + \frac{\omega}{\kappa_2} \right) \right] E_2. \quad (5.8)$$

These equations can easily be brought into the form of (5.5) in order to reach the reflection coefficients as functions of the parameters and the intra-cavity field intensities

$$r_1 = \frac{h_1}{1 - \frac{(1 - i\alpha_1)\gamma_1 J_1}{\gamma_1 + |E_1|^2} - i \frac{\omega}{\kappa_1}} - 1, \quad (5.9)$$

$$r_2 = \frac{h_2}{1 - \frac{(1 - i\alpha_2)\gamma_2 J_2}{\gamma_2 + s|E_2|^2} - i \left(\delta + \frac{\omega}{\kappa_2} \right)} - 1. \quad (5.10)$$

They can be used to match the model to given experimental conditions.

Figure 5.1 shows reflectivity curves of $|r_2|^2$ as a function of the injection wavelength at various field intensities for an exemplary absorber mirror. The resonance of the microcavity is assumed to be at $1.06 \mu\text{m}$. A photon decay rate of $\kappa_2 = 1.17 \times 10^{13} \text{ s}^{-1}$ yields a full width at half maximum of circa 14 nm . For very small injection amplitudes a maximum absorption of about 25% is reached with the absorber bias set to $J_2 = -0.0718$. Increasing the amplitude leads to more saturation of the carriers and the relative losses reduce. The other parameters were chosen as follows: the injection coupling factor $h_2 = 2$, the linewidth enhancement factor $\alpha_2 = 0$, the carrier relaxation rate $\gamma_2 = \frac{\kappa_1}{10}$ and the saturation ratio $s = 10$.

When considering a low power CW injection reach the unsaturated limit where the carriers reach the scaled bias values

$$\lim_{|E_j|^2 \rightarrow 0} N_j = J_j. \quad (5.11)$$

Here, the unsaturated reflectivities read

$$\bar{r}_1 = \frac{h_1}{1 - (1 - i\alpha_1)J_1 - i \frac{\omega}{\kappa_1}} - 1, \quad (5.12)$$

$$\bar{r}_2 = \frac{h_2}{1 - (1 - i\alpha_2)J_2 - i \left(\delta + \frac{\omega}{\kappa_2} \right)} - 1, \quad (5.13)$$

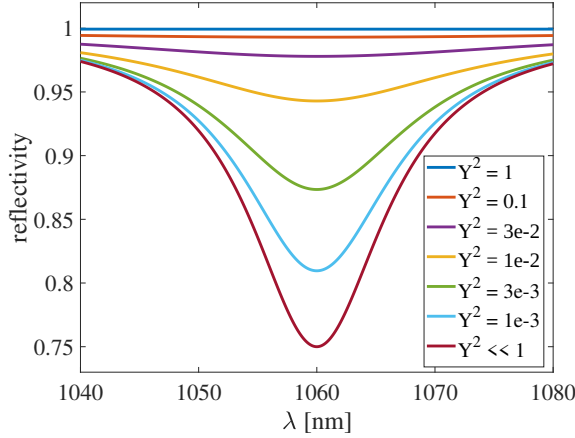


Figure 5.1: Reflectivity $|r_2|^2$ of the absorber mirror for different levels of injection intensity.

At large intensities the carrier density saturates to the transparency level. $J_2 \approx -0.0718$ is chosen for a maximal absorption of 25% and $\kappa_2 \approx 1.0885 \times 10^{13} \text{ s}^{-1}$ for a FWHM of 14 nm.

whereas the fully saturated cases are simply

$$\hat{r}_1 = \frac{h_1}{1 - i \frac{\omega}{\kappa_1}} - 1, \quad \hat{r}_2 = \frac{h_2}{1 - i \left(\delta + \frac{\omega}{\kappa_2} \right)} - 1. \quad (5.14)$$

Note, that in the limit of perfectly reflective bottom DBRs, where the coupling factors go to $h_j \rightarrow 2$, the fully saturated reflectivities have unit modulus $|\hat{r}_j| \rightarrow 1$.

Figure 5.2 shows curves of the unsaturated reflectivity of $|\bar{r}_1|^2$ as a function of the injection wavelength at different pump rates for an exemplary gain mirror. The resonance of the microcavity is again assumed to be at 1.06 μm . The photon decay rate is set to $\kappa_2 = 2.51 \times 10^{-12} \text{ s}^{-1}$ which yields a full width at half maximum of about 3 nm. A gain bias of $J_1 \approx 0.0455$ leads to a maximum amplification of around 20%. Further, in this example the injection coupling factor was set to $h_1 = 2$, the linewidth enhancement factor $\alpha_1 = 0$.

5.1.2 Lasing threshold

Using the CW ansatz from before in (2.234)–(2.235) we have

$$Y_1 = \eta [E_2 - Y_2] e^{i\omega\tau} = \eta O_2 e^{i\omega\tau} = \eta r_2 Y_2 e^{i\omega\tau}, \quad (5.15)$$

$$Y_2 = \eta [E_1 - Y_1] e^{i\omega\tau} = \eta O_1 e^{i\omega\tau} = \eta r_1 Y_1 e^{i\omega\tau}. \quad (5.16)$$

When looking at the devices in series we can substitute and get

$$Y_1 = \eta^2 r_2 r_1 Y_1 e^{2i\omega\tau}, \quad (5.17)$$

which leads to the CW condition

$$r_1 r_2 \eta^2 e^{2i\omega\tau} = 1. \quad (5.18)$$

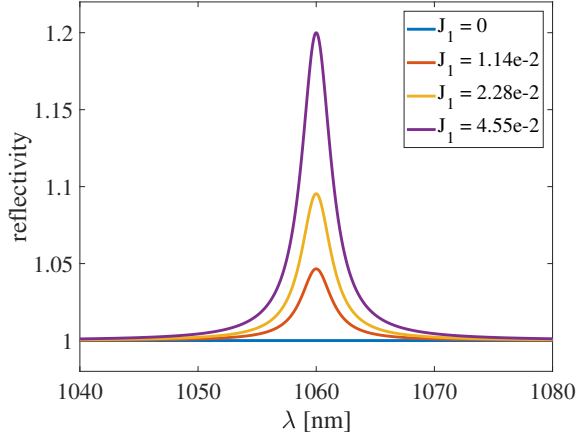


Figure 5.2: Unsaturated reflectivity $|\bar{r}_1|^2$ of the gain mirror for different pump rates. A maximal gain of 20% is reached at $J_1 \approx 0.0455$ and $\kappa_1 \approx 2.51 \times 10^{12} \text{ s}^{-1}$ yields a FWHM of 3 nm.

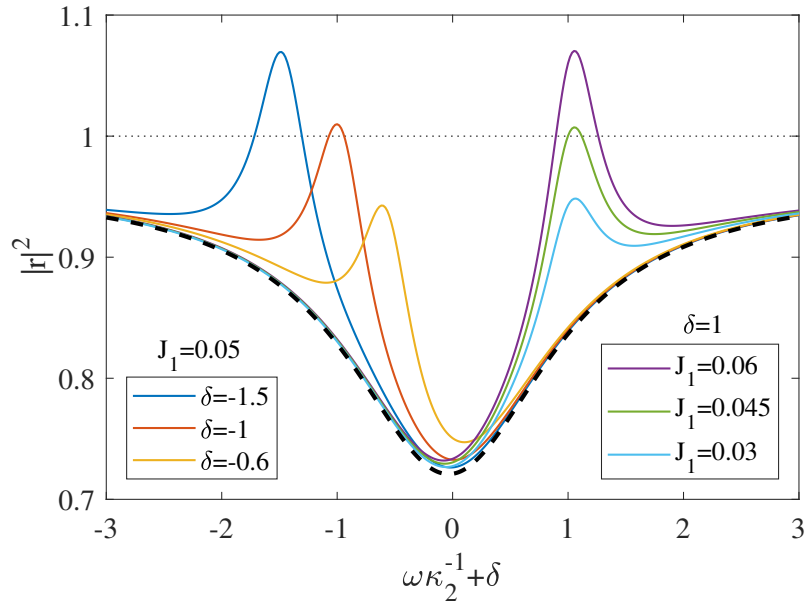


Figure 5.3: The combined attenuation factor as a function of ω for different combinations of the gain current J_1 and the detuning δ for unsaturated reflectivities \bar{r}_j of the mirrors. When the local maximum of the curve touches the dotted line at $|r|^2 = 1$ the lasing threshold is reached. This can be achieved by simply increasing J_1 (right half) or by changing the detuning, effectively moving the resonances of the mirrors apart (left half). As emission is dominated by the gain, this means less absorption over all. The frequency axis is shifted by the detuning for clarity and the zero gain asymptotic $J_1 = \delta = 0$ is marked by a dashed line for reference.

In the long delay limit $\tau \rightarrow \infty$ any small variation of ω can lead to an arbitrary phase to compensate for the other phase contributions. Therefore virtually any ω is a possible mode and we can treat it as a continuous function (quasi-continuous spectrum). We define the combined attenuation factor per roundtrip in the low intensity regime where the unsaturated reflectivities hold

$$r = \bar{r}_1 \bar{r}_2 \eta^2. \quad (5.19)$$

The lasing threshold is reached when its absolute value is unity $|r^{(\text{th})}| = 1$.

The pump rate J_1 and the detuning δ between the microcavities are experimentally easily accessible in some interval; in the latter case by changing the temperatures and thus the widths and resonances of the cavities and distributed Bragg reflectors. Threshold can be reached with either enough J_1 or enough δ as demonstrated in Figure 5.3. Typically, the gain cavity bandwidth is narrow as compared to the absorber. Emission is always close to the peak gain, thus the detuning can be used to set the level of absorption by moving out of the absorber resonance. In principle, with enough pump one can always reach threshold but experimentally this is limited. Setting the detuning can be vital to reach threshold when operating in the strong absorber regime required to create temporal localized structures. The parameters of the example in Figure 5.3 are: $\kappa_1 = 1$, $\kappa_2 = 3.5$, $h_1 = 2$, $h_2 = 1.997$, $\alpha_1 = 2$, $\alpha_2 = 0.5$, $J_2 = -0.07$ and $\eta = \sqrt{0.98}$. It is often convenient to scale time by the photon-lifetime of the gain, i.e. $\kappa_1 = 1$. The absorber injection coupling factor $h_2 < 2$ can be used to model the unsaturable losses of the absorber.

5.2 Temporal localized structures

Temporal localized structures have been realized in an experimental setup and published in [3] together with simulations of the corresponding to the model (2.230)–(2.235). A 1/2-VSCEL gain mirror and an RSAM were put face to face in a self-imaging condition using focusing lenses in front of mirrors. These mirrors have been crafted to meet the specific requirements of this experiment [GHT⁺02, LMB⁺10, CZF⁺18]. For signal extraction a beam splitter with 98% intensity transmission was positioned in between such that it is passed twice per external cavity roundtrip of circa 10.7 ns. The photon lifetimes of the gain mirror was 343 fs and of the RSAM 80 fs corresponding to bandwidths (FWHM) of 3.5 nm and 15 nm, respectively. A maximum gain of 129% can be achieved at a resonance wavelength of the mirrors around 1.06 μm . The saturable absorption had a modulation of 25% and only 0.3% nonsaturable losses. The saturation energies of the gain and absorber were 10 $\mu\text{J}/\text{cm}^2$ and 2 $\mu\text{J}/\text{cm}^2$, respectively. By varying the temperatures of the mirrors individually their resonances could be shifted, thus making a small detuning between them an easily accessible control parameter of the experiment. Indeed the lasing threshold cannot be reached at resonance due to the strong absorber modulation. A minimum detuning of 1.5 nm is needed where the modulation has dropped to 19%. The TLS were measured at 3.4 nm where modulation is 17%.

This section is on the simulation results for the described experiment. Regarding the carrier relaxation times 800 ps were assumed for the gain medium and 50 ps for the absorber. Time was scaled such that the photon decay rate of the gain $\kappa_1 = 1$. The other rates then read $\kappa_2 = 4.2875$, $\gamma_1 = 4.3 \times 10^{-4}$ and $\gamma_2 = 6.9 \times 10^{-3}$ and the delay time

$\tau = 15600$ where 2τ corresponds to one roundtrip. Typical semiconductor linewidth enhancement factors were used; $\alpha_1 = 2.5$ for the gain and $\alpha_2 = 1$ for the absorber. The gain bottom Bragg mirror was assumed to be perfectly reflective giving $h_1 = 2$ while the absorber bottom DBR was used to model nonsaturable losses leading to $h_2 = 1.9985$. In order to match the RSAM used in the experiment the absorber parameters were set to $J_2 = -0.07$ for the bias and $s = 5$ for the saturation ratio. The beam splitter attenuation in amplitude was $\eta = 0.99$.

5.2.1 Bistable TLS region and multistability

Figure 5.4 shows the results from direct numerical simulations of TLS in the aforementioned situation. A bistable region of stable TLS exists below the threshold curve. For this 2d-scan the functional mapping was used with complete gain recovery, i.e., in the long delay limit. Due to the size of the modeled cavity the remaining gain saturation $\sim \exp(-\frac{2\tau}{\tau_g}) \approx 1.5 \times 10^{-6}$ is negligible. The detuning parameter matching the experimental measurement is $\delta = 0.42$. Panel (a) shows the rather simple intensity profile of a typical pulse with a duration of about 3 ps. Panel (b) shows the respective spectrum while panel (c) shows the corresponding pulse train. The gain bias parameter for this pulse was set to $J_1 = 0.0525$ which corresponds to circa 24% maximum gain. Two such pulses can live in the cavity simultaneously and move around freely with respect to each other up to a point without losing intensity. If one pulse follows the other too closely it is pushed away because the gain carrier inversion has not fully recovered yet. This is proof for the regime of localized structures. Even more pulses can exist at the same time and a staircase of multistable solutions is obtained where higher numbers of pulses show a shrinking bistable region, i.e., more and more gain is needed for stable pulsation. The example of four pulses is shown in panel (e) where the pulses have come significantly closer together than the gain recovery time. Thus, there is less gain for each, resulting in smaller pulses overall. When starting the pulses at different distances to each other a transient toward equal distances and sizes is observed as the pulses feel each other via their gain depletion. This constitutes the transition from the localized regime to normal harmonic mode-locking. The maximum number of pulses was 8 as shown in panel (f). With even more at least one of them becomes too small to saturate the absorber and survive. All of the pulse trains in panels (c)-(f) were obtained by integrating the full DAE system. The theoretical results mirrored the experimental data to high accuracy.

5.2.2 Influence of the linewidth enhancement factors

Figure 5.5 shows results from a parameter study in both linewidth enhancement factors using the functional mapping in the long delay limit. Multiple panels are arranged in a grid with absorber linewidth enhancement factor increasing to the right in an interval of $\alpha_2 \in [0.5, 1.5]$ and the gain linewidth enhancement factor increasing downward an interval of $\alpha_1 \in [1.5, 5]$. One can observe the pattern that larger α_2 is good for a large bistable region while increasing α_1 has an adverse effect. From the sharp corners of the border visible at e.g. $(\alpha_1, \alpha_2) = (2, 1)$ it can be inferred that more than one bifurcation is limiting the stable region. For the low α_1 with high α_2 combination the border appears to stem

from the principal saddle-node of the TLS manifold, whereas for the high α_1 low α_2 case a subcritical torus bifurcation seems responsible. While the transient dynamics of the pulses differ qualitatively, still, the type of the bifurcation cannot be fully ascertained from numerical simulations alone.

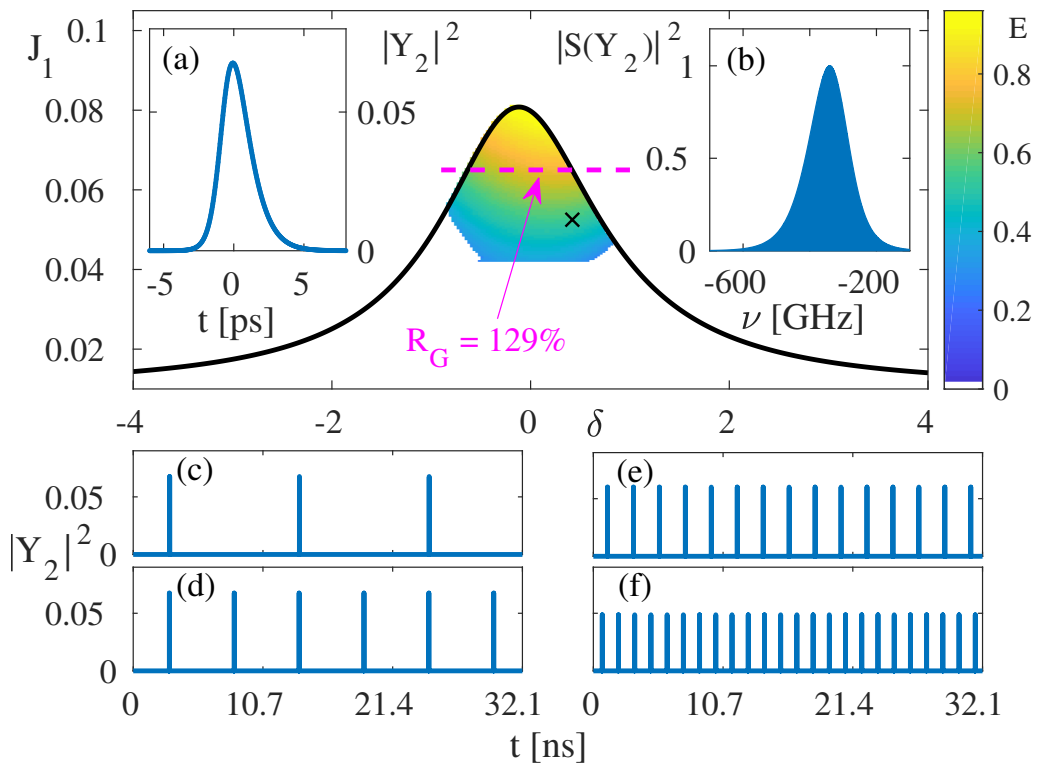
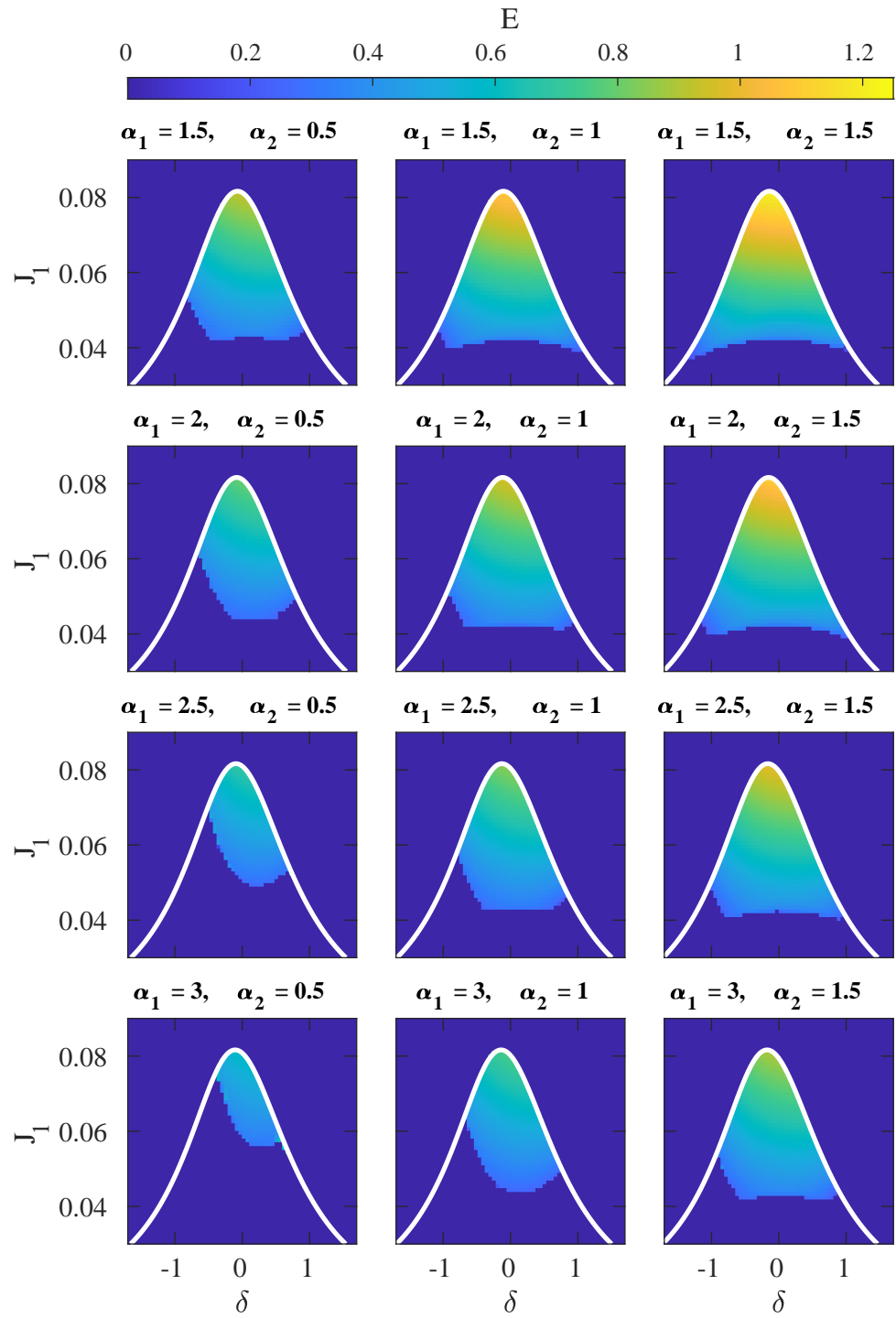


Figure 5.4: Region of existence of stable temporal localized structures in the J_1, δ plane where the color scale indicates the dimensionless integrated pulse energy E . The solid black line marks the lasing threshold. The dashed magenta line indicates a gain of $\sim 29\%$ at $J_1 = 0.065$, corresponding to a gain mirror reflectivity R_G of 129%. An exemplary TLS is marked by a black cross at $J_1 = 0.0525$, $\delta = 0.42$. The insets (a) and (b) show the temporal intensity profile and the power spectrum of this TLS, respectively. Panels (c-f) show pulse trains of such pulses with one, two, four and eight in the cavity at the same time. All of these solutions are multistable. In the first two cases the pulse energy does not change, indicating a good localization regime. The last two show dropping of the intensity as the gain does not have enough time to fully relax, i.e. the pulses feel each other and their positions are not mutually independent. Thus, a regime of higher harmonic mode-locking is reached and the pulses are no longer localized structures. A similar version of this figure was used in [3].



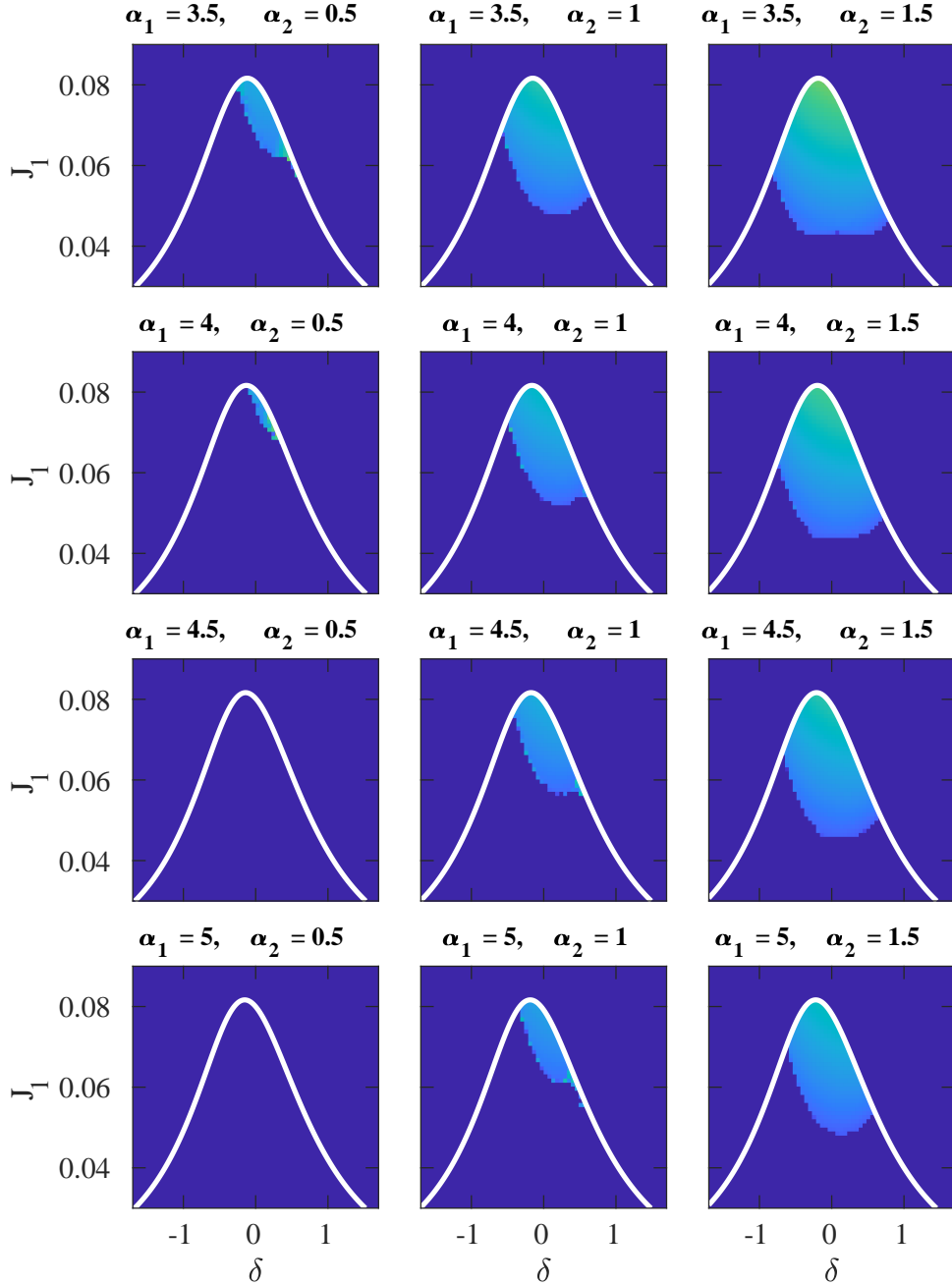


Figure 5.5: Bistable TLS region as in Fig. 5.4 for $\alpha_1 \in [1.5, 5]$ and $\alpha_2 \in [0.5, 1.5]$. The stable region grows with α_2 and shrinks with α_1 .

5.3 Satellites on the leading edge

We now take a look at a specific effect of the coupled microcavities which is that pulses can develop a series of leading satellites. This can readily be explained when taking a look at the underlying cavity geometry. The corresponding delay algebraic description naturally induces higher order dispersion which is otherwise very difficult to introduce into DDE models [HBM10, PSHV17].

5.3.1 The case of the empty cavity

We take a look at Eqs. (2.206), (2.207) without susceptibility and detuning. For proper scaling we set $\kappa_1 = 1$

$$\frac{\partial E}{\partial t} = -E + hY, \quad (5.20)$$

$$Y = \eta [E_\tau - Y_\tau]. \quad (5.21)$$

This is the simplest case of an empty microcavity with a feedback mirror and shall serve as an instructive example to explain the existence of satellites.

For the VCSEL-RSAM system this would correspond to a gain bias $J_1 = 0$ such that the carrier inversion will stay at $N_1 = 0$ and the QWs are transparent to the field. The top DBR of the absorber mirror is assumed to be perfectly reflective which corresponds to an injection coupling factor $h_2 = 0$. This way no photons may enter the mirror and its field simply vanishes $E_2 = 0$. Under these conditions the model simplifies significantly

$$\kappa_1^{-1} \frac{\partial E_1}{\partial t} = -E_1 + h_1 Y_1, \quad (5.22)$$

$$Y_1 = \eta^2 [E_1(t - 2\tau) - Y_1(t - 2\tau)]. \quad (5.23)$$

Indeed this has the same form as the previous equations except for the indices, η^2 and the double τ that can all be removed or scaled appropriately.

When assuming a perfect bottom DBR of the microcavity the injection coupling factor is $h = 2$. In this limit the microcavity resembles a Gires-Tournois interferometer (GTI) [GT64] which is an optical element to control and usually cancel other sources of group velocity dispersion. It is typically constructed as a glass plane on top of a mirror and can thus be considered a Fabry-Pérot interferometer operated in reflection. Photons with resonant frequencies can be trapped for significant times in the small glass cavity. The typical trapping time depends on the detuning from the modes of the GTI. Thus, the different frequencies that make up a pulse are delayed differently, thereby creating the group velocity dispersion. Note, that at resonance the second order dispersion actually goes through zero and changes sign as a function of the detuning. Still, higher order terms can remain finite.

Figure 5.6 shows direct numerical simulations of Eqs. (5.20) and (5.21) in this situation. Pulses develop a series of leading satellites over many roundtrips. This process is much faster for narrow pulses than for broad pulses. The pulses in the example have a FWHM of $\tau_p = 1$ and $\tau_p = 5$, respectively.

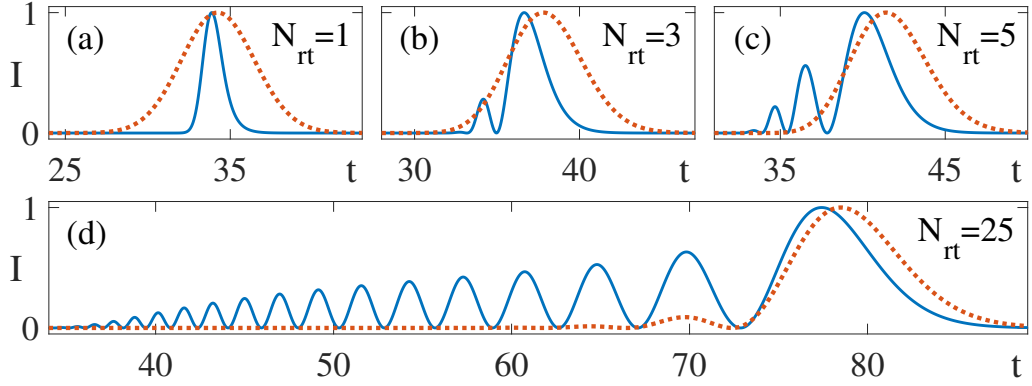


Figure 5.6: Snapshots of different roundtrips showing the empty cavity response to pulses of different width. The intensity is normalized to the peak intensity of the pulse profile. A series of satellites develops in front of the pulse as part of it is directly reflected from the top DBR while the rest is filtered by the microcavity. The effect is much stronger for narrower pulses. A similar version of this figure was used in [5].

During each roundtrip part of the pulse is reflected immediately from the top DBR of the microcavity while the rest enters and is filtered before being re-emitted into the external cavity. Qualitatively, the reflected and filtered signals combine again with a small delay due to the filtering and the process repeats. Thus the highest order satellite can be interpreted as those photons that never entered the microcavity, the second to last satellite is made up from photons that entered once, the next consists of those that entered twice and so on. In the intensity representation the phase of η remains unimportant until the satellites have populated the whole cavity and feel the parent pulse in front because of periodic boundary conditions. After normalizing the intensity the modulus of the feedback attenuation factor $|\eta|$ also becomes irrelevant. Indeed, the picture looks the same for any complex valued $\eta \neq 0$.

For an alternative view we will derive a PDE model of the empty cavity using the functional mapping structure of the DAE model Eq. (5.20), (5.21). First we transform the microcavity field evolution to the frequency domain using $\frac{\partial}{\partial t} \rightarrow -i\omega$ so we can solve for \hat{E}

$$\frac{\partial E}{\partial t} = -E + hY, \quad (5.24)$$

$$\hat{E} - i\omega \hat{E} = h\hat{Y}, \quad (5.25)$$

$$\hat{E} = \frac{h}{1 - i\omega} \hat{Y}. \quad (5.26)$$

When integrating in steps of single roundtrip numbered n we can identify the delay terms as the previous iteration of a discrete mapping and plug in the expression for \hat{E}

$$\hat{Y}^{(n+1)} = \eta \left[\hat{E}^{(n)} - \hat{Y}^{(n)} \right], \quad (5.27)$$

$$\hat{Y}^{(n+1)} = \eta \left[\frac{h}{1 - i\omega} - 1 \right] \hat{Y}^{(n)}. \quad (5.28)$$

Assuming $h = 2$ we get a conservative microcavity as no photons are lost through the bottom DBR and all are eventually re-emitted into the external cavity. For this case we can define the linear operator

$$\mathcal{L} = \frac{2}{1 - i\omega} - 1 = \frac{1 + i\omega}{1 - i\omega} = \frac{C^*}{C}, \quad (5.29)$$

that is a fraction of complex conjugates and is therefore unitary $|\mathcal{L}|^2 = 1$.

We notice that we have a constant ratio between steps

$$\frac{\hat{Y}^{(n+1)}}{\hat{Y}^{(n)}} = \eta \mathcal{L}. \quad (5.30)$$

This type of discrete mapping can be solved by an exponential ansatz

$$\hat{Y}(\sigma_0 + \Delta\sigma) = (\eta \mathcal{L})^{\Delta\sigma} \hat{Y}(\sigma_0), \quad (5.31)$$

where we introduced a slow timescale σ that corresponds to roundtrips but is continuous. Increments of $\Delta\sigma = 1$ reproduces the original discrete mapping.

When assuming a slow continuous transformation of the pulse profile we may write the derivative with respect to σ

$$\frac{\partial \hat{Y}}{\partial \sigma} = (\ln \eta + \ln \mathcal{L}) \hat{Y}. \quad (5.32)$$

To get an approximate PDE form of the model we expand the logarithm of the linear operator in $i\omega$

$$\ln \mathcal{L} = 2(i\omega) + \frac{2}{3}(i\omega)^3 + \mathcal{O}(\omega^5). \quad (5.33)$$

For the sake of simplicity we truncate after the third order and substitute in Eq. (5.32)

$$\frac{\partial \hat{Y}}{\partial \sigma} = \left(\ln \eta + 2(i\omega) + \frac{2}{3}(i\omega)^3 \right) \hat{Y}, \quad (5.34)$$

We can now transform back to time using $i\omega \rightarrow -\frac{\partial}{\partial t}$

$$\frac{\partial Y}{\partial \sigma} = \left(\ln \eta - 2 \frac{\partial}{\partial t} - \frac{2}{3} \frac{\partial^3}{\partial t^3} \right) Y, \quad (5.35)$$

to reach an approximate PDE model for the empty cavity.

In this representation the derivatives with respect to time t are the different orders of dispersion. The advection term $-2 \frac{\partial}{\partial t}$ only causes the period T to be a bit larger than the delay time τ but causes no deformation. Therefore, it can be canceled by properly choosing a co-moving frame. Third order dispersion thus becomes the dominating term. It is the lowest order effect to break the parity symmetry—apart from the aforementioned advection—and can induce drift [TBC⁺13, LMK⁺13, PRGL⁺14] or convective instabilities [CC97, WOTG00, MLA⁺08]. In general the terms read $-\frac{2}{k} \frac{\partial^k}{\partial t^k}$ with $k \in \mathbb{N}$ and odd. These asymmetric terms are responsible for the creation of satellites to only one side. It

is only in this empty cavity at resonance where the symmetric terms are zero. With other parameters, e.g. some detuning, the symmetric terms no longer vanish but TOD can still be very strong as compared to second order dispersion that causes pulse broadening. In active systems with carrier interactions such a PDE cannot be found as easily and satellites will only appear under specific combinations of parameters, notably when the influence of TOD is not overpowered by second order dispersion.

Operating the microcavities in the GTI regime with small detuning yields a filtering characteristic very different from the bandwidth limiting element assumed in the unidirectional ring model. No photons are lost via transmission through the bottom DBR, irrespective of frequency. Indeed, high frequency damping approaches a small asymptotic value instead of a typical parabolic shape. Thus, only the phase is affected upon reflection. Resonant photons can enter and stay in the microcavity but are transmitted back into the external cavity eventually. Others get reflected immediately from the top DBR. Upon recombination of the signal this causes strong TOD which can still dominate over second order dispersion in the in the VCSEL-RSAM system. One could therefore wonder where gain filtering appears in this VCSEL-RSAM model.

5.3.2 Satellites replacing the main pulse

An interesting regime of unstable pulses can be found for $\alpha_1 = \alpha_2 = 0$. The pulse possesses a series of satellites on the leading edge that are caused by the cavity geometry as explained in the previous section. For sufficiently large feedback and gain the satellites can become large enough to saturate the absorber mirror and consequently receive gain. This means that the net-gain window of the pulse is opened prematurely. As a consequence the satellite grows and starts to use up more and more gain carrier inversion before the main pulse even arrives. Thus, the gain available to the main pulse decreases as it becomes increasingly saturated by the leading satellite and it finally dies out. Indeed the first satellite grows into a new pulse of the same shape as its parent which it effectively replaces and the process repeats in a continuous cycle.

Figure 5.7 shows a pseudo-space-time representation of the dynamics that appear as a forward staggering motion of an oscillating pulse. The full set of parameters of this example reads: $\kappa_1 = 1$, $\kappa_2 = 10$, $\alpha_1 = 0$, $\alpha_2 = 0$, $h_1 = 2.0$, $h_2 = 1.9985$, $\gamma_2 = 1.4 \times 10^{-4}$, $J_1 = 0.044$, $\gamma_2 = 0.01$, $J_2 = -0.03$, $s = 5.4$, $\delta = 0$, $\eta = 0.985$ and $\tau = 6000$. Except for the linewidth enhancement factors and the detuning these parameters are intentionally kept very close to the ones in the following Section 5.4.2 Note, that this corresponds to a normal passive mode-locking regime with the cavity being relatively short as compared to the gain relaxation $2\tau\gamma_1 = 1.68$. However, the same kind of dynamics can be obtained in the localized long cavity regime as well with appropriately less gain.

5.3.3 Low frequency dynamics

The instability shown in the previous subsection exhibits a very long period close above the bifurcation point. This is due to a barely unstable first order satellite that is only just able to overcome the absorber and open the premature net-gain window. Thus the effective gain per roundtrip is very small and the intensity of the satellite grows exponentially slow

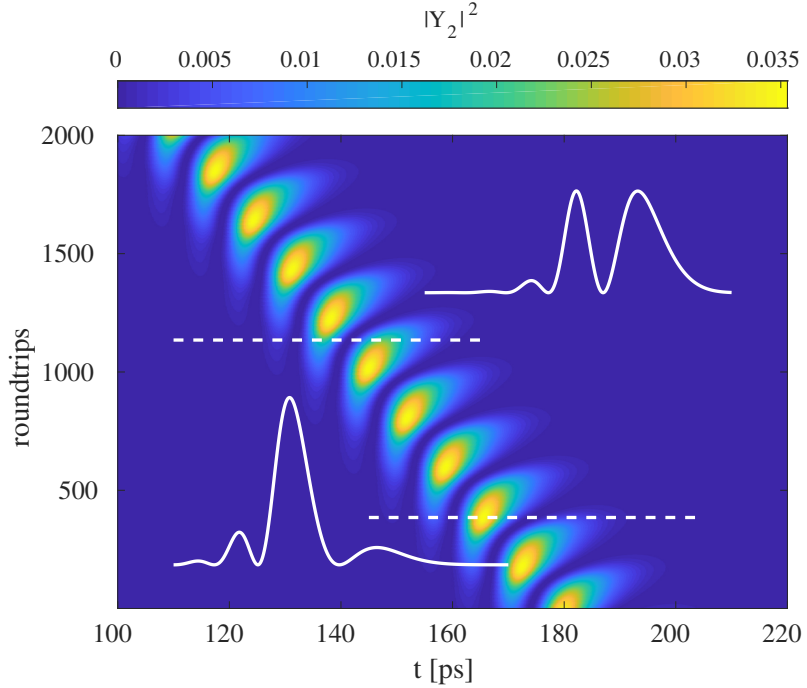


Figure 5.7: Unstable regime for zero linewidth enhancements $\alpha_j = 0$ and detuning $\delta = 0$. An unstable satellite grows in front of the pulse that causes an increasing early gain saturation. The parent pulse is deprived of gain and dies out. It is replaced by the satellite that grows to the same shape as its parent. This process repeats giving rise to a quasi-periodic oscillation.

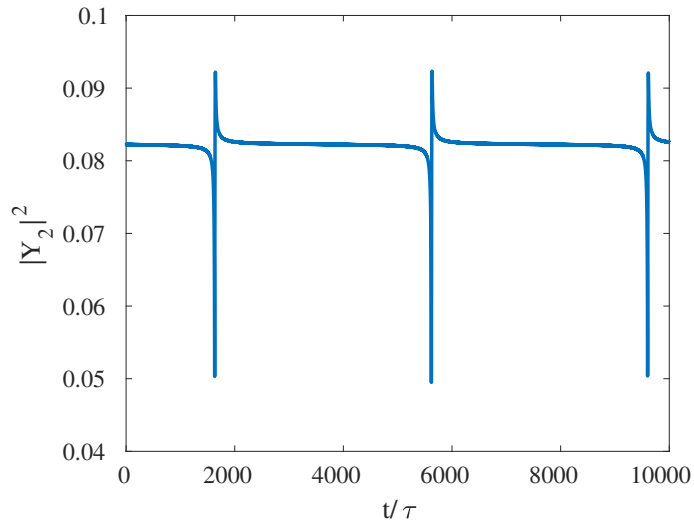


Figure 5.8: A time series of the peak intensity per roundtrip shortly after the onset of the satellite instability. The pulse remains almost stationary, then rapidly erupts. Closer to the bifurcation, the period becomes increasingly larger.

for a very large amount of roundtrips. Finally it erupts in an almost point like manner when looking at the pulse train. Figure 5.8 shows an example of this situation where the peak intensities of the pulses are plotted as a time series.

5.4 Satellite instability

In semiconductor lasers the linewidth enhancement factors play a strong role, limiting the $\alpha_i = 0$ scenario discussed in the previous subsections to an academic interest. Under certain conditions, however, they can appear for realistic parameters as well and destabilize the pulse train.

5.4.1 Progression of the dynamics

Under the influence of linewidth enhancement pulses typically undergo chirped broadening. The additional third order and higher dispersive effects induced by the cavity geometry are usually not apparent in this situation where the pulse is relatively broad as compared to the transform limit. However, for the right combination of parameters, especially with the correct detuning δ , the linewidth enhancement effects of the gain and absorber can almost cancel out and satellites appear. Where this happens depends intricately on all the parameters since the interplay of the fields and carriers is very complex. The manifold of pulses with satellites proves very difficult to trace exactly in simulations. At least three parameters have to be changed appropriately at the same time, otherwise one quickly starts to exit the regime. In the intensity profile the satellites tend to smear out and fuse with the leading edge when changing any one parameter alone. From a technical point of view this can be good for stabilization. In an experiment one might avoid satellites and related instabilities by, e.g., changing the detuning. Note, that even for parameters where no satellites appear on stable pulses their effects can be very strong on transients. An instability found in a similar experimental setup was presented in [MLA⁺18] and may be directly related.

Figures 5.9–5.13 show pseudo-space-time representations of time series obtained from DNS using the FM in the long delay limit for experimentally realistic parameters: $\kappa_1 = 1$, $\kappa_2 = 10$, $\alpha_2 = 1$, $h_1 = 2$, $h_2 = 1.9985$, $\gamma_1 = 5 \times 10^{-4}$, $\gamma_2 = 0.01$, $J_2 = -0.03$, $s = 3.66$, $\delta = 0$. The remaining parameters α_1 , J_1 and η are varied as control parameters. They illustrate the progression from a stable pulse with leading satellites to a stably oscillating regime that is reminiscent of the staggered parent pulse replacement instability discussed in the previous section. In addition to the intensity evolution in the upper left panels the signal of a simulated photo detector with a bandwidth of 15 GHz is shown in the lower left panels. The corresponding evolution of the spectrum is shown in the upper right panels. Its average is depicted in the lower right panels.

Figure 5.9 shows the stable pulse with leading satellites for $\alpha_1 = 2.5$, $J_1 = 0.0463$ and $\eta = 0.985$. It undergoes an AH instability and starts to oscillate as shown in Figure 5.10 for $\alpha_1 = 2.4$, $J_1 = 0.0463$ and $\eta = 0.985$. The satellites appear to oscillate along with the main pulse. In Figure 5.11 for $\alpha_1 = 2.5$, $J_1 = 0.046$ and $\eta = 0.983$ the satellites appear to oscillate at twice the frequency of the main pulse which slightly moves back and forth while growing and shrinking. This indicates a varying attraction to its first satellite that

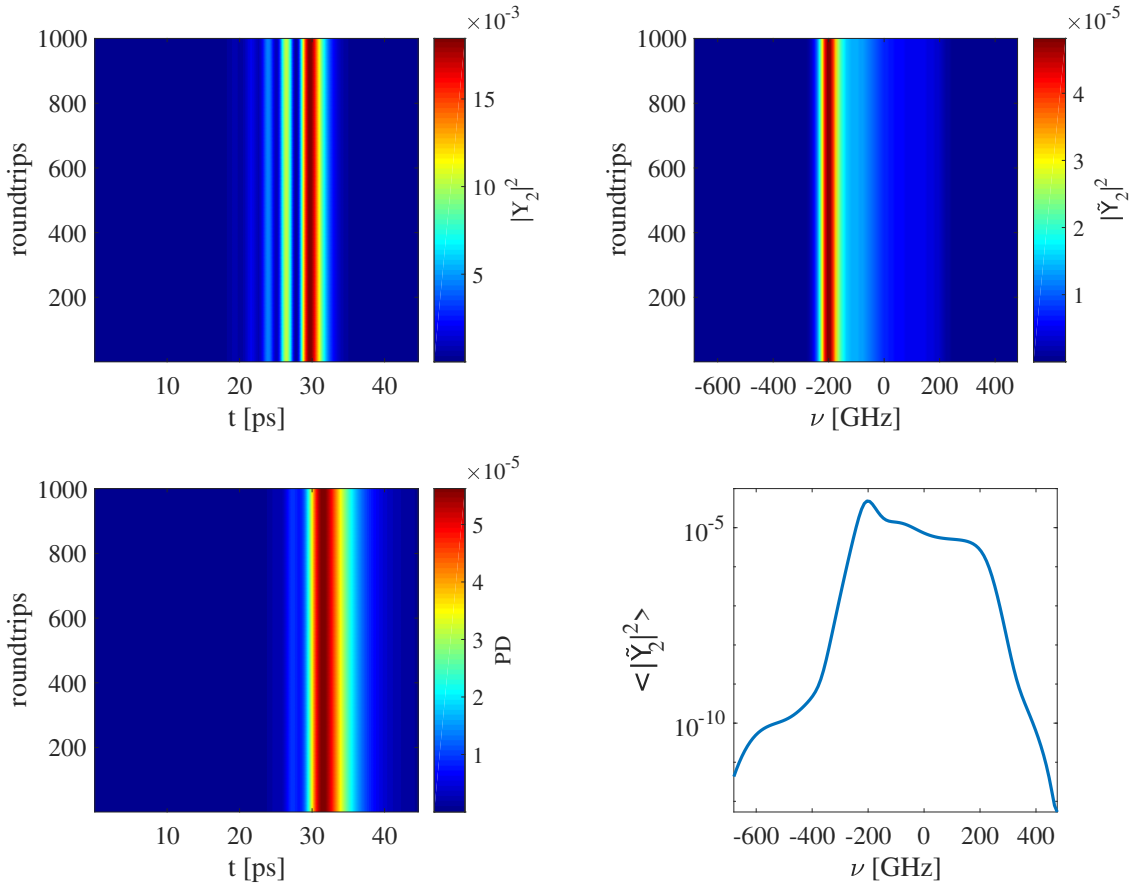


Figure 5.9: A pulse with satellites on the leading edge that are hardly visible in a corresponding simulated photo detector signal. In an experiment with realistic noise levels this would not be expected to be apparent. The spectrum has strongly asymmetric slopes to either side. Other parameters are $\alpha_1 = 2.5$, $J_1 = 0.0463$, $\eta = 0.985$.

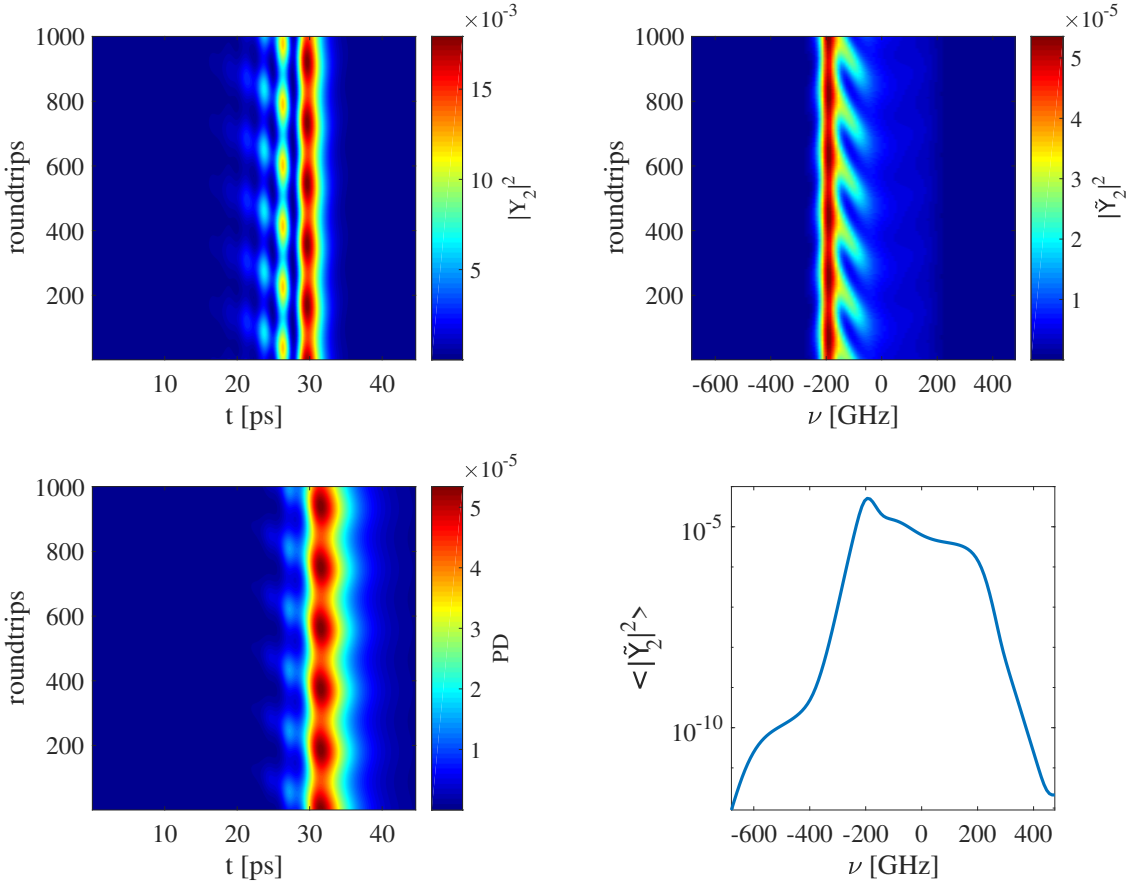


Figure 5.10: The pulse oscillates slightly in a breathing manner and its satellites just follow, growing and shrinking with it. They remain hard to see in photo detector signal. The spectrum develops tails on blue side, i.e., local maxima that appear and disappear. The average spectrum remains monotonous. Other parameters are $\alpha_1 = 2.4$, $j_1 = 0.0463$, $\eta = 0.985$.

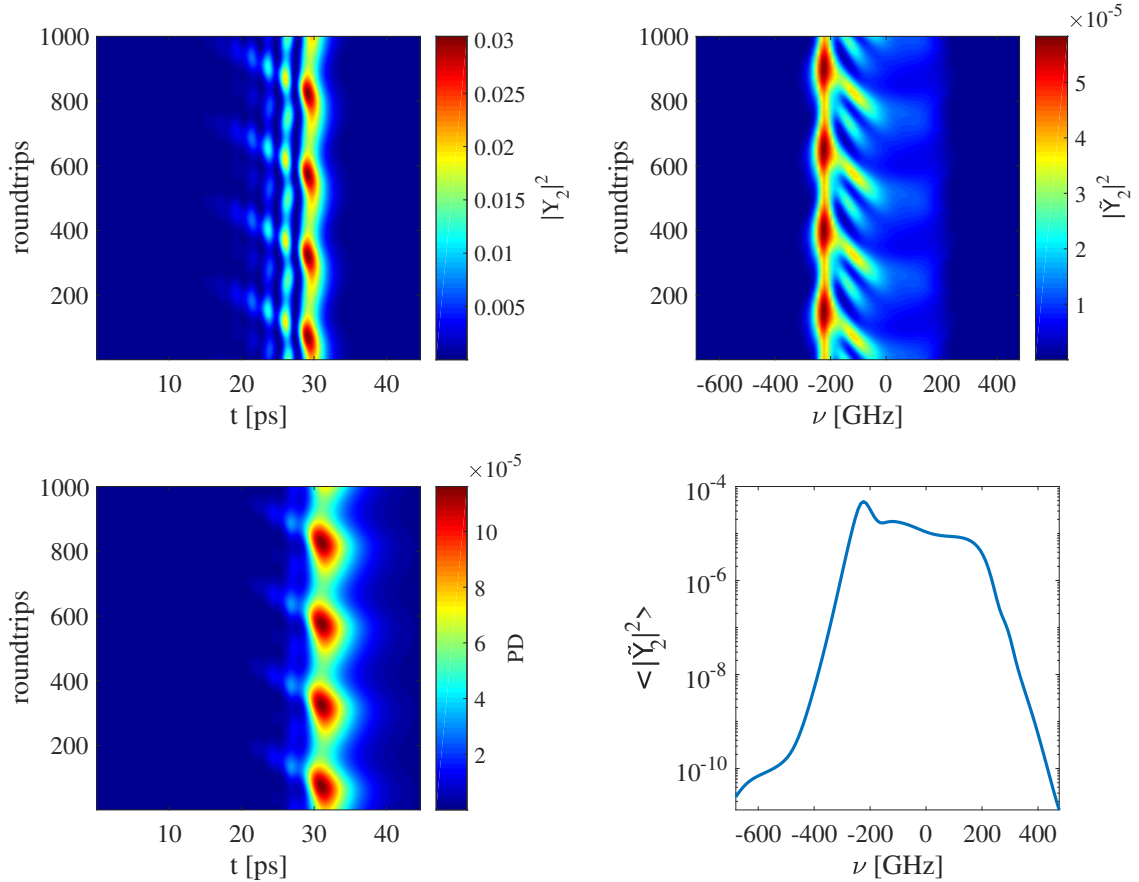


Figure 5.11: The satellites oscillate with half the period of parent pulse forming a spotted pattern. The secondary peak of the oscillation is smaller and higher order satellites more damped. In the photo detector signal the oscillation of the main pulse is visibly stronger but the satellites are still not prominent. The spectrum has developed a second set of tails and the average shows local maximum on blue side. Other parameters are $\alpha_1 = 2.5$, $j_1 = 0.046$, $\eta = 0.983$.

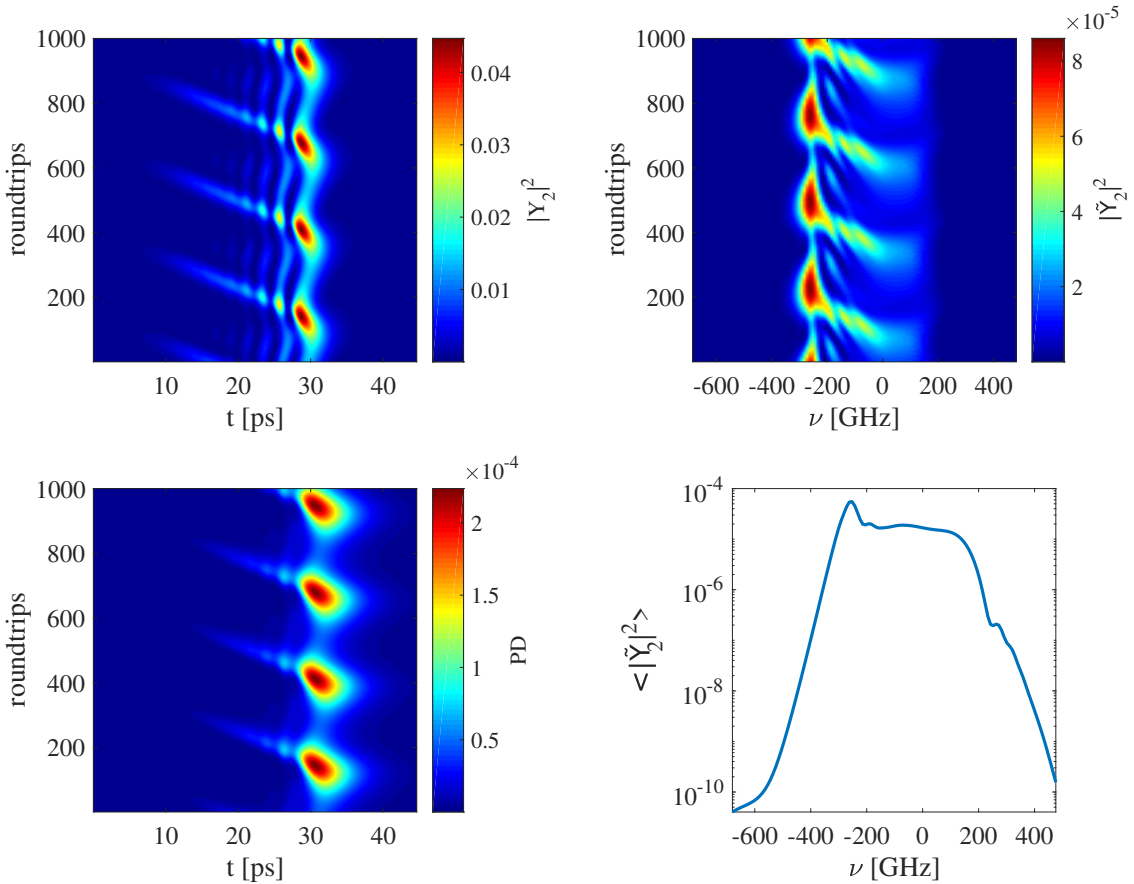


Figure 5.12: The secondary satellite oscillation peak is stretched much longer in time. At the end of it, the main pulse is attracted by it and slides toward it. In photo detector signal the satellites are only slightly more visible. The spectrum has become strongly asymmetric. Other parameters are $\alpha_1 = 2.5$, $j_1 = 0.046$, $\eta = 0.9835$.

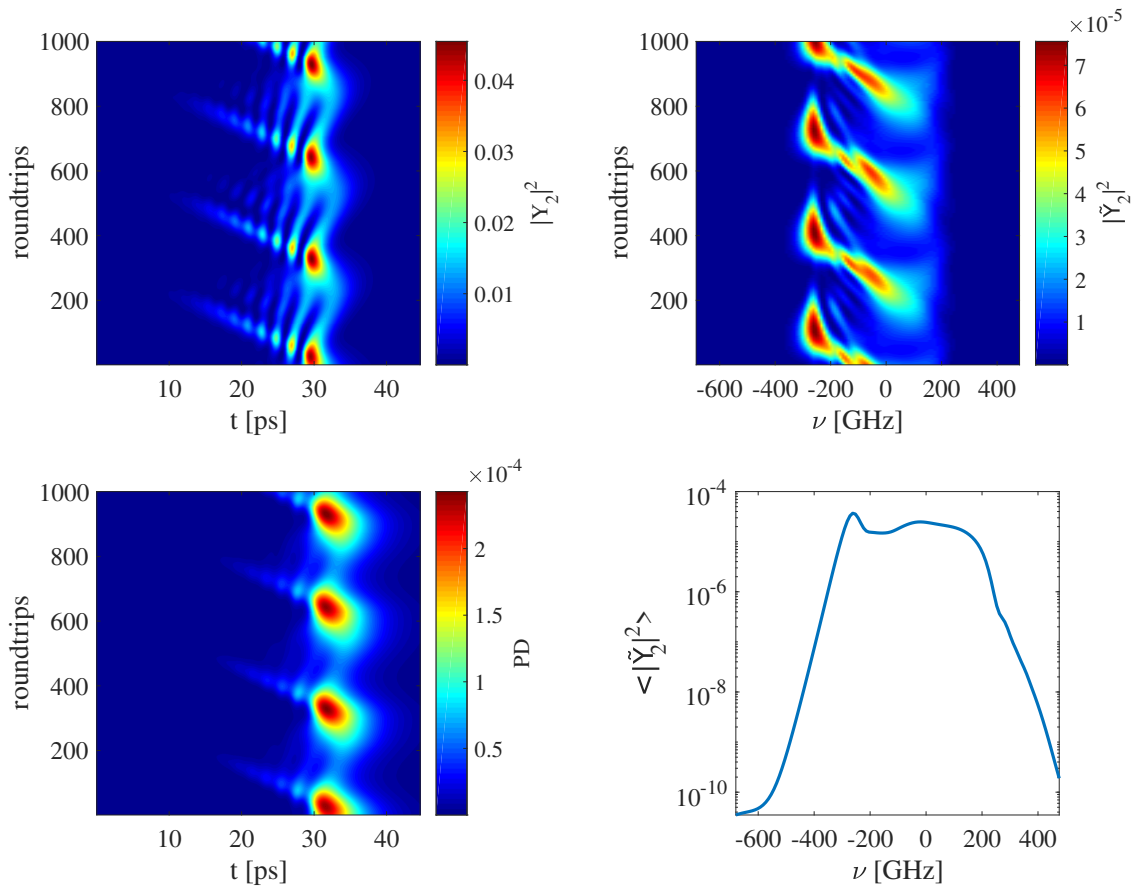


Figure 5.13: Finally, the parent pulse jumps onto the first satellite and merges with it to remain at this position. Details are not obvious in photo detector signal. The part of the spectrum due to satellites has reached a comparable amplitude as for the parent pulse. A broad second frequency range is prominent in the average spectrum. Other parameters are $\alpha_1 = 2.5$, $j_1 = 0.0477$, $\eta = 0.982$.

might be due to the varying chirp or the changing gain saturation that both result from the intensity oscillation. Indeed, pulses and their satellites cannot clearly be identified as two separate things. There is always an interplay of amplitude-phase coupling and higher order dispersion. Figure 5.12 shows an even stronger version of the instability at $\alpha_1 = 2.5$, $j_1 = 0.046$ and $\eta = 0.9835$. The attraction makes the pulse visibly slide toward the first satellite. Finally, in Figure 5.13 the main pulse even jumps to the location of the first satellite and apparently absorbs it. Here the other parameters are $\alpha_1 = 2.5$, $j_1 = 0.0477$ and $\eta = 0.982$.

Generally the satellites remain barely visible in the photo detector signal. The noise in an experimental measurement is likely going to hide their existence altogether. Only a strong oscillation in intensity and width can be observed. Evidence of the satellite instability should be visible in the average spectrum, though, that becomes increasingly asymmetric and even develops a local maximum to one side where the satellite induced dynamics are most visible.

5.4.2 Experimental parameters

Figure 5.14 shows two examples of satellite induced stable oscillations using the following parameter set: $\kappa_1 = 1$, $\kappa_2 = 10$, $\alpha_2 = 1$, $h_1 = 2.0$, $h_2 = 1.9985$, $\gamma_2 = 1.4 \times 10^{-4}$, $\gamma_2 = 0.01$, $J_2 = -0.03$, $\delta = -0.5$, $\eta = 0.985$ and $\tau = 6000$. These parameters correspond to an experimental setup using the same gain mirror from Section 5.2 with a slightly different RSAM that has a bandwidth (FWHM) of 40 nm and a maximum modulation of 12%. The panels from left to right show pseudo-space-time representations of the intensity, the resulting signal of a simulated photo detector with 15 Ghz bandwidth and the corresponding spectrum.

The upper panels show a satellite instability similar to Figure 5.12 for $\alpha_1 = 2.5$, $J_1 = 0.044$ and $s = 5.4$. The lower panels show another regime with a lower period for the parameters $\alpha_1 = 2.3$, $J_1 = 0.041$ and $s = 5.1$ that only slightly differ from the previous example. Here, the pulse is chasing its building satellites, thus quickly drifting forward and loosing intensity. It then stays still for a while to grow back. Similar dynamics have been found in the corresponding experiment. Note, that the picture has been straightening using the average period so that these dynamics appear as a sharp back and forth motion. Whether this is interpreted as only forward or only backward motion in a stair shape is up to choice. Physically the drift is always toward larger time.

These dynamics are slightly above the lasing threshold but remain stable because the carrier inversion never fully recovers, at least $\exp(-2\tau\gamma_1) \approx 18.64\%$ of the gain saturation caused by a pulse remains on its return. The threshold $J_1^{(th)} \approx 0.0404$ differs only negligibly between the two examples (as function of α_1).

Both shapes of dynamics actually appear as part of a continuous manifold of stable quasi-periodic orbits in the simpler MIXSEL system that will be the topic of the next chapter. In the VCSEL-RSAM system they are most likely connected as well, but due to the additional complexity a set of parameters where they are connected through a stable transition remains elusive.

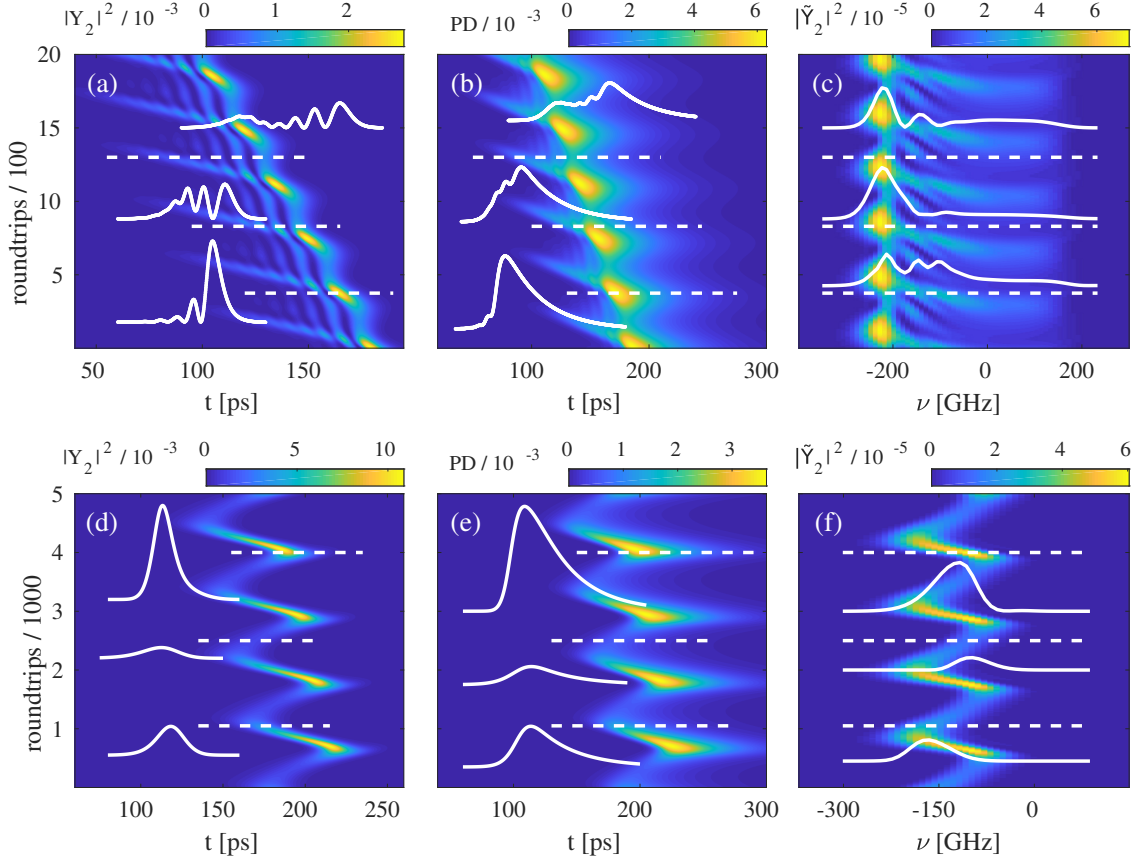


Figure 5.14: (a-c) Satellite instability with nonzero detuning and very similar characteristics to the situation in Figure 5.12. Parameters are $\alpha_1 = 2.5$, $J_1 = 0.044$, $s = 5.4$. (d-f) A pulse slowly sliding back and forth for slightly different parameters $\alpha_1 = 2.3$, $J_1 = 0.041$, $s = 5.1$. The higher order dispersive effects manifest in an oscillatory drift motion instead of leading satellites. An oscillation like this has been observed in a corresponding experiment. A similar version of this figure was used in [5].

5.4.3 Comparison with the CCQGLE

The Ginzburg-Landau equation is the normal form of a finite wavelength instability in spatially extended systems while its complex variant is the normal form for a respective Andronov-Hopf bifurcation. With cubic terms the bifurcations are supercritical, but the addition of a quintic term allows for stable solutions that emerge subcritically. It is thus prevalently investigated in the context of pattern formation, see [AK02] for a review. It can also be considered as a generic PDE for PML in optical fibers where the extremely slow gain can be averaged over the cavity as it remains uniform. The interplay of the cubic and quintic terms describes the saturation of gain and absorption, respectively. Thus, given appropriate parameters, it encompasses the subcritical Andronov-Hopf regime that corresponds to TLS. Next to the unidirectional ring model (2.96)–(2.98) it offers another, yet more generic, opportunity for comparison of TLS behaviour.

The complex cubic-quintic Ginzburg-Landau equation (CCQGLE) appears in the context of soliton explosions [SCAA00]. Such explosions were first experimentally found in Kerr lense mode-locking of a Ti:sapphire lasers [CSCA02]. A similar effect exists in the mode-locking of Yb-doped fibers [RBE15]. Here, the CCQGLE was used successfully to described the system with the addition of higher order terms [CD16].

The CCQGLE with higher order terms reads

$$\begin{aligned} \frac{\partial A}{\partial z} = & \delta A + (\epsilon + i) |A|^2 A + (\mu + i\nu) |A|^4 A + \left(\beta + i \frac{D}{2} \right) \frac{\partial A}{\partial t^2} \\ & + \beta_3 \frac{\partial A}{\partial t^3} - s \frac{\partial}{\partial t} (|A|^2 A) - i\tau_R A \frac{\partial |A|^2}{\partial t}, \end{aligned} \quad (5.36)$$

with, the complex electric field amplitude A , the propagation distance or roundtrip number z and the (fast) time t . The net gain is described by δ while ϵ and μ parameterize the nonlinearities of gain and absorption, respectively, and ν measures to saturation of the nonlinear refractive index. D represents the group velocity dispersion and β the spectral filtering. The additional higher order terms in the second line of Eq. (5.36) contain the coefficients for TOD β_3 , self-stepping s and intrapulse Raman scattering τ_R .

A special kind of soliton explosions is one-sided, asymmetric explosions where the whole soliton appears to have jumped to the side after a full cycle [LF10]. In the absence of higher order terms these explosions happen equally likely to both sides thus resulting in a random walk motion. With higher order terms, however, this symmetry is broken and the probabilities of left and right sided explosion are no longer the same. Figure 5.16 shows examples for these situations. Indeed, the bifurcations responsible for these instabilities split in the parameter space [4] such that, given appropriate parameters, explosions may only ever occur on one side.

Another type of soliton instability is the so-called breather solution [AK87, AEK88]. Third order dispersion can induce such an oscillation with a strongly asymmetric space-time profile as shown in Figure 5.16. It possesses rather similar features as the dynamics shown in panel (a) of Figure 5.14, albeit on the trailing edge as this example was calculated with a positive TOD coefficient. A specific PDE model for the VCSEL-RSAM system will require spatial derivative terms at least up to third order to encompass the appearance of satellites and their instability.

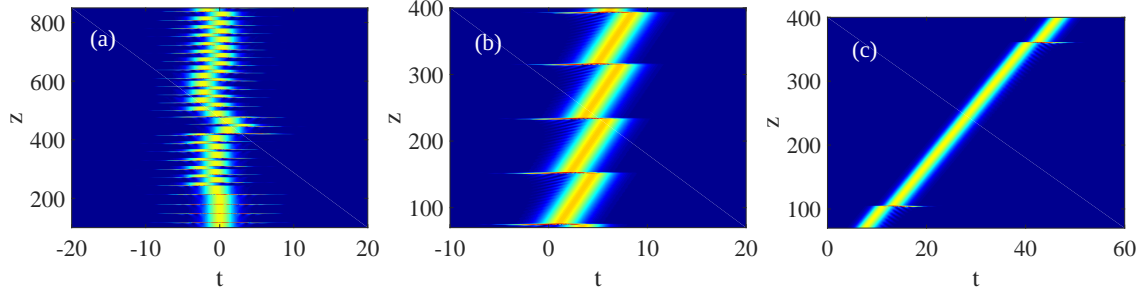


Figure 5.15: Space-time diagram of solitons explosions in the CCQGLE with higher order terms. (a) For vanishing higher order terms $\beta_3 = 0.0$, $s = 0.0$, $\tau_R = 0.0$ the explosions happen equally likely to both sides. The net gain is set to $\delta = -0.3$. (b) For small third order dispersion $\beta_3 = 0.001$ explosions are favored to the left. The net gain is set to $\delta = -0.45$. (c) For larger third order dispersion $\beta_3 = 0.01$ explosions are favored to the right. The net gain is set to $\delta = -0.5$. If not stated otherwise, the remaining parameters are $\epsilon = 1.0188$, $\mu = -0.1$, $\nu = -0.6$, $\beta = 0.125$, $D = 1$, $s = 0.009$ and $\tau_R = 0.032$. A similar version of this figure was used in [4].

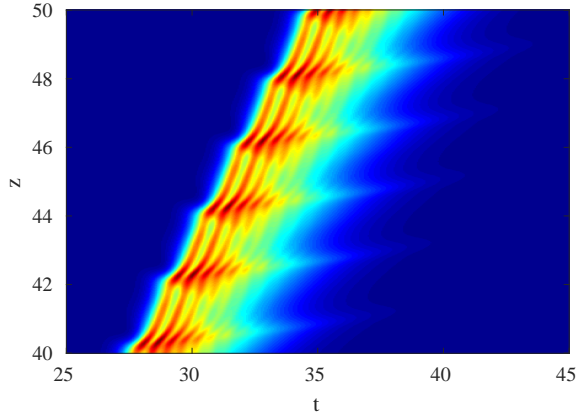


Figure 5.16: Space-time diagram of an oscillating breather soliton solution in the complex quintic-cubic Ginzburg-Landau equation under the influence of third order dispersion. The TOD induces a serrated temporal intensity profile of the soliton that asymmetrically trails off to the right side due to the TOD coefficient being positive. Like in the VCSEL-RSAM example from Fig. 5.14 the oscillations on the small intensity side reach their maxima increasingly late as compared to the main pulse. Parameters are $\delta = -1.0$, $\epsilon = 1.0188$, $\mu = -0.1$, $\nu = -0.6$, $\beta = 0.125$, $D = 1$, $\beta_3 = 0.075$, $s = 0.0$ and $\tau_R = 0.0$. A similar version of this figure was used in [4].

Note that the model (5.36) does not include carrier dynamics. In contrast to the VCSEL-RSAM model, the absorber carriers have been assumed to react to the electric field instantaneously and have been adiabatically eliminated. The gain carriers on the other hand have been assumed to react slowly and have been averaged out. Notwithstanding, the dynamics of the CCQGLE bear some striking resemblance with the satellite instability discussed before. This reinforces the notion that the satellite instability is induced principally by TOD. The unidirectional ring model does contain carrier dynamics but not TOD and such instabilities are not found.

6 Mode-locked Integrated External-Cavity Surface-Emitting-Laser

This chapter describes the results obtained for the MIXSEL system that can be viewed as a simplified version of the VCSEL-RSAM system. Compared qualitatively, the single microcavity design removes the detuning δ between the coupled microcavities as well as the ratio of their bandwidths κ_j . However, the cavity geometry still induces TOD in the same way. Thus, the system exhibits the same types of behavior, specifically pulses can have satellites that cause instabilities or strongly influence oscillatory dynamics. Due to the smaller number of variables and the reduced parameter set the satellites are easier to analyze and bifurcation analysis was possible within limits. Some of the results presented in this chapter have been published in [7].

6.1 Lasing threshold

To calculate the lasing threshold of the MIXSEL model (2.248)–(2.251) we start with the continuous wave ansatz $E(t) = E_0 e^{-i\omega t}$ with the frequency shift ω and the constant electric field amplitude E_0 in the microcavity. The carrier evolutions are assumed to have reached the corresponding steady equilibrium state so we have

$$-i\omega E_0 = [(1 - i\alpha_1)N_1 + (1 - i\alpha_2)N_2 - 1] E_0 + hY, \quad (6.1)$$

$$0 = \gamma_1(J_1 - N_1) - |E_0|^2 N_1, \quad (6.2)$$

$$0 = \gamma_2(J_2 - N_2) - s|E_0|^2 N_2, \quad (6.3)$$

$$Y = \eta[E_0 - Y]e^{i\omega\tau}. \quad (6.4)$$

In this case the injection field Y can easily be solved for E

$$Y = \frac{\eta e^{i\omega\tau}}{1 + \eta e^{i\omega\tau}} E_0, \quad (6.5)$$

ready to be substituted in the field evolution equation. The amplitude E_0 remains only as a linear factor and can thus be discarded to reach the CW condition

$$0 = (1 - i\alpha_1)N_1 + (1 - i\alpha_2)N_2 - 1 + i\omega + \frac{h\eta e^{i\omega\tau}}{1 + \eta e^{i\omega\tau}}. \quad (6.6)$$

The field amplitude still appears implicitly since the carrier inversions N_j are functions of it. For the threshold we have to consider the low intensity limit $|E_0| \rightarrow 0$ where the carriers simply equilibrate to their respective bias values $N_j = J_j$. We will separate the modulus and complex phase of the feedback parameter $\eta = |\eta|e^{i\psi}$ so we can reduce the

number of complex expressions in the time-delayed feedback term in the CW condition to one which simplifies the interpretation of this fraction in the following. After separating the real and imaginary parts of the remaining equation we have

$$0 = (J_1 + J_2 - 1) + i(\omega - \alpha_1 J_1 - \alpha_2 J_2) + \frac{h|\eta|}{e^{-i(\omega\tau+\psi)} + |\eta|}. \quad (6.7)$$

This can be simplified by introducing the natural frequency shift of the unsaturated microcavity $\omega_0 = \alpha_1 J_1 + \alpha_2 J_2$ and the remainder $\Delta\omega = \omega_0 - \omega$

$$J_1 = 1 - J_2 - i\Delta\omega - \frac{h|\eta|}{e^{-i(\Delta\omega\tau+\varphi)} + |\eta|}, \quad (6.8)$$

with the shifted feedback phase $\varphi = \omega_0\tau + \psi + 2\pi\mathbb{Z}$ where we can choose an appropriate integer to limit its value into a single cycle $|\varphi| \leq \pi$.

We now need to find the external cavity modes ω_k that solve this relation to give a real valued J_1 . The smallest $J_1(\omega_k)$ will then define the lasing threshold. In the long delay limit $\tau \rightarrow \infty$ the external cavity modes become a pseudo-continuous spectrum, i.e., the distance to the neighboring external cavity modes vanishes. One can produce an arbitrary finite phase in the feedback term with an infinitesimally small $|\Delta\omega| \sim \frac{\varphi}{\tau} \leq \frac{\pi}{\tau}$ to counteract the phase of the $-i\Delta\omega$ term in Eq. (6.8). Therefore, we may safely set $|\Delta\omega| \rightarrow 0$ and $\Delta\omega\tau = -\varphi$ and see that ω_0 is indeed the threshold mode yielding the minimal

$$J_1^{(th)} = 1 - J_2 - \frac{h|\eta|}{1 + |\eta|}. \quad (6.9)$$

6.2 Satellite instability

To analyze the satellites and their instabilities in the MIXSEL system we choose a set of parameters with a focus on instructiveness over experimental feasibility. The time scales still need to have realistic ratios but we may choose simple numbers. For the carrier relaxation rates we use $\gamma_1 = 3 \times 10^{-3}$ for the gain and $\gamma_2 = 0.1$ for the saturable absorber. Assuming a photon lifetime of $\tau_c = 3$ ps this corresponds to carrier relaxation times of 1 ns and 30 ps, respectively. A delay value of $\tau = 1000$ then corresponds to a 3 ns external cavity roundtrip time. Most of the remaining parameters are chosen in order to emphasize the first order satellite in order to showcase the general pattern of behavior. The case of a perfect bottom DBR is experimentally sound and yields the simple value $h = 2$ for the injection coupling. An absorber bias of $J_2 = -0.5$ gives a very strong modulation of 88.9%. Along with this the saturation ratio $s = 10$ is also chosen to be relatively large so the absorption becomes easy to saturate in spite of its strength. With these values we get very pronounced modulation and hence a very wide range of bistability of pulses with the off solution. In this situation of otherwise very stable pulses we can make a clear case for the destabilization due to satellites. The feedback attenuation factor is chosen quite low $\eta = 0.7$. This causes the higher order satellites to be strongly damped and only the first satellite to remain relevant. A higher η close to one is interesting for the experimental case as it minimizes linear losses where gain and absorber modulation are limited. However,

with $\eta \approx 1$ the dynamics can involve several orders of satellites that interact with the main pulse and each other via inversion saturation and amplitude-phase coupling. While originating from the same principle, the resulting dynamics are very complex and thus difficult to interpret.

The pure form of the satellite instability appears for vanishing linewidth enhancement factors $\alpha_1 = 0$ and $\alpha_2 = 0$ where the satellites are fully developed, unperturbed by the effects of chirp broadening. Figure 6.1 shows the dynamics obtained for a gain bias of $J_1 = 0.65$ and a delay time of $\tau = 1000$. This bias corresponds to about 96.1% of the

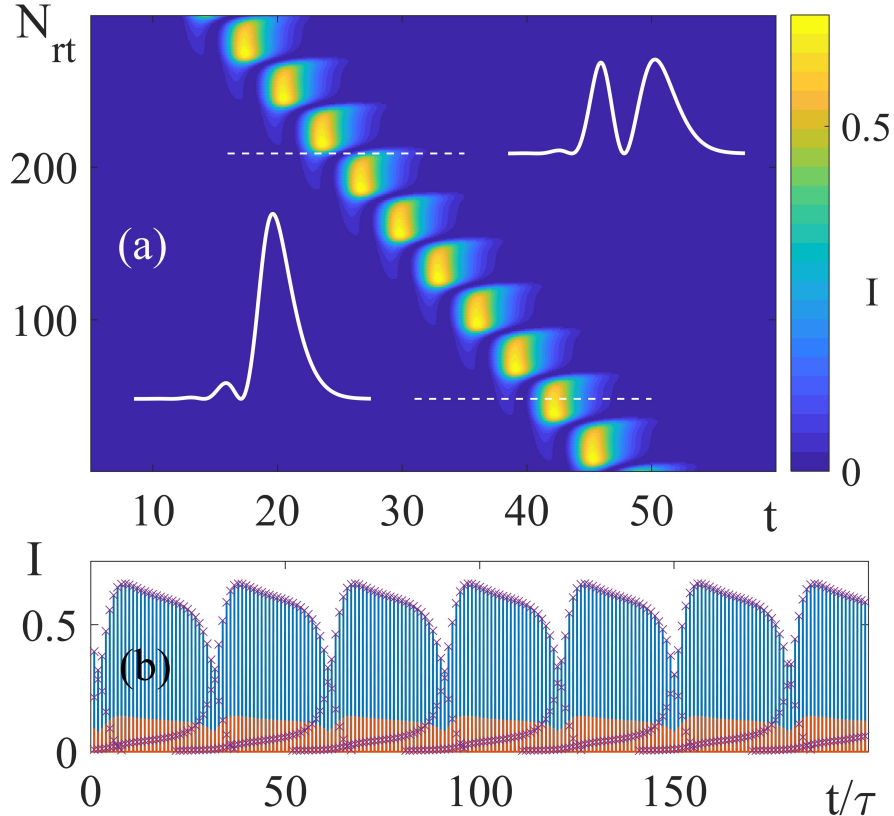


Figure 6.1: Pure satellite instability dynamics for zero linewidth enhancement factors $\alpha_1 = \alpha_2 = 0$. A sufficiently large satellite in front of the main pulse is able to open a premature net-gain window and becomes unstable. The satellite grows into a new full pulse thereby replacing its parent pulse that is deprived of gain. (a) Pseudo-space-time diagram where a staggered forward movement of the pulse becomes apparent, similar to Fig. 5.7. (b) Time trace with intensities of the microcavity field $|E|^2$ in blue and of the injection field $|Y|^2$ in orange. The replacement oscillations are visible as dips in the intensity. The local intensity maxima are highlighted by purple crosses where the early satellite growth becomes visible. Other parameters are: $J_1 = 0.65$, $\tau = 1000$. A similar version of this figure was used in [7].

threshold value $J_1^{(\text{th})} \approx 0.6765$. Panel (a) shows a pseudo-space-time diagram where the intensity profiles $I = |E|^2$ of the microcavity field are stacked for each roundtrip N_{rt} . The pulse performs a forward staggering movement that appears as of a series of jumps. In front of the pulse a small satellite exists due to a higher order dispersive effect caused by the cavity geometry as explained in Section 5.3.1. For the given parameters this satellite is large enough to saturate the absorber sufficiently on its own to open a premature net-

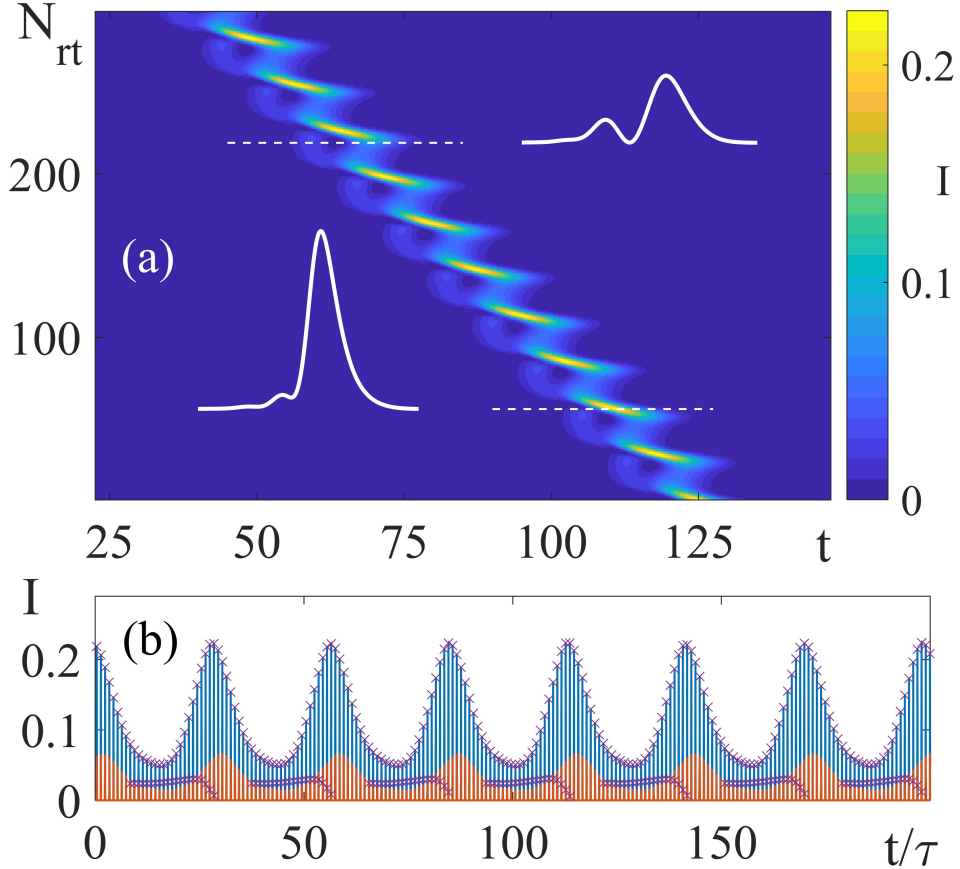


Figure 6.2: Satellite influenced quasi-periodic dynamics for realistic linewidth enhancement factors $\alpha_1 = 2.1, \alpha_2 = 0.5$. A satellite separates from main pulse on the leading edge at about half of the maximum intensity. Both the satellite and main pulse grow and separate more until the main pulse is attracted by its satellite and moves forward quickly. The main pulse grows very quickly while the satellite disappears again. Finally the main pulse shrinks back and the cycle begins anew. This dynamics results from a mix of the satellite instability and amplitude-phase coupling. (a) Pseudo-space-time diagram of the dynamics. (b) Time trace with intensities of the microcavity field $|E|^2$ in blue and of the injection field $|Y|^2$ in orange. The local intensity maxima are highlighted by purple crosses. Other parameters are: $J_1 = 0.65, \tau = 1000$. A similar version of this figure was used in [7].

gain window and consequently builds up more intensity over many roundtrips. Finally the satellite erupts exponentially and grows to the same size and shape of its parent pulse. Due to the increased gain saturation the parent is deprived of gain and dies, thus being replaced by its satellite. The main pulses remain mostly unchanged until their satellites start to grow quickly. This dynamics corresponds to Figure 5.7 for the closely related VCSEL-RSAM system discussed in the previous chapter. Panel (b) shows the corresponding time trace of the microcavity field intensity $|E|^2$ in blue and the injection field intensity $|Y|^2$ in orange. The local maxima of the $|E|^2$ pulse profiles are highlighted with purple crosses. This makes the slow build-up of the satellites visible. Otherwise, the dynamics only appear as dips in the intensity.

This constitutes the pure satellite instability that causes a stable pseudo-periodic orbit as the pulse replacement repeats in an almost constant number of roundtrips. One can define the moment of replacement as the roundtrip where the satellite has outgrown the parent. Due to the non-continuous characteristics of dynamics per roundtrips only an average period of the oscillation can be defined. One cycle takes some minimum number of roundtrips N_p but will sometimes need one more. This holds in the absence of noise; the effects of noise on the period are discussed in Section 6.6. For a barely unstable satellite very close above the bifurcation point causing this instability the growth phase of the satellite can become very large and can even diverge to infinity as discussed in Section 6.5.

For realistic linewidth enhancement factors the satellite instability does not appear in the pure form described above. The chirp broadening due to amplitude-phase coupling often interferes with a clean separation of the main pulse and its satellites. However, the dynamics of the pulse can be influenced by satellites significantly. A pulse that oscillates significantly in its energy causes varying saturations of the carrier inversions and thus is exposed to varying amounts of amplitude-phase coupling in turn. Figure 6.2 shows results from direct numerical simulations with realistic values for the linewidth enhancement factors $\alpha_1 = 2.1$ and $\alpha_2 = 0.5$. The peak intensity time trace of the pulse appears to oscillate almost harmonically when compared to the case of the pure satellite instability discussed above. However, when looking at the full intensity profile of the pulse this oscillation looks very different from the trailing edge instability caused by amplitude-phase coupling. When the pulse is small a satellite separates from the leading edge of the pulse with about half the peak intensity at that time. The parent pulse then grows again while its newborn satellite dies out. During this phase the pulse changes its drift velocity significantly and moves quickly to the position where the satellite had been. This separation and the subsequent attraction is one example of the interplay of amplitude-phase coupling and higher order dispersion due to cavity geometry. Depending on the combination of the linewidth enhancement factors these dynamics have rather different shapes but they all contain satellite dynamics mixed into the oscillations.

6.2.1 Bistability

Stable pulsation and satellite influenced oscillations can be bistable for certain parameter regions. For $\alpha_1 = 1$ and $\alpha_2 = 0$ a stable quasi-periodic orbit exist that can be reached by lowering the gain bias from above the lasing threshold. Figure 6.3 shows a pseudo-space-time diagram depicting both the stationary and stably oscillating pulse solutions.

Indeed the two pulses are TLSs coexisting in a single long external cavity with a roundtrip time of $\tau = 10000$. The diagram is adjusted using the period of the stationary TLS thus highlighting the difference in the respective drift velocities. Compared to the cavity length this drift would only be important on macroscopic timescales where the TLSs would finally run into each other. For the purpose of illustration the time between the TLS is trimmed. The pulses are really much further apart and do not interfere with each other. The stationary pulse is comparatively small and has no satellites. The oscillating pulse has a larger peak intensity is lead by a series of satellites. The first satellite grows significantly and attracts the main pulse that at some point quickly moves forward and merges with its satellite into a large intensity pulse situated at the former satellites position. At the same time the next satellite starts growing. This is likely triggered by the overgrown pulse loosing photons to the next order satellite due to the cavity geometry. Thus, the satellite becomes large enough to open a net-gain window and keep growing thereby starting the next cycle. This scenario is the basic version of the one presented in Figure 5.13 for the

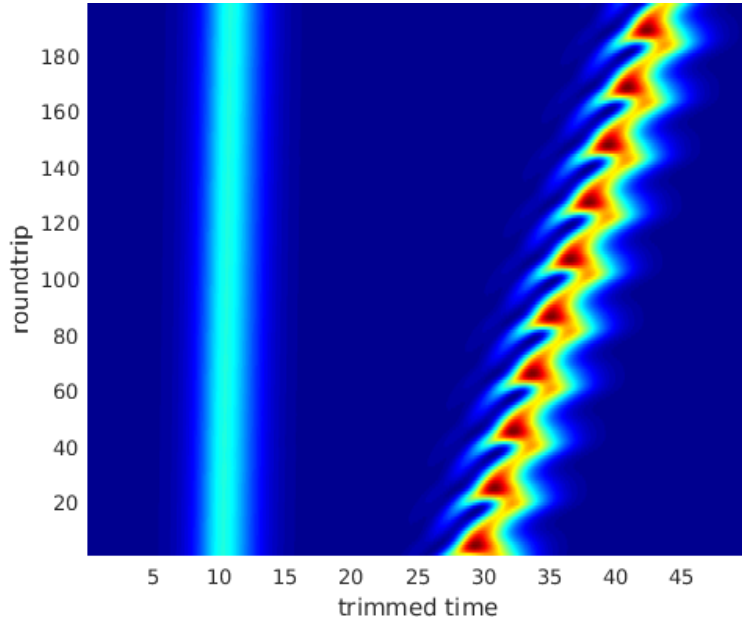


Figure 6.3: Pseudo-space-time diagram for $\alpha_1 = 1$, $\alpha_0 = 0$ in a long cavity $\tau = 10000$. A stable TLS and another stably oscillating TLS exist in the same cavity with the oscillating one having significantly higher energy overall and has leading satellites. The first satellite grows until the parent moves toward it and they merge into a single high energy pulse at the former position of the satellite. The large pulse then shrinks again, the next satellite grows and the process repeats. This behavior is similar to Fig. 5.13. Time is trimmed around the TLS for the sake of illustration and the snapshot interval is set to period of the stable pulse. The TLS are actually much further apart and do not interact with each other. Though the drift of the TLSs is not the same, traversing the actual distance would take a very large number of roundtrips.

VCSEL-RSAM system. The difference to the pure satellite instability is the non-zero gain linewidth enhancement factor. The chirp resulting from increased amplitude-phase coupling has a tendency to broaden the enlarged pulse. In stable pulses this typically suppresses the satellites. The attraction to its satellite can be explained by the TLS trying to focus its energy in order to saturate the losses more efficiently.

Figure 6.4 shows time traces corresponding to the pseudo-space-time diagram in Fig-

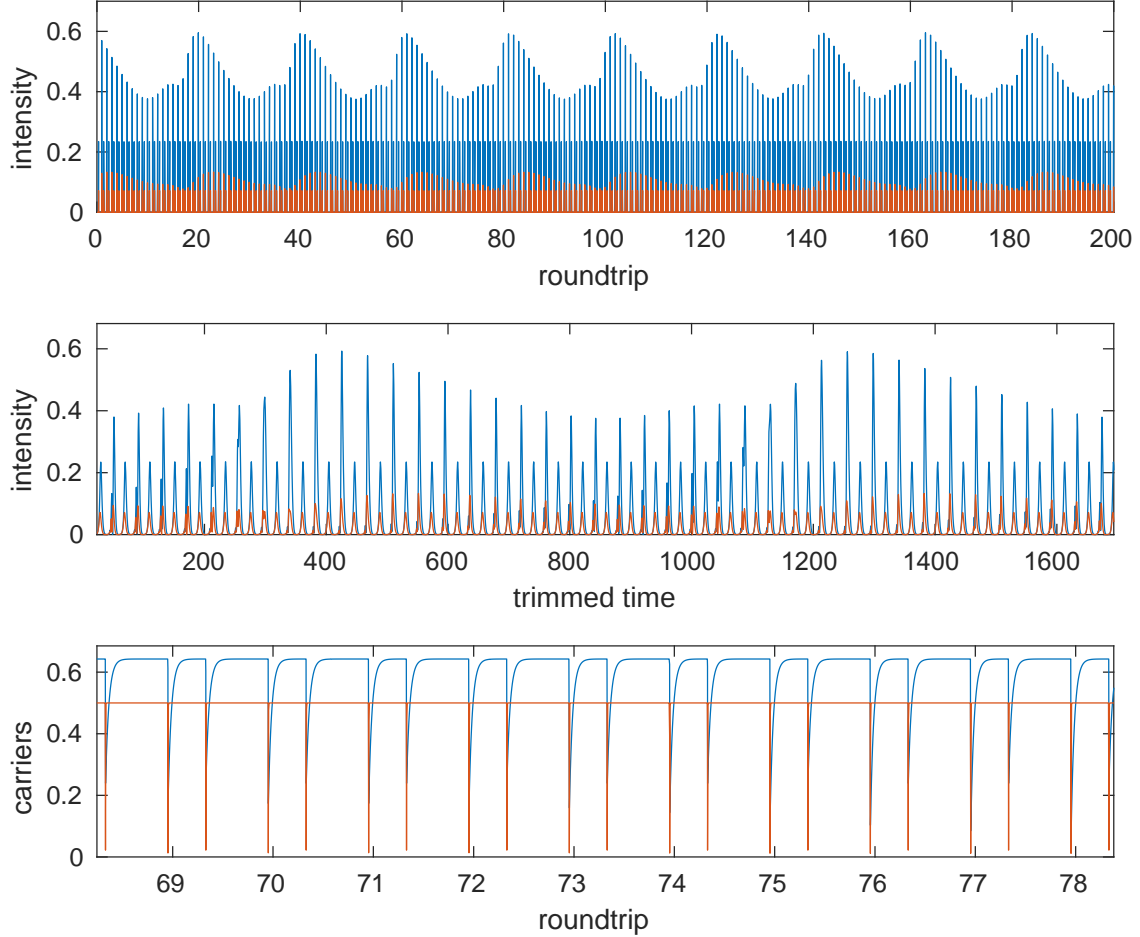


Figure 6.4: Full time trace of the bistable TLSs presented in the previous Fig. 6.3. (upper panel) The intensities of microcavity field $|E|^2$ are depicted in blue and of injection field $|Y|^2$ in orange. The larger of the TLS is oscillating under the influence of a growing satellite. (middle panel) Time is trimmed around the pulses to reveal details of the dynamics. The growing satellite merges with the main pulse causing the observed oscillation in peak intensity. (lower panel) The carrier inversions of the gain in blue and the absorber in orange. Due to the very long cavity both inversions have sufficient time to fully relax before the other pulse arrives. This illustrates that both pulses are in the localized regime. Other parameters are: $\alpha_1 = 1$, $\alpha_0 = 0$, $\tau = 10000$.

ure 6.3. In the upper panel the full time trace for several periods is presented by the intensity of the microcavity field $|E|^2$ in blue and of the injection field $|Y|^2$ in orange. The oscillation features an intensity bump on rising side before reaching the maximum and is clearly far from harmonic. Interspersed, the stationary pulse remains at a constant intensity. The middle panel shows the pulses with the time in between cut out so the full profiles including the satellites remain visible. The growth of the satellite can be observed as well as the subsequent merging with the main pulse which significantly grows in peak intensity as a consequence. The lower panel shows the carrier inversions of the gain in blue and of the absorber in orange. The cavity is large enough for the carrier inversions to fully relax after each of the pulses, i.e., both are in the localized regime and do not feel each other.

6.2.2 Regions of dynamical behaviors

Figure 6.5 shows results obtained from DNS with a delay of $\tau = 1000$. Two dimensional parameters scans were performed in the gain bias J_1 normalized to the lasing threshold J_1^{th} and linewidth enhancement factor α_1 . From a common starting point for two types of stable pulses the scans worked through the parameter space continuously by using the final state of one point as the initial state of the next neighboring point. The off solution could be easily detected by the integrated pulse intensity dropping below a small critical value. Pulses can be distinguished using the time series of their peak intensities per roundtrip. Stable pulses are characterized by a constant value each. For oscillations the extrema of the peak intensity form clusters. Normal oscillations have a pair of values that just stem from the minimum and maximum while higher order oscillations have four clusters for period doubling, six for period tripling and so on. Finally for quasi-periodic oscillations of the pulses the extrema fill an interval. These analyzes can be automated to obtain a 2d-diagram of the different regions. By looking at the respective time traces one can then characterize these regions.

The off solution is shown in blue and a large region of stable pulses is shown in cyan. These pulses behave, for the most part, similarly as the ones in the unidirectional ring model discussed in Chapter 4 (cf. especially Fig. 4.18). They are largest for low α_1 and become Andronov-Hopf unstable for large α_1 . This instability is virtually identical to the trailing edge instability with the main differences that the bifurcation is supercritical everywhere and a small part of the oscillating region overlapping the stable pulse region which is depicted in bright green. Dynamically this oscillation looks basically the same in both models. Unlike in the ring model, however, the high intensity pulses at the low α_1 edge exhibit a series of leading satellites that originates from the cavity geometry as discussed in Section 5.3.1. An exemplary intensity profile of such a pulse is shown in Figure 6.5 just in front of the satellite instability region. The first of these satellites becomes unstable for a sufficiently large gain bias thus causing the satellite instability discussed at the beginning of this section. At the border of the unstable region, again, we find a small part that is bistable with the underlying stationary pulse and is drawn in pink. In the unidirectional ring model a series of higher order pulses with an increasing number of bumps on the leading edge was found by means of numerical path continuation but not in simulations since all of them remained unstable for the chosen parameter ranges. The

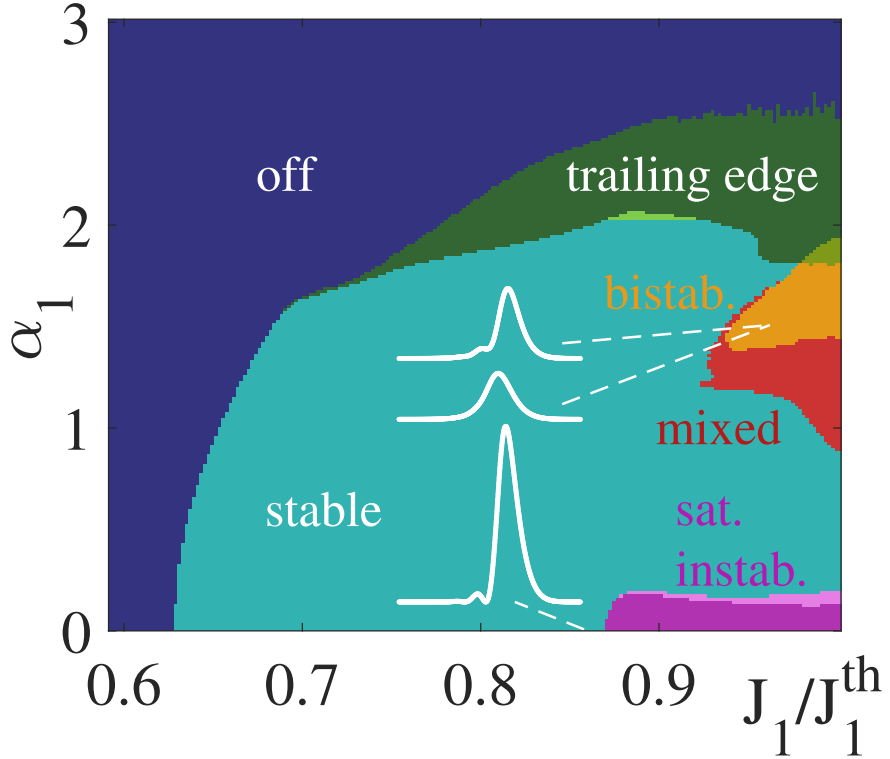


Figure 6.5: Bifurcation diagram showing the regions of dynamical behaviors. The off solution is presented in blue and stable pulses in cyan. At high α_1 the area in green marks the trailing edge instability. The purple region at low α_1 represents the pure satellite instability. The stable pulse profile in front of it exhibits a leading satellite that is responsible for this instability. Parts at the edges of both instabilities are bistable with the stable pulse background. An additional larger stable pulse exists in the orange region for medium gain and α_1 values. It is bistable with the smaller pulse, i.e., the cyan region extends up to threshold underneath. Two pulse profiles at the same parameters are shown where the upper profile corresponds to the orange region and the middle profile to the cyan region, respectively. The pulse of the orange region starts to oscillate for lower α_1 which is indicated in red. This oscillation shows mixed characteristics of the other two. Where regions overlap otherwise the colors are blended. The delay time used in the DNS was $\tau = 1000$. A similar version of this figure was used in [7].

first additional (single bump) solutions were born in a saddle-node bifurcation that in turn began in a cusp bifurcation as shown in Figure 4.15. In the MIXSEL model we can find such single bump solutions to be stable with an example profile presented in Figure 6.5. These pulses are indeed bistable with the smaller pulses belonging to the underlying cyan region. The respective profile of the small pulse at the same parameters is shown below the single bump solution for comparison. The region of existence of the bistable single bump

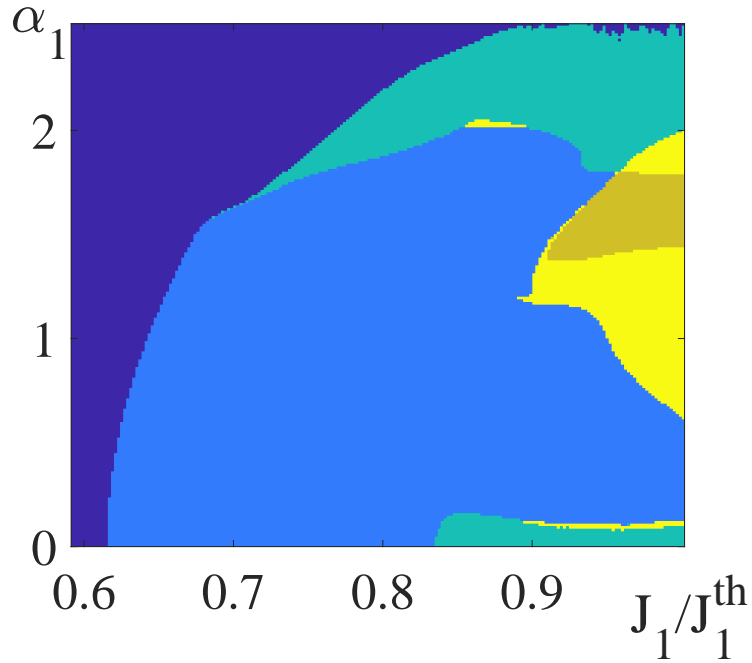


Figure 6.6: Bifurcation diagram obtained from DNS using the functional mapping in the long delay limit. Blue means off, cyan stable pulses and green oscillation. The brown area indicates the existence of two different bistable pulses and yellow where either of them is oscillating. Due to the long cavity the pulses experience more effective gain than in Fig. 6.5 and the bifurcations appear a bit earlier. However, there are no qualitative differences indicating that $\tau = 1000$ is already close to the localized regime.

pulse is shown in orange and red and shares the cusp shape of the ring model. Orange stands for this pulse being stationary while in the red, lower α_1 part of the region it is oscillating. This oscillation has mixed characteristics of both amplitude-phase coupling and satellite dynamics and the example of the previous subsection is directly related to it. The overlap with the trailing edge instability at larger α_1 is color-blended. Here, the situation is the reversed, i.e., the single bump pulse is stable while the simple pulse is oscillating.

Figure 6.6 shows results for similar two dimensional parameter scans using the functional mapping approach corresponding to an infinite delay time $\tau \rightarrow \infty$ where the TLS are perfectly localized. The data was processed in the same way as described above. Blue stands for the off-solution, light blue marks the stable principal TLS and green means oscillations. Bistability is indicated with ochre for two stable pulses and yellow where either is oscillating. The example of the previous subsection can be considered to be a single point of this diagram. Due to the longer relaxation time of the carrier inversions the effective gain is slightly higher than in the previous case for $\tau = 1000$. Thus, the solution manifolds and bifurcations move toward smaller normalized gain bias. Pure TLS do not add anything qualitatively new so $\tau = 1000$ is sufficient to analyze them.

6.3 Numerical path continuation

This section is on the results obtained using the singular perturbation approach discussed in Section 3.5 and its limitations.

6.3.1 Typical pulse profiles

The singular perturbation approximation necessitates the introduction of an additional stiffness factor $1/\epsilon$. For $\epsilon = 1/30$ the solutions obtained with DDE-BIFTOOL reproduce DNS with high fidelity. Figure 6.7 shows results obtained from both direct numerical simulation and numerical path continuation for comparison. The parameters of the presented TLS are $J_1 = 0.55$ for the gain bias and vanishing linewidth enhancement factors $\alpha_j = 0$. The rest of the parameters are the same as introduced in the previous section. In order to reach the localized regime the delay time was set to $\tau = 2000$ which leaves a residual gain saturation of circa $\exp(-\gamma_1\tau) = \exp(-6) \approx 0.25\%$ after one roundtrip. Note, that the time interval of these state vectors is not exactly the same. For the DNS it is fully defined by the delay time τ while in the continuation a full periodic orbit with period

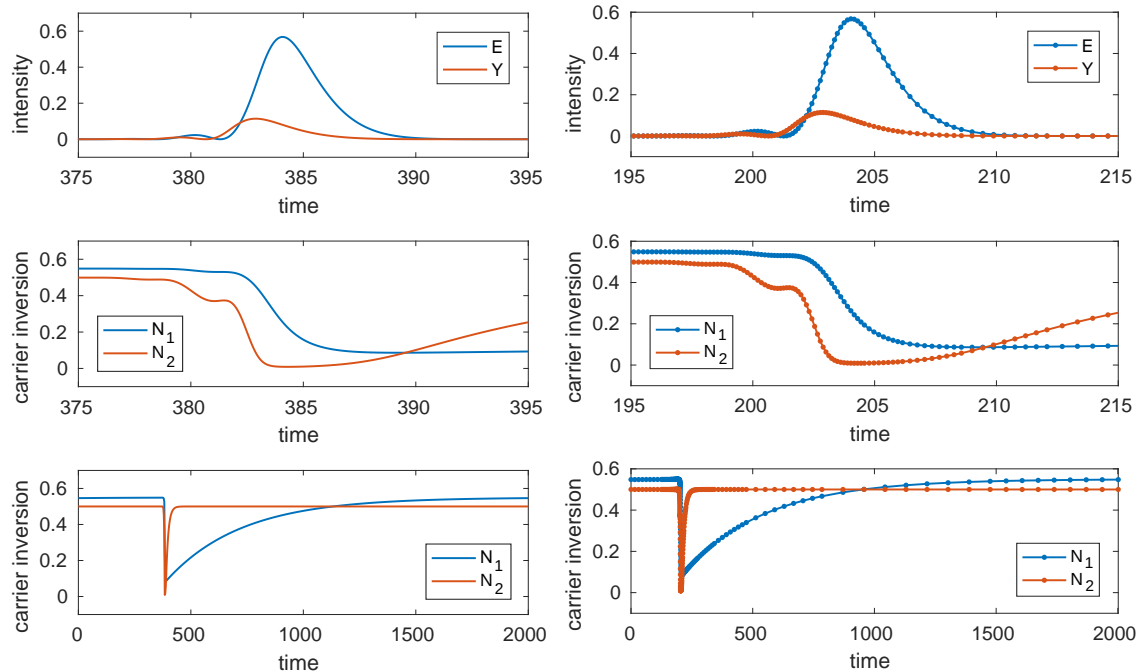


Figure 6.7: Comparison of temporal profiles of TLS obtained from direct numerical simulation (left column) and from numerical path continuation (right column). (upper row) Zoom on the intensity profile around the pulse. The first satellite is clearly visible. (middle row) Carriers inversions in the zoom interval. The saturation occurs in steps which is clearly visible for the absorber. (lower row) Carriers inversions for the full roundtrip. They relax virtually to the bias values indicating that the localized regime is already reached.

$T > \tau$ has to be considered. Interestingly, the carriers do not only saturate in steps but the absorber even slightly recovers between the first pulse and its parent indicating their clear separation in the zero linewidth enhancement case.

DDE-BIFTOOL uses mesh adaption to represent periodic orbits efficiently. Indeed, the computational effort of its algorithms does not scale favorably with the overall system size and calculations of whole branches of the TLS at interest already take significant amounts of time. Thus, the mesh points are mostly concentrated at and in front of the main pulse where the stiffness of the system comes into play. They are needed for a good resolution of the satellites while the quasi-exponential relaxation of the gain carrier inversion needs very few mesh points in comparison. This, however, has negative repercussion concerning stability analysis as discussed at the end of this section. The details of the series of leading

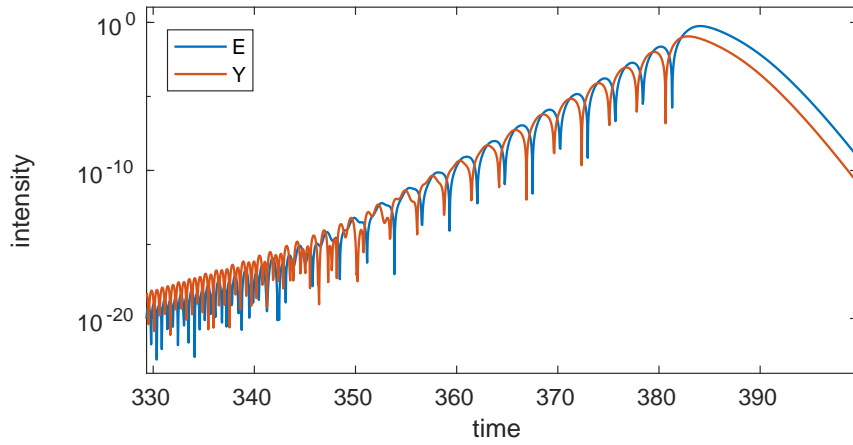


Figure 6.8: Zoom on the temporal intensity profile of the pulse in log scale obtained from direct numerical simulation. The satellites continue down continuously but interfere with the training edge due to periodic boundary conditions.

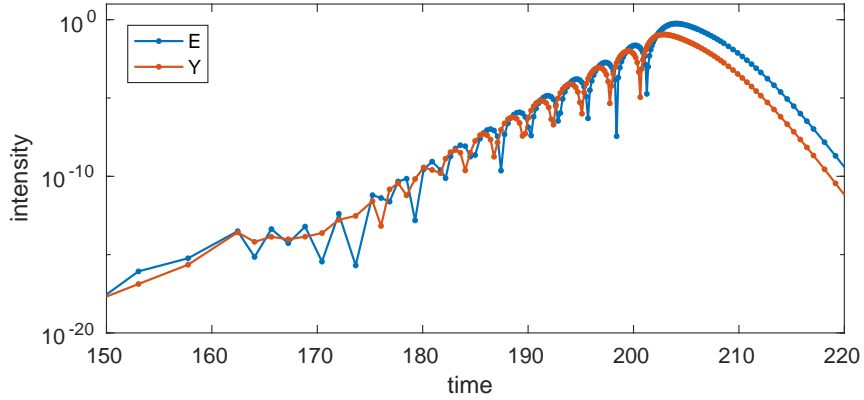


Figure 6.9: Zoom on the temporal intensity profile of the pulse in log scale obtained from numerical path continuation. The low order satellites are fully resolved. For high order satellites the resolution is not sufficient which is irrelevant in practice.

satellites is most readily visible in log scale. In DNS the satellites go all the way down until they feel the trailing edge of their parent pulse as can be seen in Figure 6.8. Only the high order satellites are not fully resolved by the numerical continuation, see Figure 6.9. In practice, this is of no concern.

6.3.2 Singular perturbation convergence

The convergence of the pulse profile with $\epsilon \rightarrow 0$ is rather fast as can be seen in Figure 6.10. For $\epsilon = 1/10$ the first five satellites are already clearly developed. At $\epsilon = 1/30$ there is virtually no more change to the intensity profile of the higher order satellites while the resolution becomes a limiting factor as we saw in the previous subsection. Before the first satellite enters the microcavity the higher order satellites use up some gain inversion. However, the convergence error in their influence on the onset of the satellite instability becomes negligible very quickly. Thus, considering the first satellite a value of $\epsilon = 1/20$ appears justified and was used in the following analysis of its effects.

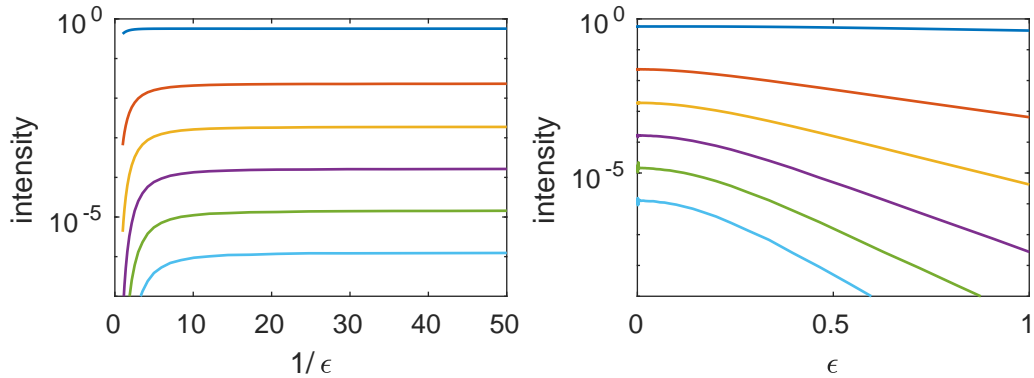


Figure 6.10: Convergence of the intensity maxima of the pulse profile in the singular perturbation approximation of the delay algebraic term. The smaller, higher order satellites converge slower but, over all, the convergence of the profile is quite fast.

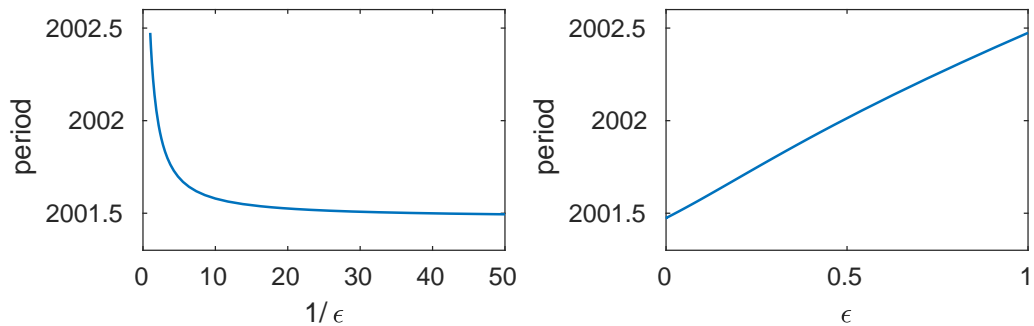


Figure 6.11: The period of a TLS converges virtually one to one with the singular perturbation smallness factor ϵ . This is equivalent to a small artificial increase of the drift.

The singular perturbation also has an effect on the period of a TLS solution that is shown in Figure 6.11. It acts as an artificial filter whose inertia causes some additional drift of the pulse. For small ϵ this turns out to be simply a one to one relation $\delta T \approx \epsilon$. This additional drift is not physical but it does not create any problems in the localized regime where the additional carrier relaxation is negligible.

6.3.3 Stability limitations

The long cavity needed for TLS in conjunction with the singular perturbation approximation results in a very large stiffness proportional to τ/ϵ . As a consequence, profile continuation is only feasible by using mesh adaption such that points are far apart in most of the interval. Typically, there is not enough resolution to accurately represent the Floquet modes of a given solution and thus the linear stability analysis in DDE-BIFTOOL becomes spurious. Several Floquet multipliers move in a highly erratic and non-continuous fashion when continuing a branch of solutions or even when recorrecting a solution after optimizing its mesh. Often the multipliers jump in and out of the unit circle thus wrongly indicating bifurcations. Figure 6.12 shows an example to illustrate this issue. Consequently, continuation of bifurcations of periodic orbits in the long cavity regime was not possible in combination with the singular perturbation approximation.

6.3.4 Folding solution branch

The branch belonging to the TLS that undergoes the satellite instability can be followed via numerical path continuation. It folds back and forth several times as can be seen in Figure 6.13 for the zero linewidth enhancement case $\alpha_1 = \alpha_2 = 0$. In this example the delay was set to $\tau = 1000$ and the singular perturbation parameter $\epsilon = 1/20$. The stability can be determined by comparison with results obtained in direct numerical simulations.

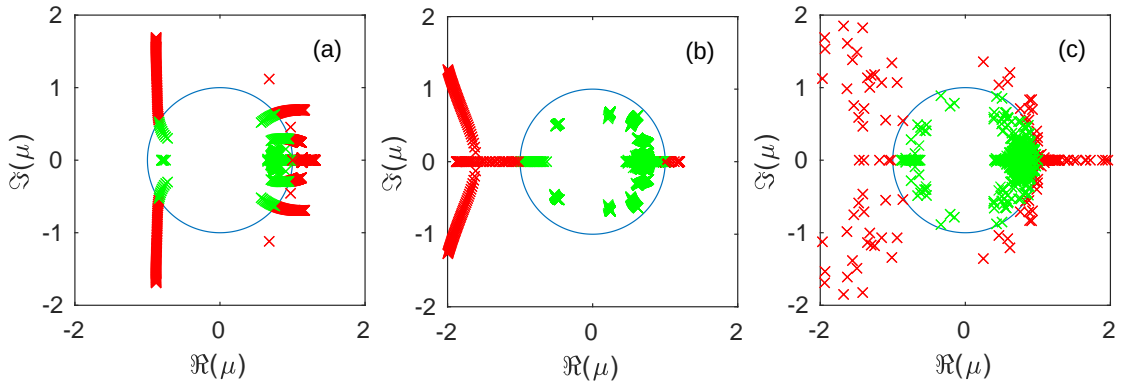


Figure 6.12: Floquet analysis of a branch along the interval $\epsilon \in [0.001, 1]$. All Floquet multipliers of all solutions along the branch are shown simultaneously. (a) and (b) show path continuations from different starting points without mesh adaption. Though both represent the same branch, the spectra are qualitatively very different. (c) With enabled mesh adaption the spectrum behaves erratically along the branch.

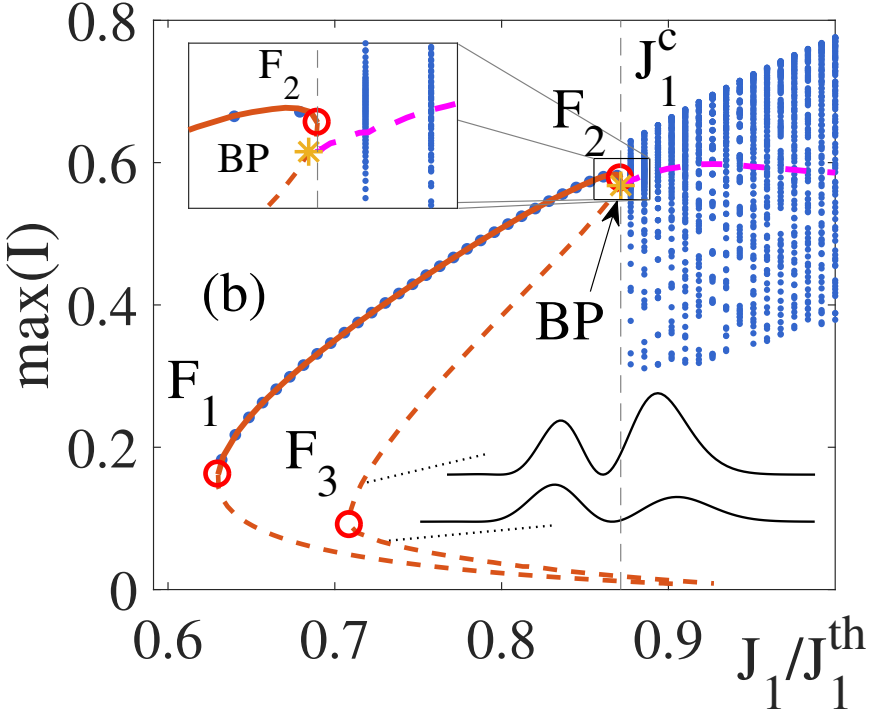


Figure 6.13: Bifurcation diagram for zero linewidth enhancement factors $\alpha_1 = \alpha_2 = 0$. The TLS branch obtained from continuation is shown in orange with a solid line where stable and dashed where unstable. It folds back and forth several times indicated by the red circles. The extrema of corresponding peak intensity time traces obtained from DNS are superposed as blue dots. The first fold \mathbf{F}_1 limits the bistable TLS region. The second fold \mathbf{F}_2 lies where the satellite instability sets in abruptly with full amplitude at the critical gain current J_1^c . Shortly after, an additional degenerate unstable branch drawn as a dashed magenta line appears at the branching point \mathbf{BP} marked by a yellow star. At the third fold \mathbf{F}_3 the peak intensity of the first satellite surpasses that of the parent pulse. Other parameters are $\epsilon = 1/20$ and $\tau = 1000$. A similar version of this figure was used in [7].

On the low gain side the bistable TLS region is limited by a typical saddle-node \mathbf{F}_1 . The satellite instability starts at a critical gain bias J_1^c with instantly full amplitude and coincides with the second fold \mathbf{F}_2 . This indicate that it does not stem from an Andronov-Hopf bifurcation. After the last fold \mathbf{F}_3 the peak intensity of the satellite has become larger than that of the parent pulse. A corresponding profile is shown in detail in Figure 6.14.

After the second fold an additional branch appears at the branching point \mathbf{BP} . This branch is degenerate with a complex conjugate pair of nonzero frequency shift in spite of the vanishing linewidth enhancement while for $\alpha_1 \neq 0$ it has two different parts. In the $\alpha_2 = 0$ case the system is symmetric in α_1 via complex conjugation, making the two parts switch with each other. The degenerate case is where these two parts cross over, i.e., \mathbf{BP} marks a transcritical bifurcation.

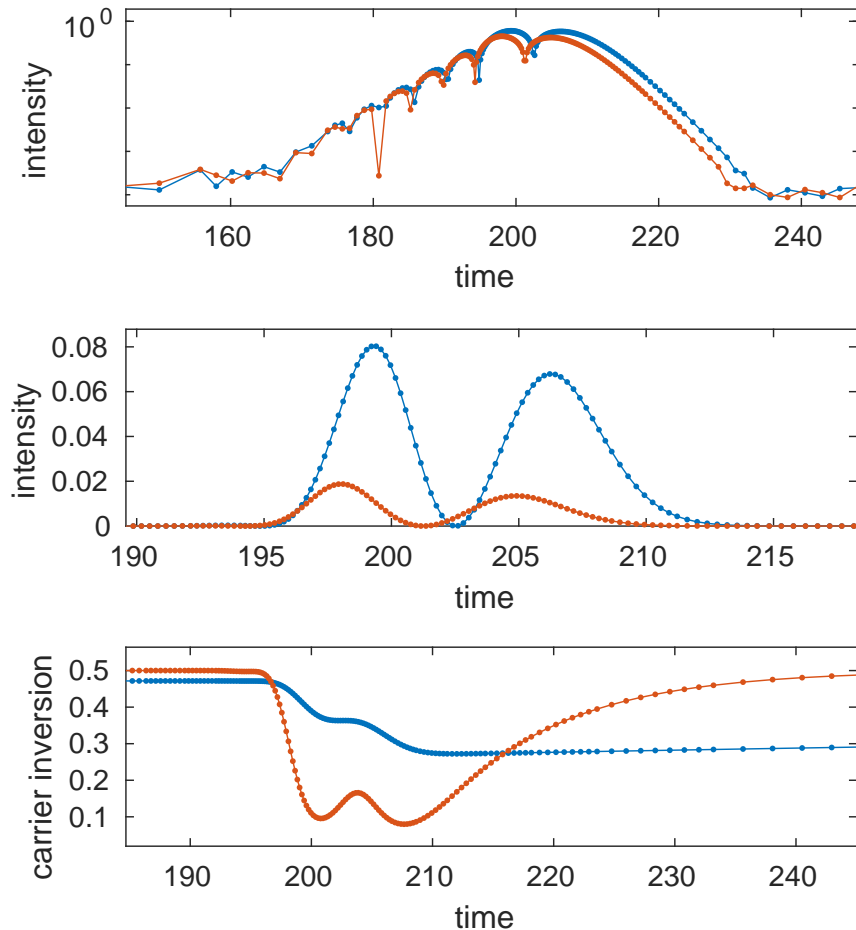


Figure 6.14: Unstable pulse profile shortly after the third fold \mathbf{F}_3 in Fig. 6.13. The peak intensity of the first satellite has superseded the main pulse. The two large peaks are far apart and the absorber saturation relaxes significantly in between.

6.4 Linear stability analysis using the functional mapping

This section describes a first attempt to implement linear stability analysis using the functional mapping in the long delay limit. It is inspired by Floquet theory, however, it should not be considered mathematically rigorous nor complete. Furthermore, some Floquet modes and their multipliers are spurious or missing when comparing with the full system.

In the functional mapping approach (cf. Sec. 3.4) a small integration box is sufficient to calculate the evolution of a TLS such that only a limited number of mesh points is required. For a perfect shift variable $v = T - \tau$ the pulse becomes a true steady state Y_s of a discrete mapping. The shift will generally not be an integer multiple of the mesh spacing so it must be implemented in Fourier space or with the use of interpolation. For non-zero linewidth enhancement one has to correct for the phase shift per roundtrip in

addition. The shift values of the position and complex angle are thus part of the steady state and determined along with it.

Let us consider a Dirac delta perturbation of small size $\epsilon \ll 1$ at time t_p

$$Y_p(t) = Y(t) + \epsilon \delta(t - t_p). \quad (6.10)$$

We will integrate a single roundtrip using the shifts of the steady state. From the resulting profiles we subtracting the steady state profile and divide by epsilon

$$Y_r = \frac{F[Y_p] - Y_s}{\epsilon}, \quad (6.11)$$

where F is the operator for one step of the functional mapping. This gives us the linearized response Y_r of the system to an elementary perturbation over the next roundtrip.

For all the possible Y_p , i.e. t_p at each mesh point, the Y_r form an $n \times n$ matrix with n being the number of mesh points in the integration box. This matrix of responses to perturbations is somewhat similar to the monodromy matrix calculated in Floquet theory, though it has a much smaller size. It thus becomes numerically feasible to diagonalize which yields self consistent perturbations as the eigenvectors. Their eigenvalues give the growth rates per mapping step. In the following we shall call them pseudo-Floquet modes and multipliers, respectively.

Modes with at least one multiplier $|\mu_k| > 1$ will grow over several roundtrips corresponding to an unstable perturbation. Bifurcations of periodic orbits are characterized by multipliers that cross the unit circle. Figure 6.15 shows results from performing the analysis for a stable pulse where a real multiplier is about to cross at $\mu = 1$. This corresponds to the fold on limit cycle bifurcation where the satellite instability sets in. Another example is the onset of the trailing edge instability which can be identified as a secondary Andronov-Hopf or torus bifurcation. It consists in the crossing of a complex conjugate pair of multipliers. Note, that the scheme works for both stable and unstable TLS. Unstable profiles can be obtained from continuation where v is trivially found since T is part of the solution.

The Floquet spectrum of a TLS in the long delay limit consists of a discrete part of modes with profiles centered around the TLS and a pseudo-continuous spectrum with modes that are close to harmonic perturbations around a constant background solution [YRSW19]. The technique described in the aforementioned work assumes all system variables to quickly approach a constant away from the TLS. For our case this would include the carriers. Consequently, the whole TLS would be effectively much larger than the pulse alone due to the long gain recovery. Together with the resolution required by the stiffness of the electric field the overall system is thus still too big to handle directly in this framework. However, it might be sufficient to restrict the analysis to a short interval around the net-gain window of the pulse. While the gain recovery phase is far from constant yet, perturbations of the field will already be strictly damped, since the absorber recovers much more quickly and net-losses set in. This could allow for finding the localized modes responsible for destabilizing the pulse in a more efficient way.

Since the integration box of the mapping is finite only modulations with sufficiently large frequencies can be represented by it. Thus, parts of the quasi-continuous spectrum

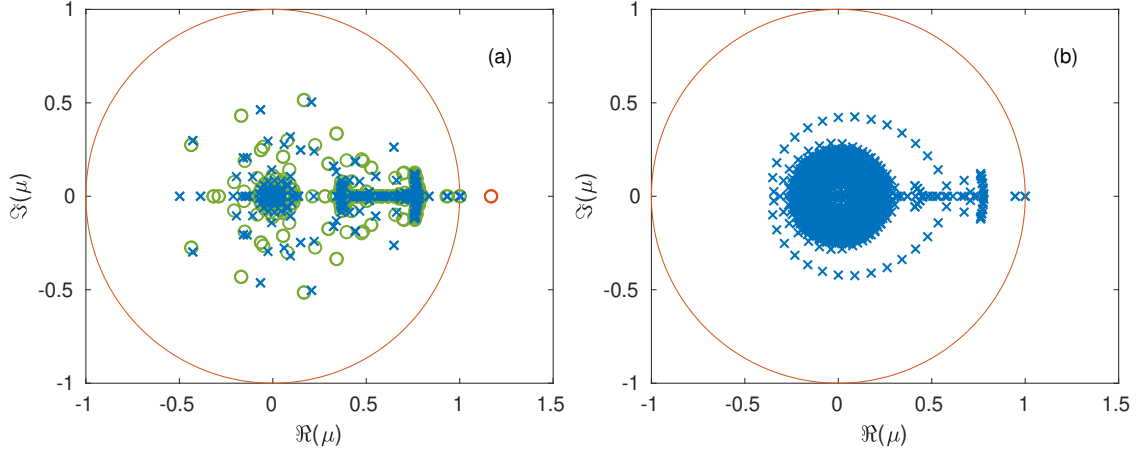


Figure 6.15: Linear stability of a stable pulse close to the fold at the onset of the satellite instability. (a) Floquet multipliers calculated in DDE-BIFTOOL before and after an additional mesh adaption drawn as crosses and circles, respectively. The locations of the multipliers change and, importantly, the number of unstable multipliers is not conserved. (b) Pseudo-Floquet multipliers calculated by diagonalizing the monodromy matrix obtained from integrating a single step using the functional mapping in the long delay limit. The discrete spectrum of modes localized around the TLS are found accurately and there are no spurious unstable multipliers. In both approaches the pseudo-continuous spectrum is incomplete and partly spurious. A real multiplier close to one is about to cross, thereby causing the fold. A doubly degenerate neutral multiplier at $\mu = 1$ corresponds to the time and phase symmetries present in the system.

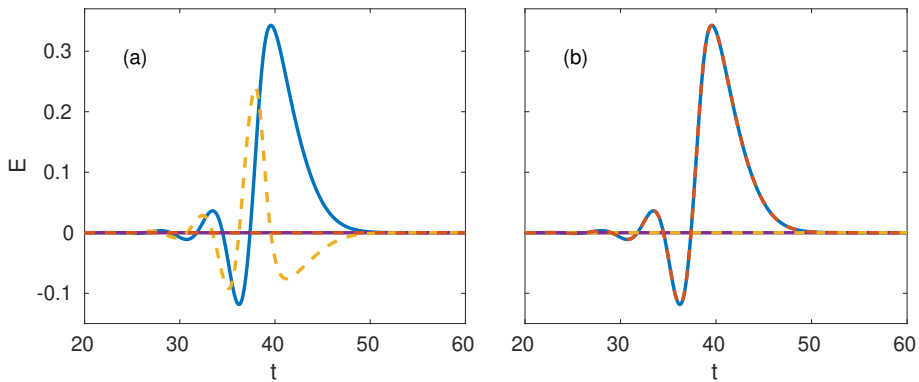


Figure 6.16: Neutral modes of the stable pulse yielding the pseudo-Floquet spectrum in Fig. 6.15. They correspond to the translational (a) and phase shift (b) invariances and offer an easy way to check whether the algorithm is producing sensible results. Real and imaginary parts are drawn in dashed yellow and orange for the modes and in solid blue and purple for the pulse profile, respectively.

will be missing in this approach. In addition, the boundary conditions cause some modes to be inaccurate. When using interpolation one end of the box is padded with zeros while the corresponding part on the other side is discarded. This results in some modes having growing profiles toward the edges which is unphysical as they would correspond to non-square-integrable modes in the full system. These modes are, however, strongly damped. The modes of the discrete spectrum are reproduced accurately. They are responsible for all bifurcations below threshold since the underlying off-solution remains strictly stable.

Figure 6.16 shows the intensity profiles of the neutral translation modes that equal the derivatives of the complex amplitude profile of the pulse with respect to time and the complex phase. These modes correspond to the degenerate real Floquet multipliers at $\mu = 1$. The algorithm actually yields linear combinations of the two modes, since they form a degenerate eigenspace, so they had to be separated manually. Comparing them with the expected shape served as a sanity check for the algorithm.

6.5 Saddle-node infinite-period to Andronov-Hopf transition

This section is on the origin of the pure satellite instability at low linewidth enhancement. The responsible bifurcation transforms from saddle-node infinite-period to Andronov-Hopf for increasing α_1 .

6.5.1 Period scaling

Figure 6.17 shows the period scaling of the satellite instability. Direct numerical simulations were performed using the functional mapping approach in the long delay limit. The period can easily be determined from the separation of the either the maxima or minima of the peak intensity time trace. Conveniently, for the pure satellite instability the shift variable v of the mapping can be saved. It has a virtually constant positive value except when the replacement of the parent pulse occurs. Here, one finds a single large negative shift value as the position of the maximum intensity jumps from the position of the parent to the one of the satellite.

For $\alpha_1 = 0.01$ the period tends to infinity at the bifurcation point. The scaling law is $1/\sqrt{\mu}$, where $\mu = J_1 - J_1^c$ is the distance from the critical gain bias value. This is characteristic of a saddle-node infinite-period (SNIPER) bifurcation which consists in the collision of a saddle-node bifurcation of a steady state with a limit cycle that has an infinite period at the bifurcation point. Due to the diverging period the accurate detection of the bifurcation point is not possible directly with finite computation time. Indeed, using the scaling law is the most viable option to determine the critical gain bias $J_1^c \approx 0.5637$ by fitting data points above the bifurcation. Another type of bifurcation where the periodic orbit is born with infinite period is the homoclinic bifurcation with a distinct scaling law $-\ln(\mu)$. For $\alpha_1 = 0.02$ the period starts at a constant finite value of about one thousand roundtrips but quickly starts to follow the α_1 SNIPER curve as well. In this case the bifurcation is of the Andronov-Hopf type.

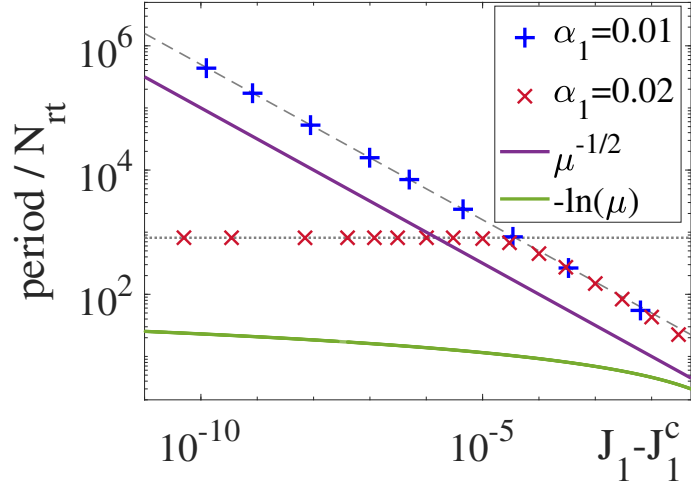


Figure 6.17: Scaling of the period close above the bifurcation points that cause the satellite instability. For $\alpha_1 = 0.01$ the scaling is proportional to $1/\sqrt{\mu}$ which indicates a SNIPER bifurcation. For $\alpha_1 = 0.02$ the period starts at a finite period characteristic of an Andronov-Hopf bifurcation. However, it soon follows the SNIPER trend as well. The scaling of a homoclinic bifurcation $-\ln(\mu)$ is shown for comparison. The dashed and dotted gray lines are meant as guides for the eye. A similar version of this figure was used in [7].

6.5.2 Andronov-Hopf oscillation

Figure 6.18 shows a bifurcation diagram for $\alpha_1 = 0.02$ where the satellite oscillation sets in with an infinitesimal amplitude. In the corresponding Figure 6.13 for zero linewidth enhancement the oscillation started with full amplitude. The branches from the $\alpha_1 = 0$ case have reconnected at the branching point **BP**. The stable part of the multi fold branch has joined with one half of degenerate branch while the unstable part has joined with the other half of degenerate branch. For finite values of α_1 the degeneracy is no longer present, i.e., in the high J_1 interval where the satellite instability resides the two branches differ slightly in the $\alpha_1 = 0.02$ case. At small but finite α_1 the first branch has two folds. One is just **F₂** that existed already at $\alpha_1 = 0$ and the other one stems from the branch recombination where **BP** turned into another fold. As long as **F₂** exists the satellite instability bifurcation remains to be of the SNIPER type. At some $\alpha_1 \in (0.015, 0.02)$ the two folds have merged into the Andronov-Hopf bifurcation point **H**. The other branch has no folds and remains entirely unstable.

Figure 6.19 shows time traces of the maximum pulse intensity in a very small gain interval directly above the critical value J_1^c for $\alpha_1 = 0.02$. For the first trace in solid blue only a small amplitude modulation is observed having a finite period. The responsible bifurcation is of the Andronov-Hopf type. The second trace depicted in dashed orange has already deformed into a strongly unharmonical shape with a significantly lower period. Next, it develops a pronounced dip directly in front of the maximum of the oscillation shown in dash-dotted yellow while the period keeps decreasing. Finally, the dotted purple

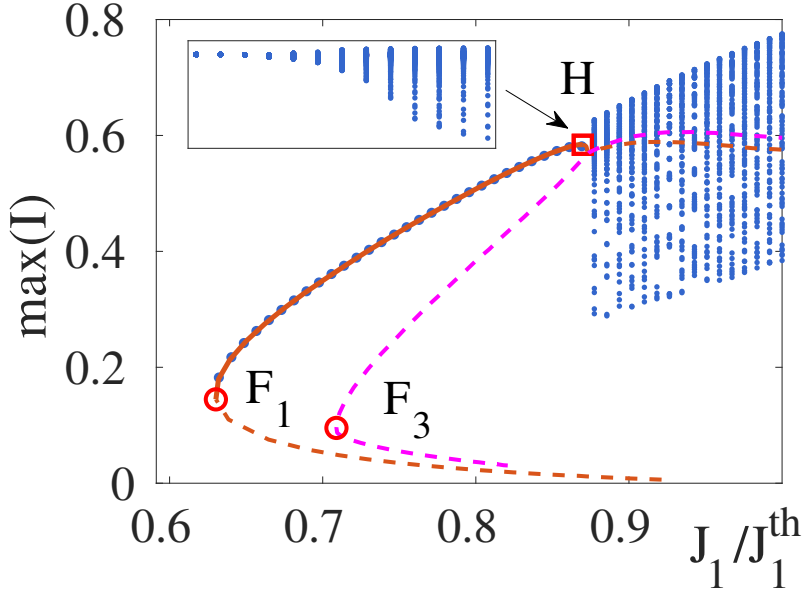


Figure 6.18: Bifurcation diagram for $\alpha_1 = 0.02$ similar to Fig. 6.13 for $\alpha_1 = 0$ whose branches have reconnected at the branching point its **BP**. The satellite instability starts with infinitessimal amplitude. The responsible Andronov-Hopf bifurcation point **H** stems from a merger of the fold **F₂** and another fold that was born from **BP** in the branch reconnection. A similar version of this figure was used in [7].

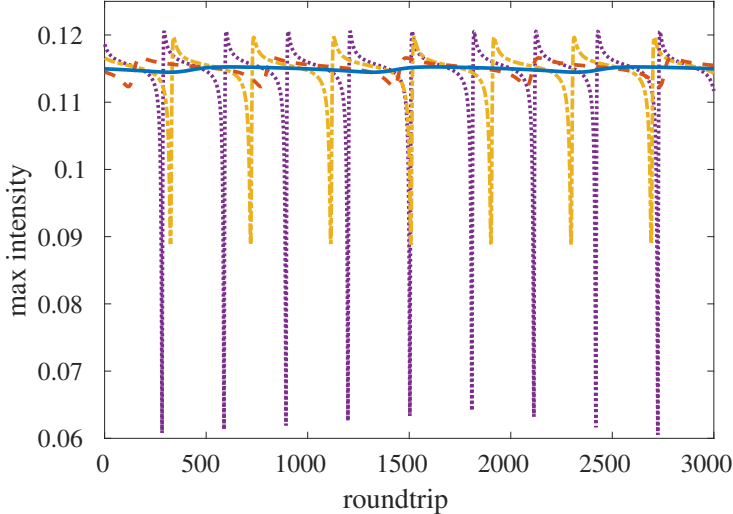


Figure 6.19: Time traces of the pulse peak intensity close above the onset of the satellite instability for $\alpha_1 = 0.02$. The oscillation starts with a finite period as a small modulation in an Andronov-Hopf bifurcation. The periodic orbit then very quickly deforms into the same eruption shape of the satellite instability at $\alpha_1 = 0$. The order of the graphical representations is solid blue, dashed orange, dash-dotted yellow and finally dotted purple.

curve is virtually indistinguishable from the eruptive satellite instability at $\alpha_1 = 0$ for the same gain bias. This transition proceeds very rapidly when increasing J_1 and afterwards the period of the satellite instability is almost constant as a function of α_1 . The different types of origin of the oscillations is thus only apparent in a tiny gain interval where its period diverges for small α_1 .

6.5.3 Transition dynamics

Panel (a) of Figure 6.20 shows the period scaling of the satellite instability for $\alpha_1 = 0.015$. This is very close to the Andronov-Hopf transition but still shows the characteristic scaling of a SNIPER bifurcation. Panels (b-d) show pseudo-space-time diagrams obtained from

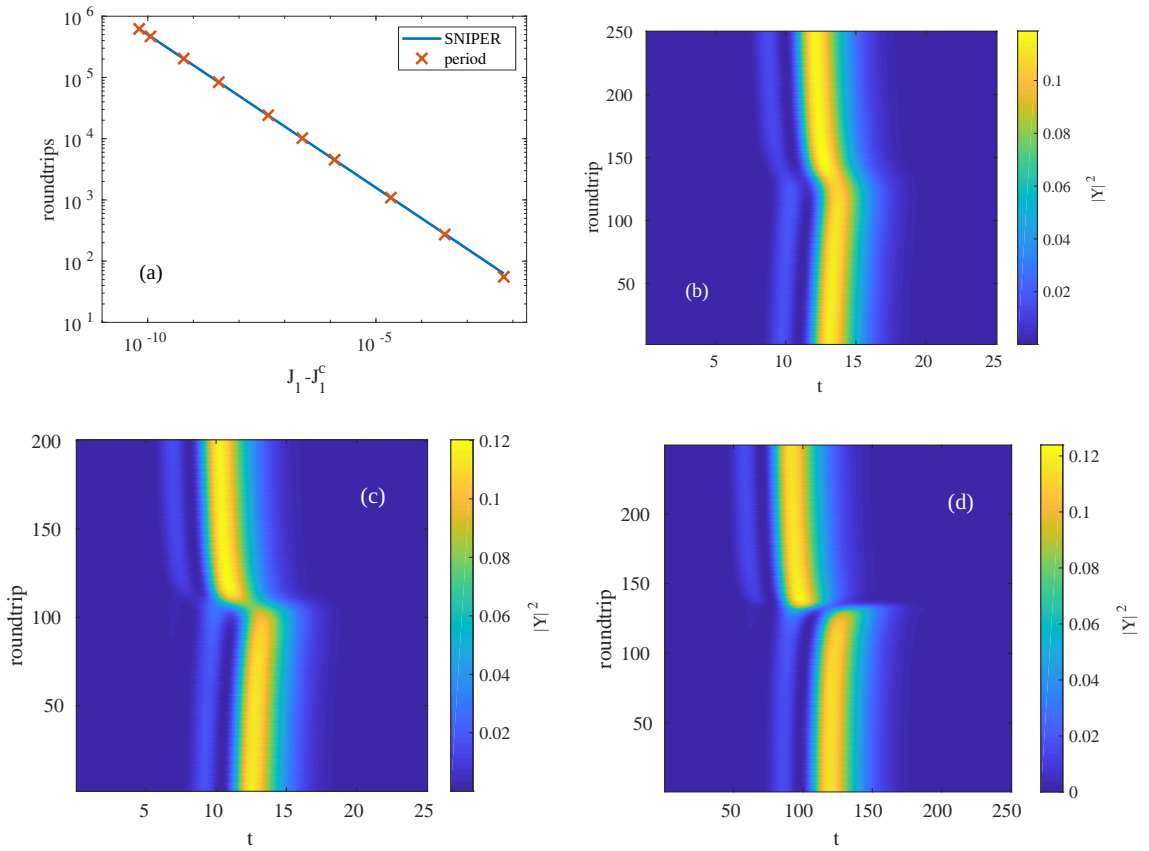


Figure 6.20: (a) The period of the satellite instability at $\alpha_1 = 0.015$ still has the characteristic scaling of a SNIPER bifurcation. (b-d) Pseudo-space-time diagrams for increasing gain very close above the critical gain bias J_1^c . The instability starts as a small modulation that causes a small shift of the main pulse toward its satellite. The attraction of the satellite becomes stronger very quickly such that the main pulse merges with it. Soon after the main pulse virtually jumps onto the satellite with only a small intensity connection left between them.

direct numerical simulations in the long delay limit using the functional mapping approach. A fast progression of the dynamics is observed in a very small gain interval above the bifurcation point. At first in panel (b) the unstable satellite only causes a small shift of the main pulse toward it. Along with this shift goes a small modulation of the peak intensity. This corresponds to the blue curve in Figure 6.19 but with very long intervals of virtually constant peak intensity between the modulations. Next in panel (c) the main pulse slides along about half the distance to its growing satellite and the two merge in the middle to form the next main pulse. Indeed, the next order satellite combines with part of the first order satellite in their middle and so forth. This corresponds to the orange curve in Figure 6.19 but again occurs much more infrequently. Finally in panel (d) most of the intensity basically jumps to the satellite with only a small rest of intensity indicating any sort of drift movement in order to merge. Most of the intensity thus stems from the unstable satellite alone using the gain inversion to grow while the main pulse mostly dies out. Again, this is similar to the yellow curve in Figure 6.19. The periods of both scenarios have come much closer to each other at this point. Soon after, virtually no further distinction remains for any α_1 , provided it is small enough for the satellite instability to persist. For high gain the oscillations look identical. This progression illustrates how the two scenarios are indeed profoundly connected and how one may deform continuously into the other as a function of the parameters.

6.6 Excitability

To introduce the concept of excitability we will take a look at a simple yet instructive model that describes a self-sustained weakly nonlinear oscillator subjected to weak periodic forcing. An approximation can be derived for the phase offset of the oscillator from the forcing [PRK01]. For the simplest case of a sine shaped forcing term it is called the Adler equation [Adl46]

$$\dot{\vartheta} = \delta - \sin \vartheta, \quad (6.12)$$

which was extensively studied in the context of synchronization. Here, ϑ is the phase offset of the oscillator to the forcing and δ is the detuning of their frequencies. In optics, with the addition of a time-delay term, this equation can model the dynamics of a slave laser injected by a master laser and subject to optical feedback which yields localized states [GJTB15].

For $-1 < \delta < 1$ Eq. (6.12) has a stable and an unstable fix point. Close to the saddle node bifurcation points $|\delta| = 1$ these two fix points lie very close. Together with the periodicity of the system, this results in two qualitatively distinct trajectories from the unstable toward the stable fix point depending on the direction. Figure 6.21 shows a schematic of such a scenario. Around the stable fixed point a small perturbation just tends back to the fixed point. A sufficiently large perturbation, however, may push the system beyond the unstable fix point, thus causing the system to go the other way round, which will take significantly more time and incur a 2π phase shift. This process can be randomly triggered under the influence of noise. Such a kind of behavior is generally referred to as excitability, i.e., a perturbation can excite the system.

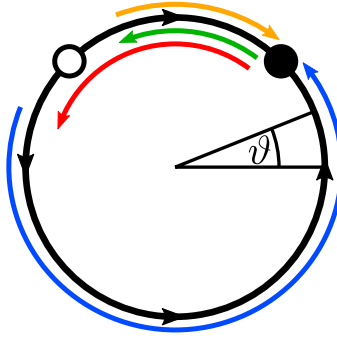


Figure 6.21: Schematic for the Adler equation (6.12). A saddle-node pair of fix points exists on a ring topology. Small perturbations (green arrow) from the stable fix point (solid circle) lead to a fast relaxation (yellow arrow). Sufficiently large perturbations (red arrow) beyond the unstable fix point (empty circle) cause a much longer relaxation (blue arrow) the other way round, thus causing a 2π phase shift in the angle ϑ .

Typically an excitable medium needs to recover for a certain time after an excitation occurred. This time is called the refractory period. Excitable media were found early in biological and chemical systems [Win01], especially in neurons [JBL46] as described by the FitzHugh-Nagumo model [Fit55, NAY62]. In nonlinear optics, excitable behavior was encountered, e.g., in a semiconductor laser with optical feedback [GGG⁺97] and can be induced by time-delayed feedback alone [PHBH05].

Figure 6.22 shows an example of the pure satellite instability dynamics for zero linewidth enhancement $\alpha_j = 0$ under the influence of strong noise. The results were obtained from direct numerical simulations using the functional mapping in the fully localized regime. Panel (a) shows a pseudo-space-time representation of three thousand consecutive roundtrips while panel (b) shows the respective intensity time trace of the microcavity field with the maximum pulse intensities highlighted. One can see a strong variance in the time intervals after which the individual satellite eruptions occur, indicating a strong influence of noise on the instability.

A satellite needs enough energy to open a net-gain window in order to become unstable and grow. Noise can interfere with the satellite constructively and increase its available energy. This can help the satellite to become large enough when it is just below the critical energy to trigger a consequent eruption. The following recovery of the gain carrier inversion can be interpreted as the refractory period of an excitable medium. Conversely, destructive interference can shrink a small satellite sufficiently to stall an ongoing eruption in its early stage where the satellite only gains little additional energy per roundtrip. Both processes can considerably influence the blow-up time of the satellite leading to a highly irregular period of the dynamics.

Figure 6.23 shows statistics for a two dimensional parameter scan using the same kind of simulations as for the Figure 6.22. The control parameters are the distance of the gain bias to the critical value of the satellite instability $J_1 - J_1^c$ and the noise level σ_{noise} that measures the standard deviation of a simulated random walk during each time step. The

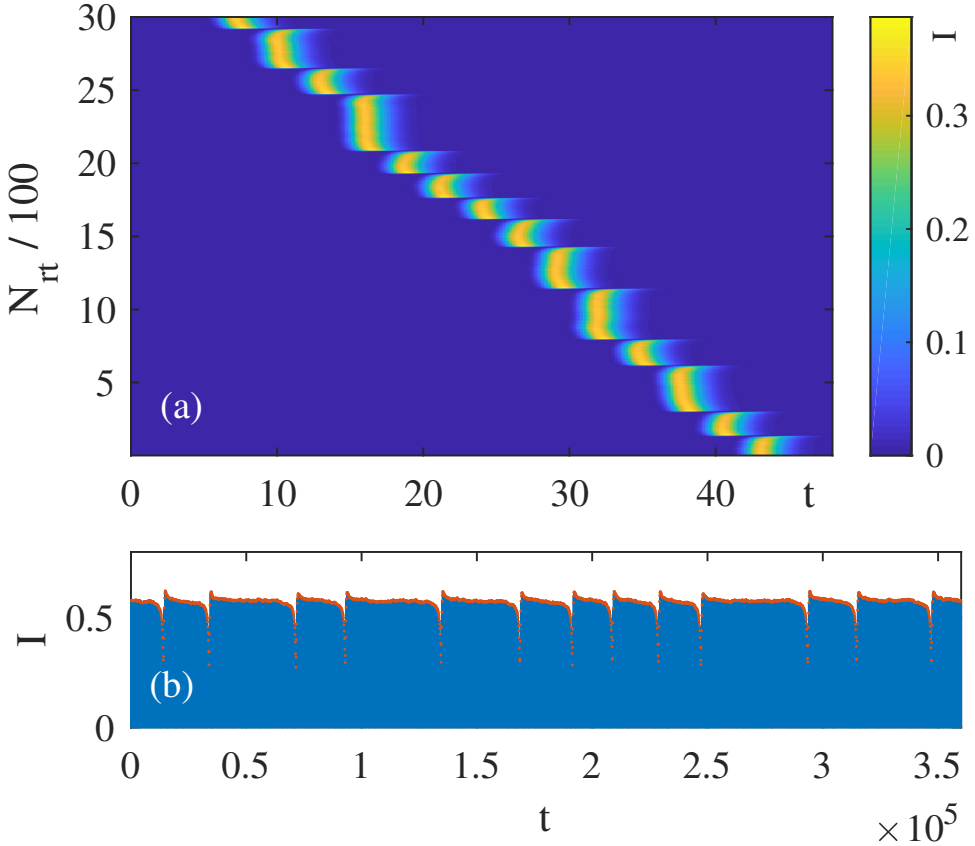


Figure 6.22: (a) Pseudo-space-time diagram of excitatory dynamics in the satellite instability regime for zero linewidth enhancement $\alpha_j = 0$. The intensity $I = |E|^2$ of the microcavity field as a function of time t is stacked for each roundtrip numbered N_{rt} . Close to the bifurcation point, noise has a strong influence on the eruption time of the satellites. (b) The corresponding full time series with the peak intensities marked by orange dots. Other parameters are $J_1 = 0.564$ and $\sigma_{\text{noise}} = 10^{-3}$. A similar version of this figure was used in [7].

statistics were performed over 100 consecutive eruptions per point with a cut-off at a maximum of ten million simulated roundtrips. In principle satellite eruptions below the critical current J_1^c may appear at any small noise level but they quickly become too rare to track them feasibly. Panel (a) shows the average time between eruptions below the critical gain bias where noise is needed to trigger them. For lower gain stronger noise is needed to push the smaller satellite above its critical energy. The limited computation time results in a visible cut-off line which appears straight in the double logarithmic axes. Thus, one can roughly infer a powerlaw for the necessary noise as a function of the gain bias distance for a given average rate of eruptions. Panel (b) shows the case above the bifurcation point where the average period is mostly unaffected by the noise. Panel (c) shows the standard deviation of the measured period in panel (a). The time between eruptions are highly irregular at the cut-off edge, indeed the standard deviation reaches

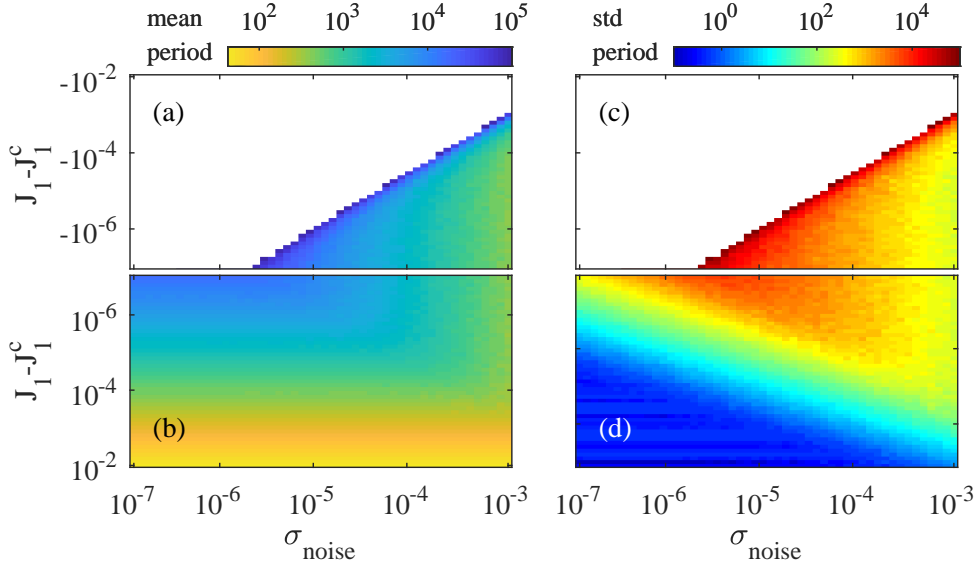


Figure 6.23: Mean value (a,b) and standard deviation (c,d) of the period of satellite eruptions close below (a,c) and above (b,d) the onset of the satellite instability J_1^c . (a) Below the bifurcation point noise can trigger satellite eruptions. The mean rate of occurrence roughly scales as a powerlaw. (b) Above bifurcation point the period remains largely unperturbed on average. (c) The statistical variance of the eruptions is particularly large where they are rarest. (d) Above the bifurcation the effect of small noise levels is less than the temporal resolution of the used simulations. Generally, noise levels larger than $\sigma_{\text{noise}} \approx 5 \times 10^{-4}$ begin to dominate all of these statistics. A similar version of this figure was used in [7].

a value similar to the average. Panel (d) shows the standard deviation of the period for the points in (b). Directly above the bifurcation point strong irregularities remain for sufficiently strong noise. For given values of the standard deviation, again, a powerlaw can be inferred. In the low noise and high gain corner the values show numerical artifacts and are virtually constant in σ_{noise} . This is due to the discrete nature of the dynamics. The pulses get filtered by the microcavity once per roundtrip and thus do not evolve continuously. Therefore the period can only be defined up to an integer accuracy. While this poses no problem for finding the average period, some finite standard deviation always remains even in the absence of noise. In all of the panels one observes that for noise levels larger than $\sigma_{\text{noise}} \approx 5 \times 10^{-4}$ the dynamics start to be dominated by the noise. Both the average period and standard deviation vary little, independent of the gain bias except close to the cut-off edge.

6.7 Comparison with a dispersive Haus-PDE model

A partial differential equation model for the MIXSEL system can be derived by applying either the functional mapping or multiple timescale analysis approaches, see the appen-

dices of [7] for the respective details. The DAE model is qualitatively different from the unidirectional ring DDE model (2.96)–(2.98); in the GTI regime $h = 2$ there is no diffusion such that third order dispersion dominates. However, like the exponential Haus PDE (4.15)–(4.17) the MIXSEL PDE is expanded around threshold so similar inaccuracies must be expected far below threshold and for large intensities. One obtains a slow time variable ξ that corresponds to the evolution of the pulse over the roundtrips but is continuous. The pulse profile itself is a function of the fast time z that can be viewed as a spatial dimension in this scheme. Expansion around the lasing threshold yields the Haus-PDE model [7]

$$\begin{aligned} \frac{\partial E}{\partial \xi} = & \frac{(1+\eta)^2}{h\eta} \left[(1-i\alpha_1)N_1 + (1-i\alpha_2)N_2 - 1 + \frac{h\eta}{1+\eta} \right] E \\ & + \left[d_1 \frac{\partial}{\partial z} + d_2 \frac{\partial^2}{\partial z^2} + d_3 \frac{\partial^3}{\partial z^3} \right] E, \end{aligned} \quad (6.13)$$

with the dispersion coefficients

$$d_1 = -\frac{(\eta+1)^2}{h\eta}, \quad (6.14)$$

$$d_2 = \frac{1-\eta^2}{2} \left(\frac{\eta+1}{h\eta} \right)^2, \quad (6.15)$$

$$d_3 = -\frac{\eta^3+1}{3} \left(\frac{\eta+1}{h\eta} \right)^3. \quad (6.16)$$

The carrier evolutions read

$$\frac{\partial N_1}{\partial z} = \gamma_1(J_1 - N_1) - |E|^2 N_1, \quad (6.17)$$

$$\frac{\partial N_2}{\partial z} = \gamma_2(J_2 - N_2) - s|E|^2 N_2. \quad (6.18)$$

Note, that the second order dispersion term $d_2 \rightarrow 0$ tends to zero in the conservative cavity limit of $\eta \rightarrow 1$ and $h \rightarrow 2$ while third order dispersion stays finite $d_3 \rightarrow -2/3$. The filtering function of the coupled microcavity geometry is asymptotically flat to the sides, not a typical downward parabola shape. For η close to 1 the linear cavity losses become especially low and therefore little net gain is required to maintain a pulse. This means the gain peak is very low relative to the flat rest of the spectrum close to unity. Consequently, this peak has a very small curvature which corresponds to very little diffusion.

Bifurcation analysis of the Haus-PDE is possible in the numerical path continuation framework pde2path [UWR14]. In order to compare the results of the PDE and DAE models a different parameter set $h = 2$, $J_2 = -0.1$, $\eta = 0.9$ and $s = 15$ was chosen. The absorber modulation and feedback strength are closer to realistic values however the absorber saturation ratio is rather large.

Direct numerical simulations in the long delay limit were performed using the functional mapping. The standard deviation of the pulse peak intensity provides a simple measure to characterize the behavior. When the laser is in the off-state virtually no deviations exist. For stable pulsation a residual oscillation remains due to the resolution of the mesh

grid. The drift per roundtrip of a TLS is generally not commensurate with it such that the discrete representation of its profile moves through the mesh points slowly. Thus, not the true maximum intensity is measured but rather the intensity at the mesh point closest to the peak. Finally, quasi-periodic dynamics of the TLSs typically exhibit a substantial variance of the peak energy. In practice the standard deviations of these three regimes prove to be many orders of magnitude apart.

Panel (a) of Figure 6.24 shows results obtained for zero absorber linewidth enhancement $\alpha_2 = 0$ similar to Figures 4.19 and 6.5. On the low gain side pulse stability is limited by the principal TLS fold. For medium α_1 the trailing edge instability sets in. It features a dip on the lower gain part for the used parameter set. A large region corresponding to

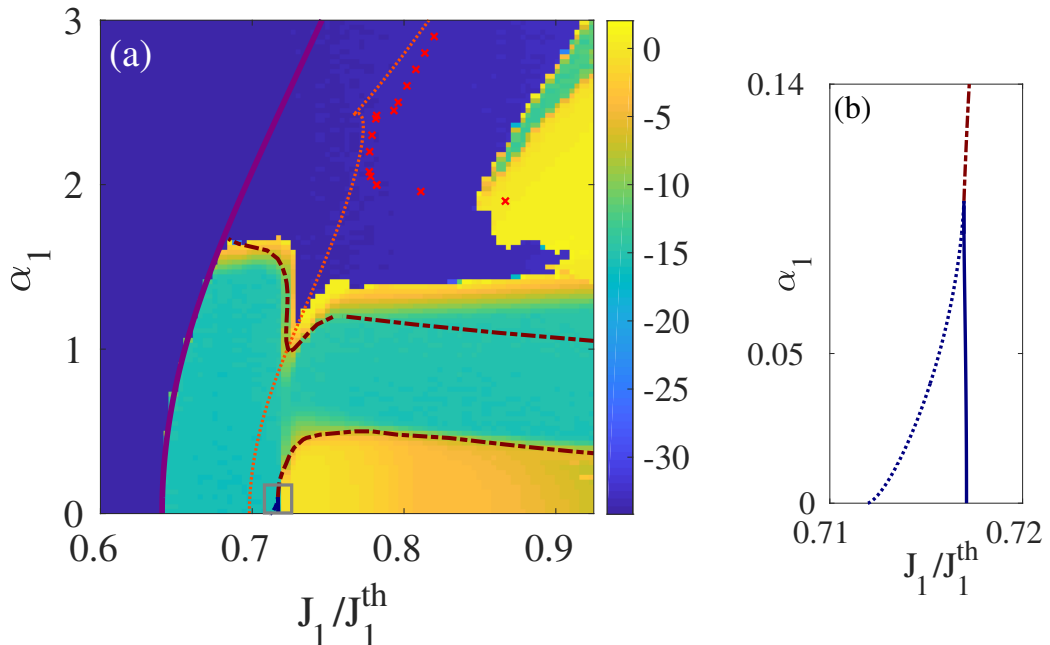


Figure 6.24: (a) Two-dimensional bifurcation diagram of the MIXSEL system for $\alpha_2 = 0$ with the gain bias J_1 normalized to the lasing threshold J_1^{th} and the gain linewidth enhancement factor α_1 as control parameters. The colors represents the standard deviation in logarithmic scale of the pulse energy found in the DAE model in long delay limit. The blue region corresponds to the off solution and the green and yellow regions to stable and oscillating pulses, respectively. Bifurcation curves from numerical path continuation of the Haus-PDE model are superposed. The solid magenta line represents a fold and the red dashed lines stand for AH bifurcations. For the secondary pulse region the fold branch is shown in dotted orange and an AH branch is indicated by red crosses. (b) Zoom on the onset of the satellite instability. A branching point in dotted blue and a fold in solid blue merge into an AH bifurcation. Other parameters are $h = 2$, $J_2 = -0.1$, $\eta = 0.9$ and $s = 15$. A similar version of this figure was used in [7].

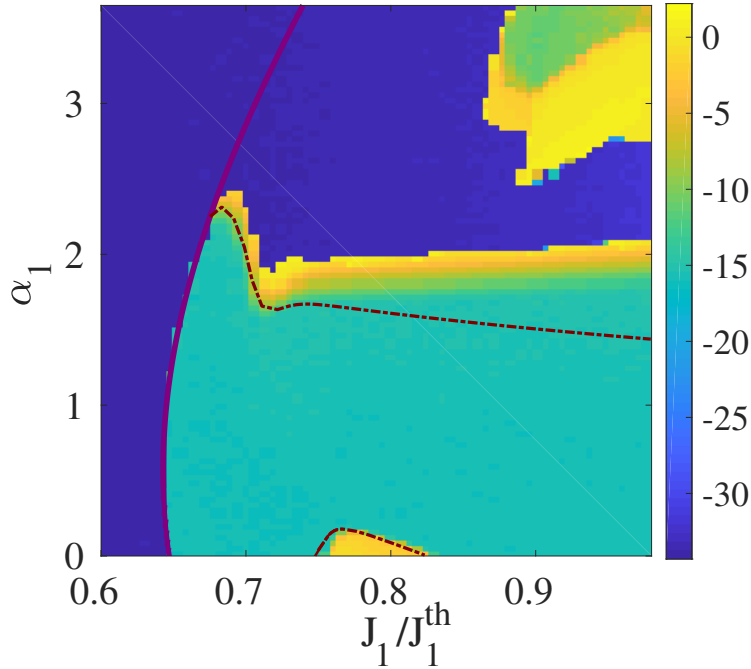


Figure 6.25: Two-dimensional bifurcation diagram similar to Fig. 6.24 but for $\alpha_2 = 0.5$. The colors and line styles follow the same pattern. For the secondary pulse region bifurcation analysis was unsuccessful. Other parameters are $h = 2$, $J_2 = -0.1$, $\eta = 0.9$ and $s = 15$. A similar version of this figure was used in [7].

the satellite instability resides at low α_1 while at high α_1 a secondary pulse region exists for high gain. These secondary pulses are stable only close to the low gain edge of this region. For comparison, continuation results obtained in pde2path are superposed. Both the principal fold and the satellite instability are in very good agreement with the DAE model. The trailing edge instability is identified as an Andronov-Hopf bifurcation while its analogue in the DAE is a secondary Andronov-Hopf or torus bifurcation. It features the same dip as in the DAE but slopes the wrong way for high gain which is somewhat similar to the unidirectional ring case (c.f. Fig. 4.19 in Sec. 4.5.4). In addition, the bifurcation curves corresponding to the secondary pulses are shifted far toward lower gain.

Like for the parameter set used earlier in this chapter the bifurcation responsible for the satellite instability is a fold and the period of the resulting oscillation diverges with the same SNIPER scaling law. The fold then merges with a branching point into a Andronov-Hopf bifurcation. The bifurcation curves of this transition are shown in detail in panel (b). They correspond to **BP**, **F₂** and **H** that appeared in the examples shown in Figures 6.13 and 6.18.

For non-zero absorber linewidth enhancement $\alpha_2 = 0.5$ the overall structure remains similar. Figure 6.25 shows the corresponding results with the same pattern of representation that was used in Figure 6.24. The principal TLS region has moved up in α_1 while the satellite instability has moved down with only a small area remaining in the positive α_1

range. Numerical path continuation of the Haus-PDE was again able to accurately predict the corresponding fold while the trailing edge instability still slopes differently on the high J_1 in the two models. The secondary pulse region has moved to even higher values of α_1 as compared to the $\alpha_2 = 0$ case and is completely disconnected from the principal pulses. In pde2path, however, searching for the bifurcations corresponding to this region was not successful.

7 Injected Kerr Gires-Tournois Interferometer

Kerr solitons may be used as addressable bits in all optical information storage and processing [LCK⁺10, HBJ⁺13]. Such TLSs can be multistable, exhibiting variable widths [CBH⁺13, LLKG15, XXL⁺15]. These can be shown to be build up from fronts that connect domains of lower and higher CW background intensities [Ros96, PRKGG16]. Under the influence of TOD, coexistence and hysteresis between dark and bright Kerr solitons can be enabled via drifting fronts [PRGG17, TMMC17]. Similarly structured TLSs were found in parametric oscillators [OSF99, PRGH⁺19] and in the unidirectional ring laser model, modified to introduce chromatic dispersion of a fiber loop, passively mode-locked pulses were recently found to coexist with variable width as well [PAV20].

The Kerr GTI system is qualitatively different from the active laser systems discussed in the previous chapters. With the microcavity only containing a Kerr nonlinear medium the whole system is rendered passive. It is driven by a CW pumping beam, hence a non-zero CW background always remains. Passively mode-locked pulses and TLSs are again found but they are not completely independent from each other in contrast to the previous chapters. There exists a fixed phase relation of the TLS to the CW background and consequently among each other. Also, the system operates at a forced frequency rather than being able to choose its frequency shift dynamically. Some of the results presented in this chapter have been published in [6].

7.1 Continuous wave solutions

The Kerr GTI system Eqs. (2.252), (2.253) can be considered a kind of forced oscillator. Its CW solutions are given by simple steady states of the form $E(t) = \tilde{E}$ and $Y(t) = \tilde{Y}$. The frequency is locked to the injection Y_0 and only a constant phase shift exists between \tilde{E} and Y_0 . There is no need to introduce a frequency shift in the ansatz, unlike the active systems discussed in the previous chapters that are free to adapt the instantaneous frequency dynamically. Using the ansatz we get

$$0 = \left[i \left(\delta - |\tilde{E}|^2 \right) - 1 \right] E + h \tilde{Y}, \quad (7.1)$$

$$\tilde{Y} = \eta \left[\tilde{E} - \tilde{Y} \right] + \sqrt{1 - |\eta|^2} Y_0. \quad (7.2)$$

We separate the injection in the second equation

$$\sqrt{1 - \rho^2} Y_0 = (1 + \rho e^{i\varphi}) \tilde{Y} - \rho e^{i\varphi} \tilde{E}, \quad (7.3)$$

where we replaced $\eta = \rho \exp(i\varphi)$. Here, $\varphi = \omega_0 \tau + \phi_e$ is the phase of the feedback, $\rho = |r_e|$ is the modulus of the amplitude reflectivity of the feedback mirror and ϕ_e its phase shift.

Next we solve Eq. (7.1) for \hat{Y}

$$\hat{Y} = \frac{1 - i(\delta - |\tilde{E}|^2)}{h} \tilde{E}, \quad (7.4)$$

that we substitute in the previous equation to reach the CW condition

$$\sqrt{1 - \rho^2} Y_0 = \left[(1 + \rho e^{i\varphi}) \frac{1 - i(\delta - |E|^2)}{h} - \rho e^{i\varphi} \right] E. \quad (7.5)$$

By taking the absolute value of both sides one obtains after some algebra

$$|Y_0|^2 = \frac{\rho^2 (h^2 - 2h) + [1 + 2\rho \cos \varphi + \rho^2] [1 + (\delta - I)^2] - 2h\rho [\cos \varphi - (\delta - I) \sin \varphi]}{h^2 (1 - \rho^2)} I, \quad (7.6)$$

where $I = |\tilde{E}|^2$ stands for the intensity of the microcavity field.

We want to find \tilde{E} as function of Y_0 . To that end, first we find I implicitly for a given $|Y_0|^2$ using (7.6) which yields the modulus of the amplitude $|\tilde{E}| = \sqrt{I}$. By putting this back into the CW condition we can easily find the matching phase of Y_0 relative to \tilde{E} . For convenience we may exploit the phase symmetry of the system by choosing to keep $Y_0 > 1$ to act as a real-valued control parameter, i.e., we simply put the phase difference in \tilde{E} . Panel (a) of Figure 7.2 shows a branch of CW solutions obtained this way. As the system is third order in E , optical bistability is possible for appropriate parameters. The values used for the example are $h = 2$ for the injection coupling, $\delta = 1.5$ for the detuning and $\eta = 0.5$ or equivalently $\rho = 0.5$ and $\varphi = 0$ for the feedback. If not stated otherwise, the analyses presented in the following sections keep to this parameter set.

7.1.1 Linear stability in the long delay limit

In the limit of large delay $\tau \rightarrow \infty$ the eigenvalue spectrum obtained by linear stability analysis separates into a discrete and a pseudo-continuous part. The pseudo-continuous spectrum consists of asymptotic curves that become densely filled with eigenvalues for large τ . Bifurcations happen when an asymptotic curve crosses the imaginary axis. In the long delay limit this means that an infinite number of neighboring eigenvalues crosses together while for large but finite τ a large number crosses virtually instantaneously. Note, that the spectrum is confined within a small region around the imaginary axis with a size proportional to $1/\tau$. Otherwise this situation is analogous to spatially extended systems and the following three types of bifurcations exist: Firstly, if the spectrum has a single tip centered around the real axis it is called a uniform instability. Turing instability means that a finite band of frequencies becomes unstable, thus causing oscillations around the central frequency. The surrounding frequencies are also unstable but grow increasingly slower. Small frequencies around zero, however, stay stable. Lastly, modulational instability is similar to Turing but the spectrum always goes through the origin. Thus, at the bifurcation point the frequencies next to zero are the first to become undamped but later some finite, possibly further growing, frequency dominates. Still, all small frequencies are slightly

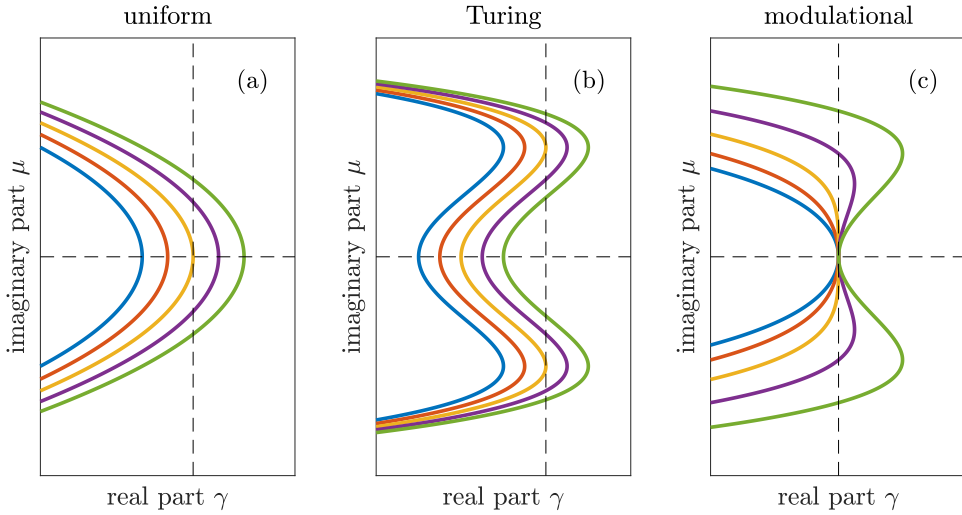


Figure 7.1: Schematics for the different instabilities of the pseudo-continuous spectrum of Eqs. (2.252), (2.253) in the long delay limit. The real and imaginary axes are indicated by the dashed lines. (a) Uniform instability: The spectrum crosses into the right complex half plane at zero. Increasingly large frequencies follow. (b) Turing instability: A finite band of frequencies crosses into the right complex half plane. (c) Modulational instability: Frequencies around zero become unstable while the zero frequency remains neutral, i.e., the spectrum always crosses the origin.

unstable for this instability. Figure 7.1 shows schematics for each of these instabilities. For the analyzed parameter set, uniform and Turing instabilities appear depending on the feedback phase φ .

In order to perform linear stability analysis of the CW solutions we can begin by substituting the delay algebraic equation (2.253) into the microcavity evolution (2.252) to get

$$\dot{E} = [i(\delta - |E|^2) - 1]E + h\eta E_\tau - h\eta Y_\tau + h\sqrt{1 - |\eta|^2}Y_0, \quad (7.7)$$

that has a $Y_\tau = Y(t - \tau)$ term. After shifting the field evolution (2.252) by the delay τ

$$\dot{E}_\tau = [i(\delta - |E_\tau|^2) - 1]E_\tau + hY_\tau, \quad (7.8)$$

we can multiply this by η and add it to the previous equation to obtain a neutral delay differential equation (NDDE) that is an equivalent form of the DAE model which no longer contains the field Y

$$\dot{E} + \eta\dot{E}_\tau = [i(\delta - |E|^2) - 1]E + \eta[i(\delta - |E_\tau|^2) - 1 + h]E_\tau + h\sqrt{1 - |\eta|^2}Y_0. \quad (7.9)$$

This form is more convenient in the following.

Next, we need to consider a small exponential perturbation around a steady CW state. Using the ansatz $E = \tilde{E} + \Delta E e^{\lambda t}$ we can expand the NDDE to first order

$$0 = \left[i(\delta - 2\tilde{E}^* \tilde{E}) - 1 - \lambda + \frac{h\eta e^{-\lambda\tau}}{1 + \eta e^{-\lambda\tau}} \right] \Delta E - i\tilde{E}^2 \Delta E^*. \quad (7.10)$$

To build the Jacobian we need to use complex conjugates as well which leads to the eigenproblem

$$\det \begin{pmatrix} i(\delta - 2\tilde{E}^*\tilde{E}) - 1 - \lambda + \frac{h\eta e^{-\lambda\tau}}{1 + \eta e^{-\lambda\tau}} & -i\tilde{E}\tilde{E} \\ i\tilde{E}^*\tilde{E}^* & i(2\tilde{E}\tilde{E}^* - \delta) - 1 - \lambda + \frac{h\eta^* e^{-\lambda\tau}}{1 + \eta^* e^{-\lambda\tau}} \end{pmatrix} = 0. \quad (7.11)$$

The resulting characteristic equation contains various combinations of λ and $e^{-\lambda\tau}$ and their respective squares and rendering it transcendental. Note, that expanding the DAE model leads to the same characteristic equation. Several zeros in the respective Jacobian cancel many terms in the determinant thereby effectively reducing the dimension. Since the DAE itself is only a condition for the evolution of E this phenomenon is indeed intuitive. We can now perform linear stability analysis in the long delay limit following the approach described in [YW10] which was originally developed in [Yan05, WY06] to deal with the λ and $e^{-\lambda\tau}$ terms that appear simultaneously for DDEs. The DAE case is only slightly more complicated as it contains products of the previous terms in addition, namely powers of $\lambda e^{-\lambda\tau}$.

We have to separately consider two types of eigenvalues that differ in the scaling of their respective real parts with τ . Those that behave like $\text{Re}[\lambda] \propto 1$ yield a discrete, strongly unstable part of the spectrum. For a large delay the contributions from $e^{-\lambda\tau}$ terms become negligible if $\text{Re}[\lambda] > 0$. In the limit $\tau \rightarrow \infty$ the eigenproblem coincides with the Jacobian for the instantaneous fields only

$$\det \begin{pmatrix} i(\delta - 2\tilde{E}^*\tilde{E}) - 1 - \lambda & -i\tilde{E}\tilde{E} \\ i\tilde{E}^*\tilde{E}^* & i(2\tilde{E}\tilde{E}^* - \delta) - 1 - \lambda \end{pmatrix} = 0. \quad (7.12)$$

It leads to the characteristic polynomial

$$\lambda^2 + 2\lambda + 3|\tilde{E}|^4 - 4|\tilde{E}|^2\delta + \delta^2 + 1 = 0, \quad (7.13)$$

that yields two eigenvalues. For the studied parameter ranges only one real eigenvalue ever enters the right complex half plane while the other is real as well but always negative. Both eigenvalues recombine to form a complex conjugate pair for some parameters but no Andronov-Hopf bifurcation stems from it. Note however, that these eigenvalues are quantitatively accurate only in the case of positive real parts.

The other type of eigenvalues scales like $\text{Re}[\lambda] \propto 1/\tau$ so we may write $\lambda = \gamma/\tau + i\mu$. We define $Z = e^{-\gamma}e^{-i\mu\tau}$ whose modulus and argument are functions of γ and μ , respectively. After substituting the exponential terms in the determinant we have

$$\det \begin{pmatrix} [i(\delta - 2\tilde{E}^*\tilde{E}) - 1 - i\mu] + \frac{h\eta Z}{1 + \eta Z} & -i\tilde{E}\tilde{E} \\ i\tilde{E}^*\tilde{E}^* & [i(2\tilde{E}\tilde{E}^* - \delta) - 1 - i\mu] + \frac{h\eta^* Z}{1 + \eta^* Z} \end{pmatrix} = 0, \quad (7.14)$$

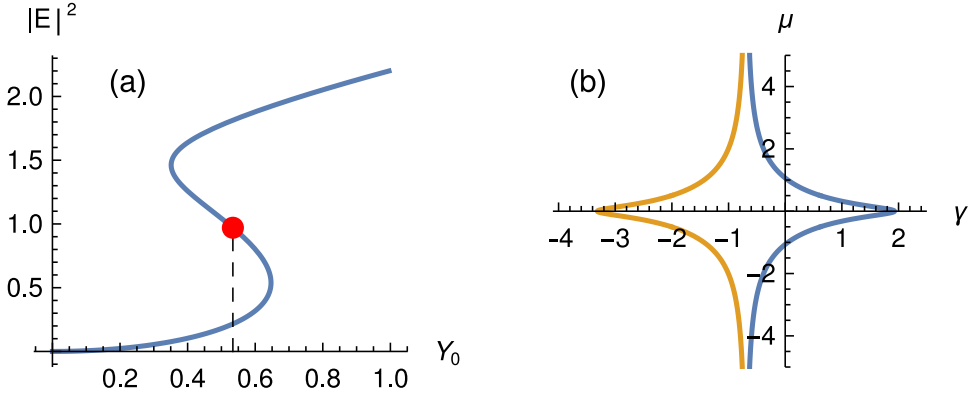


Figure 7.2: (a) Branch of CW solutions represented by the microcavity field intensity $|E|^2$ as a function of the injection amplitude Y_0 . A region of bistability exists between two folds. Both the upper and lower parts are stable while the connecting middle part is unstable. (b) Linear stability in the long delay limit for the point on the unstable part in (a) marked by a red dot at $Y_0 \approx 0.534$. The pseudo-continuous spectrum is uniformly unstable; it has penetrated into the right complex half plane symmetrically around the real axis thereby causing the folds. Other parameters are $h = 2$, $\delta = 1.5$ and $\eta = 0.5$, i.e. $\rho = 0.5$ and $\varphi = 0$.

which leads to a second order polynomial in Z . Solving for Z then yields two solutions that are functions of μ . Though the argument $\arg Z = -i\lambda\tau$ itself still depends on μ we find that in the long delay limit it effectively becomes a free parameter. Any phase can be obtained with an infinitesimal change of μ since $\tau \rightarrow \infty$. Thus, two solutions $Z_j(\mu)$ exist for any value of μ . We can then easily find $\gamma_j(\mu) = -\ln|Z_j|$ which define curves in the (γ, μ) -plane. These two branches of eigenvalues constitute the pseudo-continuous spectrum. Given any finite τ , the combinations of μ and Z must form self-consistent solutions of the transcendental characteristic equation. For larger τ the phase of Z oscillates faster and solutions are found more often along the imaginary direction. The asymptotic curves $\gamma_j(\mu)$ are populated by these solutions increasingly densely for $\tau \rightarrow \infty$ with the distance between neighboring eigenvalues tending to $\Delta\mu \approx 2\pi/\tau$.

Figure 7.2 shows the CW solution branch for the case of vanishing feedback phase $\varphi = 0$. Here, the branch folds twice thus forming a range of bistability between an upper and a lower intensity part. These are connected by a uniformly unstable part. The branch of the pseudo-continuous spectrum belonging to the uniform instability consists of an odd¹ number of eigenvalues. It possesses a single real eigenvalue at its tip that causes the folds of the CW branch, thus forming the bistable region. Due to the asymptotic spacing the first complex conjugate pair around the central real eigenvalue will have imaginary parts of approximately $\mu_{\pm 1} = \pm 2\pi/\tau$. This corresponds to a harmonic perturbation commensurate

¹ Though the eigenvalues along any branch of the pseudo-continuous spectrum form an infinite countable set, their total number is either odd or even. The spectrum is symmetric around the real axis, so most eigenvalues come in complex conjugate pairs. The question of parity comes down to whether there is a real eigenvalue in the middle or not.

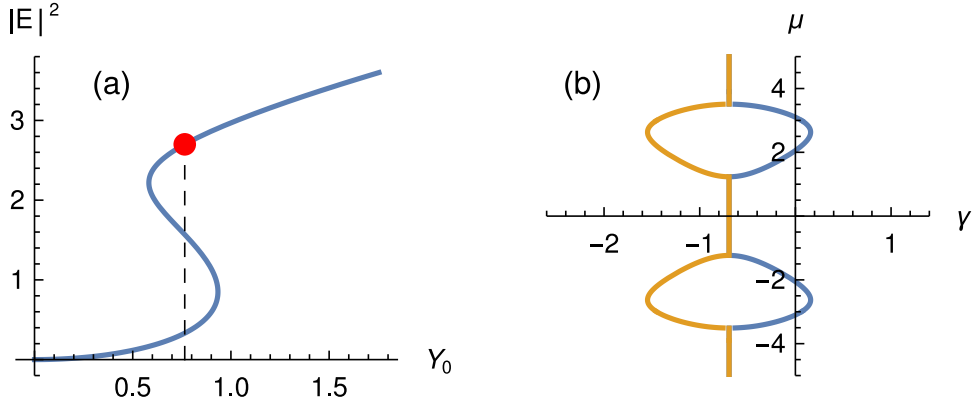


Figure 7.3: (a) Branch of CW solutions similar to Fig. 7.2. (b) Linear stability in the long delay limit for the point on the upper CW branch in (a) marked by a red dot at $Y_0 \approx 0.765$. The pseudo-continuous spectrum is Turing unstable; a complex conjugate pair of finite frequency bands penetrates into the right complex half plane thereby causing oscillations on the upper CW state. Other parameters are $h = 2$, $\delta = 1.5$ and $\eta = -0.5i$, i.e. $\rho = 0.5$ and $\varphi = -\pi/2$.

with the full external cavity, i.e. the delay time τ , and can give birth to TLSs as we will see in the following sections. Figure 7.3 shows a similar example where the upper CW state has become Turing unstable at $\varphi = -\pi/2$. The oscillations that appear in this scenario could be used to seed TLS in the system when modulating φ by slightly moving the feedbackmirror, e.g. with a Piezo stage.

In contrast to the previous situation shown in Figure 7.2, around $\varphi \approx \pi$ the second branch of the pseudo-continuous spectrum can become uniformly unstable instead of the first as shown in Figure 7.4. Here, the branch is made up entirely of pairs of eigenvalues resulting in an even number, so there is no real eigenvalue directly at the tip. The imaginary parts of the first pair are then $\mu_{\pm 1} \approx \pm\pi/\tau$ which corresponds to a period of twice the delay time and thus two external cavity roundtrips. Thus, this uniform instability causes an Andronov-Hopf bifurcation that leads to a regime of square waves where the system is alternating between two CW states with different intensities at the end of each roundtrip [Niz04, JAH15]. Note however, that there is no underlying bistability of CW solutions in this case, indeed there is no stable CW solution at all.

Transitions between odd and even numbered branches of the pseudo-continuous spectrum can occur in two ways. A complex pair at the tip may split into two different real eigenvalues. One remains at the tip of the branch while the other moves further into the right complex half plane. It thus separates from the pseudo-continuous part and enters the strongly unstable discrete part of the spectrum. This can readily be observed as the crossing of a single real eigenvalue of the instantaneous spectrum. Such a transition occurs for larger detuning for the parameters at interest. Alternatively, by crossing over each other two branches can both switch between odd and even at the same time without changing the overall number of eigenvalues constituting the pseudo-continuous part.

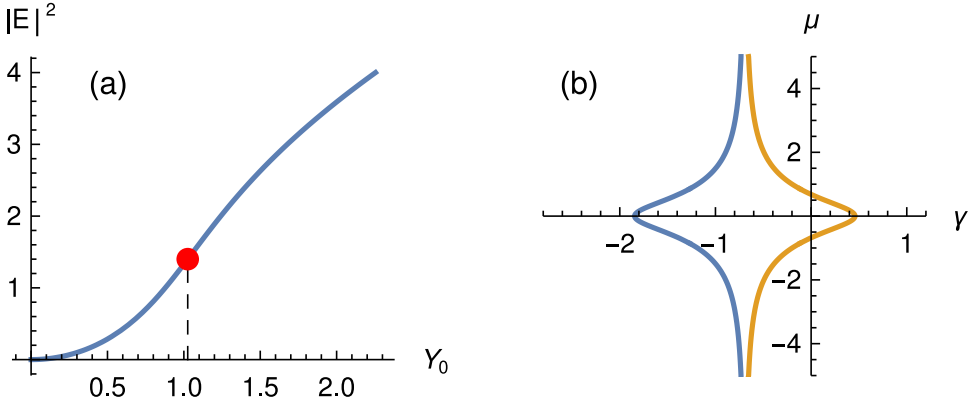


Figure 7.4: (a) Partly unstable branch of CW solutions represented by the microcavity field intensity $|E|^2$ as a function of the injection amplitude Y_0 . Unlike in Figures 7.2 and 7.3 there is no bistability. (b) Linear stability in the long delay limit for the point in (a) marked by a red dot at $Y_0 \approx 1.025$. The pseudo-continuous spectrum is uniformly unstable over an interval of the otherwise stable branch, albeit, there are no folds. Instead the instability gives rise to square waves. Other parameters are $h = 2$, $\delta = 1.5$ and $\eta = -0.5$, i.e. $\rho = 0.5$ and $\varphi = \pi$.

7.2 Temporal localized structures

The Kerr GTI is pumped by a coherent CW beam which is qualitatively quite different from the systems discussed in the previous chapters. There, temporal localized structures were sustained by the active materials in the microcavities and required a stable background of zero intensity. Thus, in the fully localized limit different pulses became truly independent. In the Kerr GTI, however, TLSs live on a constant CW background that causes them to be phase locked to it and thus to each other. Another important difference is the absence of a saturation trail in the carrier materials. This allows for the size of a TLS to indeed relate to its intensity profile, rather than to the gain recovery.

7.2.1 Dark and bright solitons

Figure 7.5 shows two different types of TLS found in direct numerical simulations of the Kerr GTI system (2.252), (2.253). The injection amplitude $Y_0 = 0.515$ is close to the middle of the bistable CW region and the delay time is $\tau = 50$. Otherwise the parameters from the CW example in Figure 7.2 are reused. Panel (a) shows a TLS that exists on top of the low intensity CW solution. It consists of a significant rise in intensity so we will refer to it as a bright TLS. It features some visible intensity oscillations on the leading edge whose origin lies in the cavity geometry and is related to the satellites encountered in the previous chapters. Panel (c) shows its counterpart on the high intensity CW solution. This TLS exhibits a stark drop in intensity and will henceforth be called a dark TLS. It features the same kind of oscillations due to third order dispersion. Via these small oscillations different TLSs can interact with each other, similar to Cherenkov radiation modeled by TOD in the Lugiato-Lefever equation [VGT18]. Note, that the peak intensity

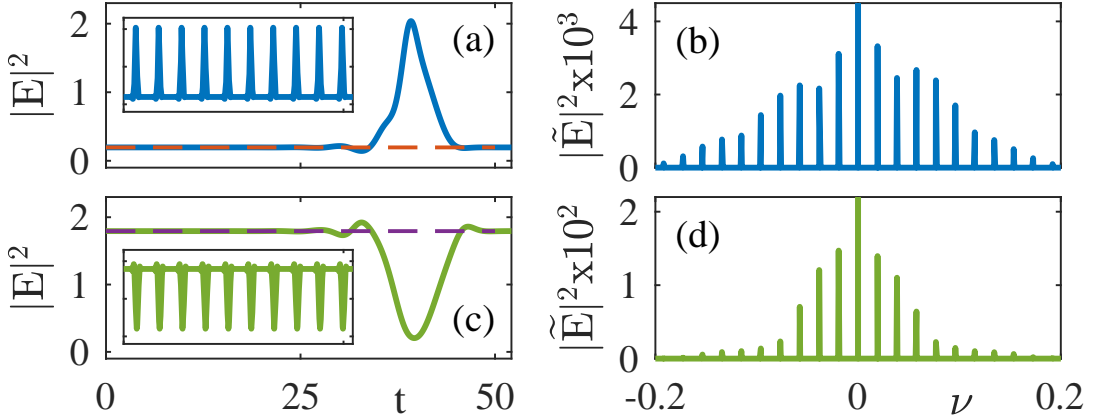


Figure 7.5: (a) Temporal profile of a bright TLS (solid blue) on a low intensity CW background (dashed orange). (c) Temporal profile of a dark TLS (solid green) on a high intensity CW background (dashed purple). The insets show corresponding pulse trains. (b,d) The respective frequency spectra. The delay is $\tau = 50$. A similar version of this figure was used in [6].

of the bright TLS is very close to the high intensity CW solution and likewise the dark TLS drops to about the level of the low intensity CW solution. The panels (b) and (d) show the frequency power spectra of the bright and dark TLSs, respectively. Because of the CW backgrounds the zero frequency is quite large and has been cut for clarity. Both feature a slight asymmetry while the bright spectrum is much broader and has extra peaks on the sides. These features correspond to the satellite oscillation due to TOD.

7.2.2 Hysteresis

Figure 7.6 shows a bifurcation diagram obtained via direct numerical simulations of both the TLS in Figure 7.5 and their respective CW background states with the injection amplitude Y_0 as the control parameter. To represent the different types of dynamics distinguishably in a single diagram the microcavity field intensity $|E|^2$ is averaged over one roundtrip. When changing the injection amplitude during the simulations different types of hysteresis are encountered. One can go back and forth between the high and low CW states when moving over the respective folds of the CW branch that limit the region of bistability, see Figure 7.2. Here, the intensity transitions smoothly to the opposite state over several roundtrips. This transition becomes quite sharp when Y_0 is far out of the bistable region. Doing this for only a few roundtrips and then going back into the bistable region can create the TLS.

For the given parameters the bright TLS branch extends further toward low injection amplitudes while the dark TLS branch extends further toward higher values. Both overlap in a large region and thus hysteresis can occur between the two types of TLS as well. Specifically dropping from the low injection edge of the dark TLS branch one can reach the bright TLS branch and, vice-versa, for sufficiently large injection one can go back to the dark TLS. At these points the TLS actually split apart into a pair of sharp front-like

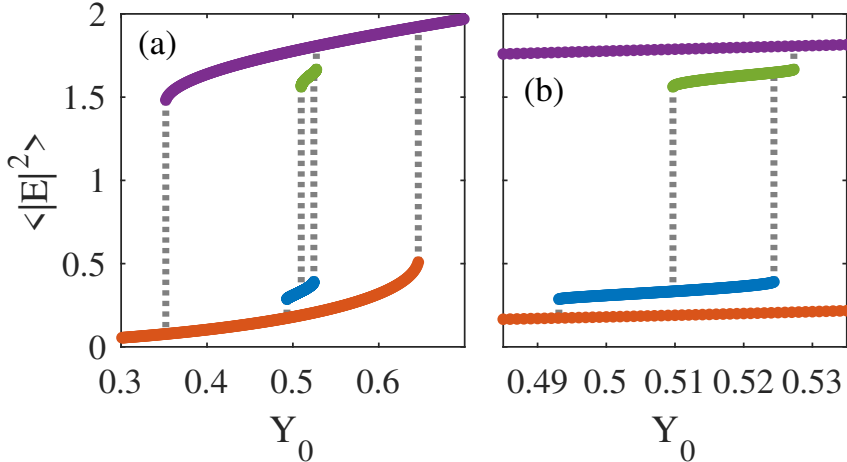


Figure 7.6: (a) Solution branches obtained from direct numerical simulations. The intensity is averaged over one roundtrip to better compare TLS and CW solutions. The upper (lower) CW solution is drawn in purple (orange) while the bright (dark) TLS is drawn in blue (green). Various hysteretic transitions between these states are observed as indicated by the dotted gray lines. (b) Shows a zoom on the TLS branches. A similar version of this figure was used in [6].

motions that switch from either CW state to the opposite. The hysteresis between dark and bright TLS is realized by those fronts moving apart and then reconnecting again to form the opposite TLS. This process is possible due to the periodic boundary conditions imposed by the external cavity. At the outer edges a transitions to the CW background happens via a simple collapse of the TLS, i.e., it just shrinks and dies out. When quickly moving far to the other side where only the opposite CW background is stable the fronts extinguish each other completely when they finally collide.

Figure 7.7 shows a pseudo-space-time diagram of a TLS transition from bright to dark obtained from a direct numerical simulation. During the simulation the injection amplitude Y_0 is changed back and forth several times between two values. At $Y_0 = 0.515$ the bright TLS starts out stable and only a small drift is observed. The value $Y_0 = 0.527$ is slightly above the bright TLS range of existence but still inside the respective dark TLS region. Here, the bright TLS speeds up and then quickly splits into a pair of fronts that drift apart. When going back to $Y_0 = 0.515$ for a while the fronts quickly go to a similar speed and hardly move with respect to each other over many roundtrips. For $Y_0 = 0.527$ they move further apart again and finally recombine the other way around as they meet again due to periodic boundary conditions. The resulting dark TLS quickly moves in the opposite direction as the unstable bright one did before splitting. Finally, back at $Y_0 = 0.515$ the dark TLS drifts at a very similar speed as the bright one did.

Stopping the relative motion of the fronts can be done at any point along the transition that is not too close to the initial or final TLS states where fronts always interlock. The exact value where the distance is perfectly constant can be called a Maxwell point [BK07, JAH15, TFHE⁺19] in analogy to systems with phase transitions where two phases coexist and the net exchange rates of particles are zero.

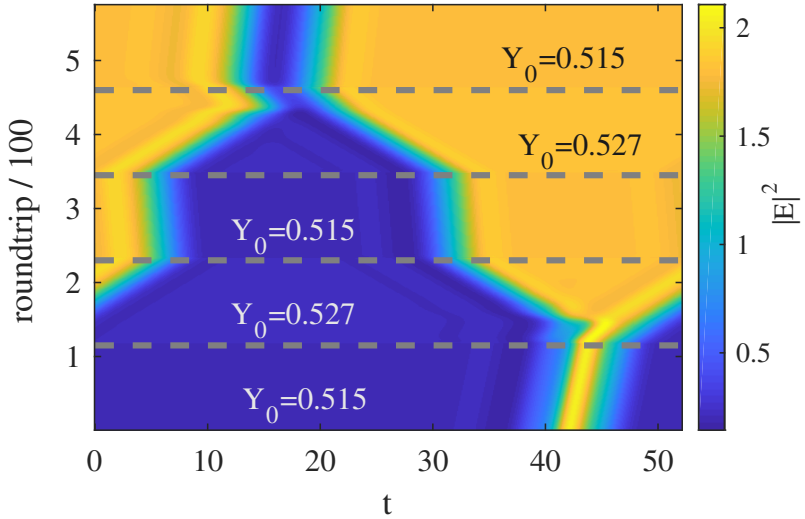


Figure 7.7: Pseudo-space-time representation of the transition from a bright to a dark TLS via a pair of moving fronts. The injection amplitude Y_0 is changed several times along the simulation as indicated by dashed gray lines. Both the bright and dark TLSs are stable at a common Y_0 . Also the distance between the fronts is virtually arrested if that value is set at any time during the transition. A similar version of this figure was used in [6].

7.3 Bifurcation analysis

Figure 7.8 shows the solution structure underlying the hysteresis discussed in the previous section. The data was obtained using numerical path continuation in DDE-BIFTOOL with a singular perturbation smallness parameter of $\epsilon = 1/20$. Two unstable periodic solutions are born close to each of the CW folds on the unstable connection in supercritical Andronov-Hopf bifurcations. Both periodic orbits start as small harmonic perturbations that grow into the dark and bright TLSs toward the middle of the bistable region and then each stabilize in a fold. The branches continue to fold back and forth with the folds converging toward a common asymptotic value $Y_0 \approx 0.51524$ where they finally combine. This point indeed corresponds to the Maxwell point encountered in the direct numerical simulations of the previous section. The stability of the periodic orbits switches with snaking. This scenario may be called a kind of double collapsing homoclinic snaking [BK07, KW05].

The Andronov-Hopf bifurcation points that create the TLS solutions move onto the CW folds asymptotically for large delays. This is due to the CW branch being uniformly unstable in the long delay limit. The tip of the pseudo-continuous spectrum is shaped like parabola around the real axis, see Figure 7.2. The bistable region is born in a cusp bifurcation when the central real eigenvalue on the tip of the spectrum crosses the imaginary axis. Toward the middle of the resulting unstable CW connection the spectrum increasingly protrudes into the right complex half plane. For larger τ the spectrum gets filled more densely with complex conjugate pairs of eigenvalues that gradually come in

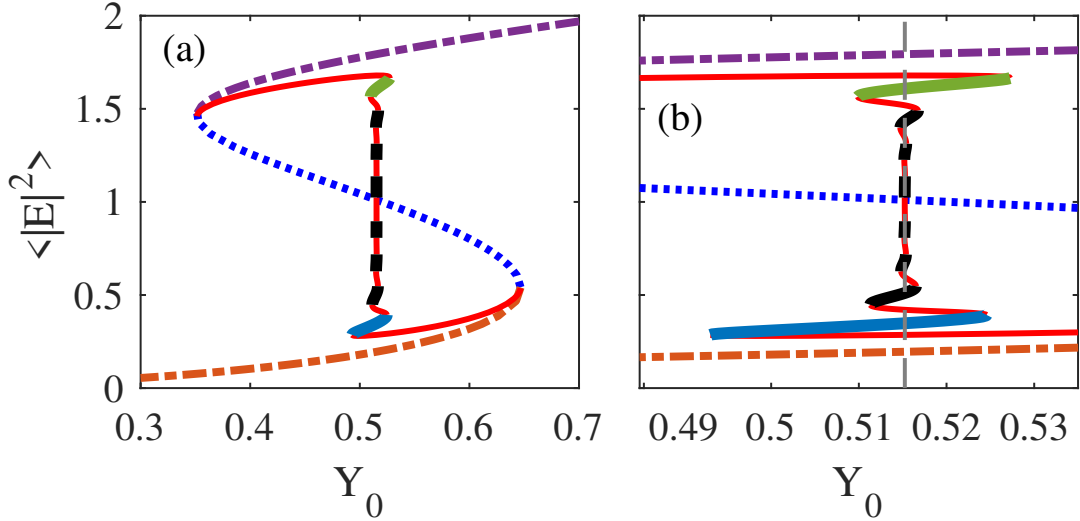


Figure 7.8: Bifurcation diagram obtained using numerical path continuation. It directly corresponds to Fig. 7.6 As a solution measure the average intensity per roundtrip is shown. (a) The stable high (low) intensity CW branch is presented in dash-dotted purple (orange) while the unstable CW connection is depicted in dotted dark blue. A TLS branch connects the CW solutions very close to the folds. It is drawn with thick black lines where stable and thin red lines where unstable. The dark and bright primary TLS branches are highlighted in green and light blue, respectively. (b) Zoom on the TLS solutions. The TLS branches exhibit a kind of double collapsed snaking from both the dark and bright sides. They all tend to an asymptotic value $Y_0 \approx 0.51524$ where a continuous connection of the TLSs takes place. This is indicated by a vertical gray dashed line. A similar version of this figure was used in [6].

from $\pm\infty$ toward the tip on the real axis. For any point on the unstable CW branch this means that increasing τ causes a series of Andronov-Hopf bifurcation similar to harmonic mode locking solutions. The first of these bifurcations creates the principal TLS. Since the grade of protrusion becomes less toward the CW folds more τ is necessary for this to occur. In the long delay limit an infinitesimal part of the spectrum is sufficient so that the fold and Andronov-Hopf bifurcations virtually coincide.

Figure 7.9 shows the temporal intensity profiles of the sequence of periodic solutions on the snaking TLS branch at the Maxwell point (MP). The profiles are stacked in the same order as the snaking TLS branch crosses the Maxwell point in Figure 7.8 where the first and last profiles correspond to the half-grown bright and dark TLS, respectively. A staggered transition between bright and dark TLS with alternating stability is found. The TLSs split into a pair of fronts whose distance changes with a roughly constant speed along the snaking. Both fronts exhibit leading satellite oscillations because of the third order dispersions induced by the cavity geometry. A front can stably interlock with the next one at any order of these oscillations leading to a series of preferred distances or slots. Close to the Maxwell point the evolution of the system will dynamically choose

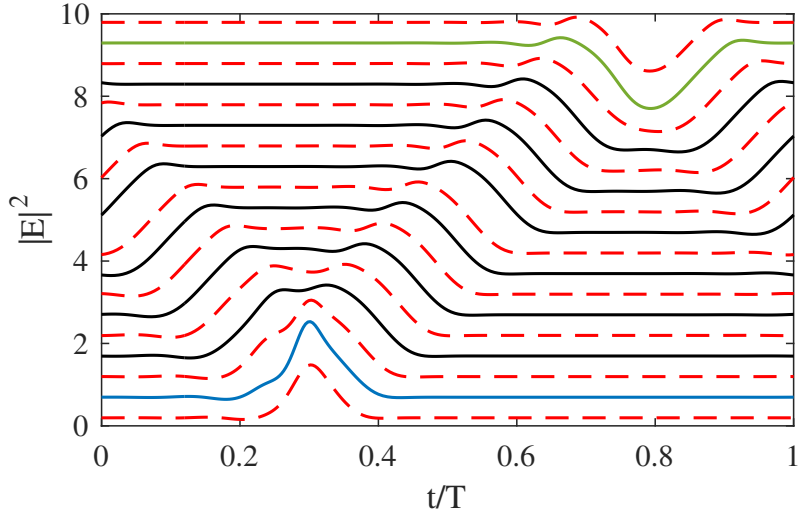


Figure 7.9: Transition of bright to dark TLS periodic solutions. The temporal intensity profiles are stacked rendering the y-axis for relative reference only. Stable (unstable) periodic orbits are shown in solid black (dashed red). The principal TLSs are highlighted in blue and green for bright and dark, respectively. A similar version of this figure was used in [6].

one of the neighboring slots and settle on it. The point where this choice flips directly corresponds to the interspersed unstable limit cycles. Thus the fronts do not actually just stop moving when setting an appropriate injection amplitude but rather form the closest stable solution. This limits the analogy to the original concept of a Maxwell point.

The amplitude of the leading satellite oscillations tapers off with increasing distance from the front. This is the reason for the snaking to collapse toward the Maxwell point. The locking force becomes weaker for higher order slots and starts to lose against the tendency of the fronts to drift apart. Thus the widths of the stable branches become increasingly narrow. For finite delays some width of the overall structure always remains. Only in the long delay limit one may strictly speak of a Maxwell point as this width shrinks to zero. Note the small shift of the front distance in the middle of Figure 7.9 that stands against the linear trend. This is indeed an effect of the rather small τ used in the continuations. Due to the stiffness introduced by the singular perturbation a significantly larger delay would disturb the stability analysis of the periodic orbits and prevent continuation of their bifurcation.

7.3.1 Coinciding drift velocities

Figure 7.10 shows a bifurcation diagram of the drift velocities belonging to the periodic solutions along the collapsing homoclinic snaking branch. In this representation the branch crosses itself many times with most of the crossings forming a cluster around the asymptotic Maxwell point. Generally the drift of predominantly bright structures increases with the injection amplitude while predominantly dark ones become slower. Also the speed of higher order parts of the snaking branch diverges from Maxwell point. For the $\tau = 50$

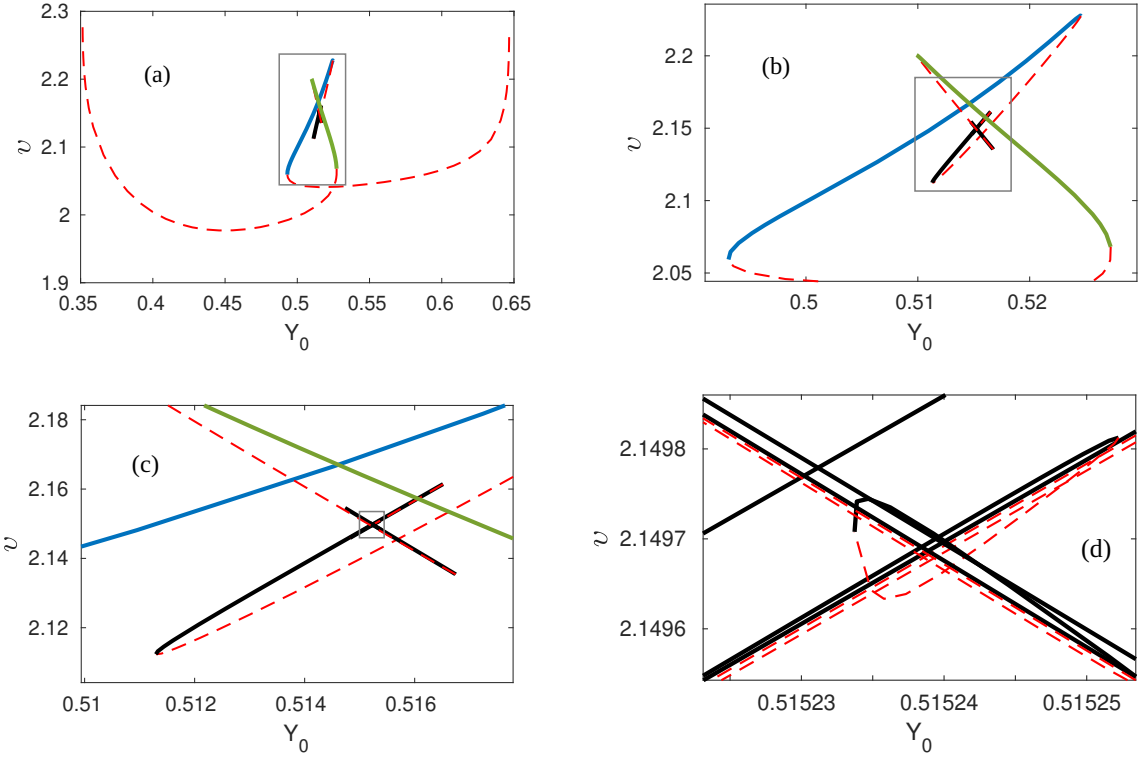


Figure 7.10: Bifurcation diagram showing the drift velocity $v = T - \tau$ of the periodic solutions on the snaking TLS branch. Stable (unstable) solutions are represented by solid black (dashed red) lines. The primary bright and dark TLS branches are highlighted in blue and green, respectively. (a) The complete snaking branch. (b-d) Consecutive zooms on the areas indicated by the gray boxes in the respective previous panel. Several crossings of stable branches exist with most of them in a cluster around the asymptotic Maxwell point.

example the branch forms a small loop around the cluster which is a direct consequence finite delay, see panel (d). Towards the long delay limit this loop would further deform to create more crossings leaving an even closer residual loop. The rest of the branch is hardly affected anymore. The corresponding solutions would generally resemble a broad rectangular bright or dark TLS of variable width. If we imagines several of such structures in a single long external cavity we can infer from this their relative drift speeds and thus estimate the time they take to run into each other. This can be used to judge the grade of metastability of the possible combinations.

In panel (c) one finds two crossings of stable solutions that clearly diverge from the Maxwell point in both drift speed and injection amplitude. They correspond to the combinations of the principle dark and bright TLSs and the principle dark TLS with the second order bright TLS. Indeed the branches of the principal TLS branches lie quite far from the others that virtually form a single cross from this point of view. This makes the principle TLS incompatible with the higher order structures on long time scales spanning many roundtrips. Indeed they cannot be metastably combined at all because this would require

switching between the CW background states somewhere in between opposite pairs of TLS. Those fronts however move with the asymptotic lines of the crossing at the maxwell point and would therefore eventually hit the TLS.

7.3.2 Regions of localized solutions

Figure. 7.11 shows bifurcation diagrams of fold bifurcation branches obtained via numerical path continuation. For the example detuning of $\delta = 1.5$ the bistability of the CW background exists in more than half of the full interval of the delay phase $\varphi \in [-\pi, \pi]$ as shown in panel (a). This region slants toward higher injection amplitude Y_0 when increasing φ and is limited by cusps in the negative φ , low Y_0 and positive φ , high Y_0 corners. It is centered around $\varphi \approx 0.2\pi$ where the bistability is widest in Y_0 . The regions of the first order TLS solutions follow the same trend with the bright TLS region almost connecting the CW folds. In contrast the dark TLS region is much narrower in Y_0 and ends roughly in the center of the bright TLS and CW bistability regions. Panel (b) shows the situation for a fixed delay phase $\varphi = 0$ and uses the detuning as the second control parameter instead. Again the bistable region slants toward higher Y_0 for more detuning but continues to grow wider. The principal CW cusp defines a minimum detuning for bistability at $\delta = 1/\sqrt{3}$ for the given parameter set.

These regions only correspond to the existence of solutions but do not imply their stability. Indeed the feedback phase is an important control parameter that can cause several bifurcations of the CW background solutions in addition to the folds that create the bistable region. When increasing it beyond about $\varphi > 0.1$ a Turing instability appears on the high intensity CW solution. Therefore dark TLS are no longer found in direct numerical simulations as the corresponding background will oscillate. In the beginning,

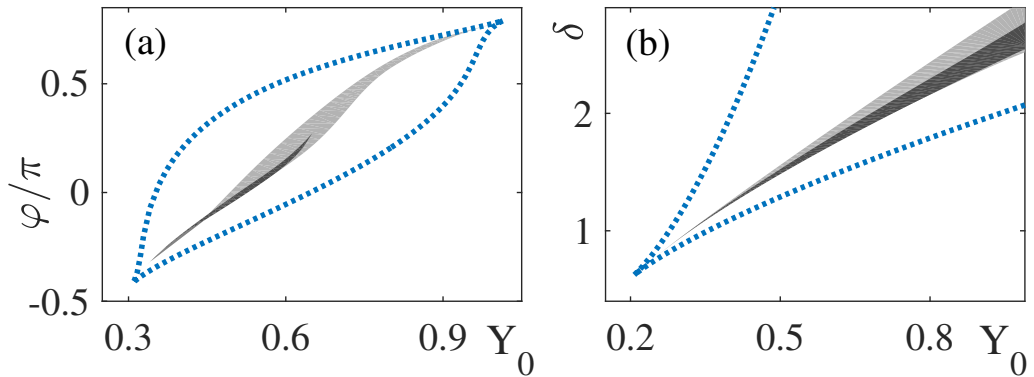


Figure 7.11: Two dimensional bifurcation diagrams showing the evolution of fold bifurcations. The folds of the CW solutions are depicted as dotted blue lines. The area between bright (dark) TLS folds is filled with light (dark) gray. (a) The feedback phase φ against the injection amplitude Y_0 . Other parameters are $\delta = 1.5$, $\rho = 0.5$. (b) The detuning δ against the injection amplitude Y_0 . Other parameters are, $\rho = 0.5$ and $\varphi = 0$. A similar version of this figure was used in [6].

the principal bright TLS is hardly affected by this but its higher order cousins begin to destabilize. This becomes intuitively clear when interpreting these TLSs as a pair of fronts switching between the lower and upper CW states. Since the upper state is unstable the time that can be spent close to it is limited. Increasing φ further causes the principal bright TLS to enter an oscillating regime. The leading low to high CW front remains stable but is followed by quasi-periodic or even chaotic oscillations of the intensity that finally drops back to the low CW background. These oscillations can even result in the creation of new leading fronts such that an oscillating TLS effectively splits and the external cavity gets populated by them. Finally, the Turing instability dominates any dynamics that are not confined to the stable lower CW state. Indeed, this effect can be exploited to create TLS when the system is in the upper CW state. By moving the feedback mirror by a sub wavelength amount the feedback phase can easily be changed. The resulting oscillations decay into TLSs when moving the mirror back toward its original position.

7.4 Complex patterns

The concept of using the interlocking of fronts at variable distances to create temporal localized structures opens up the possibility to build very complex shapes. In a long external cavity they can be combined into patterns almost arbitrarily.

7.4.1 Complex molecules

The existence of bright and dark TLSs implies that both types of fronts connecting the CW solutions can interlock to their counterpart. Thus, there is no reason why the second front should not be able to lock to a third and so on. Here, the only requirement is that fronts appear in an alternating order, and indeed always in pairs, to preserve continuity. Complicated molecular shapes can be formed when using many front pairs. In principle each front can lock to any of the leading oscillations of the next front. Figure 7.12 shows an example with three pairs that form a single localized structure. Such TLS can be categorized and labeled by the numbers of the locking slots and their background states. The example is a 0-1-1-3-2 molecule on the low intensity CW background or simply a bright 0-1-1-3-2 TLS. For an appropriate injection amplitude any number of pairs can be combined in an arbitrary fashion provided that the external cavity be long enough. The highest possible oscillation order to interlock stably depends on distance to the Maxwell point.

7.4.2 Coexistence of TLSs

Different TLS can in a sufficiently long external cavity. At large distances their mutual coupling is negligible and they remain fully localized. Figure 7.13 shows an example with a double bright 0-1-0 molecule and a single principal bright 0 TLS. By modulation of the injected CW pumping beam the TLS can be manipulated. Both amplitude and phase modulation can be used to create, erase and move them around similar to solitons in injected Kerr fibers [JECM15]. The natural relative movement of different types of TLSs

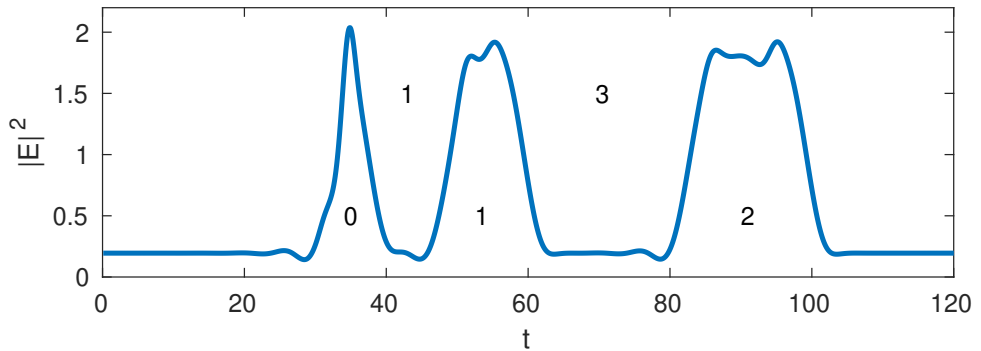


Figure 7.12: Temporal intensity profile of a single TLS molecule made up of three pairs of fronts. The numbers signify at which order of the satellite oscillations the fronts have interlocked. This example is labeled a bright 0-1-1-3-2 molecule. Arbitrary combinations are possible, limited only by the delay and the distance from the Maxwell point.

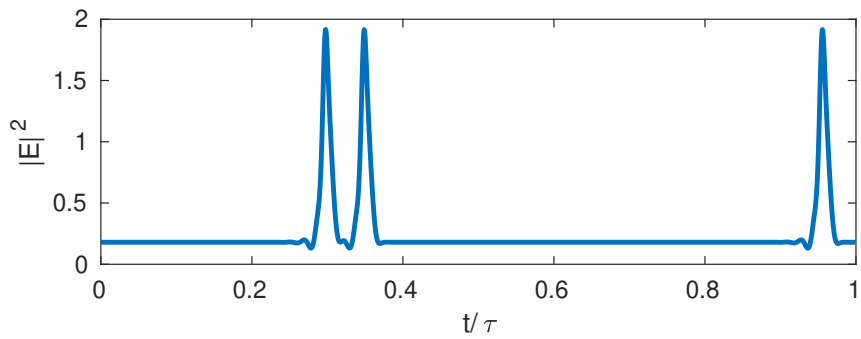


Figure 7.13: Temporal intensity profile of different TLSs coexisting independently in a long external cavity. A single bright TLS and two others locked together as a 0-1-0 molecule. Their mutual distance will vary over many roundtrips as the drift velocities are not exactly equal. Such mixed states are thus metastable.

may be suppressed by locking them to a modulation profile that has period similar to the roundtrip time.

One can build very complex combinations of fronts and move them around with respect to each other. Figure 7.14 shows an example of a long external cavity containing the simplest bright and dark 0, 1 and 2 TLS followed by the lowest order 0-0-0 and 0-0-0-0 molecules on their respective low and high intensity backgrounds. Several transitions between the background states are realized with single fronts and the simplest combinations of odd numbers, i.e., 0-0 up and down fronts. The whole temporal profile is stable except for small drift variations among the fronts and TLSs, thus recombinations occur after many roundtrips. Indeed most of the possible combinations are only metastable, see also Section 7.3.1. Such patterns correspond to highly specific frequency comb spectra.

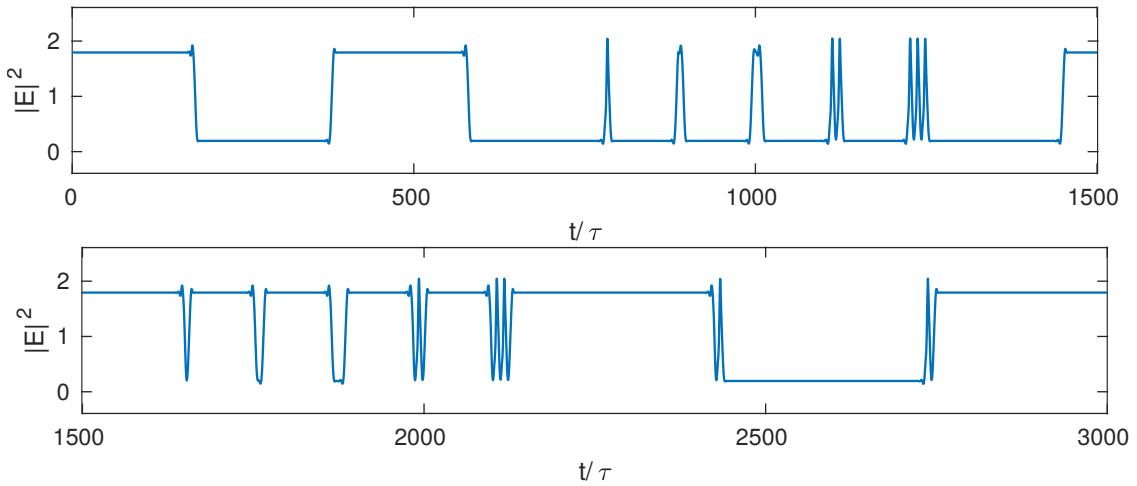


Figure 7.14: Temporal intensity profile in a long external cavity $\tau = 3000$. One can put many fronts and combine low and high CW sections containing different TLS molecules inside. Both panels together represent a single metastable state.

7.5 Time-advanced equation

Mathematically the TLSs are periodic orbits of the differential equation (2.252) that contains delayed terms. Due to causality the period of such a solution must be larger than the delay time $T > \tau$ which results in a residual drift $v = T - \tau$. In the long delay limit this drift approaches an asymptotic value, i.e., T and τ both grow to infinity with a constant difference. Virtually the whole time domain is then filled with an almost constant background state. Thus, an alternative interpretation arises by considering the TLS to be homoclinic orbits of a slightly different system, namely where the time-delay is replaced by a time-advance equal to the drift v , i.e. $E(t - \tau) \rightarrow E(t + v)$. A good approximation of v can be found via numerical path continuation when using a sufficiently long delay. The aforementioned periodic and homoclinic orbits of the respective systems indeed coincide in the long delay limit. This approach can be used for stability analysis of TLSs in delayed systems [YRSW19]. The spectrum decomposes into a discrete part of localized modes that affect the TLS directly but quickly decay to the sides and a pseudo-continuous spectrum that corresponds to the stability of the background state. Figure 7.15 shows concept of the delay to advance transformation.

We can now use the time-advance, i.e. a negative delay, in the stability analysis of the CW background solution. The obtained eigenvalues with the smallest moduli of the real parts can be interpreted as an unstable background mode in front of the TLS and a stable one behind, respectively. These (un)damped oscillations can be fitted to the temporal TLS profile in order to find matching prefactors. Figures 7.16 and 7.17 show an exemplary pulse with the matched exponential modes. The satellite oscillations due to third order dispersion are very well described by these modes. Hence, the prefactors may in principle be used to build an interaction potential that describes the interlocking of the switching fronts as a force.

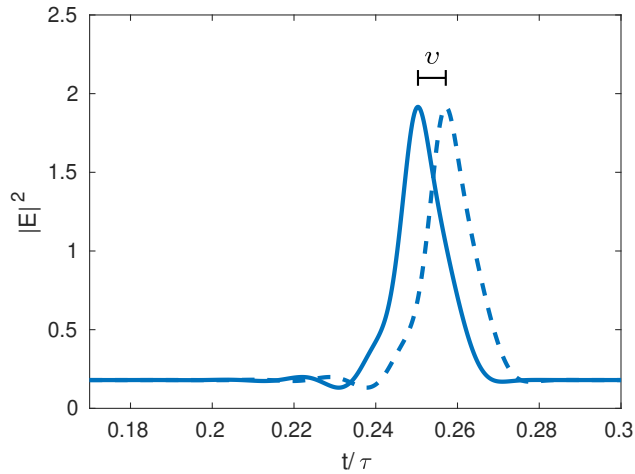


Figure 7.15: Evolution of the temporal profile of an initial principal bright TLS in solid blue and in dashed blue after one roundtrip. The offset $v = T - \tau$ can be reinterpreted as an advance $\tau \rightarrow -v$. The periodic orbit of the delayed system thus becomes a homoclinic orbit of the advanced system instead.

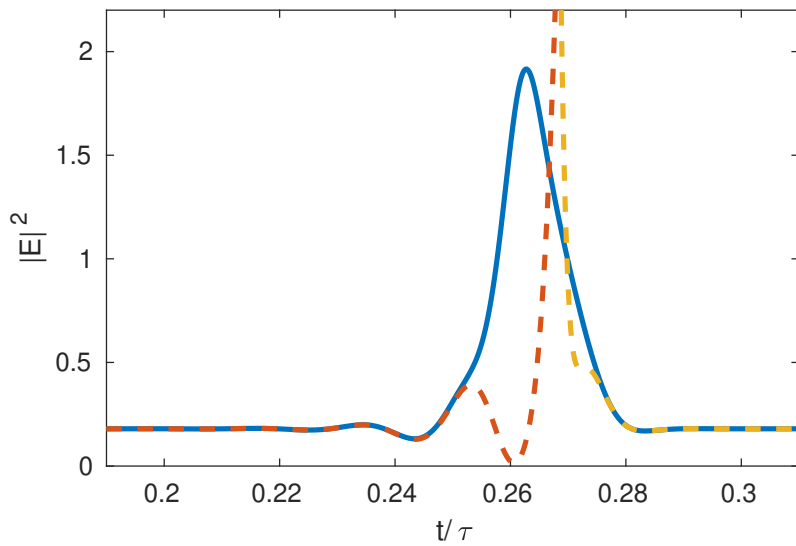


Figure 7.16: Temporal intensity profile of a bright TLS in solid blue with matching exponential modes of the background in dashed orange (yellow) for the leading (trailing) edge. The prefactors of the modes are chosen to fit the TLS.

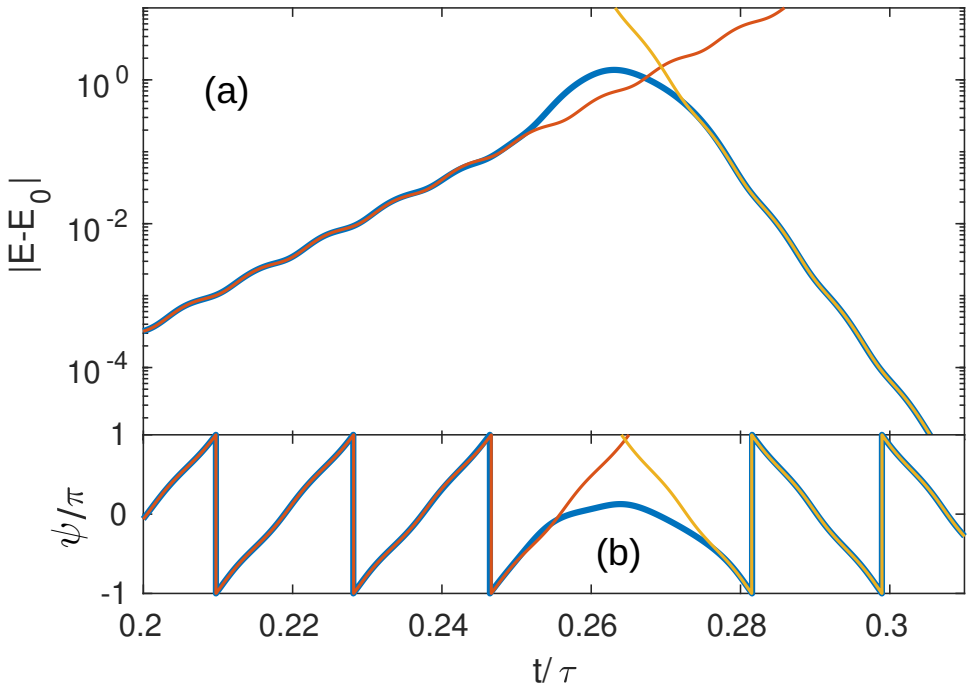


Figure 7.17: Profile of Fig. 7.16 in blue represented by the modulus of its amplitude offset to the CW background (a) and the corresponding complex phase (b). The matched modes are superposed in thin orange and yellow for the leading and trailing edges, respectively.

8 Summary and Outlook

Passive mode-locking and temporal localized structures can be obtained in vertical-external-cavity surface-emitting-lasers. Their transverse dimensions can be exploited for high power applications and TLSs can potentially be compatible with spatial pattern formation and localization in such systems. For this thesis, models specifically tailored to describing them have been derived from first principles. First, a well established unidirectional ring laser DDE model for passive mode-locking [VT05] was used for comparison with the other models that consider the specific aspects of VECSELs and coupled microcavities. They consist of differential equations for the evolution of the electric field in the microcavities that contain a thin region of quantum wells as the active material and are subjected to injection [MB05]. The microcavities are coupled in such a way that they inject each other or re-inject themselves with their outputs after one roundtrip in the external cavity. This leads to delay algebraic equations that describe all the multiple reflections which appear in the regime of strong feedback. While this DAE approach departs from models used in the literature, we argue that the DAEs simply represents the boundary conditions of the wave equation in the multiple sections. The DAE modeling approach exhibits the influence of strong TOD that emerges as a direct consequence of the coupled microcavity geometry. This can severely modify the pulse shape by creating satellites. These can destabilize the pulse, thus introducing additional regions of oscillatory dynamics in the parameter space.

A functional mapping for the efficient simulation of PML and TLSs was developed and implemented for all three of the semiconductor PML laser models discussed in this thesis. It mainly consists in the separate treatment of the so called fast and slow stages of a pulsed laser. The interval around the pulse, where the dynamics of the field and carriers are fast, is integrated fully while the recovery of the gain between consecutive pulses can be approximated by an analytic solution when assuming the field intensity to be zero. This approximation proves valid in the comparison with numerical results of the full system. Accurate results are obtained for the most important types of behavior including fundamental mode-locking, Q-switched mode-locking and slow pulse instabilities. This is a clear advantage as compared to approaches utilizing approximate partial differential equation models, also called Haus master equations [Hau00]. While having a similar computational efficiency such models lack certain behaviors like Q-switched mode-locking. The FM allows for the simulation of macroscopic time scales to analyze, e.g., timing jitter or thermal effects. Numerical path continuation of the FM itself is in principle possible and may be developed into an efficient algorithm.

Continuation of the full models has been achieved in DDE-BIFTOOL directly for the unidirectional ring laser and for the MIXSEL and Kerr GTI where the DAE can be approximated by a singularly perturbed delay differential equation. This approach, however, introduces additional stiffness that severely limits stability analysis and bifurcation point continuation of periodic solutions in combination with large delay. The DAE models con-

sidered in this manuscript can be written in the form of neutral delay differential equations that can be treated in DDE-BIFTOOL with an experimental extension [BKW06]. As they avoid the additional stiffness introduced by the singular perturbation approach this poses a promising route for improvements and further study. It could potentially be further improved using the techniques developed in [YRSW19].

The analysis of the unidirectional ring laser model provides a baseline of expectable TLS behavior. Gain linewidth enhancement induces amplitude-phase coupling and causes pulses to flatten by spreading out their intensity in time. This can induce a type of oscillation which is termed a trailing edge instability due to the shape of the dynamics when regarded in a pseudo-space-time representation. Absorber linewidth enhancement has been observed to counteracts this effect. Multiple types of solutions with an increasing number of intensity peaks have been found via numerical path continuation. The manifolds corresponding to the higher orders start unstable but they can cross over with the stable principal one and among each other in transcritical bifurcations thus forming a large interconnected structure. Without path continuation this difference in the origin of stable solutions is not obvious. A Haus PDE approximation can be derived where a slow time variable describes the roundtrip dynamics of a pulse that exists as a profile in a pseudo space dimension which corresponds to a fast time scale. Here, the pulse dynamics are influenced by spatial derivative terms instead of delayed feedback which allows for parallelization along the spatial dimension in simulations. Also, this makes the model interesting from a bifurcation analysis points of view as many techniques and tools are available for the treatment of PDEs. Overall, the solution structure and region of TLS existence is well conserved by this approximation, but the border of the oscillation region can be qualitatively different from the original DDE model.

The VCSEL-RSAM model has been successfully able to describe results obtained in a corresponding experimental realization. With parameters matching the nonlinear mirror properties the behavior of TLSs and the transition to harmonic pulse trains was predicted accurately. Further, an additional kind of instability has been found in simulations and dynamics similar to it could be seen in the experiments. This instability could not be found in the unidirectional ring laser model. The coupled microcavities constitute a significantly different geometry that causes strong third order dispersion. For appropriate combinations of the linewidth enhancement factors and the detuning between the microcavities TOD can dominate over second order dispersion. In this regime pulses can have a leading series of decaying but significantly large satellites. Intuitively, these can be interpreted as the part of the pulse that was directly reflected and not filtered by the microcavity during the previous roundtrip. These satellites can become unstable when large enough to bleach the absorber. In this situation the net-gain window is opened prematurely and the satellite grows. As a consequence the gain saturation encountered by the parent pulse is reduced and it starts to die out to finally be replaced by its satellite. Indeed, this process can repeat and thus result in a stable quasi-periodic oscillation.

The MIXSEL system can be considered a simpler version of the VCSEL-RSAM system with both gain and saturable absorber in a single microcavity. Thus, it only has half the number of electric field variables and the bandwidth ratio and detuning parameters of the two cavities no longer appear. Yet, the same types of dynamics encountered in the more complicated system are retained. This makes the analysis of the satellite instability much

easier. Using numerical path continuation the solution branches can be obtained. For zero linewidth enhancement factors a branch with multiple folds has been found. At a high gain saddle node bifurcation the satellite oscillation sets in with infinite period in a global SNIPER bifurcation. For some small gain linewidth enhancement factor the origin of the satellite instability transforms into an Andronov-Hopf bifurcation, yet the resulting dynamics remain the same for most of the satellite unstable region. With more realistic values for the linewidth enhancement parameters the situation becomes more complex. A larger pulse with leading satellites is bistable with a smaller single pulse. In a part of the bistable region the larger satellite pulse is unstable with the resulting quasi-periodic dynamics showing characteristics of both the satellite instability and amplitude-phase coupling mixed together. As a consequence, optimization of the pulse width becomes a trade-off. Too narrow a pulse will grow satellites and destabilize thus limiting the possibility of stable narrow pulses. Apart from the satellite instability the behavior of TLSs remains similar to what is already known from the unidirectional ring laser. The Haus PDE approach delivers similar results as well. Like in the ring laser model the folds responsible for the principal TLS region and the satellite instability are well preserved. So is the transition from SNIPER to Andronov-Hopf and the corresponding branch. However, the trailing edge and mixed dynamics are, again, qualitatively different.

The Kerr GTI is a different type of system as compared to the VECSEL systems discussed earlier but can also be described in a similar framework involving a DAE. Its microcavity containing a Kerr nonlinear medium is passive and coupled to an external cavity which is coherently pumped by a CW injection beam. It can be build with the same technologies applied for VECSELs. The passive microcavity can be imagined as a standard VCSEL but with the QW resonance far off the microcavity resonance and injection frequency. The Kerr GTI DAE model can be derived as well for an analogous system comprised of a short Kerr fiber loop, that resembles the microcavity, coupled to a long delay fiber loop that forms the external cavity. Thus, an alternative route for experimental implementation is accessible with established technology. Note, that one of the advantages of using mirrors over fibers lies in the ease of adjusting their mutual distance which renders the repetition rate of the system tunable.

For sufficiently large detuning the system has two bistable continuous wave solutions with distinctly different intensities. Via linear stability analysis in the long delay limit, a uniform instability has been identified to both cause the folds of the CW branch and give rise to temporal localized structures that can live on the CW backgrounds. Principally, a bright TLS shaped as a peak on the low intensity CW background and dark TLS shaped as a dip on the high background are found. A hysteretic transition exists between them. The TLS can split into a pair of fronts that each connect the two CW states, forming an intensity profile that is roughly rectangular in time. Those fronts move at different drift velocities and eventually meet again, due to the periodic boundary conditions of the external cavity, where they can recombine to form the TLS of the opposite type. This relative movement can be arrested completely at various distances, similar to systems with phase transitions. In analogy, the effect is termed a Maxwell point. Very similar behavior is known to exist in injected Kerr fibers where, in contrast, the nonlinear effects are distributed along the whole cavity.

The underlying solution structure consists of a single TLS solution branch which snakes

around and toward the asymptotic Maxwell point from both CW background states and thus connects them in the middle. This can be called a double collapsing homoclinic snaking scenario. While snaking back and forth, the branch keeps alternating between stable and unstable parts. The fronts appear together with leading satellite oscillations on the preceding CW state which are caused by third order dispersion incurred by the cavity geometry, not unlike the satellites leading mode-locked pulses in the previous systems. The satellite structure allow the fronts to lock at different orders of these oscillations, thereby creating a series of stable distances that form the transition.

While TLSs are normally regarded as periodic orbits of a system with time-delayed feedback, they can be reinterpreted as homoclinic orbits of an equivalent system with time-advanced feedback. Here, the time-advance is given by the offset between the time-delay and the actual period of the orbit. In the long delay limit this offset indeed approaches a finite asymptotic value. Stability analysis of these homoclinics yields a set of exponentially growing and shrinking oscillations on the left and right tail of the TLS peak, respectively. These oscillations fit the satellite oscillations of the pulse profiles very accurately and could be used to derive an interaction potential that describes the attraction and interlocking of fronts as a force. Several front pairs can be combined to form molecules that, in the localization regime, can be arranged into arbitrary temporal patterns. Such patterns might be useful as LIDAR (light detection and ranging) signals for being well distinguishable. Since the relative drift speeds are small, the patterns are metastable and vary little over many roundtrips, potentially leaving them recognizable in the reflection signal.

A distinct class of dynamics observed in the Kerr GTI model is square waves that appear for destructive feedback phases. The field stays at some CW intensity for a whole roundtrip and then switches to another pseudo CW state. In the simplest case the intensity alternates between two such states but there can be more. Transitions happen via period doubling as well as period tripling bifurcations and possibly even higher orders. This regime may thus exhibit chaotic behavior. It is possible to approximate the square waves by a discrete mapping. In the long delay limit the transitions between CW intensity levels become negligibly short and the field in the microcavity is merely the equilibrated reaction to a virtually constant injection of the external cavity field from the previous roundtrip. Both then combine to form the next state of this injection. The delay algebraic equation of the full model thus reduces to a simple relation of the current and following discrete states. Given this rather concise description, additional study on this regime can be carried out with reduced computational effort.

More complex setups using Kerr microcavities can be envisioned. Two separate injections beams could be coupled into a single KGTI such that, when modulating their intensities or phase offset, the cumulative injection would change. Thus, one should be able to switch the state of the microcavity field as a function of two inputs. Such a switching element might be used to build photonic logic gates to serve as building blocks for photonic circuits.

List of Publications

- [1] C. Schelte, J. Javaloyes, and S. V. Gurevich. Dynamics of temporally localized states in passively mode-locked semiconductor lasers. *Phys. Rev. A*, 97:053820, May 2018.
- [2] C. Schelte, J. Javaloyes, and S. V. Gurevich. Functional mapping for passively mode-locked semiconductor lasers. *Opt. Lett.*, 43(11):2535–2538, Jun 2018.
- [3] P. Camelin, C. Schelte, A. Verschelde, A. Garnache, G. Beaudoin, I. Sagnes, G. Huyet, J. Javaloyes, S. V. Gurevich, and M. Giudici. Temporal localized structures in mode-locked vertical external-cavity surface-emitting lasers. *Opt. Lett.*, 43(21):5367–5370, Nov 2018.
- [4] S. V. Gurevich, C. Schelte, and J. Javaloyes. Impact of high-order effects on soliton explosions in the complex cubic-quintic Ginzburg-Landau equation. *Phys. Rev. A*, 99:061803(R), Jun 2019.
- [5] C. Schelte, P. Camelin, M. Marconi, A. Garnache, G. Huyet, G. Beaudoin, I. Sagnes, M. Giudici, J. Javaloyes, and S. V. Gurevich. Third Order Dispersion in Time-Delayed Systems. *Phys. Rev. Lett.*, 123:043902, Jul 2019.
- [6] C. Schelte, A. Pimenov, A. G. Vladimirov, J. Javaloyes, and S. V. Gurevich. Tunable Kerr frequency combs and temporal localized states in time-delayed Gires–Tournois interferometers. *Opt. Lett.*, 44(20):4925–4928, Oct 2019.
- [7] C. Schelte, D. Hessel, J. Javaloyes, and S. V. Gurevich. Dispersive Instabilities in Passively Mode-Locked Integrated External-Cavity Surface-Emitting Lasers. *Phys. Rev. Applied*, 13:054050, May 2020.

List of Acronyms

Acronym	Definition
AH	Andronov-Hopf bifurcation
CCQGLE	Complex Cubic-Quintic Ginzburg-Landau Equation
CW	Continuous Wave radiation
DAE	Delay Algebraic Equation
DBR	Distributed Bragg Reflector
DDE	Delay Differential Equation
DNS	Direct Numerical Simulation
FM	Functional Mapping
FWHM	Full Width at Half Maximum
GLE	Ginzburg-Landau Equation
GTI	Gires-Tournois Interferometer
KGTI	Kerr GTI
MIXSEL	Mode-locked Integrated External-Cavity Surface-Emitting-Laser
NDDE	Neutral Delay Differential Equation
ODE	Ordinary Differential Equation
PDE	Partial Differential Equation
PML	Passive Mode-Locking
QW	Quantum Well
RK	Runge-Kutta method
RSAM	Resonant Saturable Absorber Mirror
SNIPER	Saddle-Node Infinite-PERiod
TLS	Temporal Localized Structures
TOD	Third Order Dispersion
VCSEL	Vertical-Cavity Surface-Emitting Lasers
VECSEL	Vertical External-Cavity Surface-Emitting Lasers

List of Figures

1.1	Schematics of elementary light and matter interactions	1
1.2	Schematics of gain, absorption and saturation	4
1.3	Concept of passive mode-locking	5
1.4	Concept of pseudo-space-time representation	7
1.5	Concept of temporal localized structures	9
2.1	Gain around a direct band gap of a semiconductor	17
2.2	Unidirectional ring laser schematic	21
2.3	Injected microcavity schematic	29
2.4	Generic VECSEL schematic	35
2.5	VCSEL-RSAM schematic	37
2.6	MIXSEL schematic	39
2.7	Injected Kerr GTI schematic	40
3.1	Delay integration memory arrangement	41
3.2	Hermite delay interpolation	43
3.3	Functional mapping concept	47
4.1	Modes in long delay limit	56
4.2	Development from harmonic perturbation to TLS	58
4.3	TLS branch in ring model	61
4.4	Existence range as a function of α and s	61
4.5	Multi-bump solutions	62
4.6	Trailing edge instability pseudo-space-time diagram	64
4.7	DNS of trailing edge instability for various g	65
4.8	DNS of trailing edge instability for various α	66
4.9	g - α bifurcation diagram using the functional mapping	67
4.10	Multi-bump solution loops	69
4.11	Crossover of loops	70
4.12	Transcritical bifurcation	71
4.13	Peak intensity of asymmetric nonzero β case	72
4.14	Period deviation of asymmetric nonzero β case	73
4.15	Bifurcation branches of ring model	74
4.16	Temporal profiles along secondary fold	75
4.17	Convergence analysis toward localized regime	76
4.18	Comparison of DNS and continuation	77
4.19	Comparison of DDE and Haus PDE continuations	79
4.20	Timing jitter analysis using the functional mapping	80

4.21	Q-switched mode locking in the functional mapping	81
5.1	RSAM CW reflection	85
5.2	VCSEL CW reflection	86
5.3	VCSEL-RSAM threshold	86
5.4	TLS matched to experiment	89
5.5	TLS region as function of α -factors	91
5.6	Empty cavity response	93
5.7	Satellite replacing parent pulse	96
5.8	Low frequency instability in VCSEL-RSAM	96
5.9	Stable pulse with leading satellites	98
5.10	Breathing satellites	99
5.11	Spotted satellite instability	100
5.12	Sliding satellite instability	101
5.13	Jumping satellite instability	102
5.14	Satellite instability at experimental parameters	104
5.15	Asymmetric Soliton explosions in CCQGLE	106
5.16	Third order dispersion oscillation in CCQGLE	106
6.1	Zero α_j satellite instability	111
6.2	Non-zero α_j satellite instability	112
6.3	Bistability pseudo-space-time	114
6.4	Bistability time trace	115
6.5	Regions of behavior	117
6.6	Regions in long delay limit	118
6.7	Continuation profiles	119
6.8	Log profile in simulation	120
6.9	Log profile in continuation	120
6.10	Satellite convergence	121
6.11	Period convergence	121
6.12	Spurious Floquet analysis	122
6.13	Zero linewidth enhancement bifurcation diagram	123
6.14	Unstable fold profile	124
6.15	Floquet analysis with functional mapping	126
6.16	Neutral modes	126
6.17	Period scalings	128
6.18	Non-zero linewidth enhancement bifurcation diagram	129
6.19	Andronov-Hopf time traces	129
6.20	Pseudo-space-time diagrams close to SNIPER-AH transition	130
6.21	Schematic for Adler equation	132
6.22	Excitable dynamics	133
6.23	Excitability statistics	134
6.24	PDE vs DAE comparison for zero linewidth enhancement	136
6.25	PDE vs DAE comparison for non-zero linewidth enhancement	137

7.1	Instabilities of the pseudo-continuous spectrum	141
7.2	Bistability between CW background states	143
7.3	Turing unstable upper CW state	144
7.4	Uniform instability causing square waves	145
7.5	Dark and bright TLS	146
7.6	Hysteresis of solutions	147
7.7	Transition from bright to dark TLSs	148
7.8	Double collapsing homoclinic snaking	149
7.9	Transition of front pairs	150
7.10	Different drift velocities	151
7.11	Existence regions of TLS solutions	152
7.12	Complex single TLS molecule	154
7.13	Coexistence of independent TLS	154
7.14	Complex combinations	155
7.15	Temporal drift as advance	156
7.16	Mode matching in intensity	156
7.17	Mode matching in amplitude and phase	157

Bibliography

[AA08] N. Akhmediev and A. Ankiewicz. *Dissipative Solitons: From Optics to Biology and Medicine Series*, volume 751 of *Lecture Notes in Physics*. Springer Berlin Heidelberg, 2008.

[Adl46] R. Adler. A study of locking phenomena in oscillators. *Proceedings of the IRE*, 34(6):351–357, 1946.

[AEK88] N. Akhmediev, V. M. Eleonskii, and N. E. Kulagin. Exact first order solutions of the nonlinear Schrödinger equation. *Theor. Math. Phys. (USSR)*, 72:809–818, 1988.

[AGLM92] F. T. Arecchi, G. Giacomelli, A. Lapucci, and R. Meucci. Two-dimensional representation of a delayed dynamical system. *Phys. Rev. A*, 45:R4225–R4228, Apr 1992.

[AH87] F. T. Arecchi and R. G. Harrison. *Instabilities and Chaos in Quantum Optics*, volume 34 of *Springer Series in Synergetics*. Springer Berlin Heidelberg, 1987.

[AK87] N. Akhmediev and V. I. Korneev. Modulation instability and periodic solutions of the nonlinear Schrödinger equation. *Theor. Math. Phys. (USSR)*, 69:1089–1093, 1987.

[AK02] I. S. Aranson and L. Kramer. The world of the complex Ginzburg-Landau equation. *Rev. Mod. Phys.*, 74:99–143, Feb 2002.

[AP01] Y. A. Astrov and H.G. Purwins. Plasma spots in a gas discharge system: birth, scattering and formation of molecules. *Physics Letters A*, 283(5):349 – 354, 2001.

[Bén01] H. Bénard. Les tourbillons cellulaires dans une nappe liquide. - Méthodes optiques d’observation et d’enregistrement. *J. Phys. Theor. Appl.*, 10(1):254–266, 1901.

[BG64] G. Bret and F. Gires. Giant-pulse laser and light amplifier using variable transmission coefficient glasses as light switches. *Applied Physics Letters*, 4(10):175–176, 1964.

[BK07] John Burke and Edgar Knobloch. Homoclinic snaking: Structure and stability. *Chaos: An Interdisciplinary Journal of Nonlinear Science*, 17(3):037102, 2007.

BIBLIOGRAPHY

[BKW06] D. A. W. Barton, B. Krauskopf, and R. E. Wilson. Collocation schemes for periodic solutions of neutral delay differential equations. *Journal of Difference Equations and Applications*, 12(11):1087–1101, 2006.

[BMSM05] I.N. Bronstein, H. Mühlig, K.A. Semendjajew, and G. Musiol. *Taschenbuch der Mathematik (Bronstein)*. Harri Deutsch GmbH, 2005.

[BPT⁺05] M. Bache, F. Prati, G. Tissoni, R. Kheradmand, L.A. Lugiato, I. Protsenko, and M. Brambilla. Cavity soliton laser based on vcsel with saturable absorber. *Appl. Phys. B*, 81:913–920, 2005.

[CBH⁺13] A. Coillet, I. Balakireva, R. Henriet, K. Saleh, L. Larger, J. M. Dudley, C. R. Menyuk, and Y. K. Chembo. Azimuthal turing patterns, bright and dark cavity solitons in Kerr combs generated with whispering-gallery-mode resonators. *IEEE Photonics Journal*, 5(4):6100409–6100409, Aug 2013.

[CC97] A. Couairon and J. M. Chomaz. Pattern selection in the presence of a cross flow. *Phys. Rev. Lett.*, 79:2666–2669, Oct 1997.

[CD16] C. Cartes and O. Descalzi. Periodic exploding dissipative solitons. *Phys. Rev. A*, 93:031801, Mar 2016.

[CGT64] R. Y. Chiao, E. Garmire, and C. H. Townes. Self-trapping of optical beams. *Phys. Rev. Lett.*, 13:479–482, Oct 1964.

[CJMG16] P. Camelini, J. Javaloyes, M. Marconi, and M. Giudici. Electrical addressing and temporal tweezing of localized pulses in passively-mode-locked semiconductor lasers. *Phys. Rev. A*, 94:063854, Dec 2016.

[CKSI94] W. W. Chow, S. W. Koch, and M. Sargent III. *Semiconductor Laser Physics*. Springer-Verlag, Berlin, 1994.

[CSCA02] S. T. Cundiff, J. M. Soto-Crespo, and N. Akhmediev. Experimental evidence for soliton explosions. *Phys. Rev. Lett.*, 88:073903, Feb 2002.

[CZF⁺18] B. Chomet, J. Zhao, L. Ferrieres, M. Myara, G. Guiraud, G. Beaudoin, V. Lecocq, I. Sagnes, N. Traynor, G. Santarelli, S. Denet, and A. Garnache. High-power tunable low-noise coherent source at $1.06\mu\text{m}$ based on a surface-emitting semiconductor laser. *Appl. Opt.*, 57(18):5224–5229, Jun 2018.

[DSA⁺07] P. Del’Haye, A. Schliesser, O. Arcizet, T. Wilken, R. Holzwarth, and T. J. Kippenberg. Optical frequency comb generation from a monolithic microresonator. *Nature*, 450:1214–1217, 2007.

[Ein05] A. Einstein. Über einen die Erzeugung und Verwandlung des Lichtes betreffenden heuristischen Gesichtspunkt. *Annalen der Physik*, 322(6):132–148, 1905.

[Ein17] Albert Einstein. Zur Quantentheorie der Strahlung. *Physikalische Zeitschrift*, 18:121–128, 1917.

[EJWY17] T. Erneux, J. Javaloyes, M. Wolfrum, and S. Yanchuk. Introduction to focus issue: Time-delay dynamics. *Chaos: An Interdisciplinary Journal of Nonlinear Science*, 27(11):114201, 2017.

[ELR02] K. Engelborghs, T. Luzyanina, and D. Roose. Numerical bifurcation analysis of delay differential equations using DDE-BIFTOOL. *ACM Trans. Math. Softw.*, 28(1):1–21, March 2002.

[Fit55] R. FitzHugh. Mathematical models of threshold phenomena in the nerve membrane. *Bulletin of Mathematical Biophysics*, 17:257–278, 1955.

[FLS11] R. P. Feynman, R. B. Leighton, and M. Sands. *The Feynman Lectures on Physics, Vol. II: The New Millennium Edition: Mainly Electromagnetism and Matter*. Basic Books, 2011.

[GBCC14] C. Godey, I. V. Balakireva, A. Coillet, and Y. K. Chembo. Stability analysis of the spatiotemporal Lugiato-Lefever model for Kerr optical frequency combs in the anomalous and normal dispersion regimes. *Phys. Rev. A*, 89:063814, Jun 2014.

[GBGT08] P. Genevet, S. Barland, M. Giudici, and J. R. Tredicce. Cavity soliton laser based on mutually coupled semiconductor microresonators. *Phys. Rev. Lett.*, 101:123905, Sep 2008.

[GGG⁺97] M. Giudici, C. Green, G. Giacomelli, U. Nespolo, and J. R. Tredicce. Andronov bifurcation and excitability in semiconductor lasers with optical feedback. *Phys. Rev. E*, 55:6414–6418, Jun 1997.

[GHT⁺02] A. Garnache, S. Hoogland, A. C. Tropper, I. Sagnes, G. Saint-Girons, and J. S. Roberts. Sub-500-fs soliton-like pulse in a passively mode-locked broadband surface-emitting laser with 100 mW average power. *Applied Physics Letters*, 80:3892–3894, 2002.

[GJ17] S. V. Gurevich and J. Javaloyes. Spatial instabilities of light bullets in passively-mode-locked lasers. *Phys. Rev. A*, 96:023821, Aug 2017.

[GJTB15] B. Garbin, J. Javaloyes, G. Tissoni, and S. Barland. Topological solitons as addressable phase bits in a driven laser. *Nat. Com.*, 6, 2015.

[GP96] G. Giacomelli and A. Politi. Relationship between delayed and spatially extended dynamical systems. *Phys. Rev. Lett.*, 76:2686–2689, Apr 1996.

[GSC08] P. Grelu and J. M. Soto-Crespo. Temporal soliton "molecules" in mode-locked lasers: Collisions, pulsations, and vibrations. In *Dissipative Solitons: From Optics to Biology and Medicine*, volume 751 of *Lecture Notes in Physics*, pages 1–37. Springer Berlin Heidelberg, 2008.

[GT64] F. Gires and P. Tournois. Interferometre utilisable pour la compression d'impulsions lumineuses modulees en frequence. *C. R. Acad. Sci. Paris*, (258):6112–6115, 1964.

- [GWM⁺17] B. Garbin, Y. Wang, S. G. Murdoch, G. L. Oppo, S. Coen, and M. Erkintalo. Experimental and numerical investigations of switching wave dynamics in a normally dispersive fibre ring resonator. *The European Physical Journal D*, 71(9):240, Sep 2017.
- [Hau76] H. A. Haus. Parameter ranges for cw passive mode locking. *IEEE Journal of Quantum Electronics*, 12(3):169–176, 1976.
- [Hau00] H. A. Haus. Mode-locking of lasers. *IEEE J. Selected Topics Quantum Electron.*, 6:1173–1185, 2000.
- [HBJ⁺13] T. Herr, V. Brasch, J. D. Jost, C. Y. Wang, N. M. Kondratiev, M. L. Gorodetsky, and T. J. Kippenberg. Temporal solitons in optical microresonators. *Nature Photonics*, 8:145, Dec 2013.
- [HBM10] M. Heuck, S. Blaaberg, and J. Mørk. Theory of passively mode-locked photonic crystal semiconductor lasers. *Opt. Express*, 18(17):18003–18014, Aug 2010.
- [HDT⁺00] S. Hoogland, S. Dhanjal, A. C. Tropper, J. S. Roberts, R. Häring, R. Paschotta, F. Morier-Genoud, and U. Keller. Passively mode-locked diode-pumped surface-emitting semiconductor lasers. *IEEE Photonics Technology Letters*, 12:1135–1137, 2000.
- [Hen82] C. Henry. Theory of the linewidth of semiconductor lasers. *Quantum Electronics, IEEE Journal of*, 18(2):259–264, Feb 1982.
- [HFP64] L. E. Hargrove, R. L. Fork, and M. A. Pollack. Locking of He–Ne laser modes induced by synchronous intracavity modulation. *Applied Physics Letters*, 5(1):4–5, 1964.
- [HLGJ20] J. Hausen, K. Lüdge, S. V. Gurevich, and J. Javaloyes. How carrier memory enters the Haus master equation of mode-locking. *Opt. Lett.*, 45(22):6210–6213, Nov 2020.
- [HPA⁺02] R. Häring, R. Paschotta, A. Aschwanden, E. Gini, F. Morier-Genoud, and U. Keller. High-power passively mode-locked semiconductor lasers. *Quantum Electronics, IEEE Journal of*, 38:1268–1275, 2002.
- [HPG⁺01] R. Haring, R. Paschotta, E. Gini, F. Morier-Genoud, D. Martin, H. Melchior, and U. Keller. Picosecond surface-emitting semiconductor laser with > 200 mW average power. *Electronics Letters*, 37(12):766–767, Jun 2001.
- [HPMG⁺99] C. Hönninger, R. Paschotta, F. Morier-Genoud, M. Moser, and U. Keller. Q-Switching stability limits of continuous-wave passive mode locking. *J. Opt. Soc. Am. B*, 16(1):46–56, Jan 1999.
- [HT73] A. Hasegawa and F. Tappert. Transmission of stationary nonlinear optical pulses in dispersive dielectric fibers. I. Anomalous dispersion. *Applied Physics Letters*, 23(3):142–144, 1973.

[JAH15] J. Javaloyes, T. Ackemann, and A. Hurtado. Arrest of domain coarsening via anti-periodic regimes in delay systems. *Phys. Rev. Lett.*, 115:223901, Nov 2015.

[Jav16] J. Javaloyes. Cavity light bullets in passively mode-locked semiconductor lasers. *Phys. Rev. Lett.*, 116:043901, Jan 2016.

[JB10a] J. Javaloyes and S. Balle. Mode-locking in semiconductor Fabry-Pérot lasers. *Quantum Electronics, IEEE Journal of*, 46(7):1023 –1030, july 2010.

[JB10b] J. Javaloyes and S. Balle. Quasiequilibrium time-domain susceptibility of semiconductor quantum wells. *Phys. Rev. A*, 81(6):062505, Jun 2010.

[JB12] J. Javaloyes and S. Balle. Freetwm: a simulation tool for multisection semiconductor lasers. <http://onl.uib.es/softwares>, 2012.

[JBL46] F. Brink Jr, D. W. Bronk, and M. G. Larrabee. Chemical excitation of nerve. *Annals of the New York Academy of Sciences*, 47(4):457–485, 1946.

[JCMG16] J. Javaloyes, P. Camelin, M. Marconi, and M. Giudici. Dynamics of localized structures in systems with broken parity symmetry. *Phys. Rev. Lett.*, 116:133901, Mar 2016.

[JECM15] J. K. Jang, M. Erkintalo, S. Coen, and S. G. Murdoch. Temporal tweezing of light through the trapping and manipulation of temporal cavity solitons. *Nature Communications*, 6:7370, Jun 2015.

[JHS⁺91] J. L. Jewell, J. P. Harbison, A. Scherer, Y. H. Lee, and L. T. Florez. Vertical-cavity surface-emitting lasers: Design, growth, fabrication, characterization. *IEEE Journal of Quantum Electronics*, 27(6):1332–1346, 1991.

[KBK⁺95] F. X. Kaertner, L. R. Brovelli, D. Kopf, M. Kamp, I. G. Calasso, and U. Keller. Control of solid state laser dynamics by semiconductor devices. *Optical Engineering*, 34(7):2024 – 2036, 1995.

[KMM64] P. Kafalas, J. I. Masters, and E. M. E. Murray. Photosensitive liquid used as a nondestructive passive Q-switch in a ruby laser. *Journal of Applied Physics*, 35(8):2349–2350, 1964.

[Kon02] S. Kondo. The reaction-diffusion system: a mechanism for autonomous pattern formation in the animal skin. *Genes to Cells*, 7(6):535–541, 2002.

[KW05] J. Knobloch and T. Wagenknecht. Homoclinic snaking near a heteroclinic cycle in reversible systems. *Physica D: Nonlinear Phenomena*, 206(1):82 – 93, 2005.

[LCK⁺10] F. Leo, S. Coen, P. Kockaert, S. P. Gorza, P. Emplit, and M. Haelterman. Temporal cavity solitons in one-dimensional Kerr media as bits in an all-optical buffer. *Nature Photonics*, 4:471–476, May 2010.

BIBLIOGRAPHY

- [LF10] S. C. V. Latas and M. F. S. Ferreira. Soliton explosion control by higher-order effects. *Opt. Lett.*, 35(11):1771–1773, Jun 2010.
- [LK80] R. Lang and K. Kobayashi. External optical feedback effects on semiconductor injection laser properties. *IEEE Journal of Quantum Electronics*, 16(3):347 – 355, mar 1980.
- [LL87] L. A. Lugiato and R. Lefever. Spatial dissipative structures in passive optical systems. *Phys. Rev. Lett.*, 58:2209–2211, May 1987.
- [LLKG15] V. E. Lobanov, G. Lihachev, T. J. Kippenberg, and M.L. Gorodetsky. Frequency combs and platicons in optical microresonators with normal GVD. *Opt. Express*, 23(6):7713–7721, Mar 2015.
- [LMB⁺10] A. Laurain, M. Myara, G. Beaudoin, I. Sagnes, and A. Garnache. Multiwatt-power highly-coherent compact single-frequency tunable vertical-external-cavity-surface-emitting-semiconductor-laser. *Opt. Express*, 18(14):14627–14636, Jul 2010.
- [LMK⁺13] F. Leo, A. Mussot, P. Kockaert, P. Emplit, M. Haelterman, and M. Taki. Nonlinear symmetry breaking induced by third-order dispersion in optical fiber cavities. *Phys. Rev. Lett.*, 110:104103, Mar 2013.
- [LN79] J. Lajzerowicz1 and J. J. Niez. Phase transition in a domain wall. *J. Physique Lett.*, 40(7):165–169, 1979.
- [Mai60] T. H. Maiman. Stimulated optical radiation in ruby. *Nature*, 187:493, 1960.
- [MB05] J. Mulet and S. Balle. Mode locking dynamics in electrically-driven vertical-external-cavity surface-emitting lasers. *Quantum Electronics, IEEE Journal of*, 41(9):1148–1156, 2005.
- [MBPV⁺07] C. P. Martin, M. O. Blunt, . Pauliac-Vaujour, A. Stannard, P. Moriarty, I. Vancea, and U. Thiele. Controlling pattern formation in nanoparticle assemblies via directed solvent dewetting. *Phys. Rev. Lett.*, 99:116103, 2007.
- [MBR⁺07] D. J. H. C. Maas, A. R. Bellancourt, B. Rudin, M. Golling, H. J. Unold, T. Südmeyer, and U. Keller. Vertical integration of ultrafast semiconductor lasers. *Applied Physics B*, 88(4):493–497, Sep 2007.
- [MJBG14] M. Marconi, J. Javaloyes, S. Balle, and M. Giudici. How lasing localized structures evolve out of passive mode locking. *Phys. Rev. Lett.*, 112:223901, Jun 2014.
- [MJBG15] M. Marconi, J. Javaloyes, S. Balle, and M. Giudici. Passive mode-locking and tilted waves in broad-area vertical-cavity surface-emitting lasers. *Selected Topics in Quantum Electronics, IEEE Journal of*, 21(1):85–93, Jan 2015.

[ML66] C. Magono and C. W. Lee. Meteorological classification of natural snow crystals. *Journal of the Faculty of Science, Hokkaido University. Series 7, Geophysics*, 2(4):321–335, 1966.

[MLA⁺08] A. Mussot, E. Louvergneaux, N. Akhmediev, F. Reynaud, L. Delage, and M. Taki. Optical fiber systems are convectively unstable. *Phys. Rev. Lett.*, 101:113904, Sep 2008.

[MLA⁺18] T. Malica, J. Lin, T. Ackemann, D. J. Little, J. P. Toomey, D. Pabœuf, W. Lubeigt, N. Hempler, G. Malcolm, G. T. Maker, and D. M. Kane. Mapping the dynamical regimes of a sesam mode-locked vecsel with a long cavity using time series analysis. *Opt. Express*, 26(13):16624–16638, Jun 2018.

[MSG80] L. F. Mollenauer, R. H. Stolen, and J. P. Gordon. Experimental observation of picosecond pulse narrowing and solitons in optical fibers. *Phys. Rev. Lett.*, 45:1095–1098, Sep 1980.

[NAY62] J. Nagumo, S. Arimoto, and S. Yoshizawa. An active pulse transmission line simulating nerve axon. *Proceedings of the IRE*, 50(10):2061–2070, 1962.

[Niz04] M. Nizette. Stability of square oscillations in a delayed-feedback system. *Phys. Rev. E*, 70:056204, Nov 2004.

[NO93] H. Nishimori and N. Ouchi. Formation of ripple patterns and dunes by wind-blown sand. *Phys. Rev. Lett.*, 71:197–200, Jul 1993.

[OSF99] G. L. Oppo, A. J. Scroggie, and W. J. Firth. From domain walls to localized structures in degenerate optical parametric oscillators. *Journal of Optics B: Quantum and Semiclassical Optics*, 1(1):133–138, jan 1999.

[PAV20] A. Pimenov, S. Amiranashvili, and A. G. Vladimirov. Temporal cavity solitons in a delayed model of a dispersive cavity ring laser. *Math. Model. Nat. Phenom.*, 15:47, 2020.

[PHBH05] T. Piwonski, J. Houlihan, T. Busch, and G. Huyet. Delay-induced excitability. *Phys. Rev. Lett.*, 95:040601, Jul 2005.

[PJGV18] A. Pimenov, J. Javaloyes, S. V. Gurevich, and A. G. Vladimirov. Light bullets in a time-delay model of a wide-aperture mode-locked semiconductor laser. *Philosophical Transactions of the Royal Society of London A: Mathematical, Physical and Engineering Sciences*, 376(2124), 2018.

[Pla01] M. Planck. Ueber das Gesetz der Energieverteilung im Normalspectrum. *Annalen der Physik*, 309(3):553–563, 1901.

[PRGG17] P. Parra-Rivas, D. Gomila, and L. Gelens. Coexistence of stable dark- and bright-soliton Kerr combs in normal-dispersion resonators. *Phys. Rev. A*, 95:053863, May 2017.

- [PRGH⁺19] P. Parra-Rivas, L. Gelens, T. Hansson, S. Wabnitz, and F. Leo. Frequency comb generation through the locking of domain walls in doubly resonant dispersive optical parametric oscillators. *Opt. Lett.*, 44(8):2004–2007, Apr 2019.
- [PRGK⁺16] P. Parra-Rivas, D. Gomila, E. Knobloch, S. Coen, and L. Gelens. Origin and stability of dark pulse Kerr combs in normal dispersion resonators. *Opt. Lett.*, 41(11):2402–2405, Jun 2016.
- [PRGL⁺14] P. Parra-Rivas, D. Gomila, F. Leo, S. Coen, and L. Gelens. Third-order chromatic dispersion stabilizes Kerr frequency combs. *Opt. Lett.*, 39(10):2971–2974, May 2014.
- [PRK01] A. Pikovsky, M. Rosenblum, and J. Kurths. *Synchronization: A Universal Concept in Nonlinear Sciences*. Cambridge University Press, New York, 2001.
- [PRKGG16] P. Parra-Rivas, E. Knobloch, D. Gomila, and L. Gelens. Dark solitons in the Lugiato-Lefever equation with normal dispersion. *Phys. Rev. A*, 93:063839, Jun 2016.
- [PSHV17] A. Pimenov, S. Slepneva, G. Huyet, and A. G. Vladimirov. Dispersive time-delay dynamical systems. *Phys. Rev. Lett.*, 118:193901, May 2017.
- [PTVF07] W. H. Press, S. A. Teukolsky, W. T. Vetterling, and B. P. Flannery. *Numerical Recipes: The Art of Scientific Computing*. Cambridge University Press, August 2007.
- [RBE15] A. F. J. Runge, N. G. R. Broderick, and M. Erkintalo. Observation of soliton explosions in a passively mode-locked fiber laser. *Optica*, 2(1):36–39, Jan 2015.
- [Ros96] N. N. Rosanov. I Transverse patterns in wide-aperture nonlinear optical systems. volume 35 of *Progress in Optics*, pages 1 – 60. Elsevier, 1996.
- [RWM⁺10] B. Rudin, V. J. Wittwer, D. J. H. C. Maas, M. Hoffmann, O. D. Sieber, Y. Barbarin, M. Golling, T. Südmeyer, and U. Keller. High-power MIXSEL: an integrated ultrafast semiconductor laser with 6.4 W average power. *Opt. Express*, 18(26):27582–27588, Dec 2010.
- [SCAA00] J. M. Soto-Crespo, N. Akhmediev, and A. Ankiewicz. Pulsating, Creeping, and Erupting Solitons in Dissipative Systems. *Phys. Rev. Lett.*, 85:2937–2940, Oct 2000.
- [SE03] F. Sagués and I. R. Epstein. Nonlinear chemical dynamics. *Dalton Trans.*, pages 1201–1217, 2003.
- [SH77] J. Swift and P. C. Hohenberg. Hydrodynamic fluctuations at the convective instability. *Phys. Rev. A*, 15:319–328, Jan 1977.
- [Sie86] A. E. Siegman. *Lasers*. University Science Books, 1986.

[SL66] P. P. Sorokin and J. R. Lankard. Stimulated emission observed from an organic dye, chloro-aluminum phthalocyanine. *IBM Journal of Research and Development*, 10(2):162–163, 1966.

[SLLP64] P. P. Sorokin, J. J. Luzzi, J. R. Lankard, and G. D. Pettit. Ruby laser Q-switching elements using phthalocyanine molecules in solution. *IBM Journal of Research and Development*, 8(2):182–184, 1964.

[SSP91] F. Salin, J. Squier, and M. Piché. Mode locking of Ti:Al₂O₃ lasers and self-focusing: a Gaussian approximation. *Opt. Lett.*, 16(21):1674–1676, Nov 1991.

[SSV66] F. P. Schäfer, W. Schmidt, and J. Volze. Organic dye solution laser. *Applied Physics Letters*, 9(8):306–309, 1966.

[ST58] A. L. Schawlow and C. H. Townes. Infrared and optical masers. *Phys. Rev.*, 112:1940, 1958.

[TBC⁺13] M. Tlidi, L. Bahloul, L. Cherbi, A. Hariz, and S. Coulibaly. Drift of dark cavity solitons in a photonic-crystal fiber resonator. *Phys. Rev. A*, 88:033502, Sep 2013.

[TFG⁺04] A. C. Tropper, H. D. Foreman, A. Garnache, K. G. Wilcox, and S. H. Hoogland. Vertical-external-cavity semiconductor lasers. *J. Phys. D: Appl. Phys.*, 37:R75–R85, 2004.

[TFHE⁺19] U. Thiele, T. Frohoff-Hülsmann, S. Engelnkemper, E. Knobloch, and A. J. Archer. First order phase transitions and the thermodynamic limit. *New Journal of Physics*, 21(12):123021, dec 2019.

[TG10] Mustapha Tlidi and Lendert Gelens. High-order dispersion stabilizes dark dissipative solitons in all-fiber cavities. *Opt. Lett.*, 35(3):306–308, Feb 2010.

[TMMC17] J. H. Talla Mbé, C. Milián, and Y. K. Chembo. Existence and switching behavior of bright and dark Kerr solitons in whispering-gallery mode resonators with zero group-velocity dispersion. *The European Physical Journal D*, 71(7):196, Jul 2017.

[Tre69] E. Treacy. Optical pulse compression with diffraction gratings. *IEEE Journal of Quantum Electronics*, 5(9):454–458, 1969.

[UA05a] N. G. Usechak and G. P. Agrawal. Rate-equation approach for frequency-modulation mode locking using the moment method. *J. Opt. Soc. Am. B*, 22(12):2570–2580, Dec 2005.

[UA05b] N. G. Usechak and G. P. Agrawal. Semi-analytical technique for analyzing mode-locked lasers. *Optics express*, 13:2075–2081, 2005.

- [UWR14] H. Uecker, D. Wetzel, and J. D. M. Rademacher. pde2path - a Matlab package for continuation and bifurcation in 2D elliptic systems. *Numerical Mathematics: Theory, Methods and Applications*, 7(1):58–106, 002 2014.
- [VGT18] A. G. Vladimirov, S. V. Gurevich, and M. Tlidi. Effect of Cherenkov radiation on localized-state interaction. *Phys. Rev. A*, 97:013816, Jan 2018.
- [vH92] W. van Saarloos and P.C. Hohenberg. Fronts, pulses, sources and sinks in generalized complex ginzburg-landau equations. *Physica D: Nonlinear Phenomena*, 56(4):303–367, 1992.
- [vHMSZ01] J. von Hardenberg, E. Meron, M. Shachak, and Y. Zarmi. Diversity of vegetation patterns and desertification. *Phys. Rev. Lett.*, 87:198101, Oct 2001.
- [VRW11] A. G. Vladimirov, D. Rachinskii, and M. Wolfrum. *Nonlinear Laser Dynamics*, chapter 8, pages 183–216. John Wiley & Sons, Ltd, 2011.
- [VT05] A. G. Vladimirov and D. Turaev. Model for passive mode locking in semiconductor lasers. *Phys. Rev. A*, 72:033808, Sep 2005.
- [Win01] A. T. Winfree. *The Geometry of Biological Time*, volume 12 of *Interdisciplinary Applied Mathematics*. Springer, New York, NY, 2001.
- [WOTG00] H. Ward, M. N. Ouarzazi, M. Taki, and P. Glorieux. Influence of walkoff on pattern formation in nondegenerate optical parametric oscillators. *Phys. Rev. E*, 63:016604, Dec 2000.
- [WT02] F. Wise and P. Di Trapani. Spatiotemporal solitons. *Opt. Photon. News*, 13(2):28–32, Feb 2002.
- [WY06] M. Wolfrum and S. Yanchuk. Eckhaus instability in systems with large delay. *Physical Review Letters*, 96(22):220201, 2006.
- [XXL⁺15] X. Xue, Y. Xuan, Y. Liu, P. H. Wang, S. Chen, J. Wang, D. E. Leaird, M. Qi, and A. M. Weiner. Mode-locked dark pulse Kerr combs in normal-dispersion microresonators. *Nature Photonics*, 9:594, Aug 2015.
- [Yan05] S. Yanchuk. Properties of stationary states of delay equations with large delay and applications to laser dynamics. *Mathematical Methods in the Applied Sciences*, 28(3):363–377, 2005.
- [YG17] S. Yanchuk and G. Giacomelli. Spatio-temporal phenomena in complex systems with time delays. *Journal of Physics A: Mathematical and Theoretical*, 50(10):103001, 2017.
- [YRSW19] S. Yanchuk, S. Ruschel, J. Sieber, and M. Wolfrum. Temporal dissipative solitons in time-delay feedback systems. *Phys. Rev. Lett.*, 123:053901, Jul 2019.

[YW10] S. Yanchuk and M. Wolfrum. A multiple time scale approach to the stability of external cavity modes in the Lang–Kobayashi system using the limit of large delay. *SIAM Journal on Applied Dynamical Systems*, 9(2):519–535, 2010.

[Zak68] V.E. Zakharov. Stability of periodic waves of finite amplitude on the surface of a deep fluid. *Sov. Phys. J. Appl. Mech. Tech. Phys.*, 4:190–194, 1968.

[Zak72] V. E. Zakharov. Exact theory of two-dimensional self-focusing and one-dimensional self-modulation of waves in nonlinear media. *Sov. Phys. JETP*, 35(5):908–914, 1972.

Acknowledgements

I thank my supervisors for their dedication in fostering this endeavor and for the fun we had alongside.

Ich danke meiner Familie für immerwährende Unterstützung und Ermutigung.

Ich danke meinen Freunden in Deutschland, mit denen ich über die letzten Jahre viel zu wenig Zeit verbringen konnte.

Agradezco a Fabio por toda la diversión en el despacho, en Palma y en la isla.

Agradezco a Patricia por su amistad y por un comienzo más fácil en España.

I thank the *Laser Dynamics* group at WIAS Berlin for a most fruitful and enjoyable research stay.

Ich danke der Arbeitsgruppe *Selbstorganisation und Komplexität* und der WWU unter Leitung von Prof. Dr. Uwe Thiele für die stehts angenehme Zeit und insbesondere für das Ausrichten des jährlichen Zaferna-Workshops.

Eu te amo Fofa

Lebenslauf

Name	Christian Schelte
Geburtsdatum	25.08.1988
Geburtsort	Iserlohn
Staatsangehörigkeit	deutsch

Schulausbildung

1995–1999	Grundschule im Wiesengrund, Iserlohn
1999–2008	Gymnasium an der Stenner, Iserlohn
14.06.2008	Allgemeine Hochschulreife

Zivildienst

09/2008 – 05/2009 Technische Abteilung, St. Elisabeth Hostpital, Iserlohn

Studium

10/2009 – 09/2013	Bachelorstudium der Physik an der Westfälischen Wilhelms-Universität Münster
10/2013 – 09/2016	Masterstudium der Physik an der Westfälischen Wilhelms-Universität Münster

Promotionsstudium

seit 05/2017	Binationale Promotion am Institut für Theoretische Physik der Westfälischen Wilhelms-Universität Münster sowie am Departament de Física der Universitat de les Illes Balears Unter der Betreuung von PD Dr. Svetlana Gurevich und Prof. Dr. Julien Javaloyes
02/2019 – 03/2019	Aufenthalt in der Forschungsgruppe für Laserdynamik am Weierstraß-Institut für Angewandte Analysis und Stochastik, Berlin Unter der Betreuung von Andrei G. Vladimirov

Berufstätigkeit

05/2014 – 03/2015 Studentische Hilfskraft am Institut für Theoretische Physik der Universität Münster

04/2015 – 09/2015 Studentische Hilfskraft am Institut für Didaktik der Physik der Universität Münster

10/2015 – 03/2016 Studentische Hilfskraft am Institut für Theoretische Physik der Universität Münster

02/2017 – 04/2017 Wissenschaftliche Hilfskraft am Institut für Theoretische Physik der Universität Münster

05/2017 – 04/2021 Contrat de Formación de Personal Investigador (beca predoctoral FPI), Departament de Física, Universitat de les Illes Balears

Stipendien

05/2017 – 04/2021 Formación de Personal Investigador (beca predoctoral FPI), Referencia de la Ayuda: BES-2016-077146, Referencia del Proyecto: TEC2015-65212-C3-3-P, Ministerio de Economía y Competitividad, Gobierno de España